# Development of biomimetic *in vitro* models of large airways

**Raffaello Sbordoni**

**Thesis submitted in fulfilment of the requirements for the degree of**
**Doctor of Philosophy**

**Ear Institute**
**University College London**

I, Raffaello Sbordoni, confirm that the work presented in this thesis is my own. Where information has been derived from other sources, I confirm that this has been indicated in the thesis.

**Signed:**

**Date:** 26 June 2022

# Abstract

Routinely adopted *in vitro* models of the respiratory tract do not reproduce the complexity associated *in vivo* with the cellular milieu, such as the presence of an extracellular matrix (ECM), the crosstalk between multiple cell types, and the inclusion of physiological mechanical stimuli. In this work, different strategies were assessed for the development of a biomimetic, high-throughput *in vitro* model of the human primary and secondary bronchi, replicating the complexity of the cellular environment as observed *in vivo* whilst maintaining cost-efficiency and reproducibility.

A first strategy centred on the seeding of human bronchial epithelial cells (HBECs) on decellularised bronchial tissue. However, low cell adherence on the tissue-derived scaffolds was reported. A second approach was based on the use of a commercial decellularised lung-derived hydrogel termed “DLH”. Whilst HBECs adhered on the hydrogel, they did not reach confluency. A third strategy was centred on the use of commercial high-throughput microfluidic chips. In these platforms, HBECs adhered and proliferated. Additionally, the inclusion of fluid flow increased cell survival and proliferation. However, issues associated with the contraction of the hydrogel included in the platforms and cell death at late timepoints impeded the onset of mucociliary differentiation. Finally, a fourth strategy centred on the use of high-throughput screening (HTS), 96-well plate-format transwell® systems seeded with HBECs, in co-culture with human lung fibroblasts (HLFs) seeded on DLH. The DLH did not have any adverse paracrine effects on the mucociliary differentiation of HBECs. However, variable results were

obtained with regards to the seeding of HLFs on the DLH, as the cells displayed a spindle-like or a circular shape in separate experiments. Whilst further optimisation is necessary, the combination of HBECs, HLFs and DLH on HTS transwell® systems proved to be a promising strategy for the development of a biomimetic bronchial *in vitro* model.

# Impact statement

Diseases of the respiratory tract exert a considerable toll on global health (23). For instance, as of 2019, asthma affected 262 million people (24), whilst the currently ongoing COVID-19 pandemic has caused more than 6 million deaths worldwide (28). Additionally, climate change will lead to an increase in morbidity and mortality of respiratory conditions, due to increases in the concentration of ground-level ozone, allergens and particulate matter (317).

To decrease the global burden associated with pathologies affecting the respiratory tract, it is necessary to develop more effective drugs and treatments. However, issues associated with currently adopted *in vitro* models of the respiratory tract undermine the efficiency of the drug discovery process, whilst also hindering academic research on respiratory biology. In particular, routinely utilized *in vitro* models do not replicate aspects of the cellular environment observable *in vivo*, such as the interaction between multiple cell types, the bioactive effects of the ECM, and the mechanical stimuli associated with the microenvironment of the respiratory tract. It is therefore necessary to include these features in novel *in vitro* models of the respiratory tract. Moreover, in order to be adopted on a wide scale, these models need to be cost-efficient, reproducible, and to have a high throughput.

In this work, various strategies were tested for the development of an *in vitro* model of the primary and secondary human bronchi, capable of addressing the shortcomings of routinely adopted models. Researchers involved in the development of novel *in vitro* models of the respiratory tract will benefit from the

information provided in this work, which can guide them in the selection of an appropriate cell culture platform. The findings of this study are relevant to both academic and industrial settings, as novel models will be useful to facilitate both the study of human respiratory biology and the development of novel treatments and drugs targeting pathologies of the respiratory tract. Additionally, the observations made during the course of this work can be of use to researchers working on the development of *in vitro* models of other epithelialized organs, such as the kidney and the intestine.

# Acknowledgments

Firstly, I would like to thank my supervisors, Prof. Martin Birchall, Dr Nazia Mehrban, Prof. James Phillips, and Dr Sarah Hopkins, for their scientific support and patient guidance throughout this work.

I would also like to thank the London Interdisciplinary Biosciences Consortium, GlaxoSmithKline, and the Biotechnology and Biological Sciences Research Council for funding my work.

My gratitude extends to the scientists at the GSK Stevenage facility for their technical support and for allowing me to use their laboratories, and to Prof. O'Callaghan and his group at the UCL Institute of Child Health for letting me use their high-speed camera.

Additionally, I would like to thank the members of the laboratory at the UCL Ear Institute for making a pleasant work environment. In particular, thanks to Anwen for her help with the Scanning Electron Microscopy and to Caitlin for being a great lab manager.

Finally, thanks to Rozina for relentlessly encouraging me throughout these years, and thanks to my family, for their unconditional and loving support.

# Table of contents

# Index of figures

**Chapter 4**

# Index of tables

# Acronyms

**2D:** two-dimensional

**3D:** three-dimensional

**4 % PFA:** 4 % w/v paraformaldehyde in phosphate-buffered saline

**A/A:** Antibiotic-Antimycotic solution

**Ac-tub:** acetylated tubulin

**ACF:** animal component-free

**AFS:** attenuated fibroblasts sheath

**ALI:** air-liquid interface

**ASL:** airway surface liquid

**B-ALI:** bronchial air-liquid interface medium

**BEBM:** bronchial epithelial basal medium

**BEGM:** brochial epithelial growth medium

**CD4:** cluster of differentiation 4

**CHAPS:** 3-((3-cholamidopropyl) dimethylammonio)-1-propanesulfonate

**COPD:** chronic obstructive pulmonary disease

**d:** days

**DAPT:** (2S)-N-[(3,5-Difluorophenyl)acetyl]-L-alanyl-2-phenyl]glycine 1,1-dimethylethyl ester

**DLH:** commercial decellularised lung ECM hydrogel

**DMSO:** dimethyl sulfoxide

**DPBS--:** Dulbecco's phosphate buffered saline without calcium chloride and magnesium chloride

**ECM:** extracellular matrix

**EMTU:** epithelial-mesenchymal trophic unit

**EVs:** extracellular vesicles

**FFT:** fast Fourier transform

**FGM-2:** fibroblasts growth medium 2

**GelMA:** gelatin methacrylate

**GWAS:** genome-wide association studies

**h:** hour

**H&E:** Haematoxylin and Eosin

**HBECs:** human bronchial epithelial cells

**HBSS--:** Hank's Balanced Salt Solution without calcium chloride and magnesium chloride

**HBSS:** HEPES Buffered Saline Solution

**HBSS++:** Hank's Balanced Salt Solution with calcium chloride and magnesium chloride

**HEPES:** 4-(2-hydroxyethyl)-1-piperazineethanesulfonic acid

**HepMA:** heparin methacrylate

**HLFs:** human lung fibroblasts

**HMV:** high medium volume

**Hoechst:** Hoechst 33342

**hTERT:** human telomerase reverse transcriptase

**HTS:** high-throughput screening

**ICL:** immortalised cell line

**IL-1$\alpha$:** interleukin 1 – alpha

**IL-4:** interleukin 4

**IL-5:** interleukin 5

**iPSCs:** induced pluripotent stem cells

**IPF:** idiopathic pulmonary fibrosis

**LMV:** low medium volume

**LMV2:** low medium volume-bottom

**min:** minutes

**miRNA:** microRNA

**MUC5AC:** mucin 5-AC

**MMP:** matrix metalloproteinases

**NME:** new molecular entities

**N:** newton

**OOAC:** organ-on-a-chip

**OP:** Organoplate®

**OGP:** OrganoPlate® Graft

**OP1:** Organoplate® version 1

**OP2:** Organoplate® version 2

**PALI:** Pneumacult-ALI

**PCL:** polycaprolactone

**PBS:** phosphate-buffered saline

**PEG:** poly(ethylene glycol)

**PEGDA:** poly(ethylene glycol) diacrylate

**PEGDMA:** poly(ethylene glycol) dimethacrylate

**PVA:** poly(vinyl alcohol)

**PNECs:** pulmonary neuroendocrine cells

**ROI:** region of interest

**RT:** room temperature

**SARS-CoV-2:** severe acute respiratory syndrome coronavirus 2

**SBS:** Society for Biomolecular Screening

**SDC:** sodium deoxycholate

**SEM:** scanning electron microscopy

**TEER:** trans-epithelial electrical resistance

**TGF-β:** transforming growth factor β

**TNF- α:** tumour necrosis factor-alpha

**TNS:** Trypsin Neutralising Solution

**TX-100:** Triton X-100

**UPW:** ultrapure water

**ZO-1:** Zonula Occludens-1

# Chapter 1

In this chapter, a general introduction to the main themes of the present work will be presented.

A description of the respiratory tract will be provided, with a focus on the primary and secondary bronchi. The epidemiology of the main diseases affecting human airways will also be discussed, alongside a discussion of the issues currently affecting the drug discovery process, both inside and outside the respiratory field. Additionally, animal and *in vitro* models of airways will be described, and their limitations will be delineated. Finally, the aims and objectives of this work will be outlined.

## 1. 1. General introduction

### 1.1.1. Gross anatomy and physiology of the respiratory tract

The exchange of oxygen and carbon dioxide between the human body and the external environment is performed by the respiratory tract (1). The most cephalad portion of the respiratory tract is composed of the upper airway, through which gas can both access and flow out of the human body (2). The upper airway includes the nose, oral cavity, pharynx and larynx (2). Distally, the respiratory tract is composed of a conductive zone, in which air can flow but no gas exchange between the human body and the external environment occurs, and a respiratory zone, in which the gas exchange takes place (2).

The conductive zone is composed of the respiratory tree formed by the trachea and its proximal branches or “generations” (2), as depicted in Figure 1.1. In particular, the trachea branches into 2 primary bronchi, each accessing a separate lung. The primary bronchi branch distally into secondary bronchi and further bronchial generations, with a decrease in diameter observable at each consecutive branch (3).

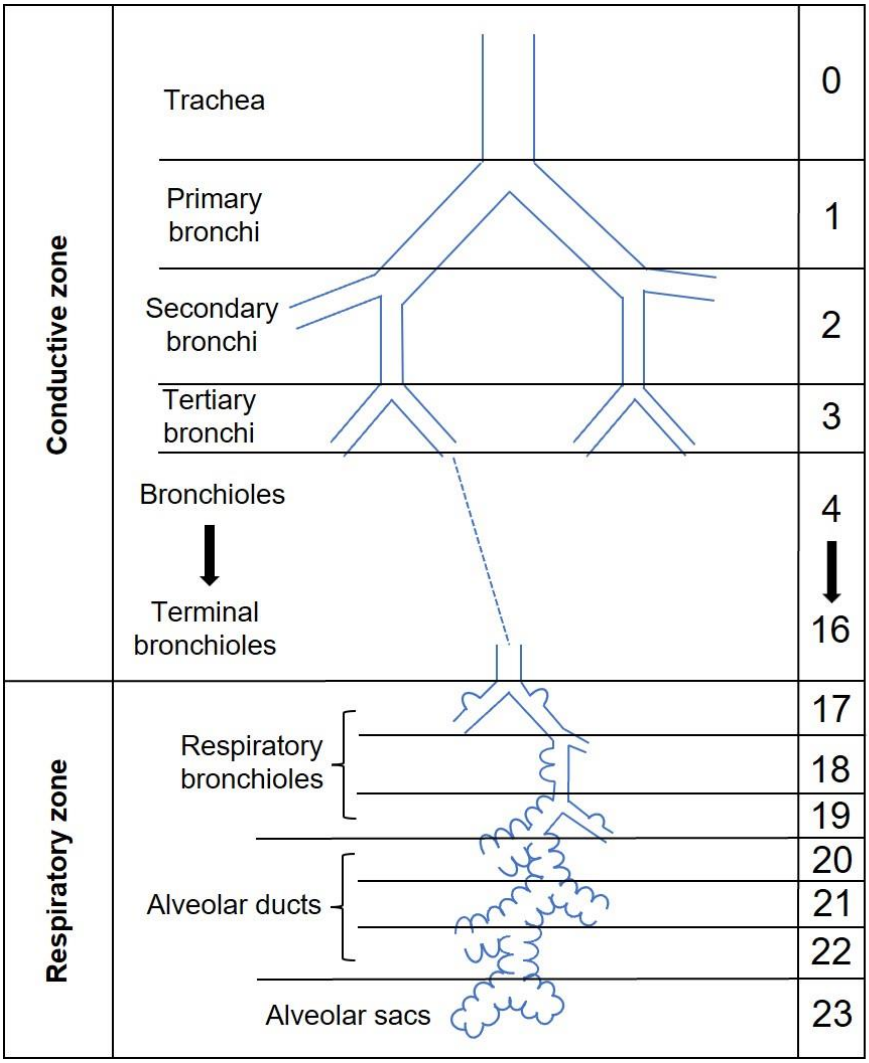


**Figure 1.1.** Schematic representation of the respiratory tract comprised between the trachea and the alveolar region.

Whilst the trachea and the proximal bronchial branches have a cartilaginous wall, the presence of cartilage diminishes in further bronchial generations, and distal branches do not include a cartilaginous layer (1). These cartilage-free bronchial

generations are classified as “bronchioles”, and they form further branches called “terminal bronchioles”, which constitute the most distal portion of the conductive zone (3). Terminal bronchioles are connected to the respiratory bronchioles, which form part of the alveolar volume. Respiratory bronchioles are connected through the alveolar ducts to the alveolar sacs, where the gas exchange with the circulatory system takes place by means of diffusion across the wall of alveoli (3). The respiratory bronchioles, alveolar ducts and the alveoli constitute the respiratory zone of the respiratory tract (3).

The airflow between the alveoli and the external environment is divided into an inspiratory and an expiratory phase (2). The inspiratory phase is initiated by the contraction of the diaphragm and of the external intercostal muscles, which increase the volume of the lungs, thus generating an airflow running through the conductive airways towards the alveoli (2). Concurrently, oxygen and carbon dioxide are exchanged between the alveoli and the circulatory system via diffusion across the alveolar wall. During the expiratory phase, airflow is directed outside of the human body. At rest, the expiratory phase is driven by the recoil of the lungs and does not involve the contraction of expiratory muscles (2). This group of muscles includes the internal intercostals and the muscles of the anterior abdominal wall (2), which contract to increase the breathing frequency, as required for example during physical activity.

### 1.1.2. Histological features of the large bronchi

The present work focuses on primary and secondary bronchi. Given their relatively large diameter as compared to more distal bronchial branches, in this work primary and secondary bronchi are collectively termed “large” bronchi. A scheme

illustrating the histological strata forming the large bronchi, and the main cell types observable in each stratum, can be found in Figure 1.2.

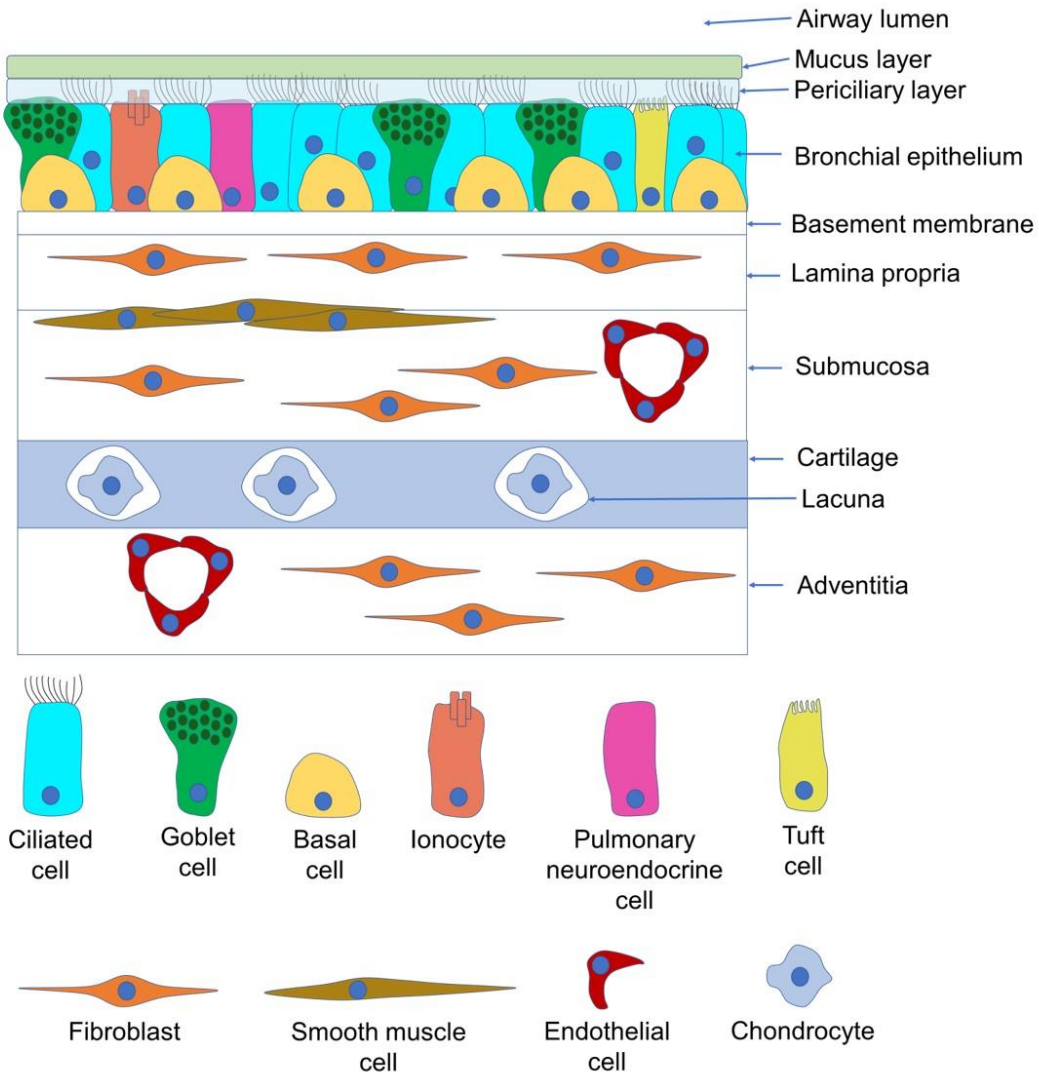


**Figure 1.2.** Histological strata and main cell types found in the human large bronchi.

The most external tissue layer associated to large bronchi is the tunica adventitia (4). Structures composed of hyaline cartilage are located below the adventitia (4). As a result of the rigidity of the cartilaginous structures, bronchial patency is maintained. In the primary bronchi, most of the cartilaginous structures encircle the entire bronchial circumference, taking the shape of rings. However, as the diameter of the bronchi decreases, cartilaginous rings are substituted by cartilaginous plaques that do not encircle the entire bronchus (4). Below the tunica adventitia

and cartilaginous structures, a submucosal layer can be found, including numerous submucosal glands which discharge mucus into the bronchial lumen (4). Additionally, blood vessels can be found in both the submucosal (1) and the adventitial (4) layers. Smooth muscle, which is assembled into helical bundles within bronchi (120) and therefore is not continuous in bronchial cross sections, can also be found between the submucosa and the mucosa, which is the tissue layer in contact with the lumen of large bronchi (4). The mucosa comprises a tissue layer called “lamina propria” and a thin tissue layer called “basement membrane”, on which bronchial epithelial cells adhere (5).

A variety of cells populate the large bronchi. Chondrocytes, located in enclosures in the cartilage called “lacunae”, secrete and maintain the surrounding extracellular matrix (ECM) (6), therefore contributing to the mechanical stability of large bronchi. Blood vessels passing through the submucosal and adventitial layers are lined with endothelial cells (7), which regulate the vascular barrier function. Smooth muscle cells can be found in the bronchial smooth muscle. Whilst the exact role of the bronchial smooth muscle in large bronchi is unclear and is the object of discussion (8), bronchial smooth muscle cells have been shown to play a predominant role in the pathophysiology of asthma (9). Fibroblasts can be found in the submucosal tissue, and their main role is to produce, maintain, and regulate the bronchial ECM (10). The large bronchi also include neural projections related to afferent sensory neurons and to efferent motor neurons (11). Additionally, airways include resident immune cells, such as macrophages and T cells (12). Finally, human bronchial epithelial cells (HBECs) form the pseudostratified columnar epithelium lining the surface of large bronchi.

The main subtypes of HBECs lining the bronchial epithelium are basal cells, goblet cells, and ciliated cells (13). Basal cells are considered to be candidate epithelial stem cells capable of differentiating into other cellular subsets composing the bronchial epithelium (14). Goblet cells, which are located both in the lumen of large bronchi and in the submucosal glands (15), secrete high molecular weight glycoproteins called “mucins”, which are mixed with other proteins, lipids, and glycoconjugates in an aqueous solution to form mucus (16). The function of mucus is to trap foreign bodies that come in contact with the mucosa of airways (16). The mucus layer overlies the periciliary layer (17), composed of periciliary fluid. This fluid is set in movement in the proximal-distal axis by the beating of motile cilia protruding from the apical surface of the ciliated bronchial epithelial cells (17). In this way, the mucus layer on top of the periciliary fluid is transported away from the bronchi (17) towards the pharynx. In addition to the main cell types forming the epithelium of large bronchi, epithelial cells found at a relatively lower frequency include pulmonary neuroendocrine cells (PNECs; 18), pulmonary ionocytes (19), and tuft cells (19). PNECs are the only innervated cells in the airways epithelium (20). PNECs can sense oxygen in the airway (322), and also have a regulatory role in the context of inflammation (18). Pulmonary ionocytes regulate mucus hydration by releasing chloride ions via the cystic fibrosis transmembrane conductance regulator (19), whilst studies on mice indicate that tuft cells might have a chemosensory function (21, 22).

### 1.1.3. Diseases of the large bronchi and problems with drug discovery

Pathologies affecting the respiratory tract, including the large bronchi, impose a vast burden on society (23). Globally, in 2019, 212 million people were affected by chronic obstructive pulmonary disease (COPD) (24). On the same year, COPD

caused 3.28 million deaths (24), thus making it the third leading cause of mortality worldwide (25). Additionally, in 2019, 262 million people worldwide were living with asthma (24): in particular, asthma is considered to be the most common paediatric chronic disease globally (26). Seasonal influenza also imposes a considerable burden on global healthcare, causing an estimated amount of 389000 deaths annually (27). Recently, COVID-19 caused more than 6 million deaths worldwide since the pandemic onset in 2019 (28) and inflicting considerable damage to the global economy (29). Asthma, COPD, seasonal influenza, and COVID-19 affect both large bronchi and distal airways. Diseases that are specifically related to large airways, such as Mounier-Kuhn Syndrome (30) and relapsing polychondritis (31) are relatively less prevalent (32). However, these pathologies can cause severe respiratory dysfunction (32). To lessen the global burden imposed by respiratory diseases, it is important to develop new treatments and drugs. In recent years, however, the output of the pharmaceutical industry has undergone a period of decline.

A major sign of drug industry crisis can be tracked to the years 1950-2010 and has been summarised by “Eroom’s Law”, described in 2012 by Scannell *et al*., (33). Inspired by Moore’s law, which states that the number of transistors in an integrated circuit doubles every 2 years (34), Eroom’s Law is the observation that, in the 1950-2010 period, the number of new molecular entities (NME) approved by the US Food and Drug Administration per billion US dollars of R&D spending halved approximately every 9 years, in inflation-adjusted terms (33). The trend associated with Eroom’s Law can be observed in Figure 1.3.

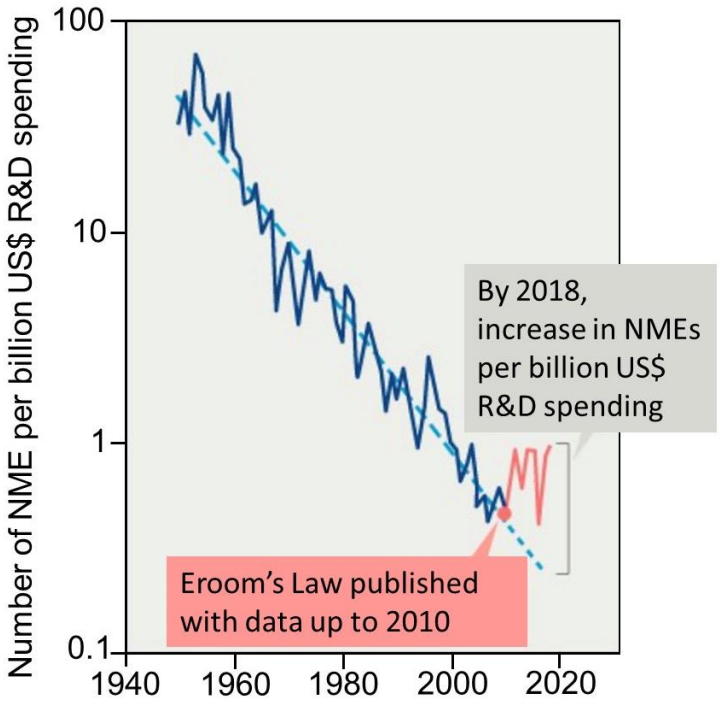


**Figure 1.3.** A graphical rendition of Eroom's Law. The X axis indicated the years between 1940 and 2020, and the Y axis indicates the number of NME approved per billion US$. Adapted with permission from Ringel *et al*., (34).

One line of explanation for this trend lies in the existence of drugs that were already considered both safe and effective for a majority of patients (33), thus raising the approval threshold for safety and efficacy associated with newer drugs. Whilst Eroom's Law is valid for the 1950-2010 period, a relative increase in NME launched per billion dollars in the 2010-2020 decade has been observed by Ringel *et al*., (34). Amongst other explanations, reasons proposed for this improvement lie in the discovery of a novel set of targets obtained from genome-wide association studies (GWAS), in concomitance with an increased effort towards the development of drugs addressing rare diseases. However, the recent relaxation of Eroom's Law might be temporary, and launches of new drugs might decline once the main targets obtained from GWAS, and those associated with rare diseases, have been exhausted (47).

Issues associated with drug discovery can be observed in the respiratory field. For example, the majority of drugs prescribed for COPD falls in the category of bronchodilators (35), and only one novel drug class, constituted by the inhibitors of phosphodiesterase type 4, has been approved for the treatment of COPD in the past 25 years (35). Moreover, the majority of currently approved drugs treat COPD symptoms, but do not address the underlying disease progression (35). In general, low efficacy of new candidate drugs, coupled with a slow pace of drug discovery, are common issues affecting the field of respiratory medicine (36). In addition to the aforementioned issues lying at the base of Eroom's law, other problems specifically related to the respiratory field hinder drug development in this area. For example, the inhalation route of drug delivery poses challenges with regards to the development of novel treatments (37). Furthermore, drug development is also complicated by the heterogeneity of clinical manifestations and pathological mechanisms that characterise inflammatory diseases of the airways, including asthma and COPD (38).

In addition to the issues described in this section, problems associated with drug discovery in the respiratory field can be ascribed to the use of animal and cellular models that poorly reflect the complex reality of human pathologies.

### 1.1.4. Animal models of large airways and their limitations

Experiments on animal models are executed in order to test novel treatments and to study pathological and physiological processes that are also observable in humans. Various types of animal models are used in biomedical science to replicate a disease (39). "Spontaneous" models rely on naturally occurring genetic variants of particular strains of animals, such as in the case of athymic nude mice

(40). “Genetically modified” models are developed through genetic modification (39). For example, loss of function or “knock-out” animal models of cystic fibrosis can be developed by disrupting the gene associated with the cystic fibrosis transmembrane conductance regulator protein (42). Another class of animal models are termed “induced” models, and are developed by experimentally inducing the targeted pathological features, for example by chemical or surgical means (39). For instance, models of COPD can be developed by exposing animals to cigarette smoke (43), whilst induced models of asthma can be developed by exposure to allergens such as ovalbumin (44). “Negative” models are animals that fail to develop a disease in response to a treatment that induces the pathology in other animals (39), which could provide information related to the biological mechanisms underlying the disease. An example of this model is represented by strains of mice that are less sensitive than other murine strains to the effects of *Bacillus anthracis*, as evident from inter-strain differences related to the $LD_{50}$ (45). “Orphan” models are used to replicate a pathological condition that occurs in a non-human species but that has not been reported in humans (46). However, if the disease is discovered in humans, previous veterinary studies related to the orphan model can provide scientists a base for the understanding of the human pathology (46). Finally, “surrogate” models are developed by infecting animals with a substitute pathogen to mimic a human disease (46). For example, human immunodeficiency virus can be modelled by infecting felines with feline leukemia virus (47), and mice are infected with *Salmonella tiphymurium* to mimic human infections with *Salmonella tiphy* (48).

Animal models are widely used by the scientific community for basic scientific research and for the development of novel drugs and therapies (324). In addition

to the various anatomical and physiological similarities with the human body, an advantageous feature of animal models lies in their biological complexity, as they are composed of different tissues and cell types. The biological complexity of animal models allows the study of inter-organ communication (350), which is essential for the maintenance of organisms' homeostasis. Additionally, inter-organ communication is implicated in the development of multiple pathological conditions (351). For example, liver cirrhosis is a causative factor for the development of acute kidney injury (352), and exacerbations of COPD are followed by an increased risk of developing ischemic stroke and myocardial infarction (353).

Animal models have proved to be useful to model pathologies of the respiratory tract. For instance, murine models can mimic typical pathological features of asthma, such as airways hyperresponsiveness, epithelial hypertrophy, goblet cell hyperplasia and remodelling of airways (44). Consequently, murine models have been successfully used to gain an understanding of the mechanisms underlying the development and progression of asthma, such as the role of Interleukin 5 (IL-5) (348, 349), Interleukin 4 (IL-4; 354, 355), and of cluster of differentiation 4 (CD4)+ T-lymphocytes (356). Mice, alongside other animals such as rats and guinea pigs, can also replicate features typical of COPD, such as small airways remodelling, emphysema and mucus hypersecretion (347). Therefore, animal models have been used to study various aspects of COPD, including for example the role of oxidative stress (357), microRNA (miRNA) 21 (358), and of tumour necrosis factor-alpha (TNF-α; 359).

Despite their widespread use, various problems have been associated with the use of animal models. Firstly, human diseases are rarely caused by a single factor or

by a single genetic mutation, which complicates the development of genetically modified and induced animal models (49). Moreover, pathologies rarely have a single set of symptoms, and animal models can fail to display the full symptomatic array related to a disease. This limitation is evident in animal models of COPD, as none of the models described capture all its pathological features (50). Additionally, whilst animal models display a level of similarity with the human anatomy, difficulties in adequately reproducing human diseases in animals partially lie in interspecies anatomical differences. For example, submucosal glands are absent in murine bronchi (51). Important interspecies differences can also be found on a cellular level. For instance, in the context of the respiratory epithelium, basal cells are only found in the trachea of mice, whilst in humans their distribution extends distally up to the respiratory bronchioles (52). Moreover, club cells, a type of secretory cell localised in human small airways, is commonly found in all murine conducting airways (52). Finally, there are ethical considerations with regards to the use of animals in academic and industrial contexts. In particular, the use of animals in biomedical research is regulated according to the guidelines elucidated by Russell and Burch in 1959, usually referred to as the “three Rs”: replacement, reduction, refinement (53). The “replacement” principle states that alternatives to the use of animals should be considered during the design of a scientific study where possible. The “reduction” concept indicates that the number of animals involved in a study should be kept to a minimum. Finally, the “refinement” principle states that pain and discomfort experienced by animals should be minimised.

The limitations of animal models described in this section contribute to the difficulties related to the discovery of new therapies for respiratory diseases. The use of advanced *in vitro* models of airways could circumnavigate these issues,

whilst raising fewer ethical concerns. However, current *in vitro* models have several limitations, which will be described in the following section.

### 1.1.5. In vitro models of large bronchi and their limitations

*In vitro* models of large bronchi have previously been developed using immortalised cell lines (ICL), such as BEAS-2B and 16HBE14o-, or primary cells, such as HBECs (54). The advantages of using ICL, as opposed to primary cells, are various. Firstly, ICL can be maintained in cell culture indefinitely, and have proliferation rates higher than primary cells (55). Since they are derived from a single donor, ICL do not display donor-to-donor variation, thus facilitating the comparison of results obtained from different studies. Additionally, multiomics data is publicly available for a number of cell lines, including for example data related to genomics and proteomics (56).

An issue associated with the use of ICL lies in the clonal selection during cell culture, which generates genetically heterogeneous strains within the same cell line. The formation of different genetic strains, or “genetic drift”, hinders the reproducibility of results obtained using cell lines (57). Importantly, ICL do not reproduce all the features of non-immortalised cells. For example, tight junctions between epithelial cells are a feature of the bronchial epithelium, and whilst this type of junction can be formed between 16HBE14o- cells, they are developed to a lesser extent in BEAS-2B cultures (58). Additionally, a major issue associated with the use of bronchial ICL lies in their limited capacity to secrete mucus and develop motile cilia (59), a process termed “mucociliary differentiation” and essential to representing the mucocilliary-mediated clearance function of typical healthy

airway. An exception is represented by the BCi.NS1.1 bronchial ICL, which derives from HBECs induced to over-express human telomerase reverse transcriptase (hTERT; 325), a process that hinders their replicative senescence (70). The BCi.NS1.1 ICL retains the capacity for mucociliary differentiation (325). However, the ciliation of the BCi.NS1.1 ICL is altered as compared to normal HBECs, as the motile cilia of BCi.NS1.1 cells display a dyskinetic ciliary beating pattern (326). Given the altered capacity of mucociliary differentiation displayed by bronchial ICL, *in vitro* models based on the use of bronchial ICL have a limited capacity to mimic the physical and functional features of the large bronchi, and the use of HBECs represents a valid alternative.

The use of HBECs in the context of *in vitro* modelling is advantageous due to their ability to undergo mucociliary differentiation and to form a pseudostratified columnar epithelial layer that closely mimics the bronchial epithelium (60). Also, HBECs obtained from patients affected by respiratory diseases such as asthma and COPD retain pathological features, including for example an altered cytokine release (61-65).

A problem associated with the use of primary cells is donor-to-donor variability, which increases the difficulties associated with the design of statistically robust studies. Also, primary cells have a limited proliferation capability, which decreases with population doublings. In HBECs, the decrease in proliferation capacity with increasing population doublings is paralleled by a progressive loss of mucociliary differentiation capability (66). Various strategies have been explored to increase the lifespan of HBECs whilst maintaining their differentiation potential. For example, co-culture with mitotically inhibited fibroblasts in conjunction with the

inhibition of the Rho Kinase pathway can increase the lifespan of HBECs whilst preserving their capability to undergo mucociliary differentiation (67, 68). Co-culture-free methods have also been developed, including for example the inhibition of SMAD signalling (69). However, genetic drift at high passages and resultant changes in cell behaviour could be a problem associated with the use of HBECs cultured beyond their normal proliferation limit following these methods. Other issues associated with the use of HBECs lie in the difficulties in obtaining fresh biopsies and in the cost of commercially obtained cells: to obviate these problems, induced pluripotent stem cells (iPSCs) could be used (71). Primary cells such as fibroblasts can be obtained from donors via non-invasive methods and reprogrammed to iPSC, which can then differentiate into HBECs (71). This method could increase the availability of HBECs for researchers. However, at present generating HBECs from iPSCs is a costly, long, and labour expensive procedure (72).

The earliest *in vitro* models of airways relied on submerged cultures of bronchial epithelial cells (73). Under these conditions, HBECs do not undergo mucociliary differentiation, and therefore the validity of these *in vitro* models is limited. Then, in the late 1980s, air-liquid interface (ALI) models were developed (74). In these models, HBECs are cultured on transwell® membranes within transwell® systems, which are composed of an apical well suspended on top of a larger recipient well. In particular, HBECs are seeded on top of the porous membrane of the transwell® forming the apical well of the transwell® system, as depicted in Figure 1.4.

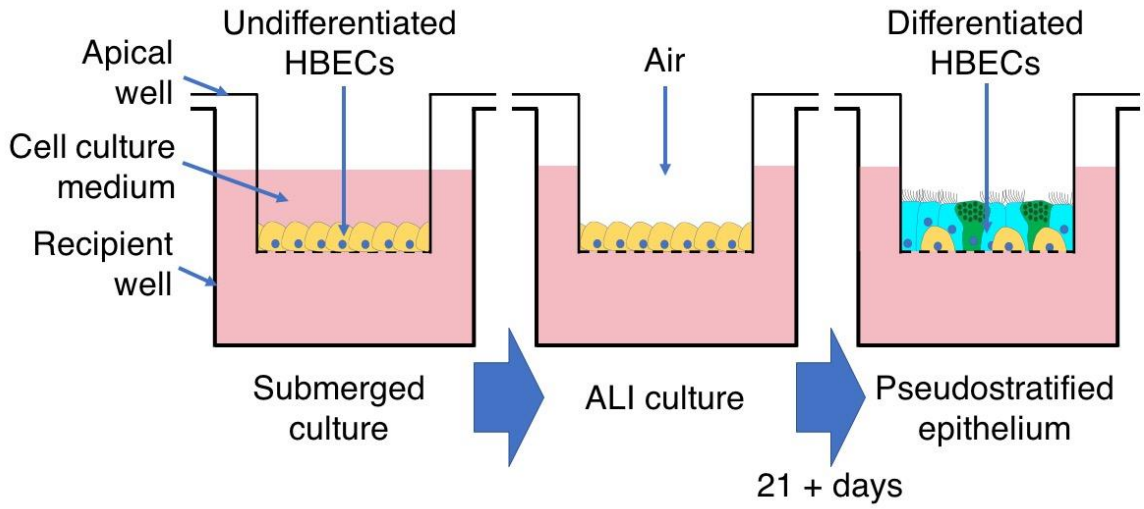


**Figure 1.4.** Stages of HBECs culture in ALI-based *in vitro* models.

When cells reach confluency, cell culture medium is removed from the apical well. In this configuration, the apical side of cells is in contact with air, whilst the basal side is in contact with the cell culture medium transuding from the recipient well to the cells through the pores of the apical well. Exposure to air induces mucociliary differentiation of HBECs (75). The presence of air on the apical side of cells also makes ALI systems better suited for toxicity studies on inhaled particles as compared to submerged models (76). Models based on ALI cultures can be used to analyse the integrity of the epithelial barrier, through the use of fluorescent dyes (78) or the measurement of trans-epithelial electric resistance (TEER; 77). Finally, bronchial *in vitro* models based on ALI cultures can incorporate other cells in co-culture, including fibroblasts (79), neutrophils (80), and macrophages (81). Given their capacity to reproduce features of the bronchial mucosa and their flexibility with regards to co-culture with other cell types, ALI-based models including HBECs represent the current gold standard with regards to the *in vitro* models of large bronchi. However, whilst commonly used *in vitro* models are useful tools for academic and industrial research, they do not provide an exact approximation of

the human large bronchi as observed *in vivo*. In particular, these models do not replicate biochemical and mechanical features associated with the bronchial ECM.

### 1.1.6. Cell – ECM interaction: role of integrins

The ECM, which is found in all human tissues, acts as a scaffold for cells to adhere to (82). Additionally, the ECM has an active role in modulating cell behaviour (82). To do so, the ECM interacts with cells through a variety of cell receptors, including integrins (83), CD44 (84), CD168 (85), syndecans (86), the discoidin domain receptors 1 and 2 (87), leukocyte-associated Ig-like receptor-1 (88) and the urokinase plasminogen activator receptor-associated protein (89). Amongst these receptors, the ECM interacts with cells mainly through integrins, a family of transmembrane heterodimeric proteins (90).

Integrins are formed by two sub-units, termed α and β (90). Eighteen types of α sub-units and eight types of β sub-units are encoded by the human genome (91). Twenty-four functional integrin receptors have been described, formed by combinations of α and β sub-units (92). The combination of α and β sub-units confers specificity to different ligands found in the ECM.

Through integrins, the ECM modulates a variety of cellular processes, including proliferation (93), survival (95), migration (94), differentiation (96), and inflammation (92). In adults, HBECs expressed at least 8 different types of integrins (97), as reported in Table 1.1.

**Table 1.1.** Integrins expressed by HBECs, including their ECM ligands. Information obtained from ref. 97.

| Integrin | Known ECM ligand(s) |
|---|---|
| α2β1 | Collagen I, Collagen IV, Tenascin V, Laminins 5, 10, 11 |
| α3β1 | Laminins 5, 10, 11 |
| α6β1 | Laminins 5, 10, 11 |
| α9β1 | Tenascin C, Osteopontin, Fibronectin |
| α5β1 | Fibronectin |
| αvβ5 | Vitronectin, Osteopontin |
| αvβ6 | Fibronectin, Tenascin C, Osteopontin, Vitronectin |
| αvβ8 | Vitronectin |

Integrins such as α3β1 and α6β4 bind ligands found in ECM components present in the basement membrane, such as laminin and collagen IV. Other integrins expressed by HBECs bind ligands related to ECM components that are not found in the basement membrane, such as tenascin, osteopontin, vitronectin and fibronectin (97). This second group of integrins likely enable the HBECs to detect and react to changes in the ECM due to inflammation and injury (97). For example, integrin αvβ6 is expressed at low levels in healthy HBECs (97), but it is markedly upregulated in HBECs found in a subset of smokers (98). Additionally, integrin α5β1 is expressed by HBECs only during epithelial injury (97) Additionally, through integrins cells can sense the stiffness (99) and topography (100) of the ECM, which stimulate a variety of cellular responses, as discussed in the next section.

### 1.1.7. Effect of mechanical and topographical properties of ECM on cell behaviour

The stiffness of a structure, such as an alveolus or a portion of bronchial ECM, can be defined as the resistance of the structure to deformation when a mechanical load is applied (101). The mechanical load applied on a structure can be a force, a moment, a stress, or a combination of these (101). However, in a

mechanobiology context, the mechanical load is typically a mechanical stress. A mechanical stress can be defined as the ratio between the force $F$, expressed in newton (N), applied on a surface of a structure, and the area $A$ of the surface, expressed in $m^2$ (102). The total mechanical stress applied on a structure consists of the sum of "shear" stress, indicated by the letter τ, resulting from forces applied parallel to the surface of the structure (102), and of "normal" stress, indicated by the letter σ, resulting from forces applied perpendicular to the surface of the structure (102). Normal stress can be "tensile" stress if it induces an elongation of the structure, or "compressive" stress if it induces its compression (102). As different types of mechanical stress can act on a structure, inducing different types of deformations, it follows that a precise definition of stiffness in the context of a scientific study would depend on the exact nature of the mechanical stress and deformation involved.

A form of stiffness can be described by the Young's modulus, which corresponds to the resistance to lengthwise deformation of a solid under compressive and/or tensile stress (102). The Young's modulus is defined in Equation 1:

$$E = \frac{\sigma}{\varepsilon}$$

(Equation 1)

where $E$ (expressed in Pascal) is the Young's modulus, $\sigma$ (expressed in $N/m^2$) is the normal stress applied perpendicular to a surface of the structure, and $\varepsilon$ (adimensional) is the lengthwise deformation of the structure (102). For example, when a thread is pulled by the effect of a tensile mechanical stress, its Young's modulus $E$ represents its resistance to elongation. The main type of mechanical stress applied by cells on the ECM is represented by the tensile stress exerted on

fibrillary structures (103). Therefore, the stiffness or resistance to deformation encountered by cells when interacting with the ECM coincides, in most studies and in the present work, with the definition of Young's modulus.

Cells can sense the stiffness of the ECM structure on which they adhere to in a variety of ways, although the precise molecular mechanisms behind this cellular function currently are not fully understood (104). A large part of the work related to the study of cell mechanotransduction is focused on the role of integrins, which relay signals related to the stiffness of the ECM to the nucleus via the cytoskeleton (105). Once the mechanical information has reached the internal side of the nucleus, it is transduced into the activation of genetic programmes that induce the cell to adapt to its surrounding environment (105). For example, a stiff ECM induces the proliferation of cell types such as endothelial cells (106) and dermal fibroblasts (107). Moreover, stiffness of the cell culture substrate modulates the differentiation of tissue-specific progenitors (108, 109). For example, cell culture on a substrate with a stiffness close to that of brain tissue induces the differentiation of neural stem cells into neurons (108), whilst the differentiation of adult cardiac progenitors into cardiomyocytes is hindered by culture on a substrate stiffer than native healthy cardiac tissue (109). In the context of cells related to the conducting airway, it has been reported that airway derived smooth muscle cell proliferation increases when cultured on substrates stiffer than healthy airway tissue (110). Moreover, increasing the stiffness of the cell culture substrate induces lung fibroblasts to differentiate into myofibroblasts (111), which secrete ECM components, such as collagens, upon lung injury and in the context of idiopathic pulmonary fibrosis (IPF; 112). A stiffer cell culture substrate also increases lung fibroblast motility (113). Additionally, cellular responses such as altered

proliferation and collagen I production induced in lung myofibroblasts by culture on stiff substrates are retained when cells are subsequently passaged to a softer substrate, and vice-versa (114). This capacity has been termed “mechanical memory” (114). The stiffness of the cell culture substrate has also been shown to influence the formation of tight junctions between bronchial epithelial cells in the work conducted by Chandrasekaran *et al*., (115). However, this study was based on the use of a bronchial ICL and not on HBECs, the latter having a phenotype closer to that observed in the bronchial epithelium *in vivo*, as previously described.

In addition to stiffness, the topography of the ECM also plays a role in directing cell behaviour. Cells can detect variations in the order of nanometres in the topography of the cell culture substrate (116). The shape, size, and arrangement of topographical features can all influence various types of cell behaviour, including cell adhesion, spreading, proliferation, and differentiation (117). For example, topographical patterns can alter human mesenchymal stem cell shape during cell culture, which in turn can influence their differentiation towards osteoblasts or adipocytes (118). In relation to cells included in the airway, it has been reported that nanotopographical features can influence human lung fibroblast proliferation and collagen I production (24). Work conducted to elucidate the effect of topographical cues on the airway’s epithelium is limited to the use of BEAS-2B bronchial ICL, in the work conducted by Soleas *et al*., (121). In this study, BEAS-2B cells aligned on a microgroove-patterned cell culture substrate, although the alignment was lost 24 h post-initiation of ALI culture. In addition to the composition, stiffness and topography of the ECM, mechanical stress exerted on cells also regulate cell behaviour, as described in the next section.

### 1.1.8. Effect of mechanical stress on cell behaviour

Cells in human tissues are exposed to a variety of mechanical stresses. For example, endothelial cells are subjected to shear stress as a result of blood flow, to tensile stress as a result of the dilation of blood vessels, and to compressive stress as a result of blood's hydrostatic pressure. As a result of mechanical stress, cell behaviour is altered in a variety of ways, including: cell proliferation, differentiation, and synthesis of ECM components, cytokines and growth factors (122). Mechanical forces also regulate various aspects of development (123).

A positive pressure value is observed in large bronchi during inspiration (124). The effect of a positive pressure within an epithelialised tube is the exertion of both tensile and compressive stress on the epithelial cells lining its lumen (125). In particular, pressure dilates the epithelialized tube, thus stretching cells and exerting a tensile stress on them, whilst at the same time exerting a compressive stress on the cell surface (125). However, the positive pressure applied on large bronchi during inspiration is relatively low, as it is estimated to be less than 3 Pa (124). For reference, the values of both blood and cerebrospinal fluid pressure in healthy adults are of the order of KPa (126, 127). In addition to the positive pressure exerted on large bronchi during inspiration, a negative pressure is exerted during expiration (124). However, analogously to the inspiration-induced bronchial positive pressure, expiration-induced negative pressure has a relatively low value, estimated to be less than 10 Pa (124). Moreover, large bronchi include cartilaginous structures that prevent their excessive dilation or collapse, thus limiting the magnitude of mechanical deformation of the airway well that could result from any intramural pressure difference across the bronchial wall. It can

therefore be assumed that breathing-associated tensile and compressive stresses have negligible values in healthy large bronchi.

Given the small amount of tensile and compressive stress applied *in vivo,* the most relevant type of mechanical stress exerted on HBECs in the large bronchi is shear stress, which is generated by the airflow induced by breathing. In particular, shear stress in large bronchi follows the proximal-to-distal verse during inspiration, and the distal-to-proximal verse during expiration (128). Shear stress in large airways, such as large bronchi, has been estimated to be higher during expiration as compared to inspiration (124), with the highest values estimated to be in proximity of the carina, where the trachea bifurcates into the primary bronchi (124). However, the amount of airflow-related shear stress exerted on HBECs *in vivo* is likely reduced by the stress-shielding effect provided by the layer of mucus covering the airways, although this phenomenon is not included in currently published fluid dynamics models of airways. The amount of shear stress exerted by airflow is increased during cough and in the case of airway obstruction, which can lead to an increase in shear stress in proximity of the obstruction (124).

The effects of shear stress on HBECs are various. Shear stress affects the secretion of mucin 5-AC (MUC-5AC) from mucus-secreting cells, as reported by Liu *et al.*, (129). The results obtained in this study are based on the use of a bronchial ICL. Similar findings were reported in primary human nasal epithelial cells exposed to shear stress (130). In addition to the modulation of mucus composition, shear stress plays a role in the regulation of periciliary fluid height (131). Shear stress can also affect mucociliary clearance by increasing motile cilia beating frequency in murine tracheal epithelial cells (132). Finally, shear stress

also reduces the abundance of aquaporin-5, a water channel protein located on the cell membrane surface of HBECs, and enhances the epithelial barrier function (133).

As described in this introductory section, the composition of the bronchial ECM, its mechanical properties, and the mechanical stimuli generated by the process of breathing alter the behaviour of cells included in large bronchi. These features therefore must be included in *in vitro* models in order to induce a cell phenotype close to the one observed *in vivo* in non-transformed cells. The resultant *in vitro* models can be considered “biomimetic”, as opposed to the currently adopted, “traditional” *in vitro* models.

The development of biomimetic *in vitro* models of large bronchi could contribute to solve the current crisis faced by the pharmaceutical industry, particularly with regards to the development of novel drugs and treatments addressing respiratory pathologies. Moreover, biomimetic *in vitro* models of large bronchi could be used in academic settings to further our knowledge of respiratory physiology and pathology, particularly if the newly developed models are reproducible, easy to use, and cost-effective.

## 1.2. Aims and objectives

The aim of this work is to develop a biomimetic *in vitro* model of the human large bronchi capable of addressing the shortcomings of traditional *in vitro* models. In particular, key features of the model will be:

- Inclusion of primary human non-transformed cells associated with the bronchial mucosa and submucosa. In particular, the main cell types included in the model will be HBECs and fibroblasts obtained from the respiratory tract
- Inclusion of materials mimicking the ECM associated with the respiratory tract, in order to replicate mechanical and biochemical stimuli associated with the bronchial environment
- Miniaturisation, in order to increase the model throughput whilst limiting the number of cells and quantity of materials used for the development of the model and its use
- Reproducibility. To this end, cost-effective, commercially available materials and cell culture platforms will be used wherever possible, as opposed to the use of materials and devices developed in-house.

The objectives of this work are listed below:

- Characterisation of ECM-mimicking materials selected as cell culture substrate. In particular, the material will be characterised through histochemistry and scanning electron microscopy (SEM)
- Optimisation of cell seeding and cell maintenance. Particularly, imaging tools will be used to assess cell survival and proliferation in the model
- Analysis via imaging tools of the mucociliary differentiation of HBECs in the newly developed model, as compared to a standard *in vitro* model of airways. The assessment of mucociliary differentiation will be carried out using imaging tools.

# Chapter 2

In this chapter, an introduction on the topic of decellularisation of biological tissue and of decellularisation-derived hydrogels will be presented to the reader, followed by a description of the *in vitro* models based on these platforms. Following the introduction, an experimental section will focus on the use of decellularised bronchi and of a commercial decellularised lung-derived hydrogel as strategies for the development of a bronchial *in vitro* model. The results obtained and their discussion will then be presented to the reader.

## 2.1. Introduction

### 2.1.1. Decellularisation of animal tissue

The term “decellularisation” refers to the process by which cells, including cellular material such as DNA, are removed from biological tissue (134) for both clinical and non-clinical applications (135, 136). In a clinical context, the use of decellularised animal tissue has been explored as an option for implantation (137). For example, the implantation of cell-repopulated decellularised lungs has been tested in rats (140). Additionally, commercial products based on decellularised tissue have been developed. For instance, decellularised skin is used as a graft to treat patients with burns (138) and decellularised blood vessels are used as peripheral arterial bypasses (139). In the context of basic research, decellularised tissue of various kinds has been used as a platform for the development of *in vitro* models capable of replicating aspects of the cell-ECM interaction observed *in vivo* (136).

A variety of animal tissues have been successfully decellularised for both clinical and non-clinical applications, including heart (141), brain (142), muscle (143), skin (144), liver (145), and the respiratory tract (146). Sources of animal tissue used in studies centred on decellularisation include mice (147), rats (148), rabbit (149), sheep (150), pigs (151) and humans (152). The treatments applied to native tissue in order to remove cellular material fall under 3 main categories: chemical, enzymatic, and physical treatments (153). Decellularisation protocols are based on one or a combination of these treatments.

Chemical treatments rely on the use of substances, such as surfactants, (154) to disarrange the cell membranes of cells adhering on native tissue (155). The disruption of cell membranes by surfactants facilitates the removal of cellular material from the tissue by subsequent washing steps, which are performed with substances such as phosphate-buffered saline (PBS; 156) or distilled water (157). Surfactants commonly used in the context of chemical treatments for decellularisation purposes include sodium dodecyl sulfate (158), sodium deoxycholate (SDC; 159), Triton X-100 (160), and 3-((3-cholamidopropyl) dimethylammonio)-1-propanesulfonate (CHAPS; 161). Another common chemical treatment lies in the use of hypotonic and hypertonic solutions (162) with the aim of generating sufficient transmembrane osmotic pressure to rupture cells. Other chemical treatments that have been explored, but that are not routinely implemented, include the use of acidic (163) or basic (164) solutions, acetone (165), alcohols (166), tributyl phosphate (167), and of chemical compounds capable of stimulating cell apoptosis such as camptothecin (168).

Enzymatic treatments for decellularisation purposes include the use of proteases such as trypsin (169) and dispase (170). Additionally, nucleases can be included in decellularisation protocols to fragment nucleic acids and facilitate their detachment from the native tissue (171).

A commonly used physical treatment is agitation of the tissue (172), which facilitates cell removal and the penetration of chemical species within the structure. Freeze-thawing cycles can also be included in decellularisation protocols (172), as the formation of ice crystals within cells during the freezing portion of the cycle disrupts cellular structures upon thawing. Other physical treatments include the use of electroporation (173) and mechanical pressure (174).

In addition to cell removal, decellularisation protocols are designed to minimize the degradation of ECM features due to the decellularisation treatments, which can alter the ECM's composition, architecture, and mechanical properties (175). The maintenance of ECM features upon decellularisation is particularly important with regards to the development of decellularisation-based *in vitro* models that aim at replicating the cell-ECM crosstalk.

### 2.1.2. Decellularisation-based *in vitro* models

Decellularised tissue can be repopulated with cells in order to develop *in vitro* models (176). A list of tissues that have been replicated *in vitro* through this strategy includes heart (177), kidney (178), liver (179), skeletal muscle (180), skin (181), lungs (184) and intestine (183). A variety of pathological mechanisms have been reproduced in decellularisation-based *in vitro* models. Cancer progression, for example, has been evaluated *in vitro* using models derived from the

decellularisation and subsequent recellularisation with cancer cells of healthy pulmonary (185) and intestinal (183) tissue. Pathologies that impact ECM features can also be modelled *in vitro* using decellularised tissue obtained from diseased animals or patients (176). Examples of this strategy include the development of *in vitro* models of fibrosis by means of recellularisation of decellularised fibrotic respiratory (186), hepatic (187) or renal (188) tissue. In a number of studies, decellularisation-based models were compared to 2D cultures (178, 185, 189). For example, an *in vitro* model of kidney based on the use of decellularised renal tissue was used as a nephrotoxicity screening tool, and in this study cells seeded on the decellularised tissue were more responsive to nephrotoxic drugs as compared to cells cultured in 2D (178).

With regards to the upper conducting airway, most of the studies related to decellularisation are focused on the development of implantable grafts as opposed to the development of *in vitro* models. In these studies, the characterisation of cells seeded on decellularised airway is limited. However, a relatively small number of studies have focused on the development of decellularisation-based *in vitro* models of the upper conducting airway. Melo *et al*. developed a tracheobronchial model by seeding the bronchial epithelial cell line 16HBE14o-, the microvascular endothelial cell line ISO-HAS-1 and the fibroblast cell line Wi-38 on decellularised porcine tracheal submucosal tissue (190). Notably, in this study the 16HBE14o- cells seeded on the decellularised structure developed clusters of cilia, whilst the same cells seeded on collagen I-coated transwell® systems did not. In the study conducted by Hedström *et al*., an *in vitro* model of bronchi was developed by seeding HBECs on decellularised human bronchial fragments (191). The authors showed that HBECs seeded on decellularised bronchi obtained from COPD-

affected donors had an altered gene expression compared to that related to cells seeded on healthy bronchi. In particular, differences were observed with regards to the expression of genes tied to proliferation, remodelling, apoptosis, vascularisation and inflammation. In a follow-up study, HBECs obtained from both healthy and COPD-affected patients were seeded on decellularised bronchi, which were also obtained from both healthy and COPD-affected donors (192). Culture of HBECs obtained from COPD-affected donors on both healthy and COPD donors-derived scaffolds negatively affected the initiation of ciliation, as compared to HBECs obtained from healthy donors and cultured in both types of scaffold (192). This effect was not observed in cultures of both cell types on collagen I-coated transwell® systems (192).

The results obtained so far indicate that decellularised airway tissue can be used for the development of *in vitro* models of large bronchi. However, the number of studies on the topic is limited, and further investigation is necessary. In addition to the use of decellularised tissue, decellularised tissue-derived hydrogels could be included in an *in vitro* model as an alternative ECM-mimicking structure.

### 2.1.3. Decellularised tissue-derived hydrogels for *in vitro* bronchial models

Hydrogels are cross-linked, hydrophilic, insoluble polymeric networks (193). Due to their elevated water affinity, hydrogels have a high water content (194). In particular, water content can vary according to parameters such as porousness of the hydrogel's structure and density of crosslinks (194), and can be higher than 99 % of the total hydrogel weight (195). Hydrogels can be derived from synthetic polymers, such as poly(ethylene glycol) (PEG), polycaprolactone (PCL) and poly(vinyl alcohol) (PVA; 196), or from natural polymers, such as collagen,

hyaluronic acid, chitosan and alginate (194). Additionally, hydrogels can be formed by a mixture of natural and synthetic polymers (197). Examples of this type of hydrogels include poly(ethylene glycol) dimethacrylate (PEGDMA) / gelatin methacrylate (GelMA) and poly(ethylene glycol) diacrylate (PEGDA) / heparin methacrylate (HepMA; 197).

Both natural and synthetic polymers can be used for the development of biocompatible hydrogels (194, 197). Moreover, physical properties of hydrogels such as stiffness and capacity for degradation can be tuned (198). For these reasons, hydrogels are used in the biomedical industry, for example for the development of contact lenses (194). The use of hydrogels has also been explored in the context of drug delivery (194) and as cell culture substrates for the development of *in vitro* models (199).

Cells included in hydrogel-based *in vitro* models are cultured in a three-dimensional (3D) environment, thus reproducing the 3D cellular milieu observed *in vivo*. This feature is a main advantage of hydrogel-based *in vitro* models as compared to traditional models based on two-dimensional (2D) cultures (200). Hydrogel-based models can be developed using naturally occurring ECM molecules, such as collagen (201) and hyaluronic acid (202). However, the ECM of biological tissues is constituted by a large variety of different chemical species, and therefore *in vitro* models that include hydrogels based on a single type of polymer fail to reproduce the complexity of the native ECM. A solution to this issue is represented by the subset of hydrogels derived from decellularised tissues (203), which in this work will be termed “ECM hydrogels”.

To obtain ECM hydrogels, a typical protocol consists of the fragmentation of the decellularised tissue to a powder form, followed by solubilisation of the powder in pepsin (204). Then, the pH of the resulting solution, or “ECM pre-gel”, is neutralised and heated to 37°C to initiate the gelation process, which is completed within an hour (204). Gelation kinetics and mechanical properties of ECM hydrogels are influenced by parameters such as protein concentration in the ECM pre-gel, type of tissue, and decellularisation procedure (204, 205).

The use of ECM hydrogels has been tested in combination with cells related to various tissues, such as brain (182), liver (206), pancreas (207), kidney (208), bone (209) and lungs (210). For example, lung fibroblasts (210) and lung vascular endothelial cells (211) have demonstrated a capacity for attachment and survival on lung ECM hydrogels. However, only a limited number of studies has included a characterisation of the response of respiratory tract-derived ECM hydrogels to cells related to large bronchi. In particular, HBECs have demonstrated the capacity for adherence on both lung (210) and tracheal (212) ECM hydrogels. When seeded on a tracheal ECM hydrogel in the study conducted by Badylak *et al*., (212), HBECs were also shown to be capable of mucociliary differentiation.

One important barrier to the use of ECM hydrogels lies in the production of the hydrogel itself. In most studies, ECM hydrogels are derived in-house. However, specialised equipment, necessary for the decellularisation and subsequent development of an ECM hydrogel, is not accessible to all researchers. This issue limits the use of ECM hydrogels across the scientific community. Furthermore, differences in protocols related to hydrogel production adopted by different groups lead to the development of hydrogels with variable properties. A lack of

standardisation can lead to issues related to the reproducibility of results obtained using ECM hydrogels. Recently, however, the development of ECM hydrogels has been exported from the academic to the industrial landscape by Xylyx, a commercial entity. So far, the lung ECM hydrogel produced by Xylyx, which in this work is termed “DLH” to differentiate it from other non-commercial lung ECM hydrogels, has been used only in two studies (214, 215), and has not been used in combination with respiratory tract-associated fibroblasts or HBECs. Its adoption to establish *in vitro* models could become a routine practice, as it is the case with Matrigel, a commercial hydrogel obtained from the solubilised basement membrane matrix secreted by murine sarcoma cells. Matrigel is used for a wide variety of applications, spanning from modelling angiogenesis to organoid culture (216, 217), and has featured in more than 12000 publications (218). On the other hand, the potential of DLH is still unexplored in the context of *in vitro* model development.

Given their commercial availability, possibility of inclusion in high-throughput platforms, and capacity to replicate the properties of native respiratory ECM, in the next sections DLH and decellularised bronchial tissue will be used as cell culture substrates for the development of biomimetic *in vitro* models of large bronchi.

## 2.2. Methods

### 2.2.1. Porcine tissue acquisition

Porcine respiratory tracts spanning from the lungs to the trachea were purchased from an abattoir (Cheale Meats, UK). Primary and secondary bronchi were then extracted from the respiratory tissue. The extracted tissue was stored in

Dulbecco's phosphate buffered saline without calcium chloride and magnesium chloride (DPBS--; Sigma-Aldrich, USA) and preserved at -80°C for later use.

### 2.2.2. Decellularisation of porcine tissue

Porcine primary and secondary bronchi were decellularised using an adapted protocol from Butler *et al*., (222). Briefly, bronchial tissue related to 3 different pigs was thawed at room temperature (RT). Upon thawing, tissue was placed in a 500 mL vacuum chamber (Biorep Technologies, USA). The chamber was then filled with 250 mL of decellularisation solutions, their exact composition depending on the protocol step, as indicated in Table 2.1. Products used for the decellularisation were sodium deoxycholate (SDC; Sigma-Aldrich), Triton-X-100 (TX-100; Sigma-Aldrich), Hank's Balanced Salt Solution with calcium chloride and magnesium chloride (HBSS++; Sigma-Aldrich), Hank's Balanced Salt Solution without calcium chloride and magnesium chloride (HBSS--; Sigma-Aldrich), Antibiotic-Antimycotic solution (A/A; ThermoFisher Scientific, USA), DNAse I (ThermoFisher Scientific), RNase I (Invitrogen, USA). The inside of the chamber was kept at a negative pressure by operating a vacuum pump (Javac, UK) and the chamber was kept in agitation at 125 RPM on an orbital shaker (Sciquip, UK) during the entire protocol. The temperature of the orbital shaker was set at different values depending on the protocol step, as indicated in Table 2.1. At the end of the decellularisation procedure tissue was preserved in 2 % v/v A/A in HBSS-- at 4°C.

**Table 2.1**. Decellularisation protocol. The table includes, for each step, the solution decanted in the vacuum chamber, the solution's concentration, the duration of the step expressed in hours (h) or minutes (min), and the temperature of the orbital shaker.

| Step | Solution | Concentration | Duration | Temperature |
|---|---|---|---|---|
| 1 | SDC,<br>TX-100 in HBSS-- | SDC: 0.25 % w/v<br>TX-100: 0.25 % v/v | 24 ± 4 h | 37°C |
| 2 | HBSS-- | n/a | 20 min | 4°C |
| 3 | HBSS-- | n/a | 20 min | 4°C |
| 4 | A/A in HBSS-- | A/A: 2 % v/v | 48 – 72 h | 4°C |
| 5 | DNAse I,<br>RNase I in HBSS++ | DNAse I: 2 Kunitz/mL<br>RNase I: 4 U/mL | 24 ± 4 h | 37°C |
| 6 | HBSS-- | n/a | 20 min | 4°C |
| 7 | HBSS-- | n/a | 20 min | 4°C |
| 8 | A/A in HBSS-- | A/A: 2 % v/v | 48 – 72 h | 4°C |
| 9 | DNASe I,<br>RNase I in HBSS++ | DNAse I: 2 Kunitz/mL<br>RNase I: 4 U/mL | 24 ± 4 h | 37°C |
| 10 | A/A in HBSS-- | A/A: 2 % v/v | 48 – 72 h | 4°C |

To obtain decellularised scaffolds, decellularised tissue was cut using a scalpel (Swann-Morton, UK) in squares of dimensions approximating 5 mm X 5 mm. Scaffolds were subsequently submerged in DPBS-- and sent to the UCL Institute of Child Health, for sterilisation with a dose of 2.5 KGy of gamma rays using an IBL 437C gamma irradiator (CIS Bio International, France).

### 2.2.3. H&E staining of porcine bronchial tissue and DLH

Decellularised and non-decellularised ("native") porcine tissue related to 3 different anatomical areas within the primary and secondary bronchi, and to 3 different

animals, were fixed in a solution of 4 % paraformaldehyde in phosphate buffered saline (4 % PFA; Cell Signalling Technologies, USA) for 24 h at RT. Subsequently, the fixed tissue was submerged in DPBS-- and sent to the UCL Cancer Institute for embedding in paraffin, cutting, and staining with Haematoxylin and Eosin (H&E). Widefield images of the sections were then acquired using a S100TV microscope (Zeiss, Germany).

Porcine-derived DLH (Xylyx, USA; lot: SLG2001J) was reconstituted according to the vendor's instructions. Briefly, the product consists of a liquid component A, a liquid component B, and a solubilised ECM solution. To initiate the formation of the DLH, 30 µL of component A was added to the solubilised ECM solution, and the resultant solution was mixed using a vortexer (Scientific Industries, USA). 35 µL of component B was subsequently added to the solution which was then mixed using a vortexer. Finally, 135 µL of DPBS-- was added to the mixture. This solution was then mixed with a vortexer and added to 3 wells of a 48 well-plate (Corning, USA), each well containing 10 µL of solution. The 48 well-plate was then incubated at 37°C for 1 h, and at the end of this step the solution had completely gelated. The wells containing the DLH were then filled with 4 % PFA for 20 min to fix the samples. The 4 % PFA solution was then removed, and the wells were washed twice with DPBS--, each washing step lasting 5 min. Afterwards, the wells containing the samples were filled with newly decanted DPBS-- for long term storage. The samples were then sent to the UCL Cancer Institute for embedding in paraffin, cutting, and H&E staining. Widefield images of the sections were then acquired using a S100TV microscope.

### 2.2.4. Scanning electron microscopy

Micrographs of DLH samples were obtained as followed. DLH was obtained as described in section 2.2.3 and added to 4 wells of a 48 well-plate, each well containing 10 µL of DLH. In this experiment, each hydrogel loaded constituted a sample. The samples were fixed by submerging them in a solution of 2.5 % glutaraldehyde in phosphate buffered saline for 2 h at RT. Afterwards, the samples were washed twice with DPBS--, each washing step lasting 10 min. Then the samples were submerged in newly decanted DPBS--. Samples were then dehydrated by submerging them for 15 min in solutions of crescent ethanol content in ultrapure water. In particular, the ethanol content of the solutions, expressed in % v/v, was 30 %, 50 %, 70 %, 85 %, 95 %, 100 %. Then, samples were subjected to critical point drying. Upon drying, samples were mounted on metal circular stubs (Agar Scientific, UK), which had been previously coated with circular carbon tabs (Agar Scientific). Silver paint (Agar Scientific) was then applied to the samples in order to form a conductive trail connecting the sample and the metal of the stubs. This step was followed by sputter-coating with platinum using a sputter coater (Quorum), performed by the UCL Ear Institute imaging team. The samples were imaged by means of scanning electron microscopy (SEM) using a field emission SEM microscope (Jeol, Japan).

For quantitative analysis of the fibre diameter, 3 images per sample were acquired, and the diameter of 5 randomly selected fibres per image was measured using the FIJI software (version 2.1.0/1.53n, for source see reference: 345). Measurements were obtained only in areas in which the fibres did not intersect with each other.

Micrographs of decellularised bronchial tissue were obtained following the same protocol adopted for DLH, with the following modifications. The processed samples, obtained as described in section 2.2.2, consisted of 6 fragments of sterilised decellularised tissue from 2 different animals. Upon fixation in 2.5 % glutaraldehyde in DPBS--, the samples were submerged in a solution of 1 % Osmium in ultrapure water (UPW). The submerged samples were placed on a rotator for 90 min, and were then washed twice in DPBS--, each washing step lasting 10 min, before proceeding with the rest of the protocol. Images were acquired by the UCL Ear Institute imaging team on the luminal surface of 3 samples per animal, and on the side of the submucosal layer of 3 samples per animal.

### 2.2.5. Rheology

DLH was reconstituted as described in section 2.2.3. A parallel plate rheometer (TA Instruments, USA) was then used to measure the rheological properties of the material. To achieve this, firstly the Peltier plate of the rheometer was set at a temperature of 10°C. Then, the solution obtained by mixing the components of the DLH kit, which was performed as described in section 2.2.3, was loaded on the Peltier plate. A parallel plate with a cylindrical geometry and a diameter of 8 mm was then lowered to the top surface of the solution. The edges at the gap between the Peltier plate and the parallel plate were sealed with mineral oil (Sigma-Aldrich) in order to avoid desiccation of the sample throughout the experiment. No oscillation was applied in the following 5.5 min, to allow the solution to reach a temperature of 10°C and settle between the Peltier plate and the parallel plate. The solution was then subjected to an oscillatory strain of 0.5 % at an angular frequency of 6 rad/s, for 30 min. Afterwards the oscillation was halted and the temperature of the Peltier plate was increased to 20°C. After the target temperature was reached,

no oscillation was applied for 30 s, and then an oscillatory strain of 0.5 % was applied at an angular frequency of 6 rad/s for 30 min. Then the oscillation was halted again and the temperature of the Peltier plate was increased to 37°C. Upon reaching the target temperature, no oscillation was applied for 30 s and then an oscillatory strain of 0.5 % was applied at an angular frequency of 6 rad/s, for 60 min. The oscillation was then halted for 30 s and afterwards the oscillatory strain of the applied oscillation and the temperature of the Peltier plate were maintained constant at respectively 0.5 % and 37°C, whilst the angular frequency was gradually increased from 0.1 rad/s to 500 rad/s. Finally, in the last step of the protocol, after halting the oscillation for 30 s, the angular frequency of the applied oscillation and the temperature of the Peltier plate were kept constant at respectively 6 rad/s and 37°C, whilst the oscillatory strain was gradually increased from 0.004 % to 500 %. The readouts of this experiment were the storage modulus G' and loss modulus G" of the tested material at each data point acquisition.

### 2.2.6. HBEC expansion and freezing

In this work, reagents used for cell culture were pre-warmed to a temperature comprised between 37°C and approximately 20°C. Also, throughout this entire work the cell culture incubator (Heraeus, Germany) was set at 37°C and 5 % $CO_2$. The HBECs used in all experiments were acquired with informed donor consent from LONZA (Switzerland), and were obtained from donors 18TL052522, 18TL290281, 0000495838. The donors had no respiratory conditions, and cells were already passaged to passage 1 (P1). Upon receipt, HBECs were stored in liquid nitrogen. HBECs were thawed and cultured according to the following protocol. Cells were thawed by placing the cryovial containing them in a waterbath (Grant, UK) set at 37°C, and the cell suspension was subsequently decanted in a

15 mL centrifuge tube (Corning). 9 mL of bronchial epithelial growth medium (BEGM; LONZA), reconstituted by adding the aliquots included in the BEGM SingleQuot Kit (LONZA) into the bronchial epithelial basal medium (BEBM; LONZA), was decanted into the centrifuge tube containing the cells, dropwise, and the tube was then placed in a centrifuge (ALC, UK) and centrifuged for 5 min at a centrifugal acceleration of 200 x *g*. Afterwards, the supernatant was removed from the centrifuge tube and the cells were divided into 4 T75cm$^2$ cell culture flasks (Greiner Bio-One, UK), each including a final volume of 20 mL BEGM. Cell culture medium was changed the day after and every 2-3 days (d), until cells reached 90 % confluency.

Cells were frozen for long term preservation according to the following protocol. Firstly, the T75cm$^2$ cell culture flasks containing the cells were washed with 4 mL HEPES Buffered Saline Solution (HBSS; LONZA). 4 mL trypsin (LONZA) was added to each flask. The flasks were placed in the cell culture incubator until cell detachment was observable. Then, to inhibit the trypsin, the cell suspension from each flask was decanted in a 50 mL centrifuge tube (Corning) containing 16 mL Trypsin Neutralising Solution (TNS; LONZA). The cell suspension was then centrifuged for 5 min at a centrifugal acceleration of 250 x *g*. Afterwards, the supernatant was discarded and cells were resuspended at a concentration of 8.8 x 10$^5$ cells/mL in a solution of 10 % v/v dimethyl sulfoxide (DMSO; Sigma Aldrich) in BEBM including Small Airways Growth Medium SingleQuots (LONZA). The resuspended cells were then divided into cryovials, each cryovial including 1 mL of cell suspension. The cryovials were placed in Cryo 1°C freezing containers (Thermofisher Scientific) and subsequently cooled to -80°C overnight. The day after, the cryovials containing cells were transferred to liquid nitrogen for long term

storage. In all subsequent experiments performed in this work, the HBECs that were used had been previously expanded and frozen as described above, and were thawed following the same procedure.

### 2.2.7. Cell culture on decellularised scaffolds

In this experiment, HBECs (donor: 18TL052522) were thawed according to the same protocol detailed in section 2.2.6 and plated on 4 T75cm$^2$ cell culture flasks. Cell culture medium was changed the day after the thawing, and every 2-3 d thereafter. When cells reached 90 % confluency, 3 decellularised scaffolds related to the same animal and obtained as described in 2.2.2 were transferred to separate wells of a 48 well-plate (Corning) and submerged in 400 µL BEGM. Then, each flask was briefly washed with DPBS--, and 6 mL of Animal Component-Free (ACF) dissociation enzyme (STEMCELL, Canada) was subsequently added to each flask, which were placed in the cell culture incubator until cell detachment was noticeable. Then, to inhibit the ACF dissociation enzyme, the cell suspension in the flasks was decanted in a 50 mL centrifuge tube containing an equal volume of ACF quenching enzyme (STEMCELL). Cells were then centrifuged at a centrifugal acceleration of 300 x *g*. Supernatant was discarded and cells were resuspended at a concentration of 120 x $10^3$/100 µL. The resuspended HBECs were then seeded into wells of the 48 well-plate containing the scaffolds at a seeding density of 30 x $10^3$ cells per well. Afterwards, the cells and scaffolds were placed in the cell culture incubator. After 2 h, the seeded scaffolds were moved to separate wells of a 24-well plate (Corning), each well containing 1 mL BEGM. The 24-well plate was then placed in the cell culture incubator. Cell culture medium was changed every

3 d, and scaffolds were fixed on day 9 post-seeding following the procedure described in section 2.2.8.

### 2.2.8. Staining of cells cultured on decellularised scaffolds

Scaffolds seeded with HBECs following the procedure detailed in section 2.2.7 were fixed by submerging them in 4 % PFA at RT for 30 min. Then, scaffolds were washed 3 times with DPBS-- and preserved at 4°C submerged in DPBS--. The same procedure was applied to 3 scaffolds that were not seeded with cells ("unseeded" scaffolds), obtained from the same animal from which the seeded scaffolds had been obtained from. Seeded and unseeded scaffolds were then stained with Hoechst 33342 (Hoechst; ThermoFisher Scientific; excitation: 350 nm, emission: 461 nm), a fluorescent nucleic acid stain, and phalloidin (Abcam, UK; excitation: 493 nm, emission: 517 nm), a fluorescent actin stain. To do so, scaffolds were submerged for 1 h at RT in a 1 : 1000 dilution of phalloidin in DPBS--. During this step, scaffolds were shielded from light. Then, scaffolds were washed 3 times with DPBS--, and subsequently submerged for 10 min at RT in a solution of 1 µg/mL Hoechst in DPBS--. The scaffolds were shielded from light during this step. Afterwards, scaffolds were washed 3 times with DPBS--. Before imaging, the cartilaginous layer of the scaffolds was carefully detached from the rest of the tissue, which was transferred to glass slides making sure that the luminal side of the scaffolds was facing upwards. Prolong Gold (ThermoFisher Scientific), a mounting agent, was applied on glass coverslips and these were then applied on top of the tissue on the glass slides. Nail varnish and super glue (Loctite, USA) was then applied on the edge of coverslips to seal them. The samples were then imaged using a LSM 880 confocal microscope (Zeiss).

### 2.2.9. Seeding of HBECs on DLH

Throughout this work, the collagen I hydrogel used was a commercial rat tail tendons-derived hydrogel (Bio-Techne, USA), sold as a liquid collagen solution. The following procedure describes the steps followed to reconstitute the hydrogel. Firstly, equal volumes of 4-(2-hydroxyethyl)-1-piperazineethanesulfonic acid (HEPES; ThermoFisher Scientific) and of a solution of 37 g/L of sodium bicarbonate in UPW were mixed in an empty mini-centrifuge tube (Eppendorf, UK). The previously mentioned rat tail tendons-derived collagen I solution, cooled on ice, was then added to the mixture of HEPES and sodium bicarbonate, obtaining a 1 : 5 dilution of the HEPES and sodium bicarbonate mixture in the collagen solution. The resulting solution was mixed thoroughly by pipetting. Once this step is completed, the resulting solution, termed “pre-gel solution” is ready for loading into the desired platform and will gelate within 15 min at 37°C, forming a collagen I hydrogel.

The following protocol describes the procedure followed to seed HBECs on DLH and collagen I hydrogel. Firstly, collagen I hydrogel was prepared as described in the last paragraph. Then, 50 µL of collagen I hydrogel was loaded into 6 wells of a 96-well plate (Corning) and in 4 transwell® membranes included in a 24-well plate format transwell® recipient plate (Corning). The diameter of the pores located on the surface of the transwell® membranes was 8 µm. The inserts were placed in recipient wells preloaded with 600 µL BEGM. The hydrogel-loaded 96-well plate and transwell® plates were then placed in a cell culture incubator for 15 min to allow gelation of the pre-gel. Then, 150 µL BEGM were added to the hydrogel-loaded inserts and wells. DLH was then reconstituted according to the protocol described in 2.2.3, with the following modification: BEGM was used instead of DPBS-- in the

last step of pre-gel preparation. Subsequently, 50 µL of pre-gel was loaded in 6 wells of the collagen I hydrogel-loaded 96-well plate and on 3 transwell® membranes of the collagen I-hydrogel loaded transwell® plate (Corning). The loaded transwell® membranes were placed in recipient wells preloaded with 600 µL BEGM. The plates were then placed in a cell culture incubator for 1 h to allow gelation of the DLH. Then, 150 µL BEGM were added to the lung ECM gel-loaded inserts and wells, and to 6 hydrogel-free wells of the 96-well plate. After this step, HBECs (donor: 18TL052522), thawed and cultured according to the protocol described in 2.2.6 until they reached 90 % confluency, were seeded into the hydrogel-loaded wells in the transwell® plate and in the 96-well plate, and in 6 gel-free wells also included in the 96-well plate. The cell seeding procedure was executed according to the following protocol.

Firstly, the flasks were briefly washed with DPBS--, and 6 mL ACF dissociation enzyme was added to each flask, which were then placed in a cell culture incubator until cell detachment from the cell culture surface was observable. The cell suspension was then decanted into one 50 mL centrifuge tube in which an equal volume of ACF enzyme inhibition solution was added. Cells in the resulting solution were counted using a haematocytometer, and the cell suspension was spun in a centrifuge at a centrifugal acceleration of 300 x *g* for 5 min. The supernatant was then discarded and cells were resuspended in BEGM. After this step, 20 x $10^3$ cells per well were added to each well and transwell® membranes previously loaded with collagen I hydrogel or DLH, and to 6 hydrogel-free wells of the 96-well plate previously filled with BEGM. The total BEGM volume in each well and insert at the end of the seeding procedure was 200 µL. Cell culture medium was changed every 2-3 d, and widefield images were acquired at day 0, 1, 2, 3 and 5 at a magnification

of 2.5X using a S100TV microscope (Zeiss, Germany). Cell culture was progressed up to day 5, when cells in the 96-well plate were stained with Hoechst according to the following protocol.

### 2.2.10. Hoechst staining of HBECs on DLH and staining quantification

Firstly, cell culture medium in cell-seeded 96-well plates was exchanged with 200 µL of 5 µg/mL Hoechst in BEGM. The plate was subsequently placed in the cell culture incubator for 25 min, and each well was then washed with BEGM 3 times. One representative image of each of the wells containing Hoechst-stained cells was then acquired at a magnification of 5X using a S100TV microscope inclusive of a filter slider including an excitation filter (wavelength filtered: 360/40 nm) and an emission filter (wavelength filtered: 460/40 nm), used throughout this work to acquire non-confocal images of Hoechst-stained cells. Nuclei quantification on the images was then performed using the software FIJI (2.1.0/1.53n, for source see reference: 345), according to the following protocol. Firstly, a fast Fourier transform (FFT) bandpass filter was applied to highlight the nuclei against the background of images. In particular, the settings for the FFT bandpass filter were the following: large structures were filtered down to 40 pixels, small structures were filtered up to 3 pixels, stripes were not suppressed, a 5 % tolerance of direction was set, images were auto-scaled and saturated after the filtering. Then a “Yen” threshold was selected to obtain a greyscale image and a median filter with a radius of 8 pixels was applied to diminish noise. The “watershed” command was then used to separate agglomerates of nuclei. The “analyse particles” command was finally used to count nuclei.

### 2.2.11. Statistical analysis

Statistical tests were performed using the software GraphPad Prism version 9.0.0 (GraphPad Software, USA). To inform the choice of statistical tests to be executed, a Shapiro-Wilk normality test was performed on all quantitative data. A one-way ANOVA was conducted to analyse the difference between the means of diameters of DLH's fibres, and the difference between the means of nuclei counts. In case of significance, a post-hoc Tukey's multiple comparisons test was executed. For all tests, if p-value < 0.05, the results were considered statistically significant. Degrees of significance were indicated in images as follows: * for $p < 0.05$, ** for $p < 0.01$, *** for $p < 0.001$, and **** for $p < 0.0001$. In the 2.3. Results section, the p value of the one-way ANOVA is reported in the main text and figure legends, whilst the degrees of significance of the post-hoc tests are reported in the figures.

## 2.3. Results

### 2.3.1. Characterisation of decellularised porcine bronchial tissue

Porcine tissue obtained from the primary and secondary bronchi of n = 3 adult pigs was decellularised as described in section 2.2.2. Non-decellularised ("native") tissue obtained from the same anatomical areas and from the same animals was used as a control. Native and decellularised tissue from n = 3 distinct anatomical areas pertaining to large bronchi, obtained from each of the n = 3 animals used in the experiment, was embedded in paraffin and stained with H&E (Figure 2.1). Hematoxylin stains nuclei deep purple, and Eosin stains cytoplasm and ECM pink or light purple. In Figure 2.1A, representative images of stained sections obtained from decellularised and native tissue are compared. Nuclei were visible in the native tissue in the submucosal / mucosal area, cartilage, and adventitia. In

decellularised tissue, nuclei could not be observed in the cartilage and adventitia. However, nuclei could still be observed in the submucosal area of decellularised tissue. In Figure 2.1B, zoomed representative images of native and decellularised submucosal / mucosal tissue illustrate the presence of nuclei within the submucosal area of decellularised tissue. In particular, nuclei in decellularised tissue appeared to be selectively located around empty circular areas in the submucosal tissue, as indicated in the red rectangle, and were not found on the lumen of the tissue. The lack of cellular material on the luminal and cross sectional surface of decellularised tissue was confirmed through SEM imaging, performed on tissue derived from n = 2 animals, including n = 3 tissue specimens of the luminal areas and n = 3 tissue specimens of the cross sectional areas from each animal. In figure 2.1C, representative micrographs of decellularised tissue are shown. Cells were not observable on the luminal surface, confirming the de-epithelialisation of the tissue.

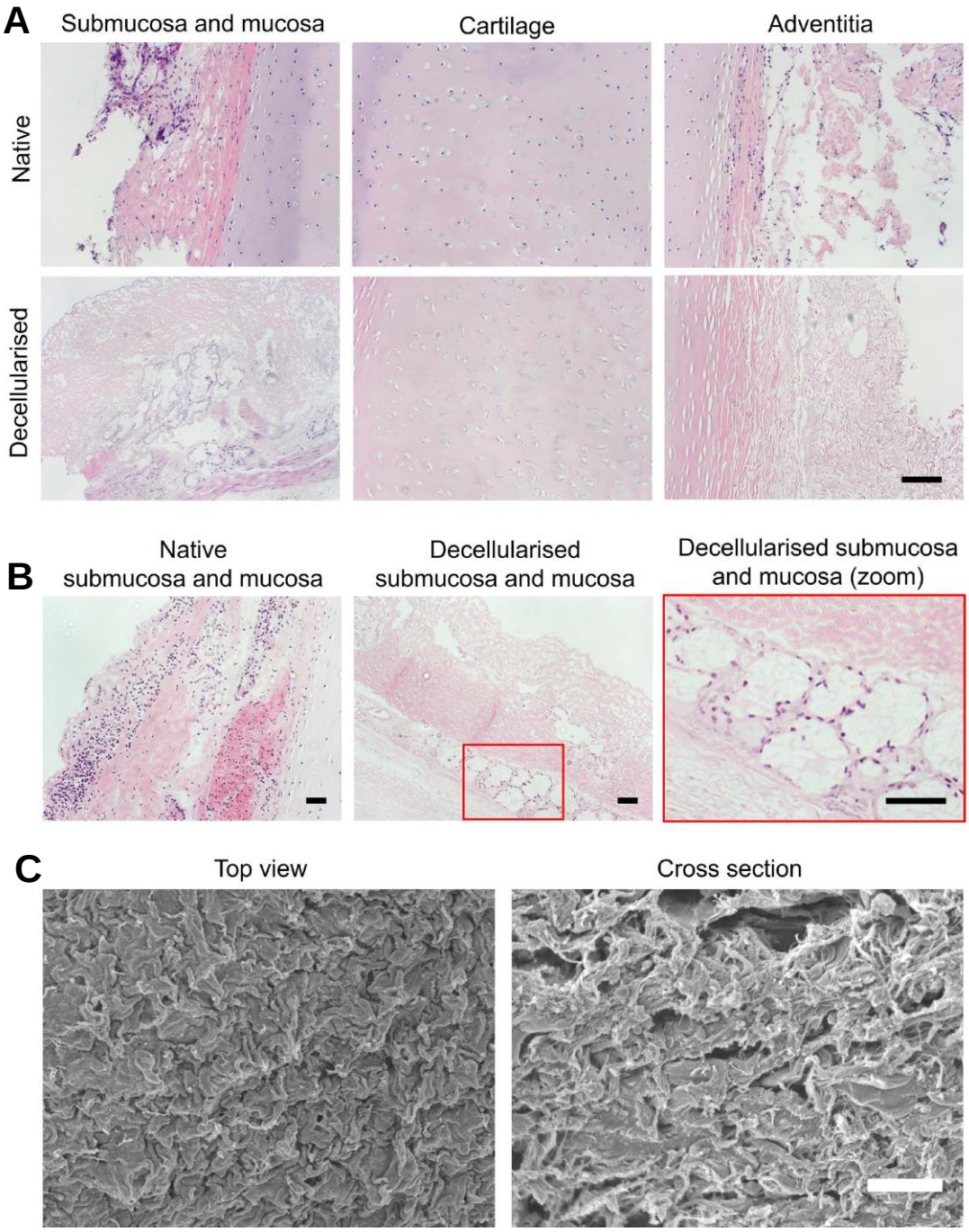


**Figure 2.1.** Representative images of H&E staining of fresh and decellularised porcine bronchial tissue, and representative SEM images of decellularized porcine bronchial tissue. Porcine tissue was decellularised using a vacuum-assisted decellularisation protocol, and native and decellularised tissue was then stained with H&E. Representative images of stained tissue were then acquired. Additional images of the decellularized tissue were acquired using SEM. No cells could be observed on the luminal side of the tissue, whilst cellular residuals could be observed in the submucosa. **A:** representative widefield images of H&E staining of native and decellularised porcine bronchial tissue. In the images, nuclei are stained deep purple whilst cytoplasm and the ECM are stained light purple (cartilage) or pink (submucosal, mucosal, adventitial layers). Native tissue is depicted on the first row, and decellularised tissue is depicted on the second row. Submucosa / mucosa, cartilage, and adventitia are respectively found in the left, central, and right column. No nuclear residuals were observed in the luminal, cartilaginous, and adventitial tissue layers. Magnification: 10X. Scale bar: 100 µm. **B:** representative widefield images of H&E staining of native (left), decellularised (centre) and post-acquisition zoomed image of decellularised (right) porcine submucosa and mucosa. In the images, nuclei are stained deep purple whilst cytoplasm and the ECM are stained light purple (cartilage) or pink (submucosal, mucosal, adventitial layers). The red rectangle in the central image corresponds to the area depicted in the zoomed image on the right. No nuclear residuals were observed on the luminal side of tissue, but nuclei could be observed in the submucosal layer. Magnification: 10X. Scale bars: 50 µm. **C:** SEM micrographs of decellularised mucosal / submucosal layers, as observed from the top of the luminal surface (left) or as a cross section (right). Magnification: 2000X. Scale bar: 10 µm. N = 3 animals, n = 3 tissue specimens from each animal used for H&E staining (Figure A, B). N = 2 animals, n = 3 tissue specimens of luminal areas and n = 3 tissue specimens of cross sectional areas obtained from each animal used for the acquisition of SEM images (Figure C).

### 2.3.2. Seeding of HBECs on decellularised scaffolds

To assess the biocompatibility of decellularised porcine bronchial tissue, HBECs (donor: 18TL052522) were seeded on 3 decellularised scaffolds obtained from 1 animal. Representative images of Hoechst-stained seeded scaffolds, and of 3 scaffolds that were not seeded ("unseeded"), used as negative control, are depicted in Figure 2.2A. The unseeded scaffolds were obtained from the same animal from which seeded scaffolds had been obtained. With regards to cell presence, there appeared to be no difference between seeded and cell-free scaffolds in most imaged regions. A small cluster of circular structures resembling nuclei could be found on the surface of a seeded scaffold, as shown in the image on the left of Figure 2.2B, and in the zoomed image on the right. However, given the strong autofluorescence of the tissue, it was not possible to assess whether the circular objects were nuclei or ECM structures.

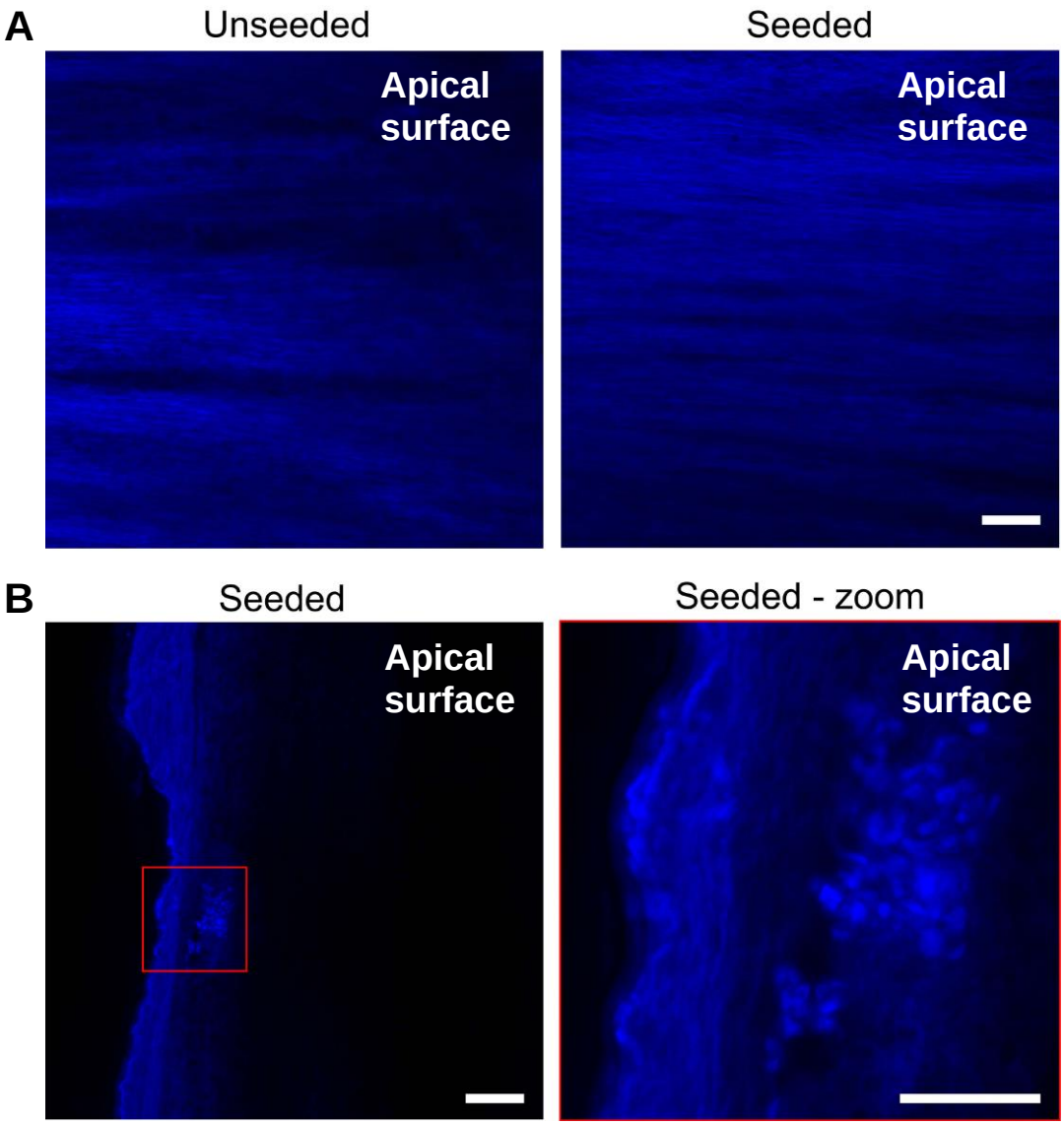


**Figure 2.2.** Representative images of scaffolds seeded with HBECs and stained with Hoechst. Decellularised porcine scaffolds were seeded with HBECs, and seeded and unseeded scaffolds were then stained with Hoechst. Representative images of the apical surface of scaffolds were then acquired. Both Hoechst-stained nuclei and the underlying ECM are blue in the images. Only a small amount of nuclei could be observed on the apical surface of seeded scaffolds. **A:** unseeded (left) and seeded (right) scaffolds. Magnification: 10X. Scale bar: 100 µm. **B:** seeded scaffold (left) including a red square indicating a cluster of circular features, and zoom (right) on the area delineated by the red square. Magnification: 10X. Scale bars: 100 µm (left), 50 µm (right). N = 3 seeded scaffolds and n = 3 unseeded scaffolds obtained from the same animal, using cells obtained from n = 1 donor.

Given the issues presented by the use of decellularised bronchi with regards to cell compatibility and imaging, the commercial lung ECM hydrogel termed “DLH” was considered as an alternative substrate for the development of the *in vitro* model.

### 2.3.3. Characterisation of DLH

Three samples of DLH were embedded in paraffin and stained with H&E (Figure 2.3A). No nuclei could be observed in the stained hydrogel, confirming that the material was acellular. To analyse the micro-structure of the hydrogel, SEM images were acquired from n = 4 DLH samples (Figure 2.3B-C). The SEM images revealed a 3D fibrous, reticular micro-structure. Additionally, from the SEM images it was possible to measure the diameter of the fibres forming the micro-structure of the hydrogel (Figure 2.3D) in order to measure the structural uniformity across different samples. In particular, n = 3 images per sample were acquired, and then the diameter of n = 5 randomly selected fibres per image was measured, for a total of n = 15 measurements per DLH sample. No statistically significant difference ($p = 0.1728$, one-way ANOVA) was found between the diameters of fibres related to the different samples.

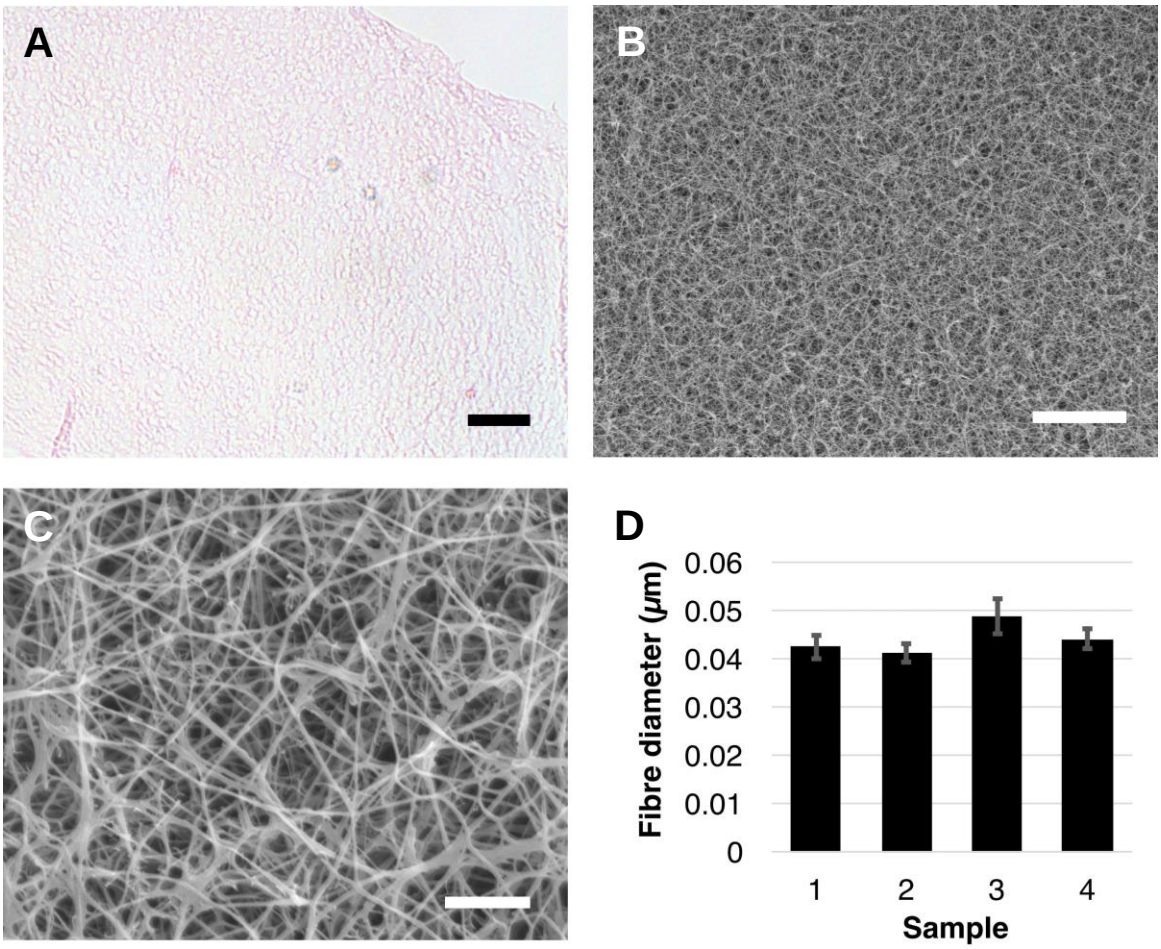


**Figure 2.3.** Structural characterisation of DLH. The structure of DLH was characterised by staining DLH samples with H&E, and by means of SEM microscopy. Representative images were then acquired, showing a 3D fibrous, reticular microstructure. From the SEM images, the diameter of fibres was quantified. Differences between the mean diameters of the samples' fibres were not statistically significant, indicating structural uniformity of the material. **A:** representative widefield image of H&E staining of DLH. In the image, nuclei are stained deep purple, whilst cytoplasm and the ECM is stained light purple or pink. Nuclei cannot be found in the images. Magnification: 10X. Scale bar: 100 µm. **B:** representative SEM image of DLH. In the image, ECM fibres appear light grey or white, and empty spaces between fibrils appear dark grey or black. Magnification: 2000X. Scale bar: 10 µm. **C:** representative SEM image of DLH. In the image, ECM fibres appear white or grey, and empty spaces between fibrils appear black. Magnification: 18000X. Scale bar: 1 µm. **D:** quantification of ECM fibre diameter measured from SEM images of DLH samples, reported as mean± SEM. The X axis identifies the sample, the Y axis indicates fibre diameter, expressed in µm. The differences observed between the values reported in the graph are not statistically significant as tested by one-way ANOVA ($p = 0.1728$). N = 3 samples of DLH used for H&E staining (Figure A). N = 4 samples of DLH used for the acquisition of SEM images (Figure B, C). N = 5 randomly selected fibres from each of the 3 representative images acquired from each of the 4 DLH samples included in the experiment, for a total of n = 15 measurements for each DLH sample used to quantify fibre diameters (Figure D).

In addition to its structural characteristics, to obtain information on the mechanical properties of the material, the rheological properties of the DLH were assessed using a rheometer. Data were obtained from n = 1 sample of DLH. Firstly, the rheometer was loaded with the solution obtained by mixing the components forming the DLH, before the gelation took place. Then the storage modulus G' and the loss modulus G'' were recorded at different temperatures, as the gelation of the DLH progressed, whilst oscillation displacement and angular oscillation

frequency were fixed. Results are summarised in Figure 2.4A. Small oscillations in the value of both moduli were attributed to experimental noise. At 10°C and 20°C, G’ and G’’ were constant over time. The absence of any relative changes between G’ and G’’ throughout all timepoints at these temperatures indicated that gelation of the DLH does not occur at 10°C and 20°C. At 37°C, both moduli increased in value over time, until a plateau was reached. In particular, G’ increased from a value of 12.5 Pa at t = 0 min to a value of 430 Pa at t = 60 min, whilst G’’ increases from a value of 2.1 Pa at t = 0 min to a value of 53.5 Pa at t = 60 min. The relative increase of G’ over G’’ indicates that gelation of the DLH took place at 37°C. The curves related to the behaviour of G’ and G’’ are at their steepest approximately between t = 10 min and t = 20 min, indicating that the majority of the gelation process takes place in this time window. Gelation was considered complete at approximately t = 50 min, when the values of both G’ and G’’ were stable. A temperature of 37°C was maintained for the remaining stages of rheological characterisation.

In the next phase of characterisation, G’ and G’’ were measured at a varying angular oscillation frequency, whilst the oscillation displacement remained fixed. Results are reported in Figure 2.4B. Measurements of the G’ increased from a value of 310.2 Pa at 0.1 rad/s to a peak value of 496.5 Pa at 21.54 rad/s. A similar behaviour could be observed in relation to G’’, although the ascension was subtler and the peak was found at a slightly higher frequency, with values increasing from 47.4 Pa at 0.1 rad/s to a peak value 56.7 Pa at 27.83 rad/s. After reaching their peak values, both G’ and G’’ decreased markedly. Negative values were recorded at frequencies higher than 46.62 Hz, and were interpreted as instrumental artefacts

corresponding to measurements too close to 0 to be correctly reported by the equipment. These values are not reported in the graph.

In the final phase of the rheological characterisation of the DLH, the angular frequency of the oscillation applied on the material was kept constant, whilst G' and G'' were measured at increasing oscillation strain. Results are reported in Figure 2.4C, and exclude negative values following the same rationale applied to Figure 2.4B. The oscillations in both G' and G'' observed at strain values lesser than 0.052 % were attributed to experimental noise. At increasing oscillation strains, G' increases up to a peak value of 526.4 Pa, measured at an oscillation strain of 8.608 %. At higher oscillation strains, the storage modulus sharply decreases to a value similar to that of the loss modulus, reaching a value close to 0 Pa. The behaviour of G'' is similar. Its value increases with increasing oscillation strains up to a peak of 71.9 Pa reached at an oscillation strain of 8.608 %. At higher oscillation strains, the value of the loss modulus decreases and approximates 0 Pa. These results show that the maximum oscillation strain that the DLH can tolerate before rupture is 8.608 %.

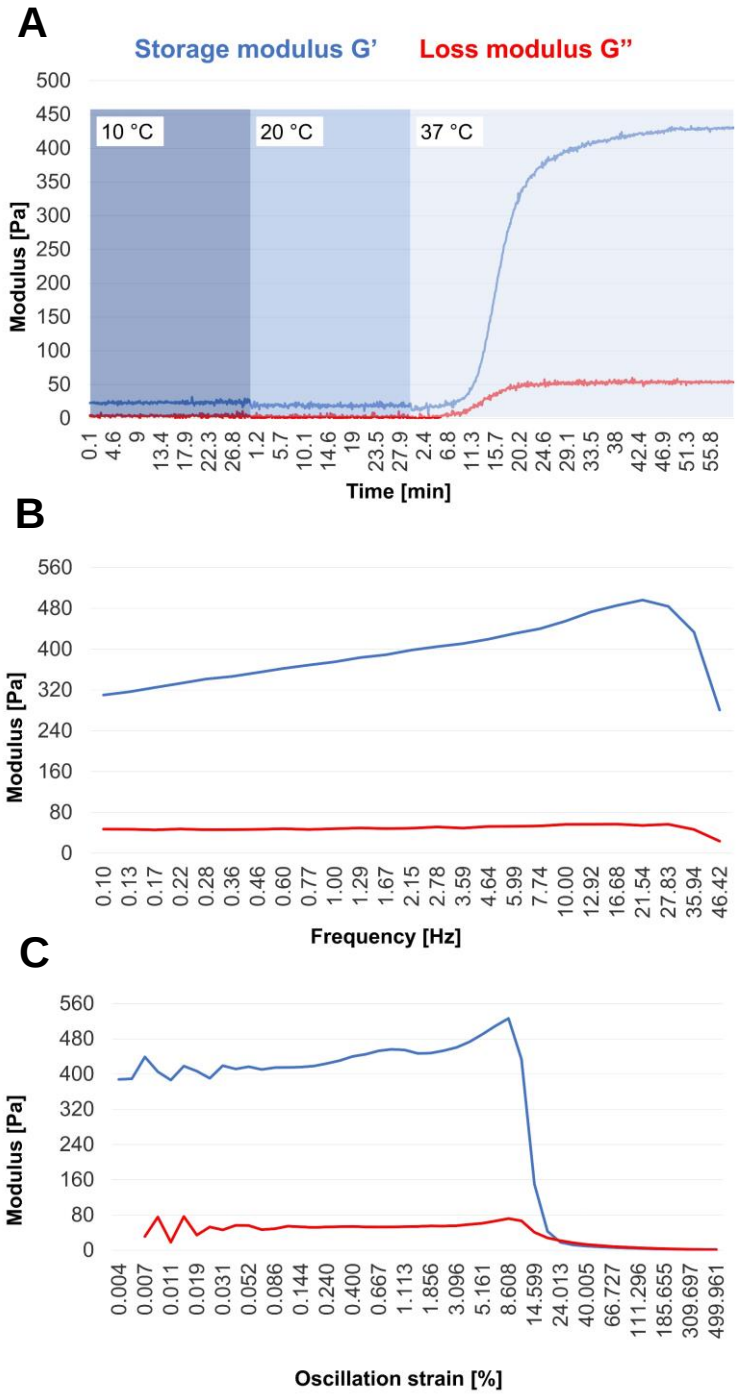


**Figure 2.4.** Rheology of DLH. The rheological properties of DLH were analysed using a rheometer, and the gelation kinetics, in addition to the frequency-dependant and oscillation strain-dependant changes in storage and loss moduli were recorded. In all the graphs, the storage modulus G' is reported in blue and the loss modulus G'' is reported in red. **A:** analysis of storage and loss moduli during gelation. Throughout the experiment, the oscillation displacement and angular oscillation frequency were fixed at 1.25 x $10^{-3}$ rad and 6 rad/s, respectively. The moduli were recorded for 30 min at 10°C, then for 30 min at 20°C, and finally for 60 min at 37°C. The temperature associated with a set of measures is indicated by the colour of the background; dark blue (10°C), blue (20°C), and light blue (37°C). The X axis reports time expressed in min and the Y axis reports the value of the modulus expressed in Pa. Gelation, marked by a relative increase of G' in relation to G'', was observed only at 37°C. **B:** analysis of storage and loss moduli at fixed temperature (37°C) and oscillation displacement (1.25 x $10^{-3}$ rad), at increasing angular frequency. The X axis reports the angular frequency expressed in rad/s and the Y axis reports the modulus expressed in Pa. Only positive measurements of the moduli are reported. The measurement of G' increased from 310.2 Pa at 0.1 rad/s to a peak value of 496.5 Pa at 21.54 rad/s, whilst G'' increased from 47.4 Pa at 0.1 rad/s to a peak value 56.7 Pa at 27.83 rad/s. After reaching their peak values, G' and G'' decreased sharply. **C:** analysis of storage and loss moduli at fixed temperature (37°C) and angular oscillation frequency (6 rad/s), at increasing oscillation strain. The X axis reports the oscillation strain expressed in % and the Y axis reports the modulus expressed in Pa. Only positive measurements of the moduli are reported. G' and G" increased with progressively higher oscillation strains, reaching a peak value of respectively 526.4 Pa and at 71.9 Pa at an oscillation strain of 8.608 %. At higher oscillation strains, G' and G" markedly decreased to values approximating 0 Pa, showing that 8.608 % was the maximum oscillation strain that could be tolerated by the material before rupture. N = 1 sample of DLH.

### 2.3.4. Seeding of HBECs on DLH

To evaluate the capacity of HBECs to adhere on DLH, HBECs (donor: 18TL052522) were seeded in cell culture-treated 96-well plates on n = 6 uncoated wells to act as a two-dimensional (2D) control, on n = 6 wells including collagen I hydrogel to act as a 3D control, and on n = 6 wells including DLH. Representative images taken on day 0, 1, and 5 post-cell seeding are shown in Figure 2.5A. By day 5, cells seeded on both uncoated wells and collagen I hydrogel-inclusive wells appeared to be confluent. Conversely, cells seeded on DLH-inclusive wells did not reach confluency and displayed a circular morphology from day 1 to day 5. Circular cell clumps could also be observed on day 5 in DLH-inclusive wells.

On day 5 post-cell seeding, cells were stained with Hoechst dye and nuclei count was performed on images acquired after the staining procedure (Figure 2.5C). In particular, 1 representative image was obtained from each seeded well. The nuclei count related to cells cultured on DLH was lower than the count related to cells cultured on collagen I hydrogel and on uncoated cell culture-treated wells, and the difference was statistically significant ($p < 0.0001$, one-way ANOVA, followed by post-hoc Tukey's multiple comparison test).

It was hypothesised that a higher volume of cell culture medium would facilitate cell growth towards confluency. To test this hypothesis, collagen I hydrogel and DLH were included in the apical wells of, respectively, n = 4 and n = 3 wells of a 24-well plate-format transwell® system, and HBECs obtained from 1 donor were then seeded on the hydrogels. Widefield images of HBECs seeded on transwell® membranes were acquired on day 5 post-seeding. As shown in Figure 2.5B, at day 5 HBECs seeded on DLH did not reach confluency, and displayed the circular

morphology observed in Figure 2.5A, whilst HBECs seeded on collagen I hydrogel reached confluency. It was therefore concluded that HBECs cannot form a confluent layer when seeded on DLH, and that increasing medium availability does not facilitate their growth on this substrate.

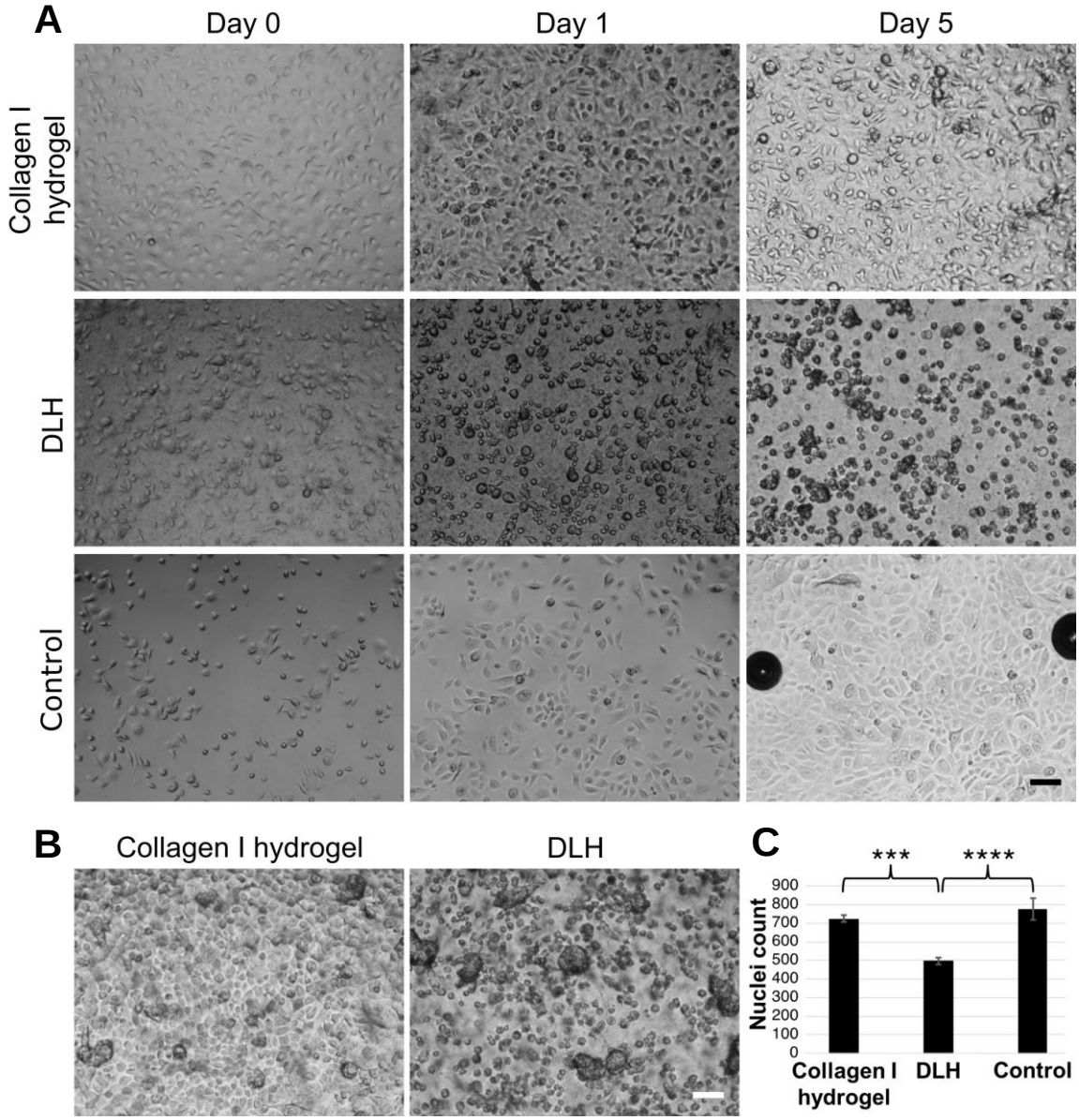


**Figure 2.5.** Widefield images and quantification of HBECs adherence on DLH as compared to collagen I hydrogel and cell culture-treated uncoated wells. Seeding of HBECs was performed on cell culture-treated uncoated wells of 96-well plates, and on wells including DLH or collagen I hydrogel. Widefield images were then acquired at day 0, 1, and 5. On day 5, cells were stained with Hoechst, and a nuclei count was performed. The cell seeding was also performed on transwell® membranes including DLH or collagen I hydrogel, and widefield images were acquired on day 5. In both 96-well plates and transwell® membranes, HBECs did not grow to confluence. **A:** representative widefield images of HBECs cultured on collagen I hydrogel (first row), DLH (second row), and on cell culture-treated uncoated wells (third row) on day 0 (first column), 1 (second column), and 5 (third column). The black circles on the edges of the image related to the control at day 5 are formed by air bubbles. Magnification: 2.5X, with a 2X post-acquisition zoom. Scale bar: 100 µm. **B:** representative widefield images of HBECs cultured on collagen I hydrogel (left) and DLH (right) on transwell® membranes at day 5 after seeding. Magnification: 2.5X. Scale bar: 100 µm. **C:** nuclei count (Y axis) of HBECs cultured on different substrates (listed on X axis) at day 5 after seeding, reported as mean ± SEM. The count is derived from images of Hoechst-stained cells. The differences observed between the values reported in the graph are statistically significant as tested by one-way ANOVA ($p < 0.0001$) followed by a post-hoc Tukey's multiple comparison test. The significance of the post-hoc test is indicated in the graph (*** indicates $p < 0.001$, **** indicates $p < 0.0001$). A minimum of n = 4 cell-seeded wells were used for each condition included in 96-well plates (Figure A), and a minimum of n = 3 cell-seeded wells were used per condition included in transwell® systems (Figure B), using cells obtained from n = 1 donor. Nuclei count was obtained from 1 representative image per well of 96-well plate (Figure C).

## 2.4. Discussion

In this work, porcine bronchi were decellularised following a vacuum-assisted decellularisation protocol. Whilst no nuclei could be found in the luminal and cartilaginous portions of the airways after the decellularisation procedure, residual nuclei could still be observed in areas within the submucosal tissue. Complete removal of cellular material is desirable if the decellularised tissue is to be used for clinical implantation, as residual cellular material in decellularised constructs can stimulate an inflammatory response in the patient, which can hinder the integration of the graft into the recipient's body (219). However, in the context of *in vitro* model development, and specifically in relation to models that lack a component of the immune system able to react to cellular residuals, the presence of cellular material in the tissue would not be able to elicit an inflammatory response. As the inclusion of immune cells in the model developed in this work was not planned, the removal of cellular material achieved with the decellularisation protocol adopted in this study was considered sufficient.

Adherence of HBECs seeded on the decellularised scaffolds was scarce. Similar results were obtained by seeding porcine tracheal epithelial cells on decellularised porcine tracheal tissue in separate studies (220, 221, 222). However, HBECs appeared to efficiently repopulate decellularised human bronchi in the *in vitro* model developed by Hedström *et al*., (191), and in a further study based on the use of the same model (192). The decellularisation procedure applied by Hedström *et al*. was markedly shorter as compared to the one adopted in this work and other studies showing incomplete scaffold recellularisation (220, 221, 222). The brevity of the decellularisation procedure followed by Hedström *et al*. might have

contributed to a better preservation of the ECM structure and therefore to the reportedly efficient cell repopulation. However, the relationship between high cell adherence and short decellularisation protocols is unclear in studies focused on the use of immortalised cells. In particular, bronchial ICL appear capable of efficiently repopulating porcine tracheas decellularised adopting both lengthy (190) and short (223) decellularisation protocols. Literature on the subject of cell repopulation of decellularised airways is therefore not univocal, and any comparison with this work are made difficult by the variety of decellularisation protocols, seeding techniques, and cell types adopted in the different studies. Studies with higher statistical robustness are required to properly define the relationship between the type of seeded cells, seeding technique, decellularisation protocol, and cell repopulation efficacy.

The physical and chemical properties of the DLH can be compared to those reported in other studies centred on the use of lung ECM hydrogels (210, 211, 224). In this work, gelation of DLH did not occur at temperatures less than 37°C, in line with other lung ECM hydrogels described in the literature (210, 211, 224). Whilst results related to the gelation temperature were in line with findings reported in the existing literature, a number of discrepancies were also evident in relation to a majority of studies centred on lung ECM hydrogels. The gelation time of the DLH was approximately 50 min, whilst in most studies centred on the characterisation of lung ECM hydrogels the gelation time ranges approximately between 10 and 36 min (225, 226, 211). Only one study based on lung ECM hydrogels reports a gelation time higher than the one observed in this work (227). The gelation time of the DLH can therefore be considered relatively high as compared to other lung ECM hydrogels, which could potentially present issues in relation to the inclusion

of the hydrogel in microfluidic platforms. In particular, the small volumes of hydrogel typically loaded on microfluidic chips could dry between the loading procedure and the completion of the gelation process (228, 229). Whilst not critical for this work, it would be advantageous for the scientific community to further explore the biochemical mechanisms underlying the gelation kinetics of ECM hydrogels such as the DLH, in order to devise methods to shorten their gelation time and thus facilitate their incorporation into *in vitro* models requiring small hydrogel volumes.

Another discrepancy with studies based on the use of lung ECM hydrogels lies in the value of the storage modulus at low oscillation frequencies and deformation. In particular, G' was found to be one order of magnitude higher than that related to the majority of ECM hydrogels related to various biological tissues analysed in literature (230). Only 2 studies centred on lung ECM hydrogels include a measurement of G' (225, 226), and amongst these studies, only the research work conducted by Pouliot *et al*. is based on hydrogels with the same protein concentration as the DLH (225). In their study, Pouliot *et al*. report a value of the G' one order of magnitude lower than the value reported in the present work (225). Therefore, DLH can be considered to be a material with a relatively high G' as compared to other ECM hydrogels, including those derived from lungs.

The HBECs seeded on DLH had a circular phenotype and failed to reach confluency. This is in contrast with other studies conducted using lung ECM hydrogels (210, 212). In the work conducted by Dabaghi *et al*., (210), HBECs adhered and covered the surface of a hydrogel derived from the decellularisation of human lungs. In this case, an explanation for the discrepancy between studies could lie in the fact that the DLH used in the present work was derived from porcine as opposed to human tissue, whilst the seeded cells were of human origin. The

study conducted by Balestrini *et al*. also points towards this explanation (275). In particular, in their study a higher number of human endothelial cells repopulated decellularised human lungs as opposed to decellularised porcine lungs (275). Therefore, an interspecies mismatch between the animal from which the DLH was derived and the seeded epithelial cells could explain the results obtained in the present work.

Another aspect to consider, in addition to any interspecies mismatch, is also the type of tissue used to obtain the hydrogel. In the study conducted by Badylak *et al*., (212), HBECs adhered and underwent mucociliary differentiation on a porcine trachea-derived gel. Therefore, growth and differentiation of HBECs might be facilitated if the cell culture substrate is based on the specific ECM found in the tracheobronchial tissue, as opposed to the parenchymal tissue-derived DLH used in the present work.

# Chapter 3

As reported in the previous chapter, decellularised bronchial tissue and DLH were not compatible with HBECs. As these strategies appeared to be unsuccessful, in this Chapter, the focus will shift towards the use of microfluidic chips in order to generate an *in vitro* model of airways. An introductory section will centre on the concept of microfluidics and its application in the field of *in vitro* model development, with a specific focus on models of the large bronchi. An experimental section will follow, in which the feasibility of a strategy based on the use of microfluidic chips for the development of a bronchial *in vitro* model will be assessed. A discussion of the results will then follow the experimental section.

## 3.1. Introduction

### 3.1.1. Microfluidic-based *in vitro* models

One option for the development of *in vitro* models of airways is the use of platforms based on microfluidics (231). Whilst there are no formal definitions of the term, “microfluidics” can be regarded as the science of liquid fluid behaviour on the micro- and nanometer scale (232). Following this definition, in a “microfluidic system” a liquid fluid is constrained in a space in which at least one dimension is sub-millimetre. In these conditions, the behaviour of liquid fluids is markedly different than that observed on the macroscale (232). For example, fluid flow in a microfluidic system tends to be laminar instead of turbulent (232), thus facilitating the mathematical modelling of its behaviour. Moreover, the effects of gravity on fluid behaviour are negligible, whilst the effects of surface tension are prominent (232).

Microfluidic systems have been developed for a variety of applications, such as energy production, detection of chemical species, and for applications in the biomedical field (233). Biomedical applications include their use as analytical arrays, gradient generators, microdiluters, diagnostical devices and as *in vitro* models (233). In particular, microfluidic systems used as *in vitro* models are referred to as “organ-on-a-chip” (OOAC; 234).

Various tissues have been replicated in OOAC. Examples include liver (235), intestine (236), kidney (237), skin (238) and the respiratory tract (239). In the context of respiratory tissue, a milestone in the field was the development of the first OOAC of lungs, developed by Huh *et al*., (240). This seminal work paved the way for further work in this direction, including the development of OOAC of large bronchi. Studies centred on the use of OOAC of large airways are summarised in Table 3.1. Most of the models reported in Table 3.1 are based on the use of microfluidic chips developed ad hoc for a specific study, and have not been used for further studies by other research groups. This situation is likely due to difficulties in replicating the chip fabrication procedure, and in following the cell culture methods adopted by the chip developers to seed and maintain cells in the custom-made OOACs.

**Table 3.1**. Cells included in OOACs of large bronchi. Cells in the studies were human-derived and were not transformed cell lines, unless specified in the "Notes" column. The "Chip system" column indicates whether the OOAC was built in-house ("proprietary") or developed by a commercial entity, indicated in the cell.

| Epithelial cells | Fibroblasts | Endothelial cells | Smooth muscle cells | Cells related to other organs | Immune cells | Pathogens | Notes | Chip system | References |
|---|---|---|---|---|---|---|---|---|---|
| ✓ | | | ✓ | | | | Epithelial cells were the ICL Calu-3, which derives from lungs. | Proprietary | **241** |
| ✓ | | ✓ | | | | | | Emulate Inc. | **242** |
| ✓ | | ✓ | | | | | | SynVivo Inc. | **243** |
| ✓ | | | ✓ | | | | Epithelial cells were the ICL Calu-3, which derives from lungs. | Proprietary | **244** |
| ✓ | ✓ | ✓ | | | | | HBECS are grown on transwell® inserts mounted on top of the microfluidic chip. HBECs are grown on vitrified decellularized trachea-derived ECM. | Proprietary | **245** |
| ✓ | ✓ | ✓ | | | | | | Proprietary | **246** |
| ✓ | ✓ | ✓ | | ✓ | | ✓ | Pathogen included was the fungus *Aspergillus Fumigatus*.<br>Immune cell included 90-95% neutrophils and 5-10 % eosinophils. | Proprietary | **247** |
| ✓ | | ✓ | | | | | | Emulate Inc. | **327** |
| ✓ | | ✓ | | ✓ | | ✓ | HBECs were obtained from both healthy donors and from donors affected by cystic fibrosis.<br>Immune cells included were polymorphonuclear leukocytes.<br>Pathogen included was the bacterium *Pseudomonas Aeruginosa*. | Emulate Inc. | **328** |
| ✓ | | | | | ✓ | | Intestinal cells were included. | | **329** |
| ✓ | | ✓ | | | | ✓ | Pathogens included were various strains of the Influenza A virus. | Emulate Inc. | **330** |
| ✓ | * | ✓ | | | ✓ | | *Airway stromal mesenchymal cells were included, possibly inclusive of fibroblasts. Airways' cells were seeded on a membrane coated with a decellularized lung-derived solution.<br>Hepatic and cardiac organoids were included. | Proprietary | **331** |
| ✓ | | ✓ | | | | ✓ | Pathogens included were various strains of severe acute respiratory syndrome coronavirus 2 (SARS-CoV-2). | Proprietary | **332** |
| ✓ | | | | | | | | Proprietary | **333** |
| ✓ | | ✓ | | | | ✓ | Pathogen included was the human rhinovirus strain 16. | Proprietary | **334** |
| ✓ | | | | | ✓ | | Hepatic cells were included. | Proprietary | **335** |
| ✓ | | | | | ✓ | | Hepatic, intestinal, endometrial, neural, cardiac, pancreatic, renal, muscle and skin cells were included. | Proprietary | **336** |
| ✓ | | | | | ✓ | | Hepatic spheroids were included. | TissUse GmbH | **337** |
| ✓ | | ✓ | | | | | | Proprietary | **338** |
| ✓ | | | | | | | | Proprietary | **339** |
| ✓ | | | | | | | | Proprietary | **340** |
| ✓ | | | | | | | | Proprietary | **341** |
| ✓ | | ✓ | | | | | | Proprietary | **342** |
| ✓ | | | | | | | | Proprietary system, including chip from Micronit B.V. | **343** |
| ✓ | | | | | | | Epithelial cells were the ICL Calu-3, which derives from lungs.<br>Includes also ICL of alveolar and nasal epithelial cells. | Proprietary | **346** |

A number of industrial entities have therefore entered the OOACs space, and have developed or are currently developing commercial large airways-on-a-chip. Examples of such companies include Alveolix, Synvivo, and Emulate. However, despite the efforts in the industrial sector, and more than 10 years after the publication of the seminal paper by Huh *et al*., the number of studies based on the use of OOACs of airways are minimal compared to those relying on transwell® systems. One of the reasons underlying this trend could be that current commercial OOACs of airways are difficult to use and have a low throughput. There is, therefore, a need for the development of a cost-efficient, user friendly, high throughput commercial OOAC of airways. To address this need, the recently commercialised microfluidic chip called "OrganoPlate®" (OP) and developed by Mimetas, which so far have not been used for the development of airway on-a-chip, could be utilized.

The use of the OP has become increasingly popular for the development of a variety of OOACs. In particular, from 2015 onwards, the use of the OP chip has been reported in 28 studies, in which it was used as the microfluidic platform for the development of OOAC of various biological structures including kidney (248), blood-brain barrier (249), and intestine (250). Briefly, the OP is a microfluidic platform with the dimensions of a standard 384 well-plate, including 40 to 64 microfluidic chips per plate. Each microfluidic chip includes 3 parallel lanes. The central lane can be filled with a hydrogel of choice, which in most studies is collagen I-derived. The two lateral lanes can be seeded with cells. The popularity of the OP lies in its cost-effectiveness, ease of use and high throughput. Moreover, a multitude of assays have been validated on the chips, which can also be easily imaged. Additionally, induction of a fluid flow and measurement of the electrical

resistance across the 3 lanes, which can be used to derive the TEER of epithelial cells seeded on the chip, can be performed with dedicated equipment also commercialised by Mimetas.

Given their high-throughput, commercial availability, capacity to include co-cultures of multiple cell types, possibility to include hydrogels capable of mimicking aspects of the ECM, and the possibility to include shear stress mimicking the respiratory mechanical environment, in the next sections the use of OP chips for the development of a biomimetic *in vitro* model of large bronchi will be tested.

## 3.2. Methods

### 3.2.1. Layout of OP

The OP (Mimetas, Netherlands) is a commercial microfluidic plate that can be used for the development of cellular *in vitro* models. The layout of the plate is illustrated in Figure 3.1.

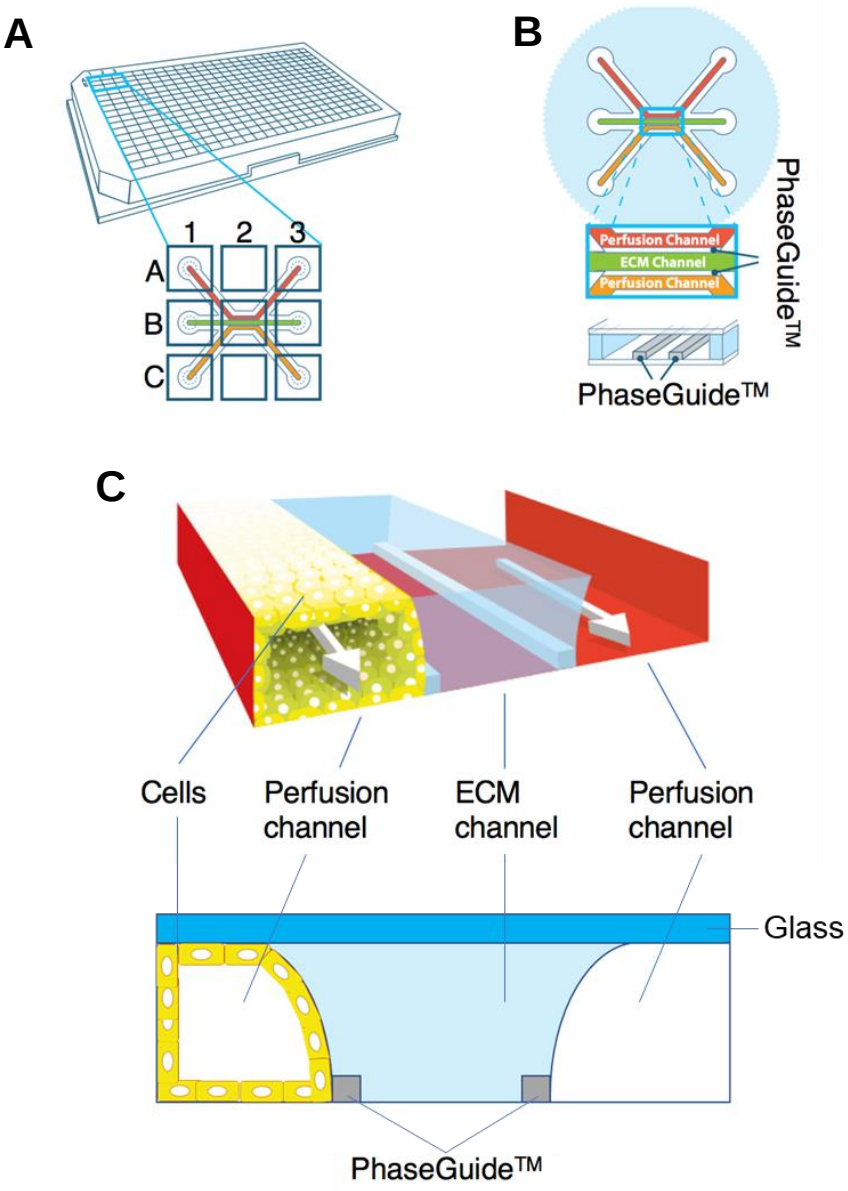


**Figure 3.1**. Layout of OP. **A:** perspective view of the OP and simplified zoomed image of a single chip. In the zoomed image, the top red channel and the bottom orange channel are perfusion channels, which can be filled with cell culture medium, and the central green channel is an ECM channel, which can be filled with a hydrogel. Each square in the zoomed image represent one of the wells composing the chip. A letter and a number is assigned to each square. Wells A1, B1, C1 include the inlets for respectively the top perfusion channel, the ECM channel, and the bottom perfusion channel. Well B2 includes the area where the two perfusion channels come in contact with the ECM channel. Wells A3, B3, C3 include the outlets for respectively the top perfusion channel, the ECM channel, and the bottom perfusion channel. Wells A2 and C2 are empty. **B:** schematics depicting one of the chips (within the blue circle), a zoomed schematic of the central well of the chip (within the blue rectangle), and a depiction of the PhaseGuides™. The PhaseGuides™ are two parallel protrusions localised in the central well of the chip, between the ECM channel and the two perfusion channels, which prevent the hydrogel loaded in the ECM channel to extravasate in the perfusion channels. **C:** perspective view (top) and cross section (bottom) of the central well of the chip, upon cell seeding in one of the perfusion channels. Cells form a tubular structure in the seeded channel, separated from the opposite perfusion channel by the hydrogel loaded in the ECM channel and kept in place by the PhaseGuide™. Images reproduced with consent by © Mimetas B.V.

The plate has the dimensions of a Society for Biomolecular Screening (SBS)-standard 384 well-plate, has a glass bottom, and includes 40 chips, each one composed of 2 perfusion channels and 1 ECM channel. One chip occupies 9 wells

of the plate. Figure 3.1A includes a schematic depicting a chip, in which a letter and a number is assigned to each well. Wells A1, B1, C1 contain inlets for, respectively, the top perfusion channel, the central ECM channel, and the bottom perfusion channel. Wells A1 and C1 can act as reservoirs for cell culture medium, which can flow through the inlet in the two perfusion channels. Hydrogels of various types can be loaded in the inlet in B1, to fill the ECM channel. Wells A2 and C2 are empty. In well B2, the 2 perfusion channels are separated from each other by the hydrogel that can be loaded in the central ECM channel. The hydrogel is kept in place in the ECM channel by two PhaseGuides™, depicted in Figure 3.1B. The PhaseGuides™ are protrusions that run parallel to each other between the perfusion channels and the ECM channel, and that stabilise the hydrogel's menisci. A glass ceiling separates the channels in well B2 from the external environment, forming a top compartment termed "observation window". Wells A3, B3, C3 contain outlets for, respectively, the top perfusion channel, the central ECM channel, and the bottom perfusion channel. Wells A3 and C3, like wells A1 and C1, can act as reservoirs of cell culture medium to feed the perfusion channels. Cells can be loaded in the OP in one or both of the perfusion channels, and can also be mixed with the hydrogel loaded in the ECM channel. In this work, cells were loaded only in one perfusion channel, as illustrated in Figure 3.1C.

Two versions of the OP chip have been produced. In this work the first version is termed "OP1" and second is termed "OP2". Both versions share the same general layout summarised in Figure 3.1. However, the OP2 version has larger channel inlets and outlets, which makes cell seeding, medium perfusion and gel loading more user-friendly. Additionally, differences between OP1 and OP2 chips are found in the dimensions of the channels and in the thickness of the glass in the

bottom of the plate. The differences between the two versions are summarised in Table 3.2.

**Table 3.2**. Dimensions of OP1 and OP2 chips, expressed in µm.

| | OP1 | OP2 |
|---|---|---|
| **Inlet and outlet aperture (mm)** | 0.4 | 1.4 |
| **Perfusion channel width (µm)** | 320 | 300 |
| **ECM channel width (µm)** | 360 | 350 |
| **Bottom glass thickness (µm)** | 170 | 150 |

### 3.2.2. Layout of the Organoplate Graft

The OrganoPlate® Graft (OGP; Mimetas) is a commercial microfluidic plate that, like the OP1 and OP2 chips, can be used for the development of cellular *in vitro* models. The layout of the OGP chip is shown in Figure 3.2.

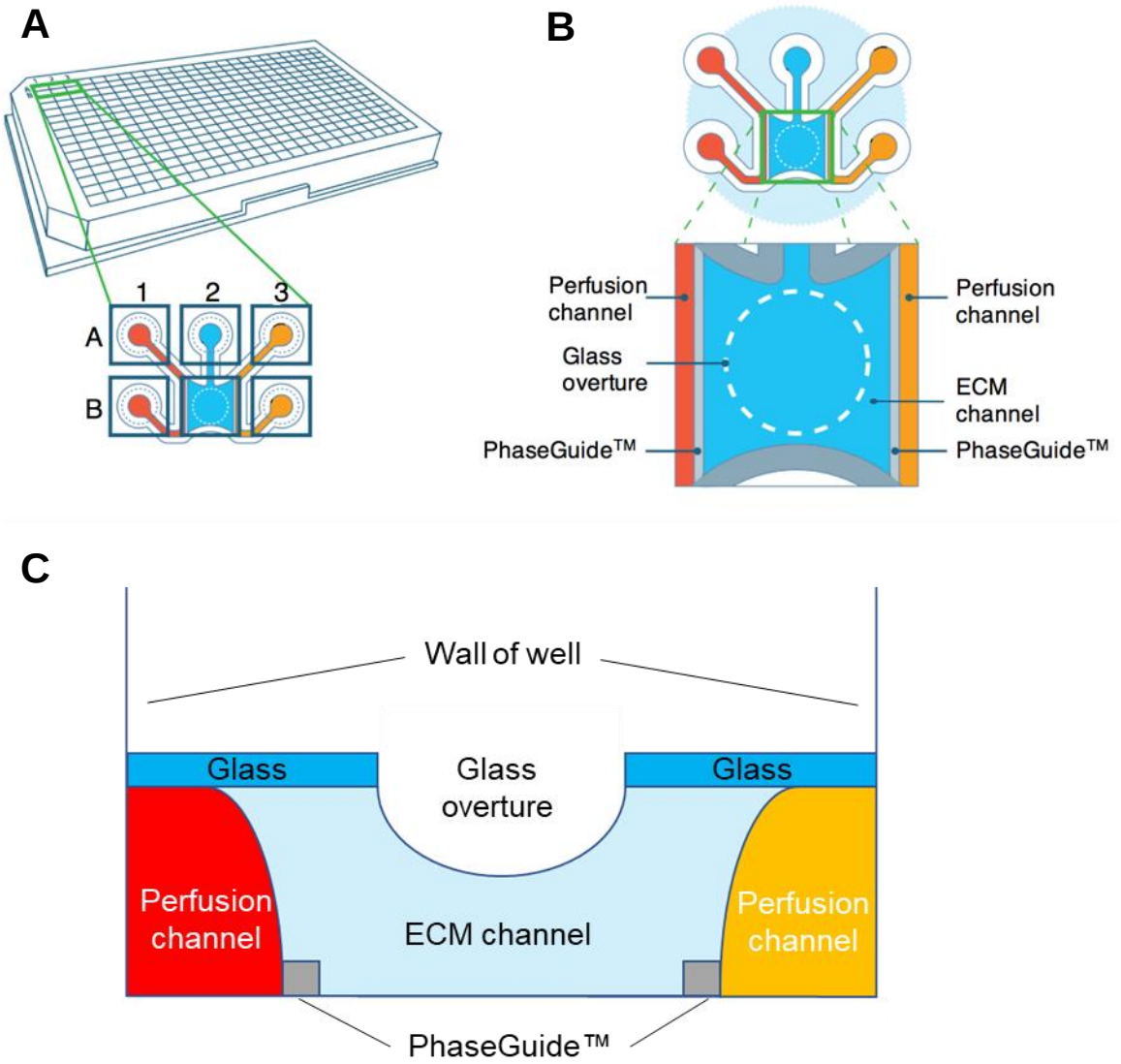


**Figure 3.2.** OGP layout. **A:** perspective view of an OGP plate (top) and schematic representation of one OGP chip (bottom). Each square in the schematic represents a well of the chip. A letter and a number is assigned to each well. Well A1, A2, A3 include the inlets for respectively the left perfusion channel (red), the central ECM channel (blue), and the right perfusion channel (orange). Wells B1 and B3 include the outlets for respectively the left and the right perfusion channels. Well B2 includes the two perfusion channels and the ECM channel. **B:** schematic representation of one OGP chip (top) and schematic zoom on well B2 (bottom). Well B2 includes the two perfusion channels (red and orange), separated by the hydrogel included in the ECM channel (blue). The hydrogel is kept in place in the ECM channel by PhaseGuides™. The channels in well B2 are separated from the external environment by a glass ceiling, which has a circular overture in the centre of the well. The overture is represented in the image by a circular white dashed line. **C:** cross section of the well B2 of an OGP chip. The two perfusion channels (red and orange) are visible on the side of the chip, divided by an ECM channel filled with a hydrogel (pale blue). The continuity of the glass layer (dark blue) on top of the ECM channel is interrupted by an overture in the glass. A circular concavity below the glass overture is visible in the hydrogel included in the ECM channel. Images reproduced with consent by © Mimetas B.V.

Similarly to the OP, the OGP has the dimensions of a SBS-standard 384 well-plate and has a glass bottom. Additionally, each OGP plate includes 64 chips. Each chip includes 3 lanes. The lateral lanes are perfusion channels, which can be filled with cell culture medium, and the central lane is an ECM channel, which can be filled

with a hydrogel. Each chip occupies 6 wells of the plate, as shown in the green rectangle included in Figure 3.2, in which a letter and a number is assigned to each well. Wells A1 and A3 include inlets for, respectively, the left and the right perfusion channel. Well A2 includes an inlet for the ECM channel, in which hydrogels of various types can be loaded. Wells B1 and B3 include outlets for respectively the left and right perfusion channels. Wells A1, A3, B1, B3 can be filled with cell culture medium, to feed the perfusion channels. Well B2, schematised in the yellow square in Figure 3.2, includes both perfusion channels, separated from each other by the hydrogel loaded in the ECM channel. The hydrogel is kept in place in the ECM channel by two PhaseGuides™. The channels in well B2 are separated from the external environment by a glass ceiling, which has a circular overture in the centre of the ECM channel. In the present work, cells are seeded in well B2, on top of the glass ceiling.

### 3.2.3. Collagen I hydrogel loading on chips

The following protocol describes the procedure applied to load collagen I hydrogel on OP1 and OP2 chips. Firstly, 50 µL of HBSS (Gibco) was added to the observation windows of the chips. Then, collagen I hydrogel pre-gel, reconstituted as described in 2.2.9, was loaded in the gel inlet of the chips. For OP1 chips the gel loading volume was 1.7 µL, and for OP2 chips it was 2 µL. The plate was then placed in a cell culture incubator for 15 min to allow gelation of the pre-gel solution, and then 30 µL HBSS were added to each well of the chips containing the ECM channel inlet, in order to avoid gel dessication. The plate could then be preserved in the cell culture incubator.

To load collagen I hydrogel on OGP chips, the same procedure described for OP1 and OP2 chips was applied, with the following exceptions. Firstly, HBSS was not added to the OGP chip prior to the gel loading. Secondly, the gel loading volume was 2.7 µL. Finally, 50 µL BEGM was added into the well containing the ECM channel inlet prior to preservation in the cell culture incubator.

### 3.2.4. Cell culture on OP1 and OP2 chips

Expanded HBECs (P2) were thawed and cultured following the protocol described in 2.2.6. When cells reached a confluency of 90 %, and 1 day after completion of the gel loading on the chips to be used for the experiment, the cells were seeded according to the following protocol. Throughout the protocol, a specific letter and number identifies the wells of the chips according to the scheme reproduced in Figure 3.3.

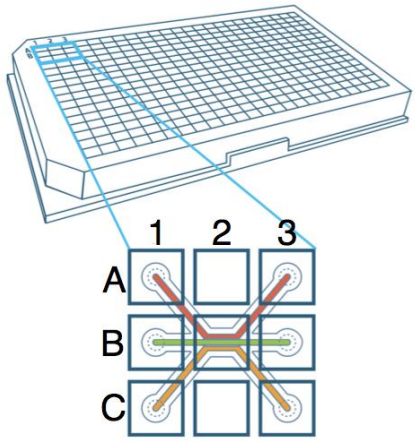


**Figure 3.3.** Schematic representation of the OP1 and OP2 chips. A letter and a number is assigned to each well composing the chip. Image reproduced with consent by © Mimetas B.V.

Firstly, to prepare the chips for the seeding procedure, 2 µL HBSS was loaded in the inlet of the perfusion channel in well A1 of each chip followed by 50 µL DPBS--. Shortly after, the DPBS-- was retrieved from the chip, and 50 µL BEGM was added to well A3. The plate could then be stored in the cell culture incubator.

To perform the seeding, the flasks of cells were briefly washed with DPBS--. Shortly after, 6 mL of ACF dissociation enzyme was added to each flask, which were then placed in the cell culture incubator until cell detachment was observable. The cell suspension from each flask was then pooled in a 50 mL centrifuge tube and mixed to a 1:1 volume ratio with ACF quenching enzyme to deactivate the dissociation enzyme. The cells were subsequently centrifuged at a centrifugal acceleration force of 300 x *g* for 5 min, and then resuspended to the desired cell concentration, which varied according to the specific experiment. The HBSS previously added to wells B1 was then retrieved, and 2 µL of cell suspension were seeded in the perfusion channel inlet in well A1. The plate was then placed in the cell culture incubator on a dedicated plate stand (Mimetas) at an angle of 75° for 2 h. Afterwards, 2 µL BEGM was loaded in the perfusion channel inlets in well C1, and then 50 µL BEGM was loaded into the wells A1, C1 and C3. The plate could then be placed in the cell culture incubator, and media was changed the day after the seeding and every 2-3 d thereafter. Medium changes were performed by removing cell culture medium in wells A1, A3, C1 and C3 and replacing it with 50 µL medium per well. The type of cell culture medium exchanged at each medium change depended on the specific experiment.

### 3.2.5. Hoechst and phalloidin staining on OP2 chips

In order to stain cells seeded on OP2 chips with Hoechst and phalloidin, the following protocol was followed. Cells were fixed by removing cell culture medium from wells A1, A3, C1, C3 and replacing it with 100 µL PFA 4 % in well A1 and 50 µL PFA 4 % in wells A3, C1, C3. The plate was then left at RT for 20 min. Afterwards, PFA was removed, and the plate was washed 3 times adding DPBS--

in the same wells and at the same volumes that had previously been selected for the 4 % PFA fixation step. Each washing step lasted 5 min. To stain the fixed cells with phalloidin, 25 µL of 1 X phalloidin staining solution, obtained by diluting the stock solution to a 1:1000 solution in DPBS--, was loaded on wells A1 and A3, and 15 µL of 1X phalloidin staining solution was added to wells C1 and C3. The plate was then incubated in the dark at RT for 1 h. Afterwards, the wells of the chips were rinsed 3 times with DPBS-- by adding 100 µL DPBS-- to well A1 and 50 µL DPBS-- to wells A3, B1, B3, C1 and C3. Subsequently, 25 µL of a 1 µg/mL Hoechst working solution, obtained by diluting the 10 mg/mL Hoechst stock solution in DPBS--, was added to the same wells and at the same volumes previously selected for the phalloidin staining. The plate was then incubated for 10 min at RT, in the dark, and subsequently washed 2 times with DPBS-- according to the same method followed for the washings applied after the phalloidin staining.

### 3.2.6. Cell culture on OGP chip

Expanded HBECs (P2) were thawed and cultured as described in the protocol reported in 2.2.6. As cells reached a confluency of 90 % and 1 day after completion of the gel loading on the OGP chips to be used for the experiment, the cells were seeded on the chips according to the following protocol. Throughout the protocol, a specific letter and number identifies the wells of the chips according to the scheme reproduced in Figure 3.4.

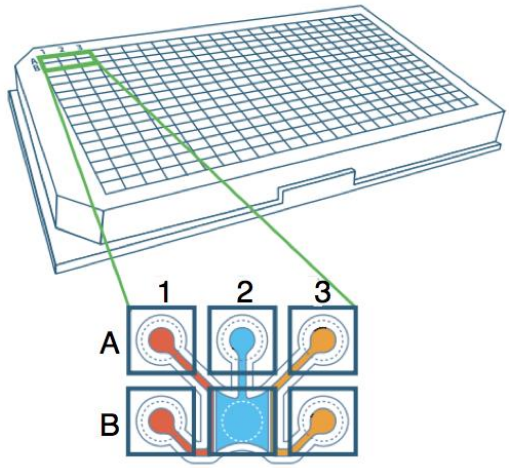


**Figure 3.4.** Schematic representation of the OGP chip. A letter and a number is assigned to each well composing the chip. Image reproduced with consent by © Mimetas B.V.

To prepare the chips for the cell seeding, 2 µL BEGM was added to the inlets of the perfusion channels in wells A1 and A3, and then 50 µL BEGM was added to wells A1, A3, B1 and B3. Cell culture medium was removed from the T75cm$^2$ flasks in which HBECs were cultured, and the flasks were briefly washed with DPBS--. Then 6 mL of ACF dissociation enzyme was added to each flask, which were subsequently placed in a cell culture incubator until cell detachment was observed. The cell suspension was then pooled in a 50 mL centrifuge tube containing an equal volume of ACF quenching enzyme to deactivate the dissociation agent. This step was followed by centrifugation of the resulting solution at a centrifugal force of 300 x *g* for 5 min. The supernatant was then removed and cells were resuspended to the desired cell concentration, which varied according to the specific experiment. To perform the seeding on the OGP, BEGM was removed from the ECM channel inlet in well A2, and cells were seeded at the desired cell concentration in a volume of 50 µL in the top compartment of the central well of the chips. The plate was then placed in a cell culture incubator for 2 h, and afterwards well B2 was washed 2 times with 50 µL BEGM. Finally, 50 µL BEGM was added

to well B2 and the plate was placed on a dedicated rocker (Mimetas) in the cell culture incubator. The rocker was set to incline the plate to an angle of 14° with a 8 min period, in order to induce a fluid flow parallel to the chips' perfusion channels. The cell culture medium was then changed the day after and every 2-3 d by removing the cell culture medium from wells A1, A3, B1, B2 and B3 and adding 50 µL newly decanted medium.

### 3.2.7. OP1 experiment 1: hydrogel optimisation

Hydrogels of different compositions were loaded on OP1 chips. The hydrogels were composed of: pure collagen I, pure Matrigel (Corning), and a variety of hydrogels obtained by mixing collagen I and Matrigel to obtain hydrogel solutions at different protein concentration ratios. The conditions are described in Table 3.3.

**Table 3.3.** Summary of conditions included in the hydrogel optimisation experiment conducted on OP1 chips. For each condition, the table indicated the hydrogels included, the protein concentration for each hydrogel in the hydrogel mixture, and the number of OP1 chips loaded.

| Condition | Hydrogels included and concentration ratio | Collagen I final concentration | Matrigel final concentration | Chips per condition |
|---|---|---|---|---|
| **1** | Collagen I only | 4 mg/mL | n/a | 8 |
| **2** | Collagen I : Matrigel 2 : 1 | 2 mg/mL | 1 mg/mL | 8 |
| **3** | Collagen I : Matrigel 1 : 1 | 2 mg/mL | 2 mg/mL | 8 |
| **4** | Collagen I : Matrigel 1 : 2 | 2 mg/mL | 4 mg/mL | 8 |
| **5** | Matrigel only | n/a | 8 mg/mL | 8 |

The pure collagen I hydrogel pre-gel was prepared according to the protocol described in 2.2.9. Matrigel is sold as a liquid pre-gel solution which gelates at

temperatures above 10°C. Therefore, the Matrigel and Matrigel-collagen I mixtures were kept ice-cold until they were loaded on the plate. Matrigel and Matrigel-collagen I mixtures were diluted to the desired protein concentrations by adding BEGM.

Once prepared, the pre-gel solutions were loaded in 8 OP1 chips per condition, following the same loading procedure described for collagen I hydrogel loading on OP1 chips detailed in 3.2.3. Then, HBECs (donor: 0000495838) were seeded at a density of 20 x$10^3$ cells/µL and subsequently cultured in the chips following the protocol described on 3.2.4. Cell culture was progressed according to the protocol described in 3.2.4, and the cell culture medium used throughout the experiment was BEGM. Widefield images were acquired on day 1, 2, 3, 6, 8 using a S100TV microscope.

### 3.2.8. OP1 experiment 2: Cell seeding protocol optimisation

Collagen I hydrogel was loaded on 36 OP1 chips according to the protocol described in 3.2.3. HBECs (donor: 18TL290281) were seeded with 2 different cell seeding densities, 20 x $10^3$ cells/µL and 30 x $10^3$ cells/µL, following the protocol described in 3.2.4 modified by altering the time window between the loading of the cell suspension in the chips and the subsequent medium change. In particular, the time windows were 2 h, 4 h, and 21 h. For each condition, 6 chips were seeded with HBECs. The conditions are summarised in Table 3.4.

**Table 3.4.** Summary of conditions included in the cell seeding protocol optimisation experiment conducted on OP1 chips. For each condition, the table indicates the cell seeding density, the time window between cell seeding and subsequent cell culture medium change, and the number of OP1 chips loaded.

| Condition | Cell seeding density | Time window | Chips per condition |
|---|---|---|---|
| **1** | 20 x $10^3$ cells/µL | 2 h | 6 |
| **2** | 30 x $10^3$ cells/µL | 2 h | 6 |
| **3** | 20 x $10^3$ cells/µL | 4 h | 6 |
| **4** | 30 x $10^3$ cells/µL | 4 h | 6 |
| **5** | 20 x $10^3$ cells/µL | 21 h | 6 |
| **6** | 30 x $10^3$ cells/µL | 21 h | 6 |

Cell culture was progressed according to the protocol described in 3.2.4, and the cell culture medium used for cell maintenance throughout the experiment was BEGM. Widefield images were acquired on day 1 and 5 of culture using a S100TV microscope.

### 3.2.9. OP1 experiment 3: cell seeding density optimisation and ALI attempt

Collagen I hydrogel was loaded on 24 OP1 chips according to the protocol described in 3.2.3, and HBECs (donor: 18TL290281) were seeded at varying seeding densities on the collagen I-loaded chips according to the protocol described in 3.2.4. In particular, HBECs at a seeding density of 5 x $10^3$ cells/µL, 10 x $10^3$ cells/µL and 20 x $10^3$ cells/µL were seeded on 8 chips per condition. Cell culture was then progressed according to the protocol described in section 3.2.4. Throughout the experiment the cell culture medium used for cell maintenance was BEGM. On day 5, ALI culture was tested on 4 chips per condition by removing the cell culture medium from the wells containing the inlet and outlet of the cell-seeded perfusion channel, and by then using a micropipette to load air into the same

channel in order to displace the residual cell culture medium in contact with the cells. Widefield images were acquired on day 1 and 5 using a S100TV microscope.

### 3.2.10. OP2 experiment 1: cell seeding density optimisation and ALI attempt

Collagen I hydrogel was loaded on 24 OP2 chips according to the protocol described in 3.2.3. Expanded HBECs (P2, donor: 18TL290281) were seeded at varying cell densities on the collagen I-loaded chips as described in 3.2.4, on 8 chips per condition. Specifically, the cell density of the cell suspension seeded on the chips was 5 x $10^3$ cells/µL, 10 x $10^3$ cells/µL, and 20 x $10^3$ cells/µL. On day 5, the induction of an ALI was tested on 4 chips per condition following the same method described in section 3.2.9. Afterwards, in chips where the test was executed, the wells including the top perfusion channel inlets and outlets were left empty, and this configuration, termed “low medium volume” (LMV), was maintained throughout the experiment. Chips in which the ALI was not tested were used as control and this configuration was also maintained throughout the experiment. Cell culture was executed following the protocol described in 3.2.4, and throughout the experiment the cell culture medium used for cell maintenance was BEGM. Widefield images were acquired on day 1 and 15 of culture using a S100TV microscope.

### 3.2.11. OP2 experiment 2: static and dynamic mucociliary differentiation

Collagen I hydrogel was loaded in 2 OP2 plates, termed “Static plate” and “Dynamic plate”. In particular, 24 chips were loaded in Plate 1 and 27 chips were loaded in Plate 2. Collagen I loading in the chips was performed according to the protocol described in 3.2.3, and expanded HBECs (P2, donor: 18TL290281) were seeded in each chip at a seeding density of 10 x $10^3$ cells/µL according to the

protocol described in 3.2.4. When cells in chips appeared fully confluent, which in this experiment was observed on day 3, BEGM was substituted with Pneumacult-ALI (PALI; STEMCELL), a commercial cell culture medium developed to stimulate the mucociliary differentiation of HBECs. Additionally, on day 3 medium from the wells containing the top channel inlets and outlets was removed from 8 chips in both Static and Dynamic plates to initiate a LMV layout. Also, medium from the wells containing the bottom channel inlets and outlets was removed from 8 chips in both plates, to initiate a “low medium volume-bottom” (LMV2) layout. As a result, in 8 chips in the Static plate and in 11 chips in the Dynamic plate the medium was left at a standard level of 50 µL in each well of the chips, and this layout was termed “standard”. The layout of each condition is schematised in Figure 3.5.

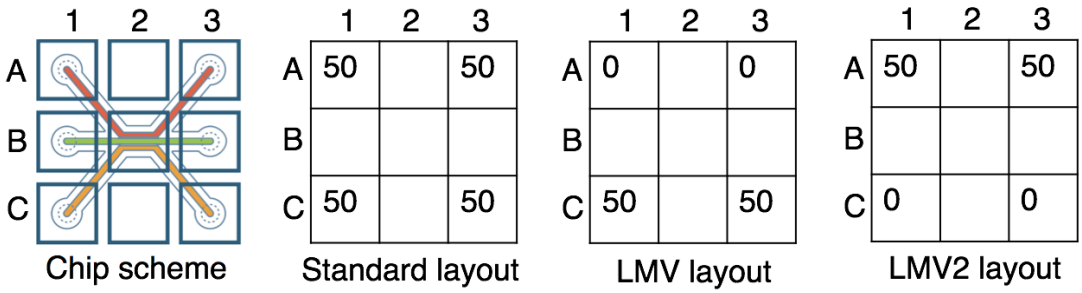


**Figure 3.5.** Schematic representations of the cell culture medium volume loaded in the wells of cell-seeded chips according to different layouts. In the schemes, each square represents a well composing an OP2 chip. A letter and a number is assigned to each well. Cells are seeded in the top perfusion channel, which has its inlet in A1 and outlet in A3. On the left hand-side, a generic scheme of an OP2 chip is reproduced. In the standard, LMV and LMV2 layouts, each square includes a number indicating the volume, expressed in µL, included in the related well of the chip. Images reproduced with consent by © Mimetas B.V.

Finally, from day 3 the Dynamic plate was cultured on a rocker placed inside the cell culture incubator (“dynamic” regimen) whilst the Static plate was cultured without the rocker (“static” regimen). The rocker was set to incline the plate to an angle of 6 degrees, changing the orientation of the plate every 8 min, in order to generate a cell culture medium fluid flow parallel to the perfusion channels. The conditions tested in this experiment are summarised in Table 3.5.

**Table 3.5.** Summary of conditions tested throughout the second optimisation experiment conducted on OP2 chips.

| Condition | Regimen | Layout | Chips per condition |
|---|---|---|---|
| **1** | Static | Standard | 8 |
| **2** | Static | LMV | 8 |
| **3** | Static | LMV2 | 8 |
| **4** | Dynamic | Standard | 11 |
| **5** | Dynamic | LMV | 8 |
| **6** | Dynamic | LMV2 | 8 |

The BEGM in the chips was changed the day after seeding, and then from day 3 the PALI in all the chips was changed every 2-3 d. The layouts were maintained throughout the experiment. Widefield images were acquired on day 14 using a S100TV microscope.

### 3.2.12. OP2 experiment 3: use of DAPT in OP2 chips

Collagen I hydrogel was loaded in 8 OP2 chips according to the protocol described in 3.2.3, and expanded HBECs (P2, donor: 18TL290281) were seeded at a cell density of 10 x $10^3$ cells/µL according to the protocol described in 3.2.4. When cells reached confluency, in 4 chips BEGM was exchanged with PALI including 10 µM (2S)-N-[(3,5-Difluorophenyl)acetyl]-L-alanyl-2-phenyl]glycine 1,1-dimethylethyl ester (DAPT; Sigma-Aldrich) dissolved in DMSO, the same concentration used in the work by Gerovac at el. (294), whilst in 4 chips BEGM was exchanged with PALI without DAPT. The OP2 plate was then maintained on a rocker inside a cell culture incubator as described in section 3.2.11. Widefield images were acquired at day 3 and 5 using a S100TV microscope. The experiment was progressed up to day 5, when cells were stained with Hoechst and phalloidin according to the protocol described in section 3.2.5. One representative image of Hoehcst-stained cells per chip was acquired, and nuclei count were obtained using the ImageJ software

(version: 1.53c, for source see reference: 344). In particular, the cell counting protocol used was the following. Firstly, each image was converted to a 32 bit greyscale format. A median filter was then applied to remove noise, and contrast was enhanced using the “enhance contrast” function. The background of each image was then subtracted using the “subtract background” command, and the nuclei were identified using a “Li” threshold and by separating clusters with the “watershed” command. The areas included in the seeded perfusion channel and ECM gels were considered for the nuclei count, excluding nuclei found on the PhaseGuides™. The nuclei were finally counted using the “analyse particles” function.

### 3.2.13. OP2 experiment 4: use of DAPT in combination with altered cell culture volume

Collagen I hydrogel was loaded in 24 OP2 chips according to the protocol described in 3.2.3, and expanded HBECs (P2, donor: 18TL290281) were seeded at a cell density of 10 x $10^3$ cells/µL according to the protocol described in 3.2.4. The BEGM was exchanged the day after seeding and every 2-3 d until cells reached confluency. Then, in a group of 8 chips BEGM was exchanged with PALI including 10 µM DAPT dissolved in DMSO. In another group of 8 chips, BEGM was exchanged with PALI including the same concentration of DMSO adopted in the DAPT-treated chips, but with no addition of DAPT to DMSO. Finally, in a group of 8 chips BEGM was exchanged with PALI free of DMSO and DAPT. Each of the 3 groups was then divided into 2 sub-groups of 4 chips. In the first sub-group cells were cultured with a medium volume of 50 µL in each well of the chip, therefore following the standard layout previously described, and in the second group the volumes of medium in each well was increased to 75 µL, a configuration termed

“high medium volume” (HMV) layout. A graphic description of the different layouts is provided in Figure 3.6, and the conditions tested in this experiment are summarised in Table 3.6.

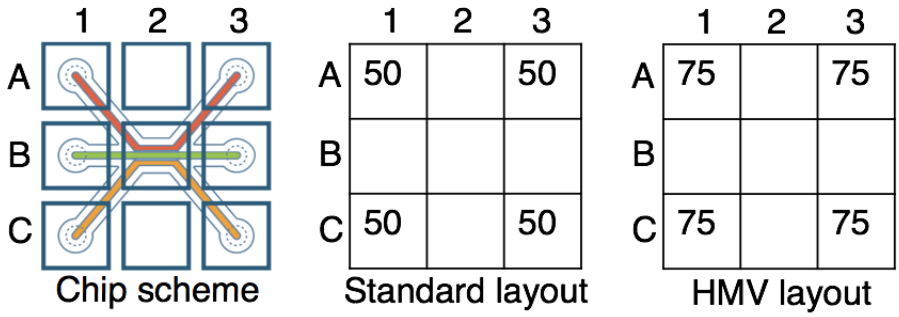


**Figure 3.6.** Schemes displaying the cell culture medium volume loaded in the wells of cell-seeded chips according to different layouts. In the schemes, each square represents a well composing an OP2 chip. A letter and a number is assigned to each well. Cells are seeded in the top perfusion channel, which has its inlet in A1 and outlet in A3. On the left hand-side, a generic scheme of an OP2 chip is reproduced. In the standard and HMV layouts, each square includes a number indicating the volume, expressed in µL, included in the related well of the chip. Images reproduced with consent by © Mimetas B.V.

**Table 3.6.** Summary of conditions tested throughout the fourth optimisation experiment conducted on OP2.

| Condition | Treatment | Layout | Chips used |
|---|---|---|---|
| **1** | DAPT in DMSO | Standard | 4 |
| **2** | DMSO | Standard | 4 |
| **3** | None | Standard | 4 |
| **4** | DAPT in DMSO | HMV | 4 |
| **5** | DMSO | HMV | 4 |
| **6** | None | HMV | 4 |

The cell culture medium in wells was then changed every 2-3 d maintaining the same layouts. The OP2 plate was then maintained on a rocker inside a cell culture incubator as described in section 3.2.11. Widefield images were acquired on day 1, 3 and 5 using a S100TV microscope. The experiment was progressed up to day 5, when cells were stained with Hoechst and phalloidin according to the protocol described in section 3.2.5. Then, 3 images were acquired for each chip in order to image the entire cell-seeded channel. Then using the software FIJI (2.1.0/1.53n, for source see reference: 345), nuclei count were acquired for each chip following

the protocol described in section 3.2.12, with the following modifications. Firstly, after the background subtraction step, the 3 images related to each chip were collated together into 1 image including the entire cell-seeded channel using the plugin “stitching”, developed by Preibisch *et al*., (318). Also, the nuclei were identified by setting an intensity threshold excluding pixels with a value inferior to 45.

### 3.2.14. OP2 experiment 5: mucociliary differentiation over 21 days

Collagen I hydrogel was loaded in 24 OP2 chips according to the protocol described in 3.2.3, and expanded HBECs (P2, donor: 18TL052522) were seeded at a cell density of 10 x $10^3$ cells/µL according to the protocol described in 3.2.4. When cells reached confluency, 4 different conditions were established, each including 6 chips. In the first condition, BEGM was exchanged with PALI, and in the second condition BEGM was exchanged with PALI including 10 µM of DAPT dissolved in DMSO. In the third condition, BEGM was exchange with Bronchial Air-Liquid Interface Medium (B-ALI; LONZA), which is a commercial cell culture medium developed to aid mucociliary differentiation of HBECs, and in the third condition BEGM was exchanged with B-ALI including 10 µM DAPT dissolved in DMSO. The OP2 plate was then maintained on a rocker inside a cell culture incubator as described in section 3.2.11. Cell culture was progressed up to day 21, when widefield images were acquired using a S100TV microscope.

### 3.2.15. Experiment on OGP 1: cell seeding test

Collagen I hydrogel was prepared according to 2.2.9 and loaded in 16 OGP chips as described in 3.2.3, and expanded HBECs (P2, donor: 18TL052522) were seeded at a concentration of 7 x $10^3$ cells/chip in 8 chips and at 14 x $10^3$ cells/chip

in other 8 chips following the protocol described in 3.2.6. The experiment was progressed up to day 1, when widefield images were acquired using a S100TV microscope.

### 3.2.16. Experiment on OGP 2: use of collagen I and Matrigel hydrogels

Hydrogels of different composition were loaded in 38 OGP chips as described in 3.2.3 modified as follows: the gel loading volume was increased to 2.8 µL. The hydrogels loaded were: 4 mg/ml collagen I in 14 chips, 2 mg/mL collagen I in 6 chips, a 1 : 1 volume : volume mixture of collagen I at a concentration of 4 mg/mL and Matrigel at a concentration of 4 mg/mL in 6 chips, a 1 : 1 volume : volume mixture of collagen I at a concentration of 2 mg/mL and Matrigel at a concentration of 2 mg/mL in 6 chips, and a 2 : 1 volume : volume mixture of collagen I at a concentration of 2 mg/mL and Matrigel at a concentration of 2 mg/mL in 6 chips. Then expanded HBECs (P2, donor: 18TL052522) were seeded at seeding density of 14 x $10^3$ cells/chip according to the protocol described in 3.2.6, modified as follows: before placing the plate on the rocker, one medium change was executed in the cell-seeded well of the chips, instead of the washing steps described in 3.2.6. Cell culture was progressed up to day 5 following the protocol described in 3.2.6. Widefield images of chips were acquired on day 2, 3 and 5 using a S100TV microscope.

### 3.2.17. Experiment on OGP 3: cell seeding optimisation

A 1 : 1 volume : volume mixture of collagen I hydrogel and Matrigel, both at a concentration of 4 mg/mL, was seeded in 12 chips of OGP according to the protocol described in 3.2.3 modified as follows: the gel loading volume was increased to 2.8 µL. Then, expanded HBECs (P2, donor: 18TL052522) were

seeded on the chips as described in 3.2.6. In particular, HBECs were seeded at a concentration of 14 x $10^3$ cells/chip in 6 chips and at a concentration of 21 x $10^3$ cells/chip in 6 chips. Cell seeding and culture were executed according to the protocol described in 3.2.6 modified as follows: before placing the plate on the rocker, one medium change was executed in the cell-seeded well of the chips, instead of the washing steps described in 3.2.6. Also, on day 1 BEGM in wells A1, A3, B1 and B3 was exchanged with PALI, and medium was removed from the cell-seeded wells B2. This configuration was maintained throughout the following cell culture medium changes, which were then performed every 2-3 d. Widefield images of the chips were acquired on day 0, 1 and 3 using a S100TV microscope.

### 3.2.18. Optimisation of hydrogel composition for HBEC culture

Expanded HBECs (P2) related to 2 donors (18TL052522 and 18TL290281) were thawed and cultured following the protocol described in 2.2.6. When cells reached a confluency of 90 %, wells of 96-well plates were loaded with hydrogels of different composition. In particular, each hydrogel was composed either collagen I, Matrigel, or of a 1 : 1 volume : volume mixture of collagen I and Matrigel at different concentrations. The different hydrogels and their constituents are listed in Table 3.7.

**Table 3.7.** Summary of hydrogels tested in the experiment related to the substrate optimisation for HBECs culture. The table includes the composition of the hydrogels used throughout the experiment.

| Hydrogel | Collagen I concentration | Matrigel concentration |
|---|---|---|
| Hydrogel 1 | 4 mg/mL | n/a |
| Hydrogel 2 | 2 mg/mL | n/a |
| Hydrogel 3 | 4 mg/mL | 8 mg/mL |
| Hydrogel 4 | 4 mg/mL | 4 mg/mL |
| Hydrogel 5 | 2 mg/mL | 8 mg/mL |
| Hydrogel 6 | 2 mg/mL | 4 mg/mL |
| Hydrogel 7 | n/a | 8 mg/mL |
| Hydrogel 8 | n/a | 4 mg/mL |

Each hydrogel was loaded on 5 wells per cell donor, at a volume of 50 µL. Cells from each donor were then seeded on the hydrogel-loaded wells and on 5 hydrogel-free wells following the same cell seeding protocol described in 3.2.4, with the following modification: after the resuspension step post-cell spinning in the centrifuge, cells were seeded in the wells of the 96-well plates at a seeding density of 20 x $10^3$ cells/well. The total cell culture medium volume per well after seeding was 200 µL, and medium changes were performed the day after seeding and every 2-3 d. Widefield images were acquired on day 1, 2 and 5 using a S100TV microscope.

### 3.2.19. Statistical analysis

Statistical tests were performed using the software GraphPad Prism version 9.0.0. To inform the choice of statistical tests to be performed, a Shapiro-Wilk normality test was executed on all quantitative data. An unpaired two-tailed t-test or a one-way ANOVA, as appropriate, were conducted to analyse the difference between the means of nuclei counts. For all tests, if p-value < 0.05, the results were considered statistically significant. Degrees of significance were indicated in

images as follows: * for $p < 0.05$, ** for $p < 0.01$, *** for $p < 0.001$, and **** for $p < 0.0001$. In the 3.3. Results section, the p value of the unpaired two-tailed t-test or one-way ANOVA is reported in the main text and figure legends.

# 3.3. Results

### 3.3.1. Gel optimisation on OP1 chips

Collagen I hydrogel, Matrigel, and mixtures of collagen I hydrogel and Matrigel at various volume ratios were loaded on OP1 chips, on 8 chips per condition. After the different types of hydrogel were loaded, HBECs obtained from 1 donor were seeded on OP1 chips at a seeding density of 20 x $10^3$ cells/µL. Cells localised in the top lane, as shown in the widefield images reported in Figure 3.7A, and progressively invaded the gel lane in all conditions, as observable in the widefield images shown in Figure 3.7B. Different hydrogels did not elicit any observable difference in cell behaviour across different timepoints. For this reason, and for its low cost relative to Matrigel, collagen I hydrogel was used in the following experiments involving OP1 chips.

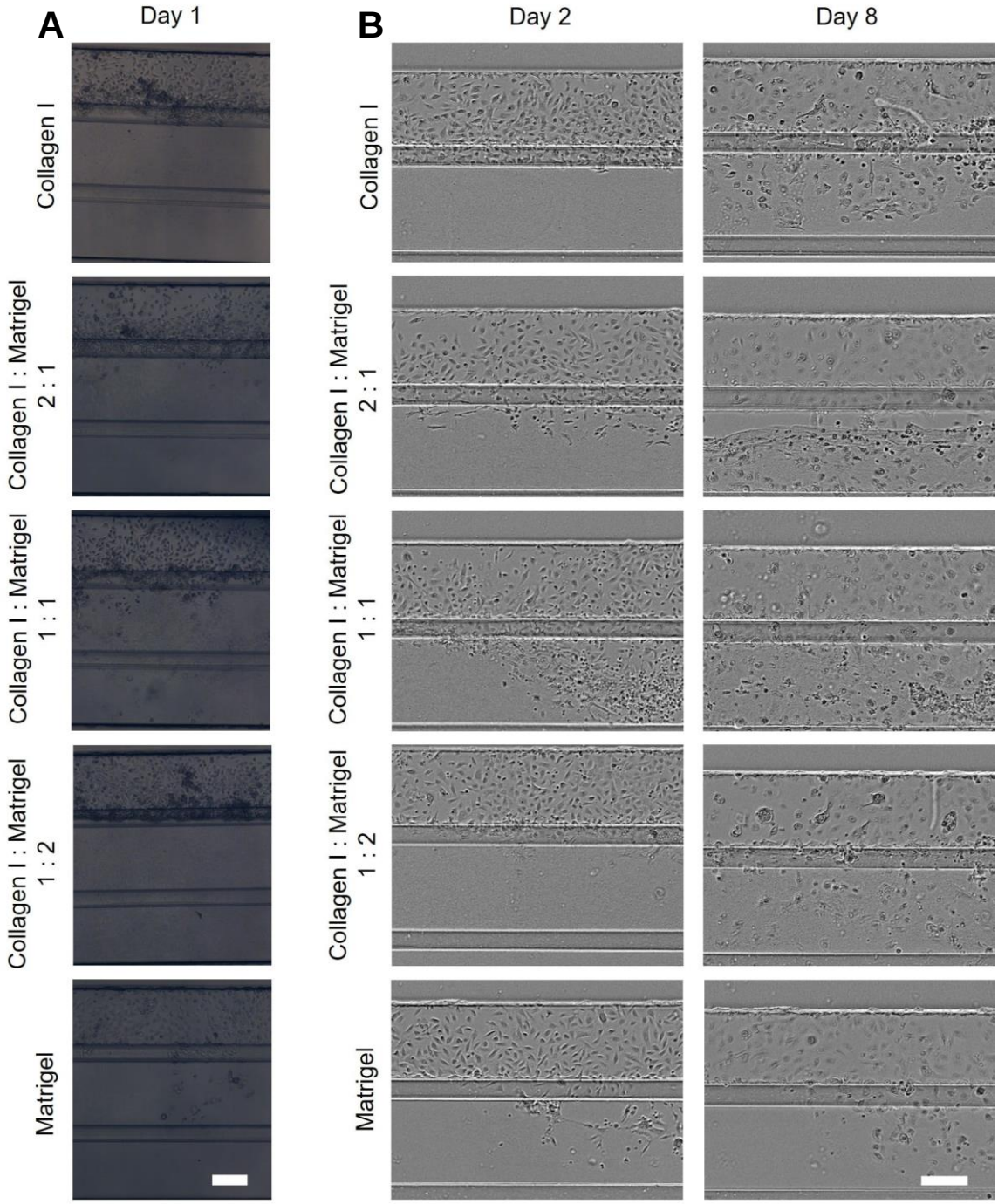


**Figure 3.7**. Representative widefield images of HBECs seeded on OP1 chips loaded with gels of different composition. Upon seeding with HBECs, widefield images of OP1 chips loaded with hydrogels of different composition were acquired on day 1, 2 and 8. Cells are seeded in the top lane of the chips, depicted at the top of each image. A phase guide separates the top lane from the gel lane. The gel lane is visible in the centre of the images reported in Figure A and at the bottom of images reported in Figure B. Upon cell seeding, cells localised in the top lane and progressively invaded the gel lane of chips, irrespectively of the type of hydrogel loaded. **A:** representative widefield images of OP1 chips seeded with HBECs, 1 day after seeding. Each row is associated with a different hydrogel loaded on the chips. First row: collagen I hydrogel. Second row: collagen I : Matrigel = 2 : 1 (v : v) mixture. Third row: collagen I : Matrigel = 1 : 1 (v : v) mixture. Fourth row: collagen I : Matrigel = 1: 2 (v : v) mixture. Fifth row: Matrigel. Magnification: 4X. Scale bar: 200 µm. **B:** representative widefield images of HBECs seeded on OP1 chips loaded with different hydrogels, obtained at different timepoints. The columns indicate the timepoint at which the images were taken. In particular, the first and second columns indicate respectively day 2 and 8. The first, second, third, fourth, and fifth rows represent respectively chips loaded with collagen I, a 2 : 1 v : v mixture of collagen I and Matrigel, a 1 : 1 v : v mixture of collagen I and Matrigel, a 1 : 2 v : v mixture of collagen I and Matrigel, and Matrigel. Magnification: 4X. Scale bar: 200 µm. N = 8 chips per condition, using cells obtained from n = 1 donor.

### 3.3.2. Cell seeding optimisation on OP1 chips

To optimise the cell number seeded on OP1 chips, HBECs obtained from 1 donor were seeded on the chips at seeding densities of 20 x $10^3$ cells/µL and 30 x $10^3$ cells/µL, on 6 chips per condition. As described in Section 3.2.4, the protocol related to the cell seeding on OP1 chips includes a time window spanning the time of cell seeding in the chip, during which cells are sustained by a limited amount of cell culture medium, and the time at which a larger amount of cell culture medium is added to the chip for long term culture. The time points adopted in this experiment were 2 h, 4 h, and 21 h. Cells at both seeding densities adhered after the 2 h time window, as evident from the widefield images acquired on day 1 and depicted in Figure 2A. For this reason, in subsequent experiments with OP1 chips, the cell seeding protocol included a 2 h time window between cell seeding and addition of extra cell culture medium. As seen in Figure 2B, at day 5 there was no visible difference between the two seeding densities in relation to the 2 h time window. Therefore, a seeding density of 20 x $10^3$ cells/µL was included in the cell seeding protocol of future experiments based on the use of OP1 chips, as it reduced the number of cells used per experiment.

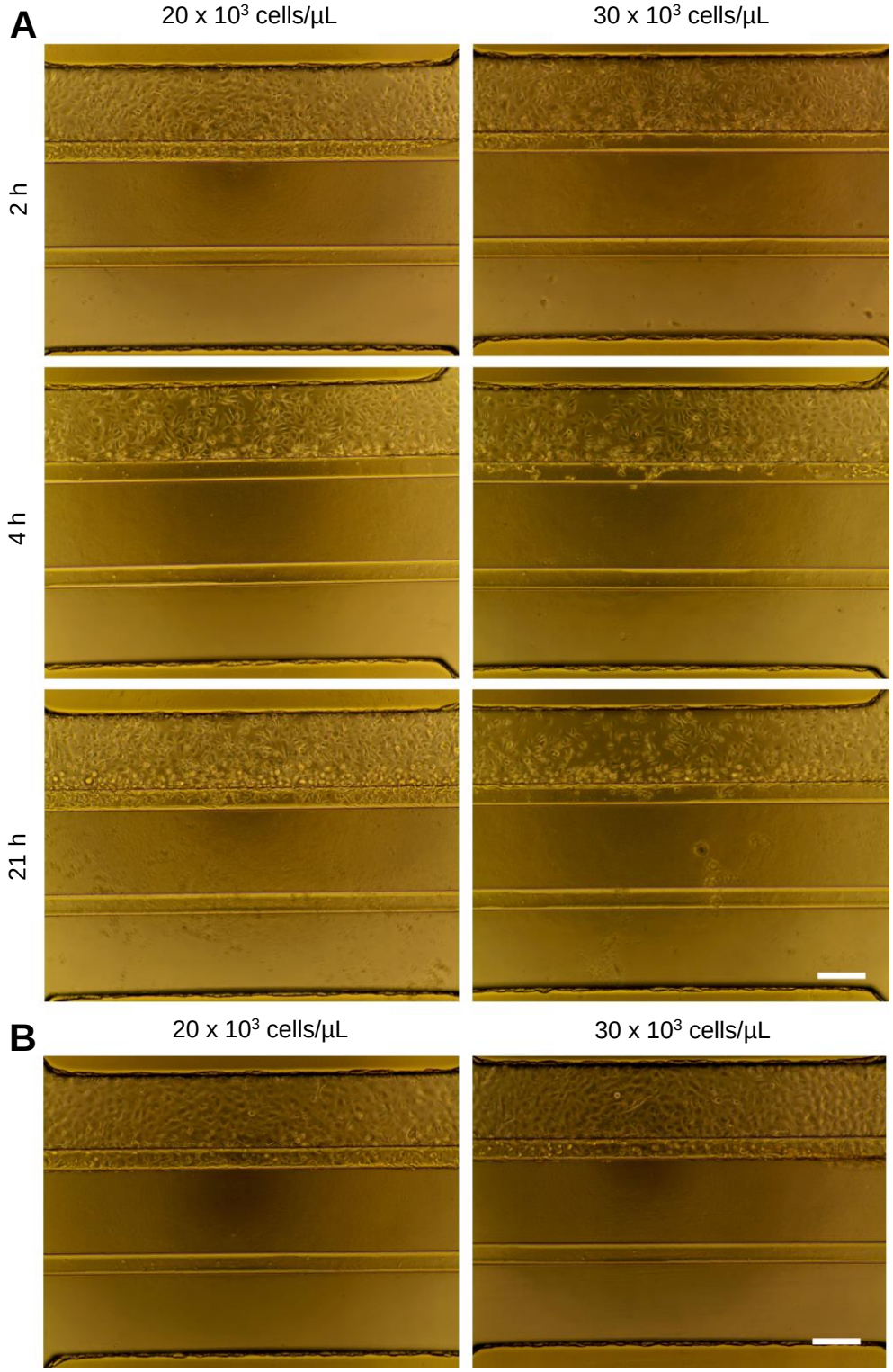


**Figure 3.8**. Representative widefield images of HBECs seeded on OP1 chips at different seeding densities and with different seeding protocols. Cell seeding of HBECs at a cell density of 20 x $10^3$ cells/µL and of 30 x $10^3$ cells/µL was performed on OP1 chips. Additionally, three different time windows (2 h, 4 h, 21 h) between the seeding of cells and the inclusion of additional medium to reach the working medium volume in the chips were tested. Widefield images were then acquired at day 1 and day 5. Cells adhered to the chips after a time window of 2 h. No observable difference related to cell coverage of the chips was found at day 5 between the two seeding densities tested in the experiment. **A:** representative widefield images acquired on day 1 after cell seeding. Cells were seeded at a seeding density of 20 x $10^3$ cells/µL (first column) or 30 x $10^3$ cells/µL (second column), at time windows of 2 h (first row), 4 h (second row), or 21 h (third row). Magnification: 10X. Scale bar: 200 µm. **B:** representative widefield images of HBECs seeded on OPs at different seeding densities. The time window associated with cell seeding was 2 h for both images, which were acquired at day 5. Left: 20 x $10^3$ cells/µL. Right: 30 x $10^3$ cells/µL. Magnification: 10X. Scale bars: 200 µm. N = 6 chips per condition, using cells obtained from n = 1 donor.

### 3.3.3. Cell seeding density optimisation and ALI culture attempt on OP1 chips

The cell seeding density on the OP1 chips was further optimised by seeding HBCEs obtained from 1 donor at 3 different concentrations, on 8 chips per condition: 5 x $10^3$ cells/µL, 10 x $10^3$ cells/µL, and 20 x $10^3$ cells/µL. Widefield images were obtained on day 1 and day 5 to monitor cell growth, as shown in Figure 3.9. No difference was observed between the different cell seeding densities with regards to cell morphology at different timepoints. On day 5, ALI culture was tested on OP1. However, ALI could not be induced, as cell culture medium could not be removed from the cell-seeded channel. For this reason, in the following experiments another version of the chip, OP2, with the same architecture but different dimensions (Table 3.2), was used.

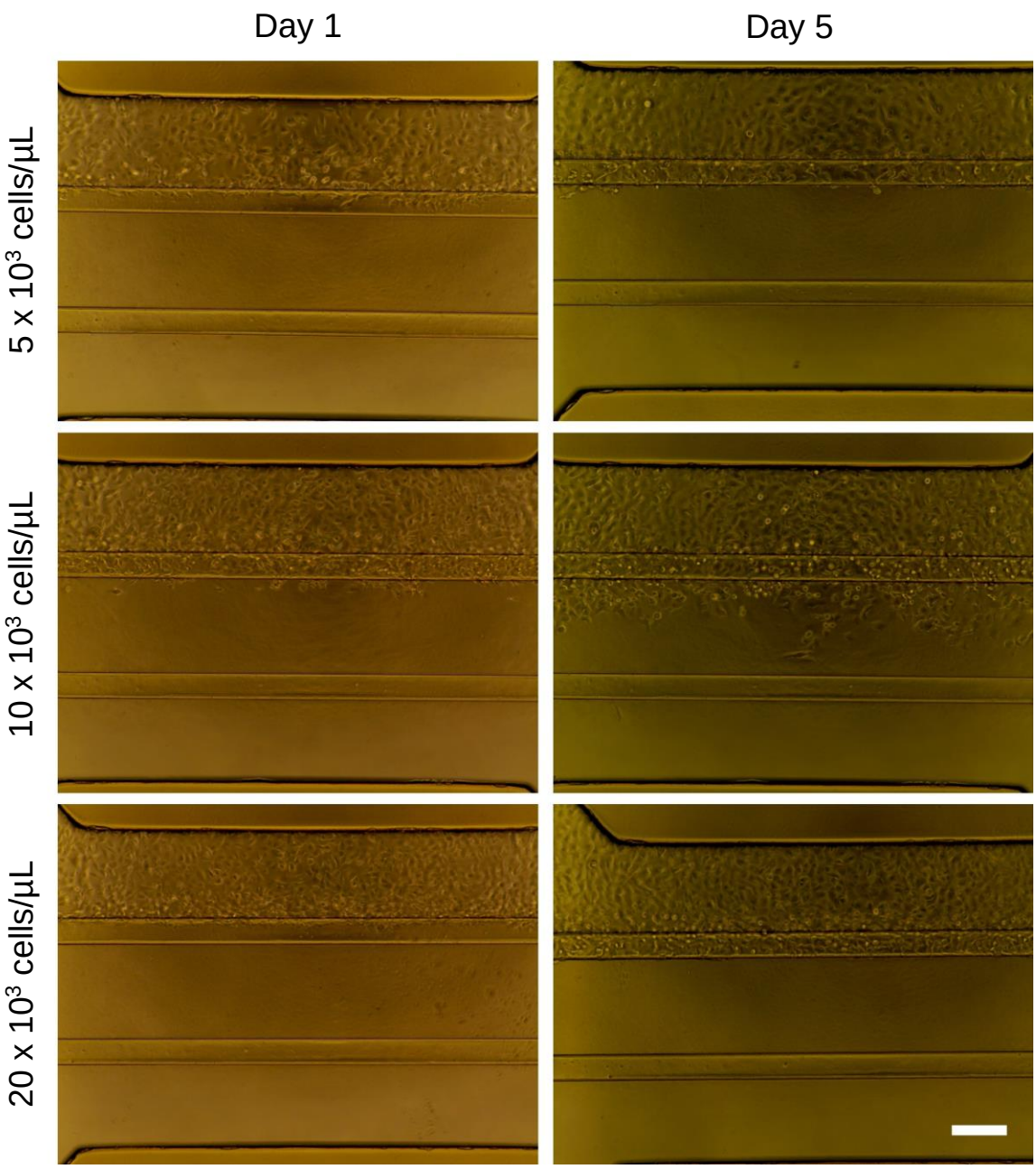


**Figure 3.9.** Representative widefield images of HBECs seeded on OP1 chips at different seeding densities and timepoints. Cell seeding of HBECs on OP1 chips was performed at a cell seeding density of 5 x $10^3$ cells/µL (first row), 10 x $10^3$ cells/µL (second row) and 20 x $10^3$ cells/µL (third row), and widefield images were acquired at day 1 (first column) and day 5 (second column). No difference was observed across conditions with regards to the cell coverage of the chips. Magnification: 10X. Scale bar: 200 µm. N = 8 chips per condition, using cells from n = 1 donor.

### 3.3.4. Cell seeding density optimisation and ALI attempt on OP2 chips

To optimise the cell seeding density on OP2 chips, HBECs obtained from 1 donor were seeded on the chips at 3 different concentrations: 5 x $10^3$ cells/µL, 10 x $10^3$ cells/µL, and 20 x $10^3$ cells/µL, on 8 chips per condition. As shown in Figure 3.10A, HBECs seeded at concentrations of 10 x $10^3$ cells/µL and 20 x $10^3$ cells/µL were

confluent on day 1. To reduce the number of cells used in each experiment, 10 x $10^3$ cells/µL was the seeding density adopted in further experiments using OP2 chips. On day 5 post-seeding, the initiation of ALI culture in the OP2 chips was attempted. However, it was not possible to remove the cell culture medium from the cell-seeded channel in any of the conditions tested. For this reason, and as previously observed in relation to OP1 chips, it was not possible to initiate an ALI culture on OP2 chips. Therefore, a “low medium volume” (LMV) condition was tested on 4 chips seeded with 10 x $10^3$ cells/µL. In the LMV condition, wells feeding the top medium channel in the OP2 chip are empty. As a result, the oxygen diffusion route from the external environment to the cells is shortened, and for this reason it was hypothesised that the LMV condition would improve cell oxygenation, which could in turn initiate mucociliary differentiation, as hypothesised by Gerovac *et al*., (294), and Kouthouridis *et al*., (321). Cells cultured with standard cell culture medium volumes in all the wells of 4 chips seeded with 10 x $10^3$ cells/µL were used as control. At day 15, cells appeared mostly adherent but not confluent in both control and LMV conditions, as shown in Figure 3.10B.

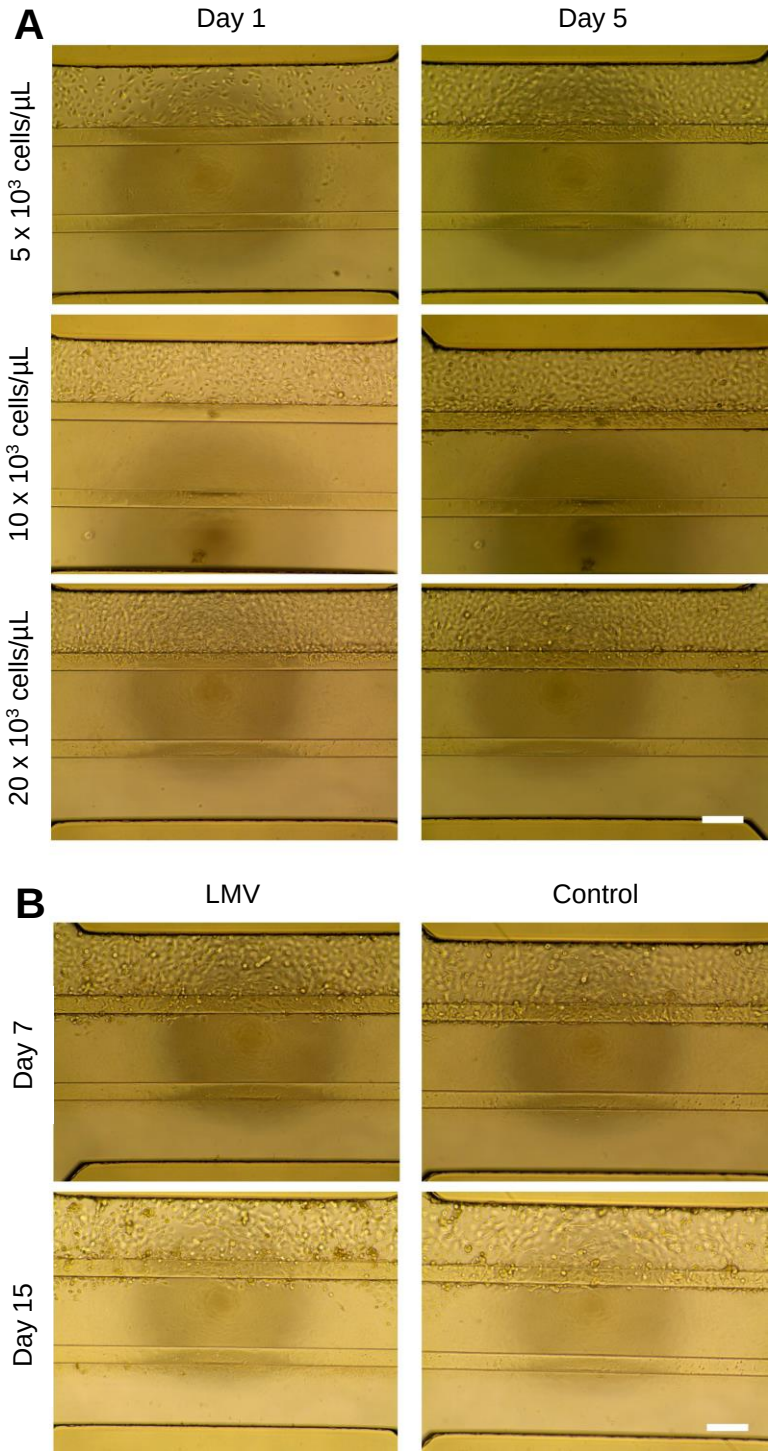


**Figure 3.10**. Representative widefield images of HBECs seeded on OP2 chips at different seeding densities, timepoints, and conditions. Upon seeding of HBECs on OP2 chips at 3 different cell densities (5 x $10^3$ cells/µL, 10 x $10^3$ cells/µL and 20 x $10^3$ cells/µL), widefield images were acquired at day 1 and day 5. Cells seeded at a cell density of 10 x $10^3$ cells/µL and 20 x $10^3$ cells/µL were confluent at day 1. As an ALI could not be induced in the chips, in order to induce mucociliary differentiation of HBECs a condition of LMV was tested. The LMV condition was based on the removal of cell culture medium from the wells adjacent to the cell seeded channel in order to facilitate the diffusion of oxygen to the cells and initiate the differentiation process. Cell-seeded chips including standard working volumes of cell culture medium in all wells were used as a control. Widefield images were then acquired at day 7 and day 15. On day 15, cells in both control and LMV conditions were not confluent. **A:** representative widefield images of HBECs seeded on OP2 chips at a seeding density of 5 x $10^3$ cells/µL (first row), 10 x $10^3$ cells/µL (second row), and 20 x $10^3$ cells/µL (third row), on day 1 (first column) or day 5 (second column) post-seeding. **B:** representative widefield images of HBECs seeded on OP2 chips at a seeding density of 10 x $10^3$ cells/µL at LMV (first column) or control (second column) regimens, at day 7 (first row) or day 15 (second row) after cell seeding. Magnification: 10X. Scale bar: 200 µm. N = 8 chips per condition included in the cell seeding optimisation (Figure A). N = 4 chips per condition included in the test of LMV regimen (Figure B). Cells were obtained from n = 1 donor.

### 3.3.5. Static and dynamic mucociliary differentiation on OP2 chips

To initiate mucociliary differentiation, BEGM medium was substituted with PALI, a commercial cell culture medium developed to stimulate the mucociliary differentiation of HBECs. Different cell culture conditions were also compared. The LMV2 condition was obtained by removing cell culture medium from the wells feeding the channel opposite the cell-seeded channel. The LMV2 condition was compared to the LMV condition and to the control condition, in which all wells contained standard volumes of cell culture medium. These conditions were applied in the presence of (dynamic regimen) or in the absence of (static regimen) a fluid flow generated by placing the OP2 chip on a rocker platform. Each condition was induced on a minimum of n = 8 chips, including HBECs obtained from 1 donor. As illustrated in Figure 3.11, on day 11 after the initiation of the mucociliary differentiation protocol, regions that were void of cells were observed in all conditions, except for the control condition under a fluid flow regimen. These data demonstrate that LMV and LMV2 conditions do not induce the formation of a confluent HBECs layer in OP2 chips, and that fluid flow in the OP2 chips is essential for HBECs to maintain a confluent state when differentiation medium is used to stimulate mucociliary differentiation. For this reason, fluid flow was included in all further experiments relying on the use of OP2 chips.

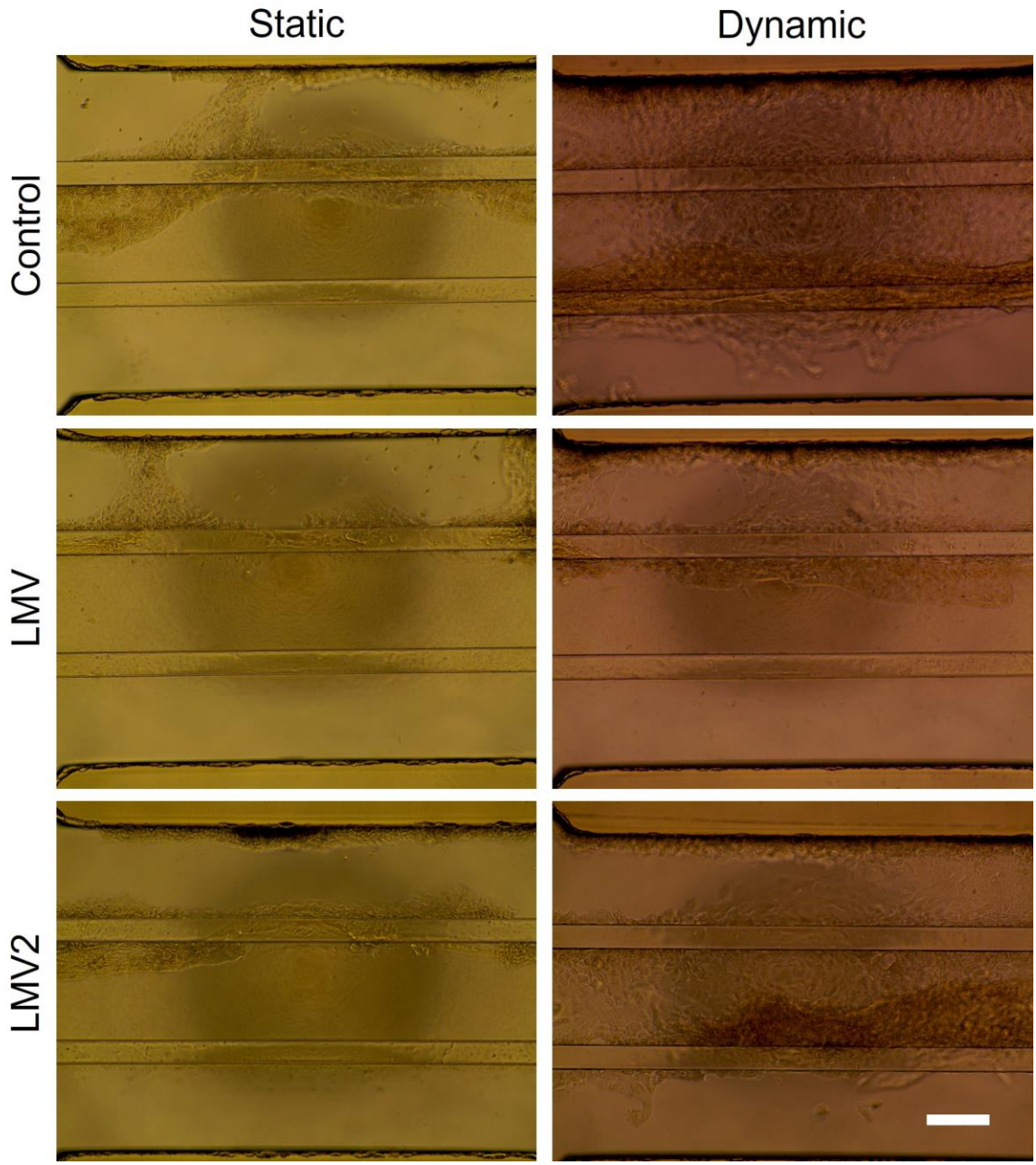


**Figure 3.11**. Representative widefield images of HBECs cultured on OP2, under different regimens of mucociliary differentiation. Cell seeding of HBECs was performed on OP2 chips, and upon reaching cell confluency the BEGM medium in HBECs-seeded chips was substituted with PALI, a commercial cell culture medium developed to induce the mucociliary differentiation of HBECs. Widefield images were acquired on day 11. Different cell culture conditions were compared, as OP2 chips were maintained either in static (left column) or dynamic (right column) conditions, the latter condition induced by placing the chips on a rocker. Additionally, cells were cultured with standard working media volumes (control, first row), at LMV (second row), or at LMV2 (third row) conditions, the latter induced by removing the medium from the wells connected to the channel opposite to the cell-seeded channel. Empty areas in the cell layer within the chips were visible in all conditions, with the exclusion of the control condition under dynamic regimen. The dynamic regimen is therefore necessary to maintain a state of cell confluency in HBECs seeded on OP2 chips and cultured with PALI differentiation medium. Magnification: 10X. Scale bars: 200 µm. A minimum of n = 8 chips per condition were used, using cells obtained from n = 1 donor.

### 3.3.6. Use of DAPT in OP2 chips

As an alternative to ALI culture and to the shortening of the oxygen diffusion distance, NOTCH pathway inhibition via the use of DAPT has been shown to

induce ciliation in HBECs in submerged cultures (294). For this reason, upon obtaining confluency in HBECs-seeded OP2 chips, the BEGM cell culture medium was switched to PALI medium including 10 µM DAPT, or to PALI medium without DAPT. Each condition was induced on n = 4 chips, including HBECs obtained from 1 donor. As the widefield images in Figure 3.12A and the Hoechst nuclear staining in Figure 3.12B show, chips including cells treated with DAPT displayed areas void of cells on day 5 after treatment with DAPT was initiated. However, as illustrated by the graph in Figure 3.12C, there was no statistically significant difference ($p = 0.1644$, unpaired two-tailed t-test) between the nuclei count obtained from Hoechst staining of both conditions. The nuclei count was performed on 1 representative image per chip.

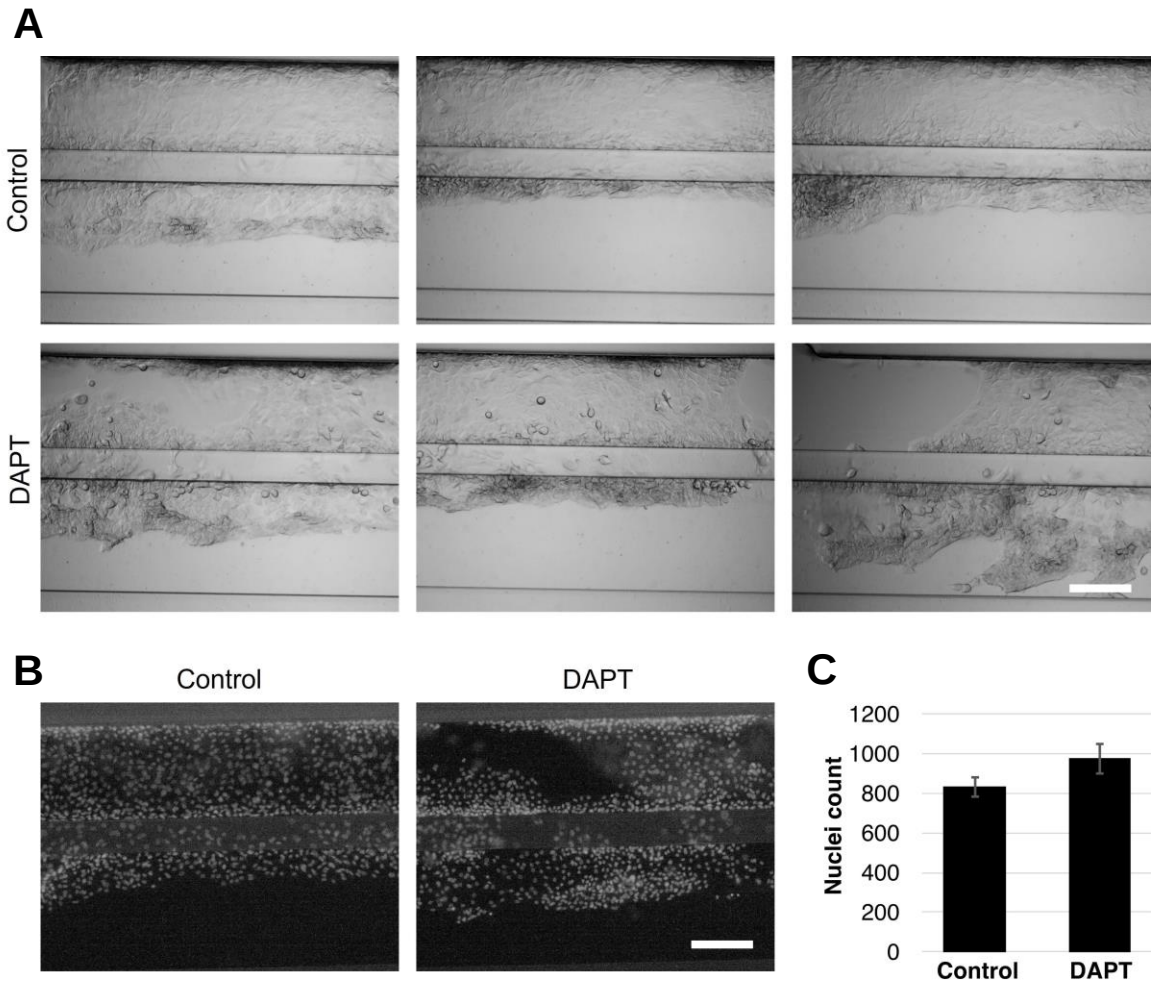


**Figure 3.12.** Culture of HBECs on OP2 chips with or without the addition of DAPT. Images were acquired 5 d after the initiation of mucociliary differentiation. The addition of DAPT was tested on HBECs cultured on OP2 chips, and untreated HBECs on chips were used as a control. Widefield images were acquired on day 5 after the addition of DAPT. Areas void of cells were observed in chips including cells treated with DAPT. On day 5, HBECs were stained with Hoechst, and nuclei were counted. No statistically significant differences were observed between the control and DAPT conditions. **A:** representative widefield images of HBECs seeded on OP2 chips, untreated (first row) or treated with DAPT (second row). Magnification: 5X. Scale bar: 200 µm. **B:** representative images of Hoechst staining of untreated (left) or DAPT-treated (right) HBECs seeded on OP2 chips. Magnification: 5X. Scale bar: 200 µm. **C:** nuclei count, expressed in absolute numbers as mean ± SEM for both the control (left) and DAPT-treated (right) conditions on day 5 after the initiation of mucociliary differentiation. The differences observed between the values reported in the graph are not statistically significant as assessed by an unpaired two-tailed t-test ($p = 0.1644$). N = 4 chips per condition (Figure A, B), 1 representative image from each chip was acquired for nuclei quantification (Figure C). Cells were obtained from n = 1 donor.

### 3.3.7. Use of DAPT on OP2 chips in combination with altered cell culture medium volume

As DAPT seemed to compromise the continuity of the HBECs layer in OP2 chips, it was hypothesised that this effect was due to nutrient depletion in the cell culture medium possibly due to an increase in nutrient demand by the treated cells resulting from the initiation of mucociliary differentiation. To test this hypothesis

and avoid the formation of cell-free areas in the cell lane of chips, HBECs were seeded in OP2 chips, and DAPT-free, DAPT-treated, and DMSO-treated conditions were compared, the first condition acting as a control and the third condition acting as a vehicle control for the DAPT-treated condition. Each condition was induced on n = 4 chips, including HBECs obtained from 1 donor. The cells in the chips were cultured following the standard protocol or in an HMV condition, initiated by filling the 4 reservoirs feeding the channels of the chips with 75 µL cell culture medium as opposed to the standard volume of 50 µL cell culture medium. Widefield images acquired at day 5 after the initiation of differentiation protocol are shown in Figure 3.13, in which discontinuities in the confluent cell layer of DAPT-treated cells are evident in both the standard and the HMV regimens. On day 5 after the initiation of the differentiation protocol, cell nuclei were also stained with Hoechst, as shown in Figures 3.13A-F. Nuclei count based on the acquired images is shown in Figure 3.14. Images of a minimum of the n = 3 chips per condition were collated to cover the entire area of the cell seeded channel that was adjacent to the hydrogel-loaded channel. Nuclei counts did not show any statistically significant differences between the conditions ($p = 0.5005$, one-way ANOVA).

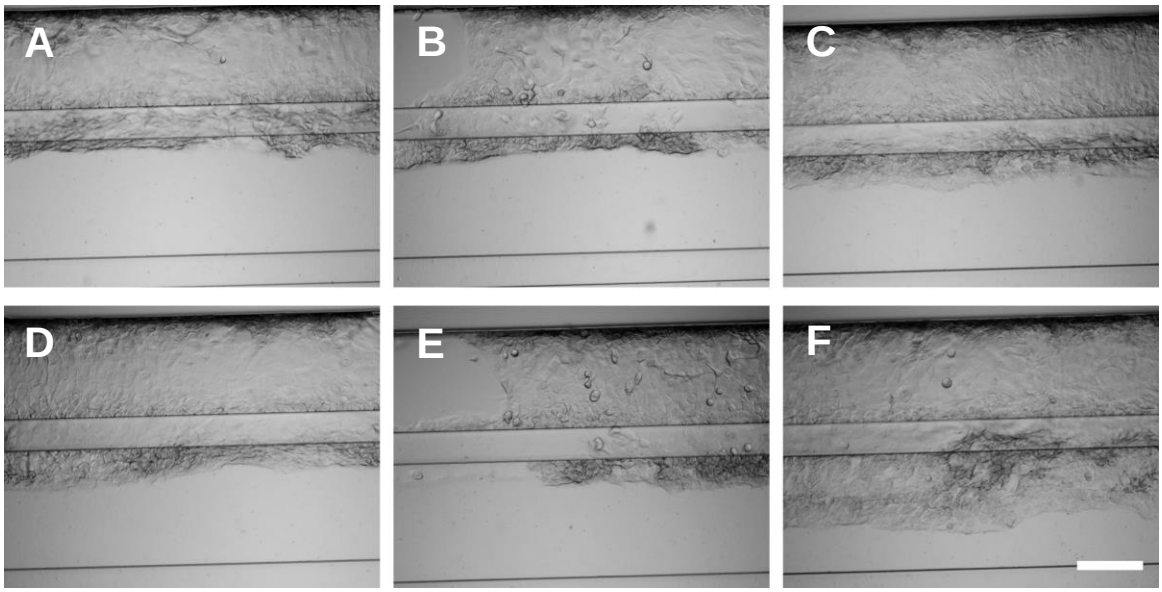


**Figure 3.13.** Representative widefield images of HBECs seeded on OP2.Treatment with DAPT was tested on HBECs on OP2 chips, and as additional conditions HBECs on chips were left untreated or were treated with DMSO to constitute a vehicle control condition. Additionally, the conditions were applied on chips including standard cell medium working volumes or at a condition of increased cell culture medium volume termed “HMV”. Widefield images were acquired 5 d after the initiation of mucociliary differentiation. Cell-free areas were observed within seeded chips related to DAPT-treated chips including both standard medium volume and at HMV. Increasing the volume of cell culture medium in the OP2 therefore did not eliminate the cell-free areas observable in HBECs-seeded chips treated with DAPT. **A:** DAPT-free. **B:** DAPT-treated. **C:** DMSO-treated. **D:** HMV condition. **E:** DAPT-treated, HMV condition. **F:** DMSO-treated, HMV condition. Magnification: 5X. Scale bar: 200 µm. N = 4 chips per condition, using cells obtained from n = 1 donor.

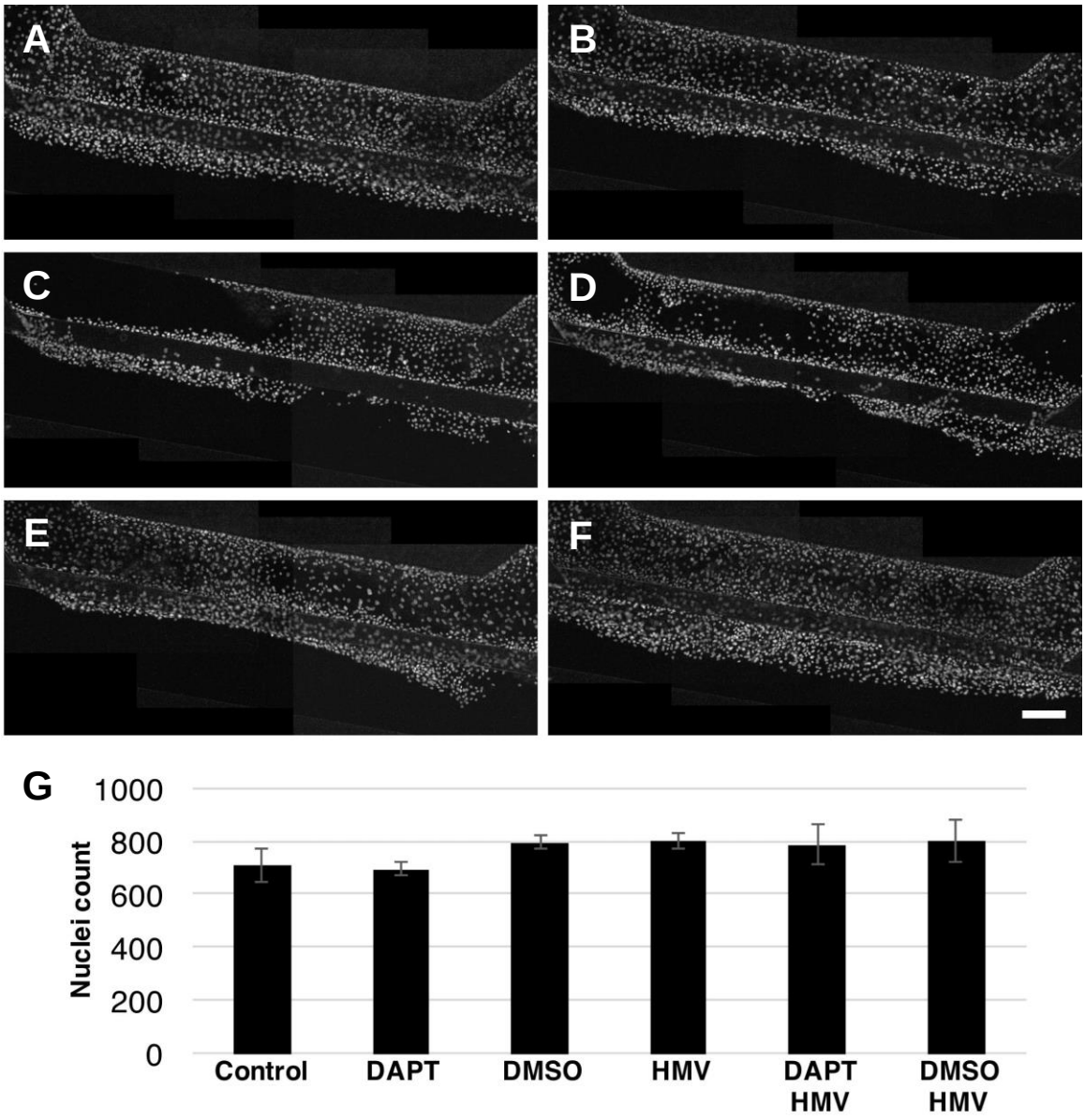


**Figure 3.14.** Hoechst staining of HBECs seeded on OP2 chips, and cell nuclei count obtained from images of Hoechst staining. To quantitatively assess the occurrence of cell-void areas in DAPT-treated HBECs seeded on OP2, as compared to the untreated control and to the DMSO-treated vehicle control conditions, at both standard medium volume or HMV regimens, HBECs seeded on OP2 chips and associated with each condition were stained with Hoechst on day 5 after the initiation of the mucociliary differentiation. Cell nuclei count were then obtained from images of Hoechst staining. Hoechst stains cell nuclei, depicted in white in the images. No statistically significant differences were observed between the nuclei counts obtained from each condition. **A-E:** images of Hoechst-stained cells in cell-seeded channels of chips associated with control **(A)**, DAPT-treated **(B)**, DMSO-treated **(C)**, HMV control condition **(D)**, DAPT-treated HMV **(E)**, DMSO-treated HMV **(F)** conditions. The depicted images were obtained by collating images covering the entire area of the cell-seeded channels adjacent to the hydrogel-loaded channel. **G:** nuclei count obtained from collated images of Hoechst-stained cells related to different conditions, listed in the X axis. Nuclei count, reported on the Y axis, are expressed in absolute numbers as mean ± SEM. The differences observed between the values reported in the graph are not statistically significant upon testing with one-way ANOVA ($p = 0.5005$). Magnification: 5X. Scale bar: 200 µm. A minimum of $n = 3$ chips were used per condition, using cells obtained from $n = 1$ donor.

### 3.3.8. Mucociliary differentiation on OP2 chips over 21 days

It was hypothesised that the mucociliary differentiation of HBECs in previous experiments might have been influenced by the composition of cell culture medium

used throughout the differentiation protocol. Therefore, in a further experiment centred on the use of HBECs seeded in OP2 chips, the use of the PALI differentiation medium was compared with the use of B-ALI, which is another commercial cell culture medium used to stimulate the mucociliary differentiation of HBECs. The addition of DAPT to induce differentiation was also tested in both PALI and B-ALI. Each condition was induced on n = 6 chips per condition, including HBECs obtained from 1 donor. Widefield images were acquired at day 21 after the initiation of the differentiation procedure. Representative widefield images can be observed in Figure 3.15, in which extensive areas void of cells can be observed in all conditions.

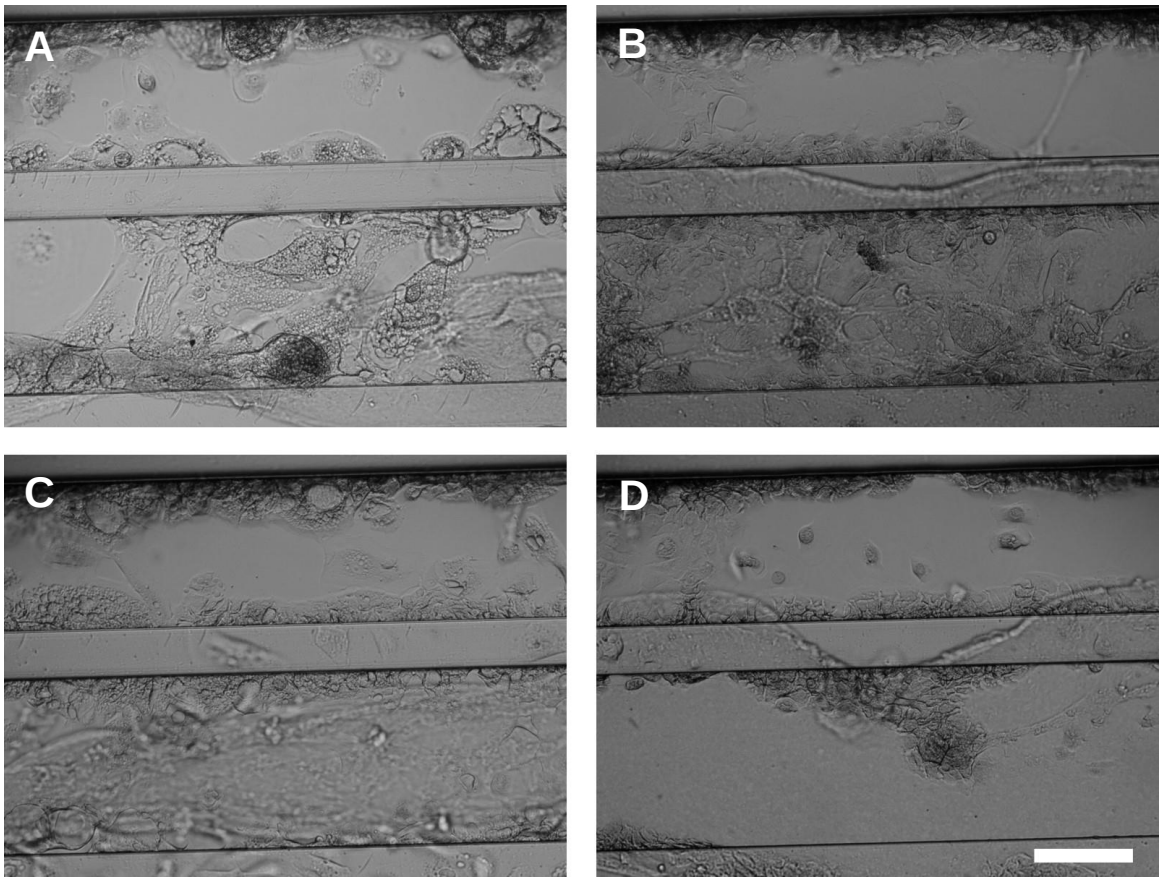


**Figure 3.15.** Representative widefield images of HBECs seeded on OP2 chips at day 21 after the initiation of the differentiation protocol. The use of PALI as cell culture medium included in HBECs-seeded OP2 chips was compared with the use of B-ALI medium, and the use of both cell culture media was tested with or without the inclusion of DAPT. Widefield images of HBECs seeded on OP2 chips at day 21 after the initiation of the differentiation protocol were acquired. The cell-seeded channel is located in the top part of the images, whilst the gel-loaded channel is in the lower part of images. Large cell-free areas were observed in all conditions. **A:** cells cultured in PALI medium. **B:** cells cultured in B-ALI medium. **C:** cells cultured in PALI medium with the addition of DAPT. **D:** cells cultured in B-ALI medium with the addition of DAPT. Magnification: 5X. Scale bar: 200 µm. N = 6 chips per condition, using cells obtained from n = 1 donor.

### 3.3.9. Cell seeding on OGP

Another type of microfluidic chip, the OGP, was tested by loading collagen I hydrogel at a concentration of 4 mg/mL in the gel lane of n = 8 chips and by seeding HBECs obtained from 1 donor on top of the observation window of the chips. However, upon cell seeding it was observed that collagen I had not filled the entire gel channel during the hydrogel loading phase of the chip, as cells formed a semi-conical concavity in the circular opening of the observation window, entering in contact with the underlying glass base of the gel lane, as shown in Figure 3.16.

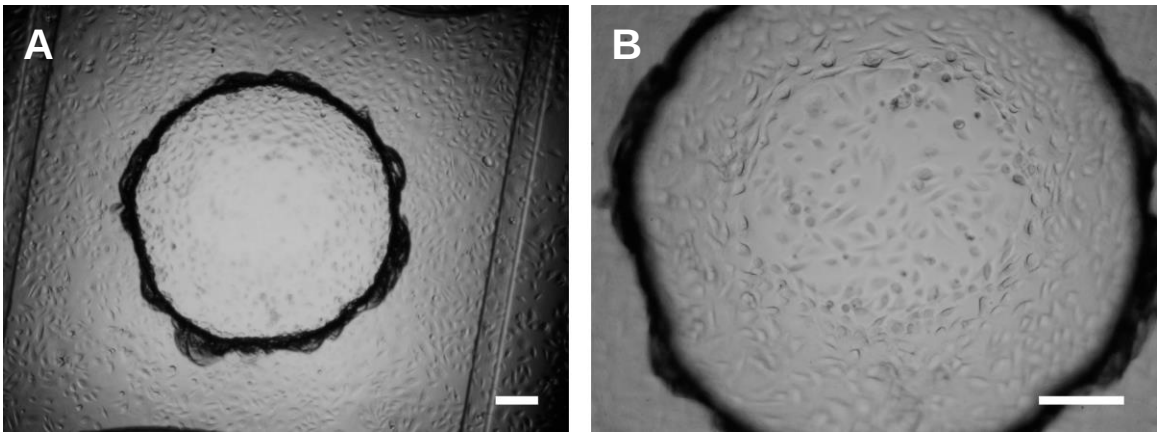


**Figure 3.16**. Representative image of HBECs seeded on OGP at different magnifications, 1 d after cell seeding. Upon loading the gel channel of OGP chips with collagen I hydrogel, HBECs were seeded on the glass observation window of the chips. Widefield images of HBECs seeded on OGP at 2.5X and 5X magnifications were acquired on day 1 after cell seeding. In the centre of the images a circular overture in the observation window is visible. Within the overture, cells were in contact with the underlying gel. Cells formed a semi-conical concavity within the circular overture in the observation window and came in contact with the glass base of the gel channel. **A:** 2.5X magnification. In addition to the circular overture in the centre of the image, the two side channels of the chips are visible on the left and right sides. **B:** 5X magnification. Scale bars: 200 µm. N = 8 chips per condition, using cells obtained from n = 1 donor.

### 3.3.10. Use of collagen I hydrogel and Matrigel in OGP

In the previous experiment, collagen I hydrogel at a concentration of 4 mg/mL failed to fill the gel chamber of the OGP, forming a semi-conical concavity in contact with the bottom of the plate. For this reason, hydrogels of different composition and concentration were loaded on the OGP chips. The hydrogels tested in this experiment were composed of collagen I and Matrigel. In particular, the hydrogels tested were: collagen I at a concentration of 4 mg/mL on n = 14 chips, collagen I

at a concentration of 2 mg/mL on n = 6 chips, a 1 : 1 v : v mixture of collagen I at a concentration of 4 mg/mL and Matrigel at a concentration of 4 mg/mL on n = 6 chips, and a 1 : 1 v : v mixture of collagen I at a concentration of 2 mg/mL and Matrigel at a concentration of 2 mg/mL on n = 6 chips. A failure rate related to gel loading was calculated as the percentage of chips loaded with hydrogel displaying signs of: gel overfill from the gel lane, gel drying, or cells forming a semi-conical concavity in the overture of the observation window on day 2 after cell seeding as shown in Fig. 3.16. The loading of the Collagen I hydrogel and Matrigel hybrid had a lower failure rate than Collagen I hydrogel alone, as shown in Table 3.8. Widefield images of HBECs obtained from n = 1 donor growing on the OGP chips over 5 d are included in Figure 3.17, from which it appears that cells contract the 1 : 1 v : v mixture of collagen I and Matrigel if both hydrogels have a concentration of 2 mg/mL, but not if the hydrogels have a concentration of 4 mg/mL.

**Table 3.8**. Number of OGP chips loaded with hydrogel, number of OGP chips with correct hydrogel shape as observed 2 d after cell seeding, and failure rate related to different hydrogel mixtures. Hydrogels of different composition, listed in the first column of the table, were loaded on OGP chips. The number of OGP chips loaded with hydrogel, number of OGP chips with correct hydrogel shape as observed 2 d after cell seeding, and failure rate related to different hydrogel mixtures are indicated in the second, third and fourth column, respectively. Data were obtained from widefield images. The hydrogel loading is considered successful only if the hydrogel occupies the gel lane without signs of drying or gel channel overfill and if cells do not form a semi-conical dome in the observation window 2 d after cell seeding. The failure rate is the percentage of chips loaded that displays an unsuccessful gel loading. The lowest failure rate were associated to chips loaded with a 1 : 1 v : v ratio of Collagen I at a concentration of 4 mg/mL and Matrigel at a concentration of 4 mg/mL and to chips loaded with a 1 : 1 v : v ratio of Collagen I at a concentration of 2 mg/mL and Matrigel at a concentration of 2 mg/mL.

| | Chips loaded | Gel loading successful 2 d after cell seeding | Failure rate 2 d after cell seeding |
|---|---|---|---|
| **Collagen I 4 mg/mL** | **14** | **2** | **86 %** |
| **Collagen I 2 mg/mL** | **6** | **1** | **83 %** |
| **Collagen I 4 mg/mL : Matrigel 4 mg/mL 1 : 1** | **6** | **6** | **0 %** |
| **Collagen I 2 mg/mL : Matrigel 2 mg/mL 1 : 1** | **6** | **3** | **50 %** |

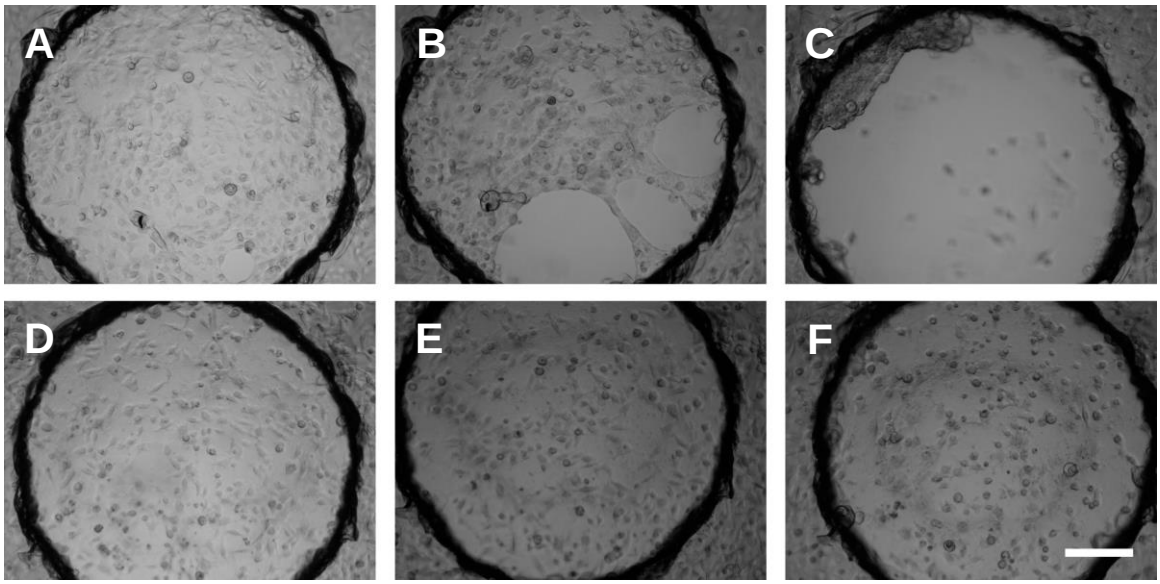


**Figure 3.17**. Representative images of HBECs seeded on OGP. Upon loading of OGP chips with hydrogels composed of a 1 : 1 v : v ratio of collagen I hydrogel and Matrigel, both at a concentration of 2 mg/mL or 4 mg/mL, HBECs were seeded on the chips. Cells were seeded on the glass observation window overlying the gel channel. In the centre of the images a circular overture in the observation window is visible. Within the overture, cells were in contact with the underlying gel. Widefield images were acquired at day 2, 3 and 5. By day 5, HBECs contracted hydrogels including Matrigel and Collagen I at a concentration of 2 mg/mL, but not the hydrogels including Matrigel and Collagen I at a concentration of 4 mg/mL. **A, B, C:** images taken at day 2, day 3, and day 5, respectively, of HBECs-seeded OGP chips loaded with a mixture of collagen I hydrogel and Matrigel, both at a concentration of 2 mg/mL, at a 1 : 1 v : v ratio. **D, E, F:** images taken at day 2, day 3, and day 5, respectively, of HBECs-seeded OGP chips loaded with a mixture of collagen I hydrogel and Matrigel, both at a concentration of 4 mg/mL, at a 1 : 1 v : v ratio. Magnification: 5X. Scale bar: 200 µm. A minimum of n = 3 chips per condition were used, using cells obtained from n = 1 donor.

### 3.3.11. Optimisation of hydrogel composition for HBEC culture.

To optimise the composition of the hydrogel to be loaded on the OGP, hydrogels composed of collagen I at a concentration of 4 mg/mL and 2 mg/mL, Matrigel at a concentration of 8 mg/mL and 4 mg/mL, and of 1 : 1 volume : volume mixtures of collagen I and Matrigel at a range of concentrations were loaded on 96-well plates. In particular, the mixtures were composed of: collagen I (4 mg/mL), Matrigel (4 mg/mL); collagen I (2 mg/mL), Matrigel (4 mg/mL); collagen I (4 mg/mL), Matrigel (8 mg/mL); collagen I (2 mg/mL), Matrigel (8 mg/mL). Each hydrogel mixture was included in n = 5 wells of a 96-well plate. To assess cell adherence and hydrogel contraction, HBECs obtained from 2 donors were seeded on the wells including the hydrogel mixtures, and on n = 5 hydrogel-free wells. Widefield images, included in Figure 3.18, were acquired at day 5. From Figure 3.18 it can be inferred that the only Matrigel and collagen I hydrogel mixture that was not contracted by HBECs

was the 1 : 1 v : v mixture of collagen I at a concentration of 4 mg/mL and Matrigel at a concentration of 4 mg/mL.

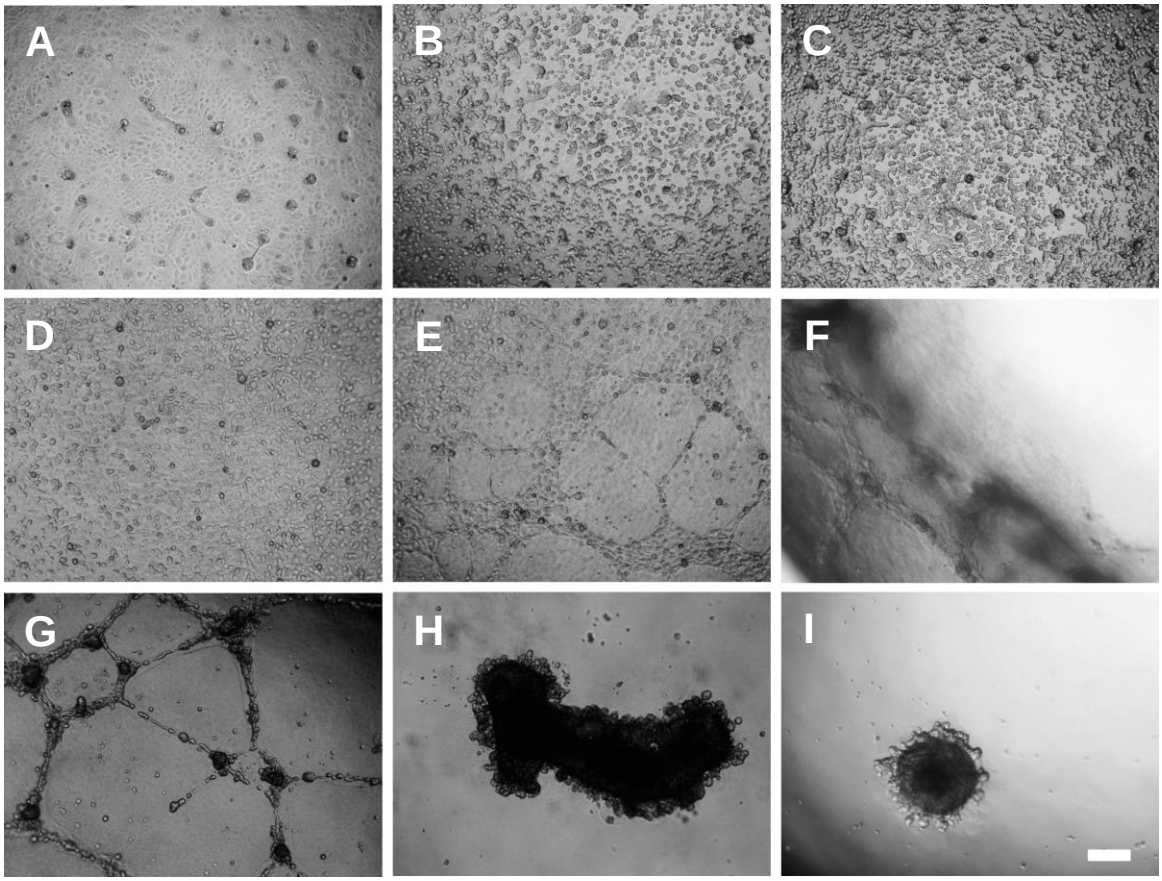


**Figure 3.18**. Representative widefield images of HBECs seeded on hydrogel-free cell culture-treated wells and on hydrogels with different composition, 5 d after cell seeding. Cell seeding of HBECs was performed on hydrogel-free cell culture-treated wells of 96-well plates and on wells including 1 : 1 v : v mixtures of Collagen I hydrogel and Matrigel with different concentrations. Widefield images of seeded HBECs were acquired on day 5 after cell seeding. Seeded HBECs formed a continuous monolayer and did not contract the hydrogel upon cell seeding on a 1 : 1 v : v mixture of Collagen I and Matrigel, both at a concentration of 4 mg/mL. **A:** gel-free cell culture-treated plastic surface. **B:** collagen I (4 mg/mL). **C:** collagen I (2 mg/mL). **D:** collagen I (4 mg/mL), Matrigel (4 mg/mL). **E:** collagen I (4 mg/mL), Matrigel (8 mg/mL). **F:** collagen I (2 mg/mL), Matrigel (4 mg/mL). **G:** collagen I (2 mg/mL), Matrigel (8 mg/mL). **H:** Matrigel (4 mg/mL). **I:** Matrigel (8 mg/mL Magnification: 2.5X. Scale bar: 300 µm). N = 5 wells per condition and donor, using cells obtained from n = 2 donors.

### 3.3.12. Cell seeding optimisation on OGP.

In the previous experiment, it was assessed that a 1 : 1 v : v mixture of collagen I hydrogel and Matrigel, both at a concentration of 4 mg/mL and placed in wells of 96-well plates, were not contracted by HBECs. In this experiment the same hydrogel mixture was loaded on OGPs, and HBECs obtained from 1 donor were seeded on the chips. In particular, to optimise the cell seeding on the OGP, cells were seeded at 2 different seeding densities: 14 x $10^3$ cells/chip on n = 6 chips, and 21 x $10^3$ cells/chip on n = 6 chips. On day 1, expansion medium was replaced

with the differentiation medium PALI. On day 3, the hydrogel was contracted by HBECs, as shown in the widefield images included in Figure 3.19.

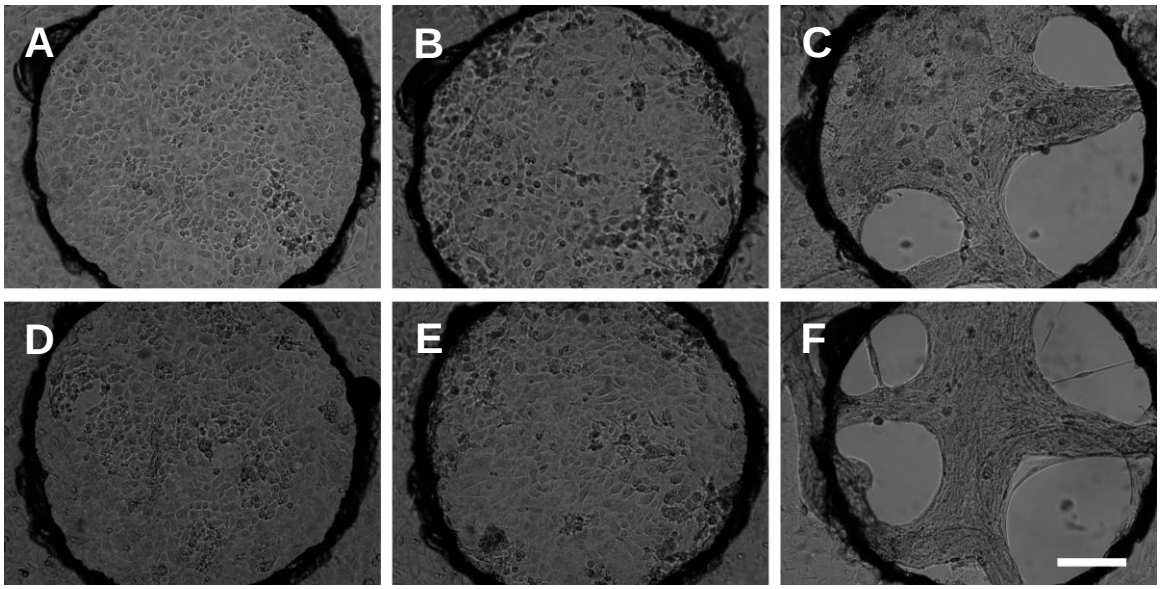


**Figure 3.19**. Representative widefield images of HBECs seeded on OGP chips. Cell seeding of HBECs was performed on OGP chips including a 1 : 1 v : v mixture of collagen I hydrogel and Matrigel, both at a concentration of 4 mg/mL. Two seeding densities, 14 x $10^3$ cells/chip and 21 x $10^3$ cells/chip, were tested. Widefield images of HBECs seeded on OGP chips were then acquired at day 0, 1 and 3. The hydrogels included in the chips were contracted by cells seeded at both seeding densities on day 3. **A:** cell density: 14 x $10^3$ cells/chip, day 0. **B:** cell density: 14 x $10^3$ cells/chip, day 1. **C:** cell density: 14 x $10^3$ cells/chip, day 3. **D:** cell density: 21 x $10^3$ cells/chip, day 0. **E:** cell density: 21 x $10^3$ cells/chip, day 1. **F:** cell density: 21 x $10^3$ cells/chip, day 3. Magnification: 5X. Scale bars: 200 µm. N = 6 chips per condition, using cells obtained from n = 1 donor.

## 3.4. Discussion

The OP1 and OP2 chips used in this work were seeded with HBECs, which formed a confluent monolayer in the cell-seeded lane prior to the initiation of mucociliary differentiation. However, seeded cells invaded the gel lane in the days following the cell seeding, and the invasion of the gel lane was conspicuous when the cell culture medium was switched to the differentiation medium. Cell invasion was problematic, as invasion of the ECM lane could hinder future work centred on the inclusion, within the hydrogel, of another cell type such as fibroblasts. Whilst there are no studies that are focused on the seeding of HBECs in OP chips, comparisons can be drawn with other works centred on the seeding on OP chips of different types of epithelial cells, such as renal (276-278) and intestinal (279-281) epithelial

cells. In these studies, epithelial cell invasion to the scale observed in this work is not reported. However, in the study conducted by Naumovska *et al*., (282), matrix metalloproteinases (MMP) inhibitors have been used to prevent the invasion of induced pluripotent stem cells-derived intestinal epithelial cells. Whilst the use of MMP inhibitors could have potentially reduced HBECs invasion in the present work, it was decided not to use them, in order avoid any potential MMP inhibitors-induced alterations of the cellular phenotype. Furthermore, MMP inhibitors could have altered the phenotype of any other cell types, such as fibroblasts, included in the model at later stages.

The introduction of fluid flow in the OP chip by means of oscillation on a rocker platform was necessary for cell survival when the cell culture medium was switched to the differentiation medium, although fluid flow was not necessary for cell survival during the initial cell expansion phase in BEGM. Additionally, HBEC growth was observably increased in the differentiation phase under a fluid flow regimen, as compared to cell growth in BEGM under static conditions. Both these phenomena can be explained by the increase in cell proliferation that HBECs undergo throughout the mucociliary differentiation phase, during which a confluent cell monolayer grows into a thicker pseudostratified columnar epithelium. This would be paralleled by an increase in nutrient demand from the growing cell population. Therefore, a condition of scarcity of nutrients in static conditions might occur during the differentiation phase, specifically in the region within the cell-seeded channel. This would lead to cell death within the channel observed in cells cultured in static conditions. In contrast, the mixing of the cell culture medium due to the fluid flow applied within the chip likely impeded the formation of a region deprived of

nutrients, therefore allowing cell survival during the initial phases of mucociliary differentiation in the OP chips.

Whilst an increase in cell proliferation can be attributed to the differentiation process itself, the shear stress generated by the fluid flow could also have contributed to the increased cell growth. In the study conducted by Balcells *et al*., (283), pulsatile fluid flow at a frequency of 1 Hz increases rat lung epithelial cells proliferation. Whilst the cited study does not conclude that continuous fluid flow of the type exerted in the OP chips induces an increase in HBEC proliferation, other studies have found that fluid flow increased mucus production (284) and decreased permeability (285) in airway epithelial cells. Taken together, these studies show a general increase in the epithelial barrier function in response to shear stress, whether that is actuated by a decrease in permeability (285), by an increase in mucus production (284), or by an increased epithelial cell proliferation (283). It is therefore conceivable that continuous shear stress could have contributed to increased HBEC proliferation in this work, and therefore might have played a role in a possible increase in nutrient demand by cells cultured in the OP chips. Further studies are required to elucidate the effects of continuous shear stress on HBECs, in order to guide the design of microfluidic-based airway models.

Whilst fluid flow was necessary to ensure cell survival during the initial phase of mucociliary differentiation, cell death was eventually observed at later time points. One explanation for this result might be related to cell proliferation leading to an increase in the demand of nutrients, which could not be fulfilled. However, increasing the medium volume in the chip, and therefore increasing the amount of nutrients available to cells, did not lead to visible improvements in cell survival at

later time points. Another explanation for the cell death observed at late time points in the OP chip might lie in a change in the metabolic profile of HBECs rather than in an increase in their number. This phenomenon could be due to mechanisms related to glucose clearance in the airway, which is effected by HBECs (286).

In the human airway, the concentration of glucose in the airway surface liquid (ASL) is 0.4 mM (287), whilst the healthy human fasting blood glucose concentration ranges between 3.9 mM and 5.6 mM (288). The high transepithelial concentration gradient is actively maintained by the glycolysis process actuated by HBECs (290), possibly to minimise the chances of bacterial proliferation in the respiratory tract (289). It has also been demonstrated that nasal epithelial cells *in vitro* increase the rate of glycolysis and of medium acidification when in contact with cell culture medium including a high concentration of glucose (291). The differentiation medium used in this study, PALI, has a reported glucose concentration of 17 mM (292), considerably higher than the glucose concentration found in ASL *in vivo* (287). Therefore, the HBECs undergoing mucociliary differentiation in the chips, submerged by PALI, might have increased their rate of glycolysis and medium acidification in order to reduce the glucose concentration in the medium to a concentration more closely matched to ASL *in vivo*. This increase in metabolic rate could then have led to cell death due to medium acidity and rapid glucose depletion. This phenomenon would have not been observed in a normal ALI culture, because in these systems the glucose concentration in the small volume of liquid on the apical side of cultured HBECs would be quickly regulated by HBECs to levels observed in ASL *in vivo,* avoiding prolonged periods of accelerated glycolysis resulting in nutrient depletion and medium acidification. In order to verify this hypothesis, it would be necessary to obtain from the manufacturer the glucose

concentration of the other differentiation medium tested in this work, B-ALI. Additionally, cells could be cultured with the low-glucose differentiation medium recently developed by Morgan *et al*., (293). Given the possibility that glucose metabolism could have hindered cell survival in the chips, researchers aiming at designing microfluidic-based models should carefully consider any possible alteration of cellular metabolism due to the cell culture conditions to which cells are subjected.

The use of a NOTCH inhibitor did not induce differentiation of HBECs in the model developed in this work, as HBECs underwent cell death before the completion of the differentiation protocol. Cell death was due to mechanisms likely unrelated to the use of a NOTCH inhibitor, as previously discussed, i.e. nutrient depletion due to elevated cell proliferation and changes in cell metabolism. Therefore, this work does not conclude that the use of a NOTCH inhibitor is unsuitable for the development of airway-on-a-chip. This study, however, indicates that submerged differentiation of HBECs can prove challenging if the geometry of the chip, the fluid flow regimen, and the cell culture medium are not optimised.

# Chapter 4

In previous chapters, the use of Mimetas chips was not conducive to the development of an *in vitro* model of large bronchi. Furthermore, the limitations associated with the use of decellularised tissue and decellularised tissue-derived hydrogels in combination with HBECs have been demonstrated.

In this chapter, an introductory section will describe the advantages related to the inclusion of fibroblasts in bronchial *in vitro* models. This introduction will then be followed by an experimental section centred on the development of an *in vitro* model based on the culture of HBECs on high throughput screening (HTS) transwell® systems, in combination with the culture of primary lung fibroblasts on DLH. The results obtained will then be discussed.

## 4.1. Introduction

### 4.1.1. Inclusion of fibroblasts in bronchial *in vitro* models

An important feature of *in vitro* models lies in the inclusion of an appropriate array of cell types. The most reductionist *in vitro* models are centred on the culture of one cell type of particular relevance for a physiological or pathological condition. Increasing the number of cell types to be included in the model can improve its capacity to replicate the biological features of the targeted tissue as observed *in vivo*. However, the choice of cells to be included in the model is complicated by the complexity of the interactions between different cells types in orchestrating a physiological or pathological mechanism. Yet, it is possible to delineate groups of cell types that are particularly relevant for a wide variety of biological mechanisms.

One such group, in the context of the airway, is formed by HBECs and by a layer of fibroblasts localised below the basement membrane, called the “attenuated fibroblasts sheath” (AFS; 251). From a conceptual point of view, the AFS extends from the conductive airway to the alveoli, where it is represented by the interstitial fibroblasts within the alveolar walls (251). The AFS is a component of the epithelial-mesenchymal trophic unit (EMTU), a theoretical framework proposed by Evans *et al*. to describe the interaction between the tracheobronchial epithelium and the other compartments of the airway’s wall in physiological and pathological contexts (251, 252). The interaction between HBECs and the AFS, actuated by mediators such as interleukin 1 – alpha (IL-1 $\alpha$ ; 41) and transforming growth factor $\beta$ (TGF-$\beta$ ; 213), is a prominent component of the EMTU, as indicated by studies related to asthma (253) and COPD (254).

In addition to the communication between HBECs and the fibroblasts included in the AFS, a long-range interaction between HBECs and the fibroblasts located in the distal portion of the respiratory tract, which have previously been termed “HLFs”, has recently been the subject of investigation (295). The crosstalk between these two spatially distant cell types is hypothesised to be mediated by extracellular vesicles (EVs) (295), which can be defined as lipid bilayer-enclosed nanoparticles that can be released by cells (296). The content of EVs varies, and can include various bioactive molecules, such as proteins and RNA (296). In the respiratory tract, EVs have been found in secretions of the airway such as sputum and bronchoalveolar lavage fluid (297). The study conducted by Kadota *et al*., (298), indicates that HBEC-secreted EVs inhibit the TGF-$\beta$-mediated differentiation of lung fibroblasts into myofibroblasts, a cell type which, in addition to contracting and remodelling the ECM during wound healing (299), also plays a key role in the

abnormal ECM deposition associated with fibrotic diseases such as IPF (300). Therefore, healthy HBECs appear to modulate the phenotype of HLFs in order to prevent aberrant ECM remodelling. However, EV-mediated communication could also have a role in initiating pathological conditions. In particular, EVs released by HBECs exposed to cigarette smoke extract promotes the differentiation HLFs into myofibroblasts, a mechanism that could underlie the pathogenesis of COPD (301). Whilst these studies indicate that HBECs can influence the phenotype of HLFs through EVs, communication in the opposite direction might also take place, as EVs secreted by HLFs obtained from IPF patients can induce senescence in HBECs (302).

Given their relevance in the physiology and pathology of the airway, various *in vitro* models based on the culture of both HBECs and fibroblasts have been developed, following different strategies (255), as depicted in Figure 4.1. One of these methods is based on the use of conditioned medium, either by culturing HBECs with medium derived from the cell culture of fibroblasts (256), or vice-versa (257). More complex models are based on the co-culture of HBECs and fibroblasts in transwell® systems. These models have been developed following different strategies (255). In particular, whilst HBECs are typically cultured on the apical well, fibroblasts can be seeded on the underside of the apical well (258) or in the recipient well (259). Another type of model can be developed by seeding both HBECs and fibroblasts on a hydrogel placed on the apical well of the transwell® system (260). Alternatively, *in vitro* models inclusive of HBECs and fibroblasts can be developed by embedding bronchial tissue biopsies in a hydrogel (261). Additionally, airway organoids including HBECs and fibroblasts have also been developed (262), and could be used as bronchial *in vitro* models.

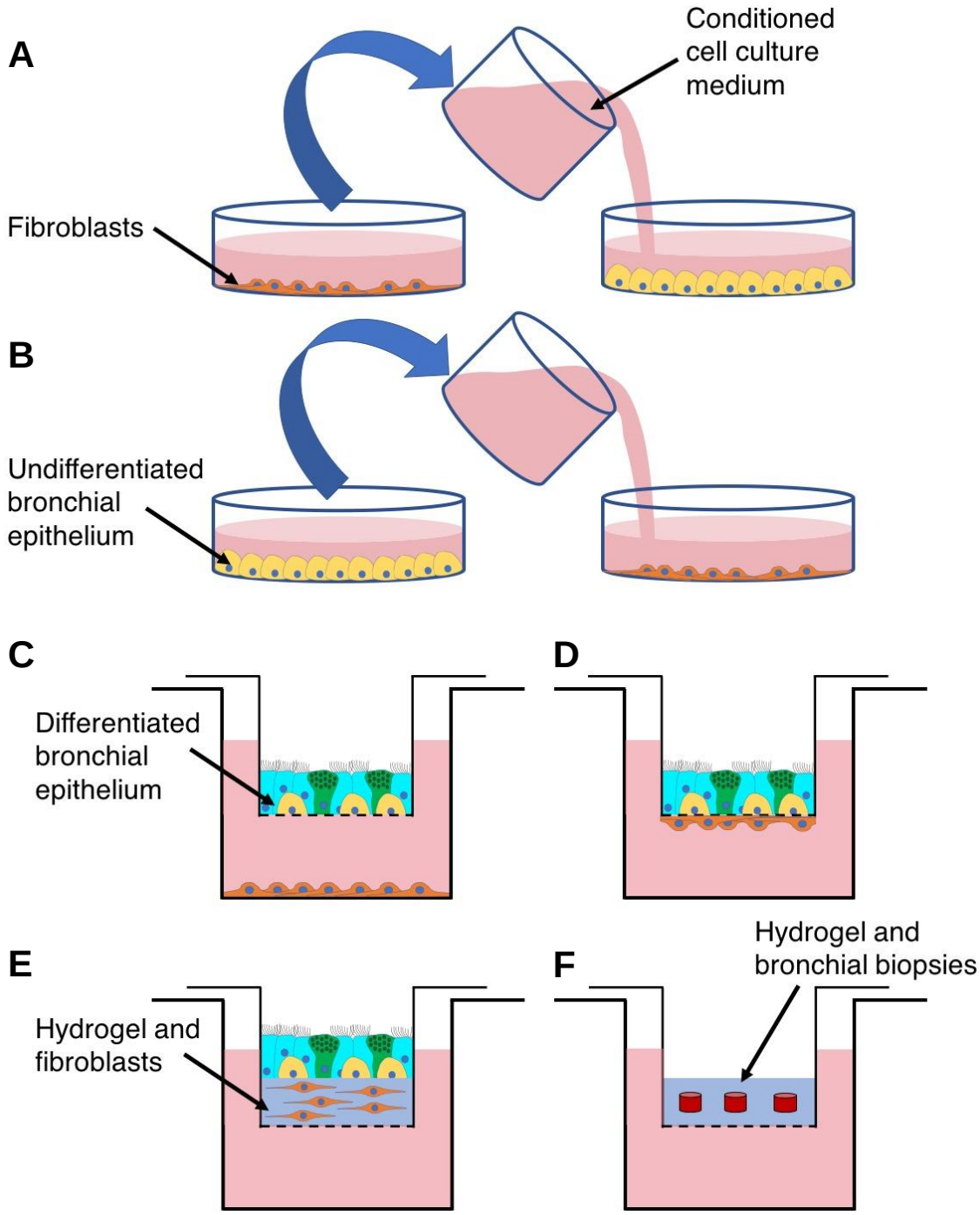


**Figure 4.1.** Configurations of *in vitro* models including HBECs and fibroblasts. **A:** culture of HBECs with conditioned medium obtained from the culture of fibroblasts. **B:** culture of fibroblasts with conditioned medium obtained from the culture of HBECs. **C:** transwell® system-based model including fibroblasts in the recipient plate and HBECs on the apical well. **D:** transwell® system-based model including fibroblasts in the bottom side of the apical well, and HBECs on the apical well. **E:** transwell® system-based model including fibroblasts embedded in a hydrogel, included in the upper side of the apical well. HBECs are cultured on top of the hydrogel. **F:** transwell® system-based model including bronchial biopsies embedded in a hydrogel, included in the upper side of the apical well.

In HBEC-fibroblast co-culture models, the ECM component in contact with fibroblasts is typically not included, or it is modelled through the inclusion of a

collagen-based hydrogel (260). The ECM found in the respiratory tract, however, is not limited to collagen and is instead formed by a variety of different components. A further improvement of existing *in vitro* models based on HBEC-fibroblasts co-cultures can therefore be implemented by including an ECM hydrogel instead of relying on materials that reflect a single ECM component.

In addition to the inclusion of appropriate cell types and ECM components, another important attribute of *in vitro* models is their throughput. Most airway models are based on the use of 24-well plate format transwell®. In this format, the inclusion of an ECM hydrogel in the recipient well is possible, but covering the relatively large surface area of the wells would require relatively high volumes of ECM hydrogel, leading to issues associated with the cost-effectiveness of the model. However, recently a 96-well format transwell® system has been commercialised. This newly developed format has presently been used only in a small number of studies (263, 264), and includes smaller recipient wells as compared to the 24-well format. The 96-well format transwell® systems could therefore be used for the development of high-throughput *in vitro* models based on the inclusion of ECM hydrogels, such as the DLH, which could be included in the relatively small recipient wells in a cost-efficient manner.

A combination of 96-well transwell® format, commercial lung ECM hydrogel, and co-culture of primary HBECs and HLFs has so far never been tested for the development of a biomimetic *in vitro* model of the airway. Given the commercial availability of its components, its high throughput, and its capacity to replicate aspects of the *in vivo* milieu such as the fibroblast-HBEC crosstalk and the inclusion of respiratory ECM, this combination could present a significant

improvement over existing *in vitro* models, and will be tested in the experimental section.

## 4.2. Methods

### 4.2.1. Human lung fibroblasts culture

The HLFs used in this work were sourced with informed donor consent from LONZA (donors: 18TL057581 and 19TL148581). HLF donors had no pathological respiratory conditions. Upon receipt, the cells, which were already at P1, were stored in liquid nitrogen. The cells were thawed and expanded according to the following protocol. Firstly, cells were thawed by quickly warming the vial to 37°C. Then, the cell suspension was decanted from the cryovial into a 15 mL centrifuge tube. Subsequently, 10 mL fibroblasts growth medium 2 (FGM; LONZA, Switzerland), reconstituted according to the vendor's instructions, were decanted dropwise into the centrifuge tube containing the cell suspension. The cell suspension was then placed in a centrifuge and spun at a centrifugal acceleration of 200 x *g* for 5 min. Upon centrifugation, supernatant was discarded and cells were resuspended in 10 mL FGM. Then, 5 mL cell suspension was added to 2 T175cm$^2$ cell culture flasks (ThermoFisher Scientific), each including a total of 35 mL FGM at the end of this step. The flasks were then placed in a cell culture incubator, and cell culture medium was exchanged the day after and every 2-3 d thereafter. On Fridays, the cell culture medium in flasks was exchanged with 50 mL instead of 35 mL fresh medium, and medium was then always exchanged back to 35 mL FGM on Mondays. Cell culture was progressed until cells reached 80-90 % confluency. Then, for long term preservation, cells were frozen according to the following protocol. Firstly, the T175cm$^2$ cell culture flasks containing the HLFs were

washed with HBSS. Then, 8 mL trypsin was added to each flask, which were subsequently placed in a cell culture incubator until cell detachment could be observed. After this step, the cell suspension from each flask was pooled in a 50 mL centrifuge tube containing 16 mL TNS. The cells in the resulting solution were counted with a haemocytometer and the cell suspension was spun in a centrifuge at a centrifugal acceleration of 250 x *g* for 5 min. Subsequently the supernatant from the 50 mL centrifuge tube was discarded and the cells were resuspended at a concentration of 8.8 x $10^5$ cells/mL in a 10 % v/v solution of DMSO in fetal bovine serum (ThermoFisher Scientific). The resuspended cells were then divided into cryovials, each storing 1 mL cell suspension. Afterwards, the cryovials were placed in freezing containers prepared as described in 2.2.6, which were cooled to -80°C overnight. The day after, the cryovials were placed in liquid nitrogen for long term storage.

### 4.2.2. Fixation of HLFs with 4 % PFA

In this experiment, HLFs (P2) from 2 donors (18TL057581 and 19TL148581), previously expanded according to the protocol described in 4.2.1, were thawed and cultured according to the following protocol. Firstly, the cryovial containing the cells was thawed by quickly raising its temperature to 37°C. Then the content of the cryovial was added to a 15 mL centrifuge tube, into which 9 mL of FGM were decanted dropwise. The cell suspension was then spun in a centrifuge at a centrifugal acceleration of 300 x *g* for 5 min. Supernatant was then discarded, and cells were resuspended in 10 mL FGM. After this step, 5 mL of the cell suspension was added to a T175$cm^2$ cell culture flask containing 30 mL FGM. The flask was then placed in a cell culture incubator, and cell culture medium was changed following the same schedule described in section 4.2.1. When cells reached 80 %

confluency, a 96-well plate was prepared by adding 190 µL FGM to 20 wells. Then, HLFs were seeded according to the following protocol, which was executed taking care not to mix donors during the procedure. Firstly, the flasks containing the cells were briefly washed with DPBS--. Then, 14 mL ACF dissociation enzyme was added to each flask, which was placed in a cell culture incubator until cell detachment was observable. The cell suspension was then added to one 50 mL centrifuge tube per cell donor, each tube containing 14 mL ACF enzyme inhibition solution. The cells in resulting solutions were then counted with a haematocytometer and the centrifuge tubes containing the cells were spun in a centrifuge at a centrifugal acceleration of 300 x *g* for 5 min. After this step, the supernatant from each centrifuge tube was discarded and cells were resuspended in FGM, and subsequently seeded in the wells of a 96-well plate previously filled with 190 µL FGM. The cell seeding density was 7.5 x $10^3$ cells per well, and the cell culture medium volume contained in the well after cell seeding was 200 µL. After 2 h, the seeded wells were briefly washed with DPBS-- and then cell culture medium was changed.

On day 1, 1 image per cell-seeded well was acquired at a magnification of 5X. Then, cells were fixed according to the following protocol. Firstly, cells were briefly washed with DPBS--. After removing DPBS--, 100 µL of 4 % PFA was added to each well. In 3 wells per cell donor, PFA 4 % was kept in the wells for 10 min. In other 3 wells per cell donor, PFA 4 % was kept for 15 min. In 4 wells, PFA 4 % was kept for 20 min. After the time specified for each group of wells, PFA 4 % was removed and wells were washed 3 times with DPBS--, and 1 image per cell-seeded well was acquired at a magnification of 5X.

### 4.2.3. Seeding of HLFs on DLH

Cryopreserved HLFs (P2) obtained from donor 18TL148581, previously thawed, expanded and frozen according to the protocol described in 4.2.1, were thawed and expanded according to the method described in 4.2.2. When cells reached 60-90 % confluency, DLH was then reconstituted according to the protocol described in 2.2.3, with the following modification: FGM was used instead of DPBS-- in the last step of gel preparation. After this step, 50 µL of DLH was loaded in 6 wells of a 96-well plate, and the plate was placed in a cell culture incubator for 1 h to allow gelation to occur. Then, collagen I hydrogel pre-gel was reconstituted as described in 2.2.9, and 50 µL of collagen I pre-gel were loaded in 6 empty wells of the 96-well plate, which was placed in a cell culture incubator for 15 min to allow gelation to take place. After this step, 150 µL FGM was added to each of the hydrogel-loaded wells, and to 6 empty wells.

The HLFs were then seeded following the protocol described in 4.2.2 at a seeding density of 20 x $10^3$ cells/well in each of the wells previously filled with FGM. After the cell seeding, the final cell culture volume included in the wells was 200 µL. Cell culture medium was exchanged 2 h after seeding and every 2-3 d. One widefield image per seeded well was acquired on day 0, 1, 2, 3, 4 and 7 at 2.5X magnification using a S100TV microscope. Then, cell orientation coherency was analysed. The orientation coherency is a number comprised between 0 and 1 which indicates if features in an image, such as cells, are oriented in a dominant direction. If the orientation coherency is 0, the image features are completely isotropic and have no shared orientation. If the orientation coherency is 1, the image features are completely anisotropic and are aligned towards one shared orientation. The orientation coherency of the cells in the widefield images was quantified by

executing the following protocol using the software FIJI (2.1.0/1.53n, for source see reference: 345). Firstly, a FFT bandpass filter was applied to highlight the cells against the background. In particular, the settings for the FFT bandpass filter were the following: large structures were filtered down to 40 pixels, small structures were filtered up to 3 pixels, stripes were not suppressed, and a 5 % tolerance of direction was set. Then a convolution was applied to highlight the contours of cells, followed by the application of a median filter with a radius of 3 pixels to exclude noise. Then the “multiply” command was executed to double the pixel values, and finally a central oval region of interest (ROI) was delineated. The ROI was maintained constant for each image. Finally, the function “OrientationJ Measure” related to the “OrientationJ” plugin was executed to obtain the orientation coherency relative to the ROI of each image. All the images were analysed, excluding images of wells in which cells had contracted into cellular complexes in which single cells were undiscernible from each other. Images showing cell orientation in one representative image per condition on day 1 were also acquired following the protocol described in this paragraph, but with the following modification: the color-survey option related to the “OrientationJ Analysis” function was applied instead of executing the “OrientationJ Measure” function.

### 4.2.4. Culture of HLFs with epithelial differentiation cell culture medium

Cryopreserved HLFs (P2) related to donors 18TL057581 and 19TL148581, previously expanded and frozen according to the protocols in 4.2.1, were thawed and cultured according to the protocol described in 4.2.2, with the following modifications: upon spinning, cells were resuspended in 14 mL FGM and then 3 mL cell suspension was added to 4 T75cm$^2$ cell culture flask, which after cell seeding included a FGM volume of 20 mL. When cells reached 90 % confluency,

they were seeded in 48 well-plates following the same procedure followed for HBEC seeding in section 2.2.9, at a seeding density of 23 x $10^3$ cells/well, in 36 wells per cell donor. At the end of the procedure, each seeded well contained 400 µL FGM. Two hours after seeding, FGM medium in wells related to each donor was exchanged, and in 18 wells per donor the cell culture medium was switched to PALI. Cell culture medium in all wells was then exchanged every 2-3 d and cell culture was progressed up to day 4. Widefield images were acquired on day 1, 3 and 4 at a magnification of 2.5X using a S100TV microscope. On day 1, 3 and 4 live Hoechst staining was performed on 6 wells per condition according to the protocol described in 2.2.10, modified by eliminating the final DPBS-- washes and by diluting the Hoechst solution in FGM or PALI according to the condition to which the wells were related to. Then, 3 images of Hoechst-stained cells per well were acquired at a magnification of 5X. Afterwards the nuclei observable in the images related to the live Hoechst staining were quantified by executing the following protocol whilst using the software FIJI (2.1.0/1.53n, for source see reference: 345). Firstly the images were converted to a 32-bit format. Then a median filter with a radius of 3 pixels was applied to reduce noise, and the contrast enhanced with the “enhance contrast” command. After this step the background was subtracted from images using the “subtract background” command and images were converted to a binary format by applying the threshold “Huang”. The “watershed” function was then used to separate agglomerates of nuclei. Finally, nuclei were counted using the “Analyse particle” function.

### 4.2.5. HLF seeding on DLH with PALI

To assess HLFs contractibility and growth in DLH, cryopreserved HLFs (P2) obtained from donor 19TL148581, previously expanded and frozen according to

the protocols in 4.2.1, were thawed and cultured according to the protocol described in 4.2.2. When cells reached 90 % confluency, 6 recipient wells of a 96-well plate-format HTS transwell® plate (Corning) were filled with 150 µL DLH reconstituted according to the protocol described in 2.2.3, with the following modification: PALI was used instead of DPBS-- in the last step of pre-gel preparation. The plate was then placed in a cell culture incubator for 1 h. Afterwards, 235 µL PALI was added to each well loaded with the hydrogel. The HLFs were then seeded at a seeding density of 5 x $10^3$ cells/well in 3 of the wells loaded with DLH, and at a seeding density of 10 x $10^3$ cells/well in the residual 3 loaded wells. After the seeding procedure, each seeded well contained 160 µL PALI. Cell culture medium was exchanged every 2-3 d, and widefield images were acquired on day 2, 7, 10 and 13 at a magnification of 5X using a S100TV microscope. Cell culture was progressed up to day 13.

### 4.2.6. Cell culture on transwell® systems

Experiments involving the combination of HBECs, DLH, and transwells® were based on the use of HTS transwells® with a 96-well plate format with a pore diameter of 0.4 µm. A total of 3 experiments were carried out using the HTS transwells®. Table 4.1 outlines the conditions and outputs associated with the experiments including the combination of HTS transwells®, DLH, and HBECs. In Table 4.1, and in the following sections of this chapter, HBECs derived from donors 18TL290281 and 18TL052522 are referred to respectively as “HBECs donor 1” and “HBECs donor 2”, whilst HLFs derived from donors 18TL057581 and 19TL148581 are referred to respectively as “HLFs donor 1” and “HLFs donor 2”. The apical transwells® used in the experiments were coated with collagen IV as described in the following section.

**Table 4.1.** Conditions and outputs associated with the experiments carried out using HTS transwells®.

| **Experiment 1** | | | | | | |
|---|---|---|---|---|---|---|
| | **Condition 1** | **Condition 2** | **Condition 3** | **Condition 4** | **Condition 5** | **Condition 6** |
| **Wells per condition** | 6 | 6 | 6 | 6 | 6 | 6 |
| **Cells in apical well** | HBECs donor 1 | HBECs donor 1 | HBECs donor 1 | HBECs donor 1 | HBECs donor 1 | HBECs donor 1 |
| **Cells in recipient well** | | HLF donor 1 | HLF donor 2 | | HLF donor 1 | HLF donor 2 |
| **DLH in recipient well?** | No | No | No | Yes | Yes | Yes |
| **Output** | Ciliary beating frequency analysis | Widefield images HLF | Widefield images HLF | | Widefield images HLF | Widefield images HLF |
| **Experiment 2** | | | | | | |
| | **Condition 1** | **Condition 2** | **Condition 3** | **Condition 4** | **Condition 5** | **Condition 6** |
| **Wells per condition** | 6 | 6 | 6 | 6 | 6 | 6 |
| **Cells in apical well** | HBECs donor 2 | HBECs donor 2 | HBECs donor 2 | HBECs donor 2 | HBECs donor 2 | HBECs donor 2 |
| **Cells in recipient well** | | HLF donor 1 | HLF donor 2 | | HLF donor 1 | HLF donor 2 |
| **DLH l in recipient well?** | No | No | No | Yes | Yes | Yes |
| **Output** | | Widefield images HLF | Widefield images HLF | | Widefield images HLF | Widefield images HLF |
| **Experiment 3** | | | | | | |
| | **Condition 1** | **Condition 2** | **Condition 3** | **Condition 4** | **Condition 5** | **Condition 6** |
| **Wells per condition** | 12 | 12 | 12 | 12 | 12 | 12 |
| **Cells in apical well** | HBECs donor 1 | HBECs donor 1 | HBECs donor 1 | HBECs donor 1 | HBECs donor 1 | HBECs donor 1 |
| **Cells in recipient well** | | HLF donor 1 | HLF donor 2 | | HLF donor 1 | HLF donor 2 |
| **DLH in recipient well?** | No | No | No | Yes | Yes | Yes |
| **Output** | Immunostaining (Ac-tub, ZO-1, MUC5-AC) | Widefield images HLF | Widefield images HLF | Immunostaining (Ac-tub, ZO-1, MUC5-AC) | Widefield images HLF | Widefield images HLF |
| | **Condition 7** | **Condition 8** | **Condition 9** | **Condition 10** | **Condition 11** | **Condition 12** |
| **Wells per condition** | 12 | 12 | 12 | 12 | 12 | 12 |
| **Cells in apical well** | HBECs donor 2 | HBECs donor 2 | HBECs donor 2 | HBECs donor 2 | HBECs donor 2 | HBECs donor 2 |
| **Cells in recipient well** | | HLF donor 1 | HLF donor 2 | | HLF donor 1 | HLF donor 2 |
| **DLH in recipient well?** | No | No | No | Yes | Yes | Yes |
| **Output** | Immunostaining (Ac-tub, ZO-1, MUC5-AC) | Widefield images HLF | Widefield images HLF | Immunostaining (Ac-tub, ZO-1, MUC5-AC) | Widefield images HLF | Widefield images HLF |

Firstly, human collagen IV (Sigma Aldrich) was dissolved in 1 mL of 1 M acetic acid to obtain a concentration of 1 mg/mL. This solution was aliquoted and preserved at – 80°C. One day before the HBEC seeding on HTS transwell® membranes, collagen IV aliquots were thawed and diluted in DI water to a concentration of 0.15 µg/µL. This solution was sterile-filtered using a 0.2 µm disposable filter, and 50 µL of the resulting solution was added to each apical well to be used in the

experiments. The wells were dried overnight in a safety cabinet, and were then washed twice with DPBS++.

Before the cell seeding on the HTS transwell® membranes took place, HBECs obtained from donors 1 and 2 were thawed and cultured as described in 2.2.6 until they were 80 % confluent. Then, HBECs were seeded on collagen IV-coated HTS transwell® membranes according to the following protocol. Firstly, 235 µL BEGM were added to each recipient well of the transwell® systems included in the experiment. Afterwards, the flasks containing HBECs were washed with DPBS--. Then, ACF dissociation enzyme was added to each flask, which were subsequently placed in a cell culture incubator until cell detachment was observable. The resulting cell suspension was added to a centrifuge tube, and the activity of the ACF dissociation enzyme was inhibited by adding an equal volume of ACF inhibition solution. Cells were then counted using a disposable haemocytometer and spun in a centrifuge at a centrifugal acceleration of 300 x *g*, for 5 min. The supernatant was then discarded and cells were resuspended in BEGM in order to obtain a cell density of 20 x $10^3$ cells/50 µL. Afterwards, 50 µL of cell suspension was added to each apical well of the transwell® systems used for the experiment, in order to seed 20 x $10^3$ cells per well according to the conditions outlined in Table 4.1. The cell culture medium in the apical and recipient wells was exchanged the day after the seeding. 2 d after cell seeding, ALI culture was initiated by removing the cell culture medium from the apical wells and by exchanging the BEGM in the recipient wells with PALI medium. The beginning of the ALI culture is defined, in this section, as day 0. Cell culture medium in the recipient plate was exchanged every 2 d throughout the experiments. On day 11, DLH was added to the recipient wells of the HBECs-seeded transwell® systems

according to the experimental conditions defined in Table 4.1, and following the protocol described in the next paragraph.

Firstly, cryopreserved HLFs (P2) obtained from donor 1 and 2, previously expanded and frozen according to the protocols in 4.2.1, were thawed and cultured according to the protocol described in 4.2.2. When cells reached 90 % confluency, 75 µL of DLH was included in the recipient wells of a new HTS transwell® plate, following the protocol described in 2.2.9. Then, 10 x $10^3$ HLFs were seeded in the designated wells according to the conditions outlined in Table 4.1 and following the protocol reported in section 4.2.5, with the following modification: instead of PALI, FGM was used throughout the procedure. At the end of the seeding procedure, each well including fibroblasts contained 235 µL FGM. The HLF-seeded transwell® plate was placed in the cell culture incubator, and 2 h later the seeded recipient wells were subjected to 2 washings with DPBS++, followed by the inclusion of 235 µL PALI in each well. Then, the apical wells previously seeded with HBECs were placed in the recipient wells including the HLFs. On day 28, high-speed videos of HBECs related to experiment 2 were acquired according to section 4.2.7. The videos were then analysed according to the procedure also described in section 4.2.7. Furthermore, on day 28 HBECs and HLFs related to all experiments were fixed following the protocol described in section 4.2.8, and HBECs related to experiment 3 were stained according to the protocol also described in section 4.2.8.

### 4.2.7. Analysis of cilia beating frequency

Transwell® systems seeded with HBECs and HLFs were transported to a different location at a walking distance of approximately 15 min. Then, 2 high-speed videos

per seeded apical well were acquired using a Hamamatsu C11440-22C high speed camera (Nikon, Japan). Cilia beating frequency (CBF) was then assessed using the CiliarMove software, developed by Sampaio *et al*., (319). The software readout was composed of a heatmap representing the frequency recorded in each pixel of the ROI selected by the user, which in this experiment was a 1002 x 1004 pixel rectangle set in the same position relatively to each high-speed video, and a graph representing the statistical distribution of the recorded frequencies, measured in Hz. Recorded CBF equal to or above 25 Hz were attributed to experimental noise. Noise was filtered out of the results, and the relative frequency of CBF was recalculated accordingly. Then, the average CBF for each video was calculated.

### 4.2.8. Fixation and immunostaining of cells included in transwell® systems

The recipient wells seeded with HLFs were fixed by adding 4 % PFA and leaving the wells at RT for 15 min at RT. This step was followed by 2 washings with DPBS++, upon which the fixed recipient wells could be preserved at 4°C until widefield images were acquired using a S100TV microscope.

In order to fix the HBECs seeded on transwell® membranes, 4 % PFA was added to HBECs-seeded apical wells. The apical wells were then left at RT for 15 min, and then washed 3 times with DPBS--. The fixed apical wells could then be preserved at 4°C until immunostaining for Acetylated Tubulin (Ac-tub), MUC5-AC, and Zonula Occludens-1 (ZO-1) was performed as described in the next paragraph.

The primary and secondary antibodies used for immunostaining, including the marker, vendor and product code are summarised in Table 4.2.

**Table 4.2.** List of antibodies used in this work, including their type (primary or secondary), the biological marker to which they are reactive, the vendor, and the product code.

| Type | Binds to | Vendor | Product code |
|---|---|---|---|
| Primary | Ac-tub | Sigma-Aldrich | T6793 |
| Primary | ZO-1 | ThermoFisher | 40-2200 |
| Primary | MUC5-AC | Abcam | ab3649 |
| Secondary | Rabbit Immunoglubulin G | Abcam | ab150080 |
| Secondary | Mouse Immunouglobulin G2B | ThermoFisher | A-21242 |
| Secondary | Mouse Immunoglobulin G1 | ThermoFisher | A-21121 |

At the beginning of the immunostaining protocol, a “permeabilisation solution” was prepared, constituted by 3 % v/v Bovine Serum Albumine (BSA, ThermoFisher Scientific) and 0.1 % v/v TX-100 in DPBS--. Also, a “staining buffer” was prepared, constituted by 1 % v/v BSA and 0.1 % v/v TX-100 in DPBS--. Then, the DPBS-- was removed from the recipient wells underlying the apical wells containing the fixed wells. All the next steps of the protocol were performed on the cell-seeded apical wells. Firstly, cells were submerged with permeabilisation solution at RT for 30 min. Then, the permeabilization solution was exchanged with a solution composed of Ac-tub and ZO-1 primary antibodies in staining buffer at a 1 : 100 dilution, or alternatively with a solution composed of MUC5-AC antibodies in staining buffer at a 1 : 100 dilution. The cells were then incubated overnight at 4°C. Then, each well was rinsed twice with DPBS--. Subsequently, secondary antibodies selected for their specific binding to the primary antibodies previously used were added to the apical, at a dilution of 1 : 400 in staining buffer. Cells were then incubated for 2 h at RT, shielded from light. Afterwards, the staining solution was exchanged with 1 µg/mL Hoechst in DPBS--. Cells were subsequently incubated for 15 min at RT, shielded from light, and then wells were rinsed twice with DPBS--. Afterwards, the cell-seeded membranes including the cells were cut

with a scalpel and placed on glass slides. Following this step, droplets of prolong gold, a mounting agent, were added on glass coverslips, which were placed on top of the transwell® membranes. The stained membranes were preserved at 4°C until imaging was performed with a confocal microscope (LSM880, Zeiss). For each stained membrane, 1-2 images were acquired.

### 4.2.9. Statistical analysis

Statistical tests were performed using the software GraphPad Prism version 9.0.0. To inform the choice of statistical tests to be performed, a Shapiro-Wilk normality test was executed on all quantitative data. An unpaired two-tailed t-test with Welch's correction was conducted to analyse the difference between the means of nuclei counts. To analyse difference between the means of cell orientation coherency, unpaired two-tailed t-test with Welch's correction or Welch's ANOVA test were executed as appropriate. If a significant difference was found between the means of the groups, Welch's ANOVA was followed by a post-hoc Dunnett's T3 multiple comparison test. For all tests, if p-value $< 0.05$, the results were considered statistically significant. Degrees of significance were indicated in images as follows: * for $p < 0.05$, ** for $p < 0.01$, *** for $p < 0.001$, and **** for $p < 0.0001$. In the 4.3. Results section, the p values of the t-tests with Welch's correction and of the Welch's ANOVA are reported in the figure legends, whilst the degree of significance of the t-tests with Welch's correction and of the post-hoc tests are reported in the figures.

# 4.3. Results

### 4.3.1. Seeding of HLFs on DLH

As described in chapter 2, HBECs failed to grow to confluency on DLH. In this chapter, the growth capacity of HLFs on this material was evaluated, with a view to include HLFs on DLH in the finalised *in vitro* model. To this end, HLFs obtained from 1 donor were seeded in 96-well plates on uncoated cell culture-treated wells to act as a control, on wells including collagen I hydrogel, and on wells including DLH. Each condition included n = 6 wells. As shown in the widefield images included in Figure 4.2A, cells seeded on uncoated wells contracted to form a sphere at day 3, whilst cells on DLH contracted the substrate on which they were seeded between day 3 and day 7. In Figure 4.2B, processed widefield images acquired at day 1 post-seeding suggest differences in collective cell orientation across different conditions. Widefield images related to all conditions and timepoints were analysed following the procedure outlined in Figure 4.2C, using one representative image per well. The results of the image analysis are summarised in Figure 4.2D. The orientation coherency, reported in Figure 4.2D for each condition, is an adimensional number comprised between 0 and 1 and closer to 1 if cells are collectively oriented towards one dominant direction. Its value was measured throughout all timepoints until cell contraction of the cellular layer or of the cell culture substrate was observed. From day 1 and across the following timepoints, the orientation coherency of cells seeded on DLH was substantially lower as compared to the orientation coherency displayed by cells seeded on collagen I hydrogel and in the control condition.

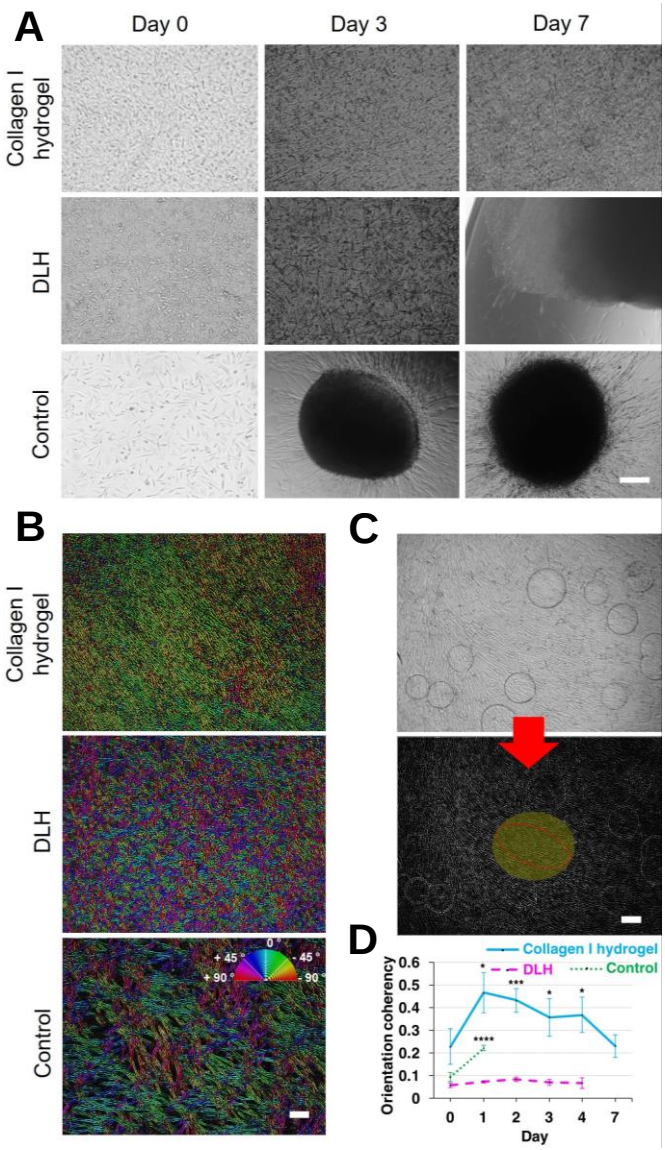


**Figure 4.2**. Widefield images and cell orientation analysis of HLFs cultured on different substrates. Wells of 96-well plates including DLH, collagen I hydrogel, or hydrogel-free, were seeded with HLFs. Widefield images were acquired on day 0, 1, 2, 3, 4 and 7, and a cell orientation analysis of HLFs based on the widefield images was performed across the timepoints. The DLH was contracted by HLFs between day 3 and day 7. Additionally, HLFs displayed less orientation coherency on DLH as compared to the other substrates between day 1 and day 4. **A:** representative widefield images of HLFs cultured on collagen I hydrogel, DLH, and cell culture-treated uncoated wells, on day 0, 3, and 7 after seeding. First, second, and third rows show respectively HLFs seeded on collagen I hydrogel, DLH, and cell culture-treated uncoated wells (control). First, second, and third columns represent respectively cells cultured at day 0, 3, and 7 after cell seeding. Data: the experiment was performed by seeding HLFs on n = 6 wells per condition. Magnification: 2.5X, with a 2X post-acquisition zoom. Scale bar: 200 µm. **B:** representative colorimetric maps of cell orientation acquired at day 1 after cell seeding on collagen I hydrogel (top), DLH (centre), and uncoated wells (control, bottom). The tangent to the semi-circular lines of the colour legend on the top-right corner of the bottom image can be used as reference for the orientation of cell contours expressed in degrees of arc. **C:** illustration of the image analysis process. The image on top is a representative widefield image used as input for the analysis process, and the image below is the post-processing output image, obtained after the orientation analysis is executed. The transparent yellow oval visible in the image on the right is the ROI, located in the same position and with the same dimensions in each image, delineating the area in which the orientation coherency was measured. The orientation of the red hollow oval, visible within the yellow oval, indicates the direction of the predominant orientation of the cells included in the ROI. **D:** quantification of cell orientation coherency (Y axis), expressed as mean ± SEM, across different timepoints (X axis), for HLFs seeded on collagen I hydrogel (blue continuous line), uncoated wells (control, green dotted line), DLH (magenta dashed line). The orientation coherency is an adimensional number comprised between 0 and 1, its value being closer to 1 if cells are oriented towards one dominant direction. Lines in the graph interrupt on timepoints at which cell or substrate contraction was observed from widefield images, thus impeding the analysis of cell orientation. Welch's ANOVA was performed to analyse data related to day 0 ($p = 0.098$) and day 1 ($p < 0.0001$), and Welch's t-test was performed to analyse data related to day 2 ($p = 0.0008$), day 3 ($p = 0.0177$) and day 4 ($p = 0.0104$). The significance of the Welch's t-test and post-hoc tests is indicated in the graph (* indicates $p < 0.05$, *** indicates $p < 0.001$, **** indicates $p < 0.0001$). For day 1, the degrees of significance indicated on top of the data points refers to comparisons with the DLH. Magnification: 2.5X. Scale bars: 200 µm. N = 6 wells per condition, using cells obtained from 1 donor. For the quantification of orientation coherency, 1 representative image per well per condition was acquired.

### 4.3.2. Culture of HLFs with epithelial differentiation cell culture medium.

In order to setup a HLFs-HBECs co-culture, it was necessary to assess whether HLFs could grow in PALI medium. The method chosen to assess HLFs growth was to perform nuclei counts on PFA-fixed cells. In particular, HLFs obtained from 2 donors were seeded on n = 10 wells of a 96-well plate per donor, and widefield images were acquired before and after fixation with PFA. It was observed that cells grown in FGM medium detached upon fixation with PFA (Figure 4.3A), leaving empty areas in wells that could interfere with subsequent nuclei count. To navigate around this issue, in subsequent experiments PFA fixation was avoided. Instead, Hoechst staining was performed on live cells. In the following experiment, HLFs obtained from 2 donors were seeded in 48 well-plates and cultured with either FGM or PALI medium. In particular, for each donor, cells in n = 18 wells were cultured with FGM and cells in n = 18 wells were cultured with PALI. Then on each of the experimental timepoints (day 1, day 3, day 4), a live staining of Hoechst was performed on n = 6 wells from each donor and for each condition. Widefield images acquired at day 4 and included in Figure 4.3B show that cells from both donors reached confluency when cultured in FGM. As compared to cells cultured with FGM, cells from both donors cultured with PALI had a different spatial distribution, leaving empty areas in the cell culture surface. Results of the nuclei count obtained from Hoechst stainings are reported in Figure 4.3C. To obtain the nuclei counts, n = 3 images of each cell-seeded well (n = 6) per condition was acquired, for cells obtained from each of the n = 2 cell donors. From the graphs, it appears that cells related to both donors were more proliferative when cultured in FGM as compared to PALI medium. Additionally, cell culture on DLH did not affect the survival of HLFs when cultured in PALI, as shown in the widefield images in Figure 4.4, in which HLFs obtained from 1 donor seeded on a 96-well plate-format HTS transwell®

recipient plate at a density of 5 x $10^3$ or 10 x $10^3$ cells/well on n = 3 wells per condition appear to be viable at day 7, and to contract the gel at day 10.

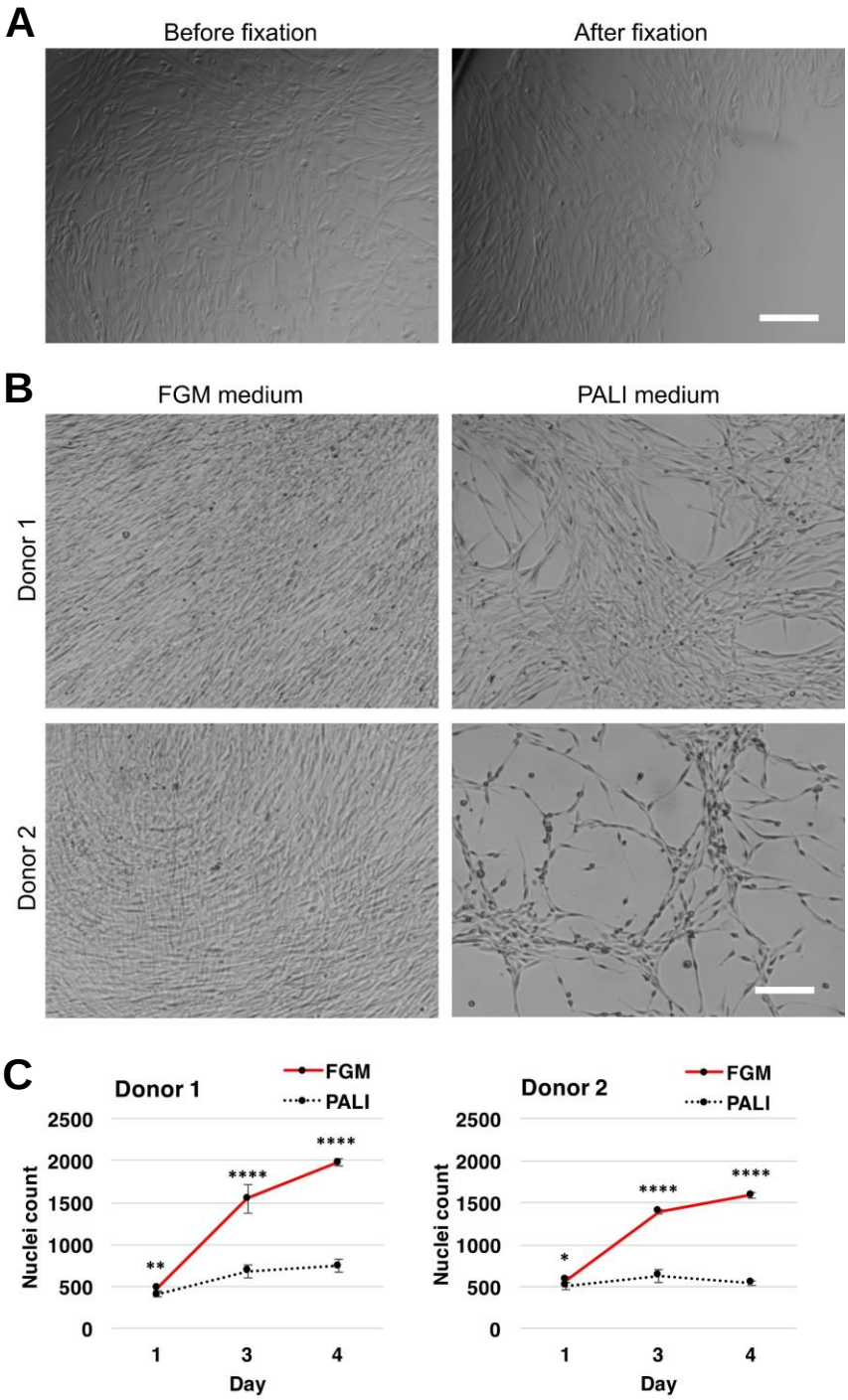


**Figure 4.3.** Fixation and culture of HLFs using different cell culture media. Widefield images of HLFs seeded on wells of 96-well plates and fixed with 4 % PFA were acquired before and after the fixation procedure. Cell-free areas were visible in wells including cells fixed with 4 % PFA. Additionally, HLFs seeded in wells of 96-well plates were cultured for 4 d with FGM or PALI, and HLFs appeared to be viable in both conditions. **A:** representative images of HLFs before fixation with PFA (left) and after fixation (right). An area void of cells is observable in the image on the right, on the right side. Magnification: 5X. Scale bar: 200 µm. **B:** representative widefield images of HLFs obtained from 2 different donors cultured with different cell culture media, acquired at day 4. First row: HLFs from donor 1 cultured in FGM medium (left) and PALI medium (right). Second row: HLFs from donor 2 cultured in FGM medium (left) and PALI medium (right). Magnification: images were acquired at a magnification of 2.5X, and a 2X zoom was then applied post-acquisition. Scale bar: 200 µm. **C:** nuclei count based on images of Hoechst staining of HLFs related to donor 1 (left) and 2 (right) cultured with different cell culture media across different timepoints. X axis: timepoints (days). Y axis: nuclei count per image, expressed as mean ± SEM. Black continuous line: culture in FGM medium. Black dotted line: culture in PALI medium. Welch's t-tests were performed to compare data related to the same timepoints. Donor 1, day 1: $p = 0.0021$. Donor 1, day 3 and 4: $p < 0.0001$. Donor 2, day 1: $p = 0.0103$. Donor 2, day 3 and 4: $p < 0.0001$. The significance of the Welch's t-test is indicated in the graph (* indicates $p < 0.05$, ** indicates $p < 0.01$, **** indicates $p < 0.0001$). N = 10 wells per donor, using cells obtained from 2 donors, for the PFA fixation experiment (Figure A). N = 6 wells per condition, timepoint and cell donor, using cells obtained from n = 2 donors, for the comparison between FGM and PALI (Figure B). Nuclei quantification was obtained from n = 3 representative images from each of the n = 6 wells associated to each condition, timepoint and cell donor, using cells obtained from n = 2 cell donors (Figure C).

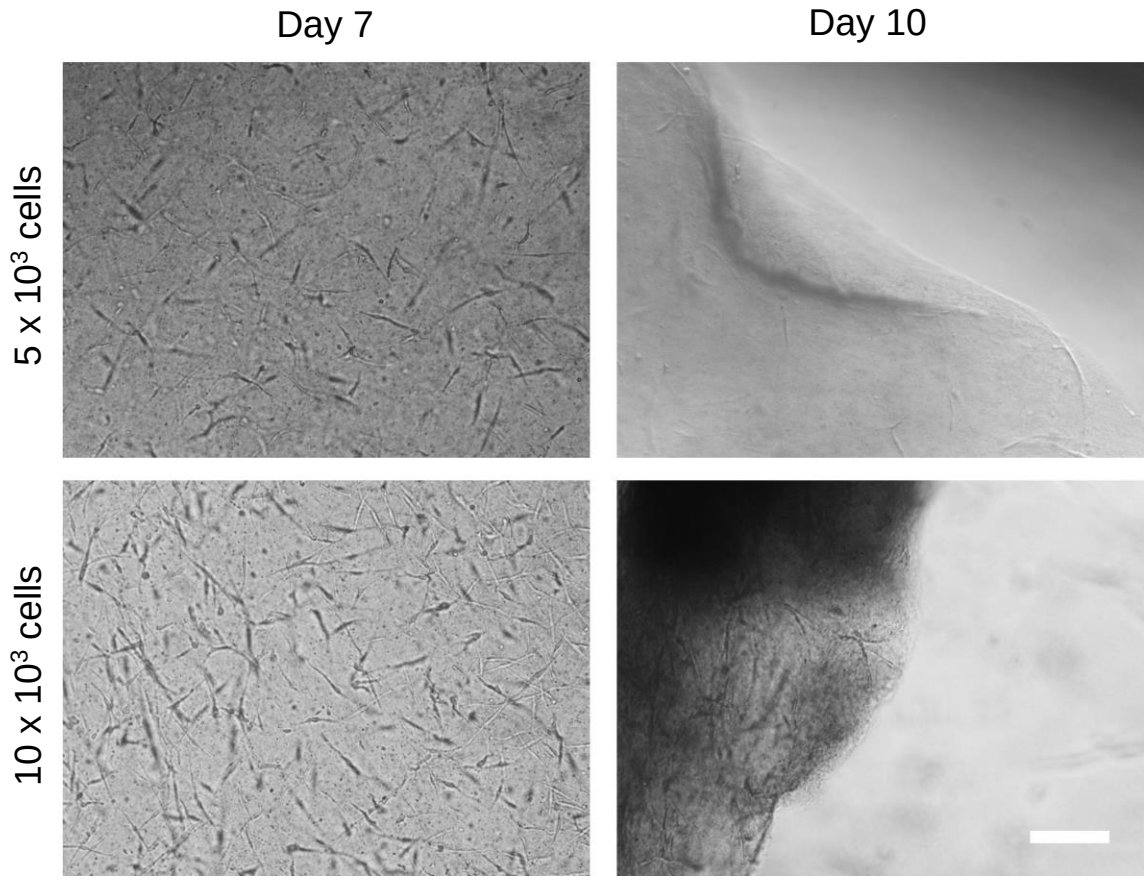


**Figure 4.4.** Representative widefield images of HLFs cultured with PALI cell culture medium on DLH, at different seeding densities. Cell seeding of HLFs was performed at a seeding density of 5 x $10^3$ cells/well or 10 x $10^3$ cells/well in wells of a 96-well plate-format HTS transwell® recipient plate including DLH, and cells were cultured with PALI cell culture medium. Widefield images were acquired throughout the experiment. On day 10, images showed signs of DLH contraction by cells seeded at both of 5 x $10^3$ cells/well and 10 x $10^3$ cells/well seeding densities. First row: 5 x $10^3$ cells/well. Second row: 10 x $10^3$ cells/well. First column: day 7. Second column: day 10. Magnification: 5X. Scale bar: 200 µm. N = 3 wells per condition using cells obtained from n = 1 donor.

### 4.3.3. Co-culture of HBECs and HLFs on HTS transwell® systems including DLH

Once it was established that HLFs can grow on DLH in combination with PALI as cell culture medium, the development of an *in vitro* model based on the combination of HBECs, HLFs, and DLH on 96-well format HTS transwell® systems was tested. In particular, in 3 separate experiments, HBECs obtained from 2 different donors were seeded on the apical wells of 96-well plate-format HTS transwell® plates, whilst HLFs obtained from 2 different donors were seeded in the recipient wells, which included DLH. The 3 experiments are termed Experiment 1, 2, and 3. In all experiments, as controls, DLH-free, HLFs-free, and DLH- and HLFs-

free conditions were also included. Furthermore, in all experiments co-culture was initiated on day 11 after the initiation of ALI culture, when both DHL and HLFs were introduced in the model. The experiments were terminated 28 d after initiating the ALI culture. Experimental details for all the 3 experiments related to the testing of this model can be found in Figure 4.5A, in which each condition associated to Experiment 1 and 2 comprises n = 6 wells, whilst conditions associated to Experiment 3 comprise n = 12 wells, each well including 1 apical and 1 recipient well. At the end of the cell culture phase of the experiments, cells in the apical and recipient wells of the transwell® systems were fixed with PFA. Subsequently, widefield images of the HLFs were acquired. The results related to the HLFs behaviour in the models are displayed in Figure 4.5C, with representative images of HLFs shown in Figure 4.5B. In all experiments, HLFs related to both donors adhered and proliferated in the DHL-free conditions. However, only in Experiment 1 HLFs displayed a fusiform phenotype in conditions including DLH, or alternatively they contracted the gel and were observed in the bottom of the recipient well. Therefore, the HBECs-HLFs-DLH combination was successful only in one experiment. In Experiment 2, HLFs related to one of the donors displayed a fusiform phenotype only in 3 out of 6 wells, whilst cells related to the second donor did not display the fusiform phenotype in any of the wells. Instead, the cells on day 28 post-ALI appeared circular or were not found in the gel. In Experiment 3, HLFs had a circular phenotype, or were not found in the hydrogel at the end of the experiment, in all wells related to conditions including DLH.

**A**

| Experiments 1 and 2 | | | | | | |
|---|---|---|---|---|---|---|
| | **Condition 1 (DLH - )** | **Condition 2 (DLH - )** | **Condition 3 (DLH - )** | **Condition 4 (DLH + )** | **Condition 5 (DLH + )** | **Condition 6 (DLH + )** |
| **Cells in apical well** | HBECs donor 1 | HBECs donor 1 | HBECs donor 1 | HBECs donor 1 | HBECs donor 1 | HBECs donor 1 |
| **Cells in recipient well** | | HLF donor 1 | HLF donor 2 | | HLF donor 1 | HLF donor 2 |
| **Output** | CBF analysis (experiment 2 only) | Widefield images HLF | Widefield images HLF | | Widefield images HLF | Widefield images HLF |
| **Experiment 3** | | | | | | |
| | **Condition 1 (DLH -)** | **Condition 2 (DLH -)** | **Condition 3 (DLH -)** | **Condition 4 (DLH +)** | **Condition 5 (DLH +)** | **Condition 6 (DLH +)** |
| **Cells in apical well** | HBECs donor 1 | HBECs donor 1 | HBECs donor 1 | HBECs donor 1 | HBECs donor 1 | HBECs donor 1 |
| **Cells in recipient well** | | HLF donor 1 | HLF donor 2 | | HLF donor 1 | HLF donor 2 |
| **Output** | Immunostaining (Ac-tub, ZO-1, MUC5-AC) | Widefield images HLF | Widefield images HLF | Immunostaining (Ac-tub, ZO-1, MUC5-AC) | Widefield images HLF | Widefield images HLF |
| | **Condition 7 (DLH - )** | **Condition 8 (DLH - )** | **Condition 9 (DLH - )** | **Condition 10 (DLH +)** | **Condition 11 (DLH +)** | **Condition 12 (DLH +)** |
| **Cells in apical well** | HBECs donor 2 | HBECs donor 2 | HBECs donor 2 | HBECs donor 2 | HBECs donor 2 | HBECs donor 2 |
| **Cells in recipient well** | | HLF donor 1 | HLF donor 2 | | HLF donor 1 | HLF donor 2 |
| **Output** | Immunostaining (Ac-tub, ZO-1, MUC5-AC) | Widefield images HLF | Widefield images HLF | Immunostaining (Ac-tub, ZO-1, MUC5-AC) | Widefield images HLF | Widefield images HLF |

**B**

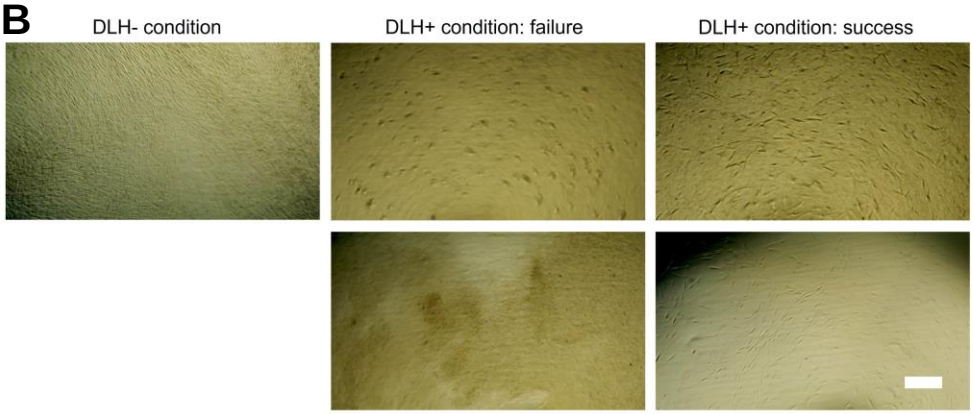


**C**

| | **Seeding outcome in experiment 1** | **Seeding outcome in experiment 2** | **Seeding outcome in experiment 3** |
|---|---|---|---|
| **HLF donor 1 DLH- conditions** | S | S | S |
| **HLF donor 2 DLH- conditions** | S | S | S |
| **HLF donor 1 DLH+ conditions** | S | S in 3 of 6 wells | NS |
| **HLF donor 2 DLH+ conditions** | S | NS | NS |

**Figure 4.5.** Tables and widefield images summarising the planning and the outcomes of the 3 experiments conducted on the HBECs-HLFs-DLH combination. The development of an *in vitro* model based on the use of HBECs, HLFs, and DLH was tested on 96-well plate-format HTS transwell® plates by including HBECs on apical wells and HLFs and DLH on recipient wells. The conditions and outcomes of the experiments are summarised in the tables and widefield images included in this Figure. The "DLH-" acronym indicates the absence of DLH in the system, whilst "DLH+" indicates the presence of DLH in the recipient wells. The seeding of HLFs on DLH was successful only in 3 out of 6 wells in 1 of the 3 experiments, whilst in the other wells of the experiment and in all the wells of other experiments the HLFs either could not be found on hydrogel on day 28, or displayed a circular phenotype. **A:** summary of the conditions included in the 3 experiments conducted on the *in vitro* model based on the combination of HBECs, HLFs, and DLH. **B:** representative images related to HLFs fixed in PFA on day 28 after the initiation of ALI culture. First column: HLFs in DLH- conditions. Second column: HLFs displaying a rounded phenotype in DLH+ conditions (top image), and HLFs absent from the gel (bottom image) in DLH+ conditions. Third column: HLFs displaying a fusiform phenotype in DLH+ conditions (top image), and HLFs displaying a fusiform phenotype on a hydrogel-free area in DLH+ conditions. Magnification: 4X. Scale bar: 250 µm. **C:** summary of results related to HLFs seeding. A successful seeding, marked by "S", was reported if HLFs fixed on day 28 post-ALI displayed confluency or a fusiform phenotype in all experimental wells. An "unsuccessful" seeding, marked by "NS", was reported if HLFs had a rounded phenotype or were not found in all the experimental wells. If the seeding was successful only in a fraction of the wells, the number of successfully seeded wells were reported. N = 6 (experiment 1 and 2) and n = 12 (experiment 3) apical and recipient wells per condition and per cell donor, using cells obtained from n = 2 donors.

It was therefore concluded that the combination of HLFs, HBECs, and DLH on HTS transwell® systems required further optimisation before a reproducible model based on these elements could be successfully set up. The optimisation required to achieve this goal was out of the scope of this work. However, to lay down the foundations of a future development of the model, the decision was made to proceed with the assessment of any paracrine effects of the DLH gel on the mucociliary differentiation of HBECs.

To observe any alteration induced by the DLH on the functionality of cilia, high speed videos of beating cilia were acquired for all wells of all conditions of Experiment 2 on day 28 post-ALI initiation, in 2 areas per well. The CBF in the videos was analysed with the CiliarMove software (319), which had not been used before on HBECs cultured at ALI. Figure 4.6A and 4.6B show respectively a representative frame of the high-speed videos and the heatmap associated with the video, in which different colours are related to different frequencies, measured in Hz. Areas of frequency equal to or higher than 25 Hz, which appear mostly green in Figure 4.6B, were ascribed to experimental noise and therefore were not considered to be associated with beating cilia. Experimental noise is represented below the red dashed line in the histogram reported in Figure 4.6C, which is associated with a high-speed video and depicts the distribution of frequencies as analysed by the software. Upon filtration of experimental noise from the results, the mean CBF associated with the DHL-free and HLF-free control was found to be approximately 4 Hz, as displayed in Figure 4.6D. This value was considered to be too low in comparison to the CBF value of 10 Hz reported in literature in relation to HBECs cultured at ALI with PALI (320). This abnormally low CBF was attributed to technical issues which arose during the acquisition of the high-speed videos. In

particular, cells were physically transported from the cell culture incubator to a laboratory some distance from where the cells were cultured to acquire the videos, and it was considered that the mechanical and thermal stress caused by the transport slowed the CBF to the reported value.

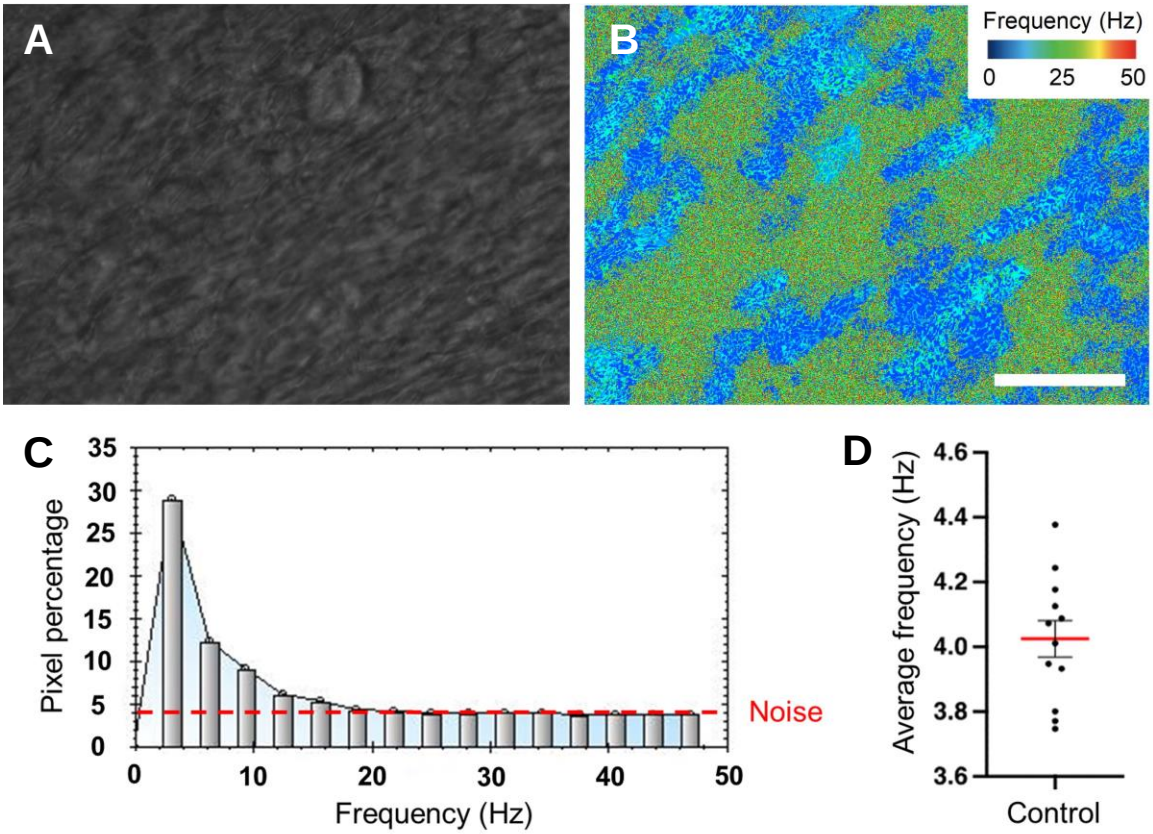


**Figure 4.6.** Use of CiliarMove software for the analysis of CBF of HBECs at day 28 post-ALI initiation in HTS transwell® systems. The CiliarMove software was used for the analysis of CBF of HBECs at day 28 post-ALI initiation in HTS transwell® systems in the second experiment performed on the combined HBECs / HLFs / DLH *in vitro* model. In particular, HBECs were seeded on the apical wells of the transwell® system, whilst the recipient plates were either left without DLH and HLFs, or included DLH, HLFs, or a combination of DLH and HLFs. The average CBF of HBECs included in the DLH-free and HLF-free condition of the experiment was approximately 4 Hz, which was considered to be too low as compared to values reported in literature (310). **A:** representative frame of high-speed video of HBECs cultured in ALI conditions. **B:** heatmap associated by the software to the high-speed video illustrated in A. Each colour in the heatmap is associated with a different frequency found in different regions of the video, as illustrated by the legend on the top-right corner of the image. Areas displaying a frequency equal to or higher than 25 Hz were considered indicative of experimental noise and not associated to ciliated regions. Magnification: 20X. Scale bar: 200 µm. **C:** histogram associated with a representative high-speed video, reporting a range of frequencies (Hz) on the X axis and the pixel percentage associated with a particular frequency in the Y axis. The area of the graph below the red dashed line constitutes experimental noise. **D:** CBF, expressed in Hz, of HBECs related to the hydrogel-free, HLFs-free condition. Each black dot represents the average frequency of 1 high-speed video. The red bar represents the mean frequency calculated for all high-speed videos, and the error bar represents the SEM. N = 2 videos from n = 6 experimental wells using cells obtained from n = 1 donor.

The effect of the DLH on mucociliary differentiation and tight junction formation of HBECs cultured at ALI was also assessed through the immunostaining of HBECs associated with Experiment 3, on day 28 post-ALI initiation. In particular, HBECs included in the DLH-free, HLFs-free control condition and in the DLH-inclusive, HLFs-free condition were stained with antibodies targeting Ac-tub, MUC5-AC, and ZO-1, using Hoechst as a nuclear counterstain. Each condition included n = 12 wells per cell donor, using cells obtained from 2 cell donors. Whilst Ac-tub was used as a marker for ciliation, MUC5-AC was used to assess mucin production and

ZO-1 to assess tight junction formation. The results are shown in Figure 4.7. The use of DLH did not affect the mucociliary differentiation nor the formation of tight junctions, which were visible in both the DHL-free, HLF-free control and in the DHL-inclusive, HLF-free condition.

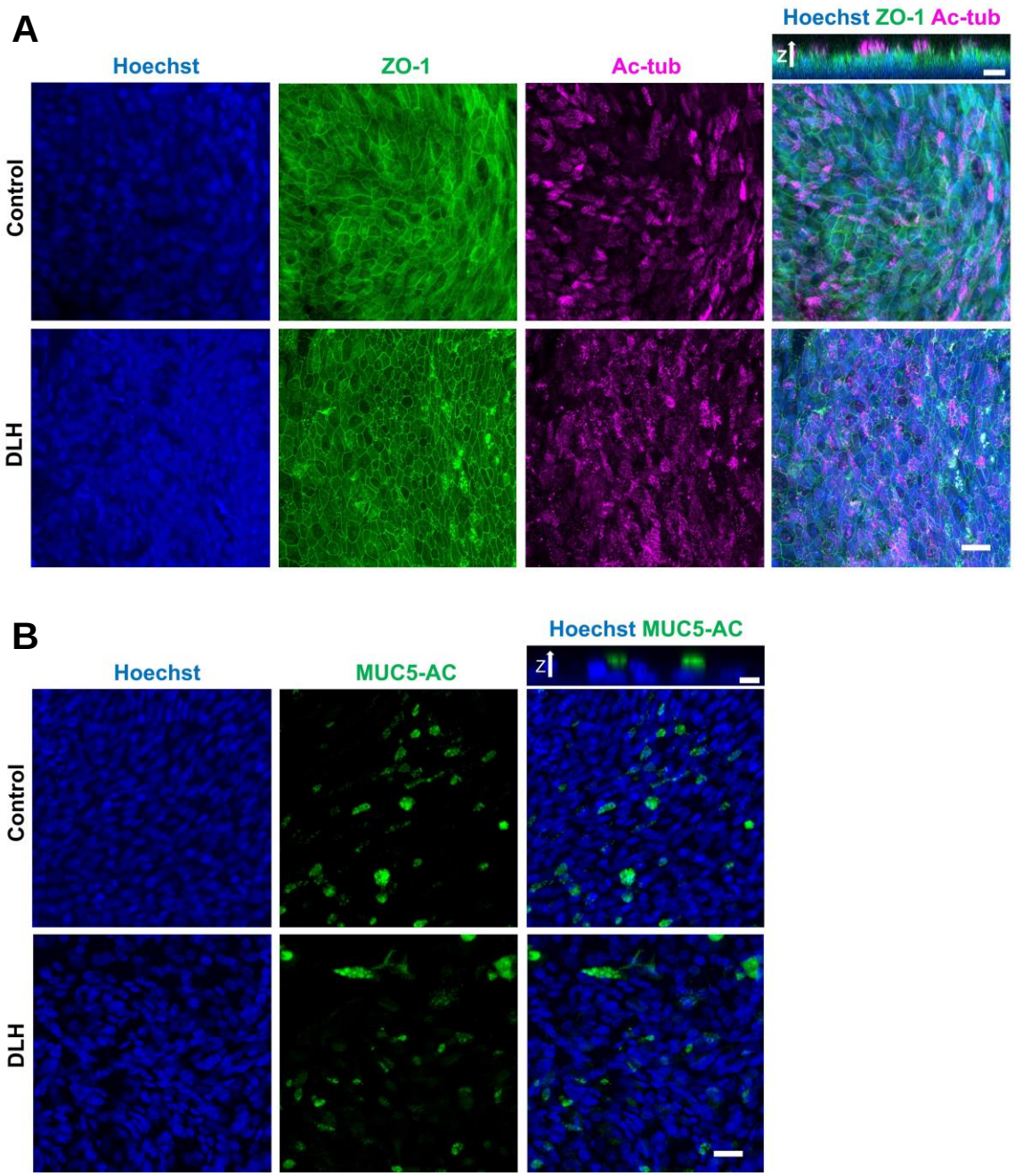


**Figure 4.7.** Representative images of HBECs fixed at day 28 after ALI initiation and stained with Hoechst and MUC5AC, or with Hoechst, Ac-tub and ZO-1. Immunostaining of MUC5AC, Ac-tub and ZO-1 and counterstaining with Hoechst was performed on HBECs on day 28 post-ALI initiation on wells of HTS transwell® systems with or without DLH in recipient wells (conditions 1, 4, 7, 10 of Experiment 3 in Figure 4.3). Images of stained HBECs were then acquired, and representative images are shown. The first row of each image refers to the DLH-free, HLFs-free condition, termed "Control" in the images, whilst second row of each image refers to the DLH-inclusive, HLFs-free condition, termed "DLH" in the images. Each image is a reconstruction obtained from the stacking of different images related to the same ROI acquired at different focal planes along the Z axis. The presence of DLH did not induce any observable changes in the mucociliary differentiation nor in the tight junction formation of HBECs. **A:** from the left to right, HBECs stained with Hoechst (blue), ZO-1 (green), Ac-tub (magenta), and a composite image including an overlay of the different immunostainings. A representative image of the cross section of part of the composite image can be observed on top of the composite image. Magnification: images were acquired at a magnification of 20X, and a 2X post-acquisition zoom was applied on top-down images. Scale bars: 25 µm for top-down images, 10 µm for cross section image. **B:** from left to right, HBECs stained with Hoechst (blue), MUC5-AC (green), and a composite image including an overlay of the different immunostainings. A representative image of the cross section of part of the composite image can be observed on top of the composite image. Magnification: images were acquired at a magnification of 20X, and a 2X post-acquisition zoom was applied on top-down images. Scale bars: 25 µm for top-down images, 10 µm for cross section image. N = 12 wells per condition and per cell donor, using cells obtained from n = 2 donors.

## 4.4. Discussion

In this chapter, HBECs were cultured on 96-well plate-format HTS transwell® systems, which have recently been developed and have been adopted only in a small number studies related to bronchial epithelial cells (263, 264). The reduced dimensions of the recipient wells of HTS transwell® systems, relatively to the commonly used 24- or 12-well plate transwell® format (265-268), made possible the inclusion of DLH in the system whilst maintaining the cost-effectiveness of the model. This strategy can be exploited for the development of other models of the airway or of other epithelialised tissues, such as the intestine.

When seeded on DLH, HLFs were capable of adherence and proliferation, although the results obtained varied. Specifically, whilst in some experiments the seeded cells displayed the spindle-shaped phenotype typically observed in healthy HLFs (269, 270), in other experiments the cells displayed a circular morphology. Additionally, in a number of experiments, HLFs were not found in some seeded hydrogels at late timepoints, indicating that cells were mechanically removed by the fluid flow associated with media changes throughout the experiments. Each experiment was executed on the same gel batch, and therefore the variability in the results obtained was unlikely to be linked to variation in the composition of each gel sample. The inconsistency was also cell donor-independent, as contrasting results were obtained using cells from the same donor in different experiments. This was verified for cells obtained from 2 different donors.

In the study conducted by Pouliot *et al.*, HLFs displayed a spindle-shaped phenotype when seeded on lung ECM hydrogels (211). However, variable results

were obtained in the work conducted by Dabaghi *et al*., (210). In their study, HLFs seeded on lung ECM hydrogels with a protein concentration inferior to 20 mg/mL assumed a spindle-shaped phenotype, whilst cells seeded on hydrogel with a protein concentration of 20 mg/mL displayed a circular morphology similar to the phenotype observed in the present work (210). However, the protein concentration of the DLH was 6 mg/mL. Therefore, the circular morphology observed in the present study is unlikely to be related to the protein concentration in the DLH.

Another explanation for the inconsistency between results related to the seeding of HLFs on DLH could lie in the stress exerted on cells during the steps associated with the cell seeding procedure, particularly in larger experiments, in which the duration of every operation is extended relatively to shorter experiments. An optimisation of the seeding procedure targeted at reducing the duration of experimental steps could therefore increase the reproducibility of the model. Another option could lie in the automatization of the seeding and cell culture procedure. Indeed, epithelial cell culture at ALI in the 96-well format HTS transwell® systems can be automatized, as demonstrated by Bluhmki *et al*., (264).

In the present work, HLFs seeded on DLH did not orient towards a dominant direction, as opposed to the alignment displayed by cells seeded on gel-free surfaces and on collagen I hydrogel. The alignment of HLFs in lung-derived ECM hydrogels has not been analysed in other studies, and the mechanisms underlying the collective orientation of fibroblasts on hydrogels are not yet fully understood. However, according to the model developed by Li *et al*., (323), fibroblasts secrete collagen and align newly formed fibrils, and the orientation of the underlying collagen fibres affects the collective orientation of fibroblasts. Therefore, the results

obtained in the present work could indicate that fibroblasts on DLH do not secrete new collagen fibres or do not orient the underlying ECM network towards a single direction, which could be assessed in future studies through SEM imaging of the DLH fibres after fibroblast seeding. Further studies aiming at increasing our understanding of the mechanisms underlying fibroblasts orientation should take into consideration the results obtained in this work.

The DLH included in recipient wells of transwell® systems did not affect the ciliation of HBECs seeded on the apical wells, as assessed by immunostaining of Ac-tub. A parallel can be drawn with the work of Badylak *et al*., (212), who observed that HBECs cultured on decellularisation-derived porcine tracheal hydrogel are capable of mucociliary differentiation. However, in contrast to their study, in the present work the source of the hydrogel was related to lower portions of the respiratory system, and cells were not in direct contact with the DLH.

The present work also showed that DLH inclusion in transwell® systems does not impede the formation of tight junctions by HBECs. This effect had not previously been verified by other research groups. Therefore, these results suggest that the inclusion of decellularised lung ECM gel in the recipient well of transwell® systems does not affect the mucociliary differentiation and barrier formation of bronchial epithelial cells, at least from a qualitative point of view.

To further assess the paracine effects of the DLH on the phenotype of HBECs in transwell® systems, high speed videos of beating cilia were recorded, with a view to analyse the CBF. Due to technical issues related to the transport of cells and high-speed video acquisition, a comparison between gel-free and gel conditions

was not possible in this work, as the CBF of the gel-free condition was below physiological values. Nonetheless, this work demonstrates that the CBF of HBECs cultured at ALI can be analysed with the recently developed CiliarMove software. This is in contrast to the majority of studies published on CBF analysis, which routinely rely on a different software, CiliaFA, to measure the CBF of HBECs cultured at ALI (272-274). CiliaFA, however, is incompatible with the current versions of FIJI / ImageJ, currently complicating its use by researchers. CiliarMove, prior to the present work, had only been used in 2 studies, which focused on cells that were not cultured at ALI. This work demonstrates the feasibility of CiliarMove as a software of choice for evaluating CBF in ALI cultures of HBECs as an alternative to CiliaFA. Additionally, the heatmaps provided by the software to highlight areas of cilia-associated movement could be used as non-destructive, real-time data to quantify ciliation in ALI cultures.

# Chapter 5

In this chapter, the findings obtained from this work will be contextualised and discussed. The main conclusions will then be outlined and future work will be suggested.

## 5.1. Discussion

The aim of this work was to develop a biomimetic *in vitro* model of human large bronchi. To ensure reproducibility, the model had to be based on commercially available platforms and materials, wherever possible. Additionally, the model had to be compatible with high-throughput applications, and to be capable of replicating aspects of respiratory biology that were not reproduced by routinely adopted *in vitro* models of the airway, such as the inclusion of non-transformed fibroblasts in a 3D culture or the incorporation of respiratory ECM. Four major strategies were tested for the development of the *in vitro* model, and each one had advantages and drawbacks.

The first strategy was based on the use of decellularised porcine bronchial tissue. Porcine tissue is readily available to most research groups, and its use in the past has shown potential for the development of *in vitro* models of the airway (190). Here, it was shown that porcine bronchial tissue can be successfully de-epithelialised following a vacuum-assisted decellularisation protocol. However, a major drawback associated with this approach was related to the poor cell adherence on the scaffolds, which had been observed in other studies related to the use of decellularised tissue (220-222). The results obtained in this work might

have been due to the degradation of the ECM resulting from the decellularisation procedure, particularly in relation to the composition and mechanical properties of the basement membrane, which could have hindered epithelial cell adherence on the scaffolds. These results should therefore be taken in consideration by researchers aiming at developing decellularisation-based models of epithelialized tissue.

A second strategy centred on the seeding of HBECs on a commercial lung ECM hydrogel termed “DLH”. The behaviour of HBECs seeded on different lung ECM hydrogels had been previously been evaluated *in vitro* in a small number of studies (210, 212). In particular, Dabaghi *et al*. showed that HBECs can adhere on a porcine-derived lung ECM hydrogel (210), and Badylak *et al*. showed that HBECs are capable of mucociliary differentiation on a porcine trachea-derived hydrogel (212). However, in spite of these promising results, these materials have not been employed by researchers for the development of bronchial *in vitro* models. One explanation for this could lie in the fact that the ECM hydrogels used in published works are developed in-house by research teams using different protocols. The lack of standardisation in the process of ECM hydrogel development significantly complicates the reproducibility of any *in vitro* model based on such materials. In the present study, in order to facilitate the adoption of the model by other research groups, a commercial DLH was used instead of relying on hydrogels produced in-house. In this work, HBECs adhered to the DLH, which therefore proved to be compatible with epithelial cell culture. However, HBECs displayed a circular phenotype and did not reach confluency. For this reason, the combination of HBECs and DLH was deemed to be unfeasible for the development of a model including a confluent, differentiated epithelial layer.

A third strategy for the development of a bronchial *in vitro* model was centred on the use of microfluidic chips. Recently, a number of microfluidic-based models of the large airways have been developed (241-247). However, as described in the context of ECM hydrogels, most of the studies centred on microfluidic-based models of airway rely on microfluidic chips developed ad-hoc, thus complicating the reproducibility of these models. Commercial microfluidic models of the airway have been developed, but their use by researchers has so far been limited. In the case of current commercial models, issues are likely related to their low throughput. For example, the microfluidic chips developed by Emulate and TissUSE, two of the major commercial entities in the organ-on-a-chip area (313), are not incorporated in plates fit for a high-throughput use. In contrast to other commercial chips, the microfluidics chips developed by Mimetas are incorporated in cell culture plates, and possess a relatively high throughput. For example, the OrganoPlate version 2, which in this work has been termed “OP2”, can include 40 to 64 chips in a single plate. Unlike other commercial microfluidic systems, the chips developed by Mimetas feature in a relatively large number of studies (303-309) and have been adapted to modelling different types of tissue (248-250). These platforms offer flexibility with regards to the combination of cells to be included, and HBECs were seeded with a view to incorporate other cell types once the protocol for seeding and differentiation of HBECs had been established. However, whilst seeding of HBECs in the OP1 and OP2 chip versions was successful, an ALI could not be induced, as cell culture medium could not be removed from the cell-seeded microfluidic channel. To navigate around this issue, inhibition of the NOTCH pathway was attempted as a way to induce mucociliary differentiation in the absence of an ALI, using the protocol developed by Gerovac *et al*., (294). This represented the first time that a mucociliary differentiation protocol based on the

submersion of HBECs was tested for the development of an *in vitro* model. This strategy could considerably simplify the development of microfluidics-based models of the airway, as it would eliminate the need for an ALI. However, HBECs seeded in the chips underwent cell death throughout the mucociliary differentiation protocol. Explanations for this behaviour likely relate to the growing metabolic demands of HBECs during mucociliary differentiation, in combination with the restricted dimensions of the microfluidic channel in which cells were seeded. Further investigation on the metabolism of HBECs during cell culture, and the factors that affect it, would therefore be useful for researchers aiming to develop microfluidics-based model of the airway. Issues were also found in relation to the use of the OrganoGraft plate version of the Mimetas chips, termed “OGP” in this work. In this case, the issue lay with hydrogel loading, and with its contraction by seeded HBECs. Notably, a model of small airways has recently been developed using the OGP as a platform for cell culture (310). This study, in combination with the present work, indicates that the use of OGP can be successful for the development of *in vitro* models of the respiratory tract, if the hydrogel composition and gel loading procedure are optimised. In particular, the hydrogel loaded on the chip should include components of the bronchial basement membrane, such as collagen IV, whilst at the same time it should not be contracted by seeded HBECs. Additionally, the hydrogel loading procedure could be automated, in order to reduce any variability in the outcomes of the loading step.

A fourth strategy devised to develop a biomimetic *in vitro* model of large bronchi was centred on the use of 96-well plate-format HTS transwell® systems, which had recently been developed. The HTS transwell® systems have only been used in a small number of studies focused on the culture of epithelial cells of the airway (263,

264). In this work, HTS transwell® systems were used for the development of a co-culture of HBECs and human lung fibroblasts, termed “HLFs” in this work. Also, for the first time, a lung ECM hydrogel was included in a bronchial epithelium-fibroblasts co-culture model. In particular, HLFs were cultured on a layer of DLH loaded on the recipient well of the HBECs-seeded HTS transwell® systems. The inclusion of DLH in the model was made economically feasible by the relatively small dimensions of the recipient plates of HTS transwell® systems, which can be covered by a small volume of hydrogel compared to the recipient wells of the 24-well plate format. The inclusion of DLH did not have an adverse effect on the mucociliary differentiation of HBECs. In particular, ciliation and mucus secretion were observable in the co-cultures including the DLH. Moreover, the DLH did not affect the formation of tight junctions in cultured HBECs, as evaluated by the immunostaining of ZO-1.

Whilst the DLH did not appear to exert any negative paracrine effects on mucociliary differentiation and barrier formation of HBECs, results related to the seeding of HLFs on the hydrogel were variable. This variability points to the necessity of further optimisation of the model, in order to improve its reproducibility. In particular, cell culture on HTS transwell® systems can be automatized, as demonstrated by Bluhmki *et al*., (264), and multiple batches of DLH could be tested. Although optimisation is needed, the combination of HTS transwell® systems, HBECs, HLFs, and DLH proved to be a promising strategy for the development of a biomimetic bronchial *in vitro* model.

Practical limitations with this work lay in the restricted number of donors used for the development of the *in vitro* model. Restrictions in the cell-donors’ pool were

motivated by considerations tied to the cost-effectiveness of *in vitro* model development. In order to develop a reproducible *in vitro* model, several optimisation experiments need to be carried out, and the costs associated to the purchase of non-transformed cells and the reagents used for their culture are substantial. For example, the cost of a vial of non-transformed HBECs capable of mucociliary differentiation, purchased from LONZA, is £ 1080, and the cost of 500 mL of PALI differentiation medium, purchased from STEMCELL, is more than £ 100. Therefore, the strategy that was followed in this work was a pragmatic compromise, based on the optimisation of the model using cells obtained from a small number of cell donors, with a plan to expand the donor pool for validation experiments to be carried out once the *in vitro* model was optimised. This strategy may benefit other investigators that aim at developing biomimetic *in vitro* models.

## 5.2. Conclusions and future directions

In this work, different strategies for the development of a biomimetic *in vitro* model of large bronchi were tested.

Porcine bronchial tissue was successfully de-epithelialized following a vacuum-assisted decellularisation protocol. However, the adherence of HBECs on the de-epithelialized tissue was scarce. Future work could focus on the modification of the surface of de-epithelialized structure, in order to increase its cytocompatibility. For example, riboflavin-mediated crosslinking could be used to modify the mechanical properties and superficial micro-architecture of the decellularised tissue (311), and coatings of bioactive molecules could facilitate cell adherence post-decellularisation (312).

Microfluidics-based *in vitro* models of the airway rely on the inclusion of an ALI to initiate mucociliary differentiation of HBECs, which can complicate the design of the model from an engineering perspective as compared to other microfluidic constructs. In this work, the differentiation of HBECs in commercial microfluidic chips was attempted by means of NOTCH inhibition instead of relying on an ALI. This strategy could simplify the design of microfluidic chips of the airway. However, this approach was not conducive to mucociliary differentiation in the microfluidic chips that were tested in this study. It was hypothesised that this failure was due to HBECs requiring an amount of nutrients higher than that delivered by the device, due to an increased cell growth rate or to an altered cellular metabolic profile. Future work could centre on the development of microfluidic chips with an optimised geometry, in order to guarantee the survival of HBECs during the differentiation phase. To optimise the geometry of the chips, both computational fluid dynamics modelling of the fluid flow in the chip and *in silico* models of cell metabolism could be combined.

Finally, an *in vitro* model was developed by including a commercial lung ECM hydrogel, DLH, into a 96-well format HTS transwell® system, and by adding HLFs on the hydrogel whilst seeding HBECs on the apical inserts. The inclusion of a lung ECM hydrogel into a high-throughput model had not been tested in other studies. In this work, the seeding of HLFs was only partially successful, as the outcome of HLF seeding was variable. Whilst this work only covered an initial phase of model development, future work should focus on further optimisation of the model, such as further characterization of the HLFs' response to DLH, and the automatization of the cell seeding and culture on the platform. Once the optimisation stage is

completed, commercial lung ECM hydrogel derived from diseased human donors could be included in the model as opposed to the porcine-derived DLH used in this work. For example, the lung ECM hydrogel could be obtained from donors affected by COPD or idiopathic pulmonary fibrosis, in order to develop a high-throughput model capable of mimicking the HBEC-fibroblast-ECM crosstalk in a pathological environment.

A number of observations were made in the course of this work, which could constitute the base of further scientific inquiry. For instance, the proliferation rate of HBECs visibly increased when exposed to the shear stress generated by the fluid flow in the OP2 chips. Whilst the initiation of the flow regimen coincided with the introduction of differentiation medium into the culture system, and although the fluid flow might have contributed to improving the delivery of nutrients to cells, a role of continuous shear stress with regards to the increase in proliferation of HBECs cannot be excluded. Studies have been conducted on the effect of fluid flow on differentiated HBECs (284-285), but the role of fluid flow-associated shear stress during the process of mucociliary differentiation is unclear. According to the literature centred on lung development, from the 10$^{th}$ week of gestation contractions of the foetal diaphragm induce breathing-like movements termed “foetal breathing” (314), which generate a fluid flow along the foetal respiratory tract. The occurrence of foetal breathing precedes the beginning of ciliation in epithelial cells located on the cartilaginous trachea by only 2 weeks (315), a time window which *in vitro* is sufficient for HBECs to develop motile cilia (316). Therefore, shear stress associated with foetal breathing could play a role in the onset of mucociliary differentiation of the tracheobronchial epithelium, and an increase in the proliferation of HBECs stimulated by fluid flow could also be a part

of this mechanism. Further studies on this subject are required to test this hypothesis.

Another observation made in the course of this work is related to the cell behaviour of HBECs on the DLH hydrogel. In particular, HBECs seeded on the hydrogel displayed a circular phenotype and formed cell aggregates. This behaviour could point to a rearrangement of HBECs into bronchial organoids, possibly resulting from the inclusion in an ECM environment resembling the lung parenchyma. Indeed, ECM hydrogels derived from organs such as brain (226) and intestine (303) have shown to support the growth of, respectively, neural and intestinal organoids. Further investigation is required to assess the capacity of DLH to support the growth of bronchial organoids.

# References

1. Murray J, Nadel J, Broaddus V, Mason R, Ernst J, King Jr T et al. Textbook of respiratory medicine. 6th ed. Philadelphia: Saunders; 2016.

2. Barrett K, Barman S, Brooks H, Yuan J. Ganong's review of medical physiology. 26th ed. New York: McGraw Hill Education; 2019.

3. West. J, Luks A. West's Respiratory Physiology: The Essentials. 10th ed. Wolters Kluwer; 2016.

4. Mescher A. Junqueira's Basic Histology: Text and Atlas. 15th ed. McGraw Hill; 2018.

5. Tsartsali L, Hislop A, McKay K, James A, Elliot J, Zhu J et al. Development of the bronchial epithelial reticular basement membrane: relationship to epithelial height and age. Thorax. 2011;66(4):280-285.

6. Zorzi A, de Miranda J. Cartilage repair and regeneration. Intech Open; 2018.

7. Aird W. Endothelial biomedicine. Cambridge: Cambridge University Press; 2007.

8. Mitzner W. Airway smooth muscle: the appendix of the lung. American Journal of Respiratory and Critical Care Medicine. 2004;169(7):787-790.

9. Zuyderduyn S, Sukkar M, Fust A, Dhaliwal S, Burgess J. Treating asthma means treating airway smooth muscle cells. European Respiratory Journal. 2008;32(2):265-274.

10. McAnulty R. Fibroblasts and myofibroblasts: Their source, function and role in disease. The International Journal of Biochemistry & Cell Biology. 2007;39(4):666-671.

11. Grace M, Dubuis E, Birrell M, Belvisi M. Pre-clinical studies in cough research: Role of Transient Receptor Potential (TRP) channels. Pulmonary Pharmacology & Therapeutics. 2013;26(5):498-507.

12. Hewitt R, Lloyd C. Regulation of immune responses by the airway epithelial cell landscape. Nature Reviews Immunology. 2021;21(6):347-362.

13. Crystal R, Randell S, Engelhardt J, Voynow J, Sunday M. Airway Epithelial Cells: Current Concepts and Challenges. Proceedings of the American Thoracic Society. 2008;5(7):772-777.

14. Ruysseveldt E, Martens K, Steelant B. Airway Basal Cells, Protectors of Epithelial Walls in Health and Respiratory Diseases. Frontiers in Allergy. 2021;2.

15. Fahy J, Dickey B. Airway Mucus Function and Dysfunction. New England Journal of Medicine. 2010;363(23):2233-2247.

16. Rogers D. The airway goblet cell. The International Journal of Biochemistry & Cell Biology. 2003;35(1):1-6.

17. Fahy J, Dickey B. Airway Mucus Function and Dysfunction. New England Journal of Medicine. 2010;363(23):2233-2247.

18. Kobayashi Y, Tata P. Pulmonary Neuroendocrine Cells: Sensors and Sentinels of the Lung. Developmental Cell. 2018;45(4):425-426.

19. Montoro D, Haber A, Biton M, Vinarsky V, Lin B, Birket S et al. A revised airway epithelial hierarchy includes CFTR-expressing ionocytes. Nature. 2018;560(7718):319-324.

20. Bordon Y. Neuroendocrine cells regulate lung inflammation. Nature Reviews Immunology. 2016;16(2):77-77.

21. Krasteva G, Canning B, Papadakis T, Kummer W. Cholinergic brush cells in the trachea mediate respiratory responses to quorum sensing molecules. Life Sciences. 2012;91(21-22):992-996.

22. Saunders C, Reynolds S, Finger T. Chemosensory Brush Cells of the Trachea. A Stable Population in a Dynamic Epithelium. American Journal of Respiratory Cell and Molecular Biology. 2013;49(2):190-196.

23. Ferkol T, Schraufnagel D. The Global Burden of Respiratory Disease. Annals of the American Thoracic Society. 2014;11(3):404-406.

24. Vos T, Lim S, Abbafati C, Abbas K, Abbasi M, Abbasifard M et al. Global burden of 369 diseases and injuries in 204 countries and territories, 1990–2019: a systematic analysis for the Global Burden of Disease Study 2019. The Lancet. 2020;396(10258):1204-1222.

25. The top 10 causes of death [Internet]. Who.int. 2022 [cited 14 June 2022]. Available from: https://www.who.int/news-room/fact-sheets/detail/the-top-10-causes-of-death

26. Asthma [Internet]. Who.int. 2022 [cited 14 June 2022]. Available from: https://www.who.int/news-room/fact-sheets/detail/asthma

27. Paget J, Spreeuwenberg P, Charu V, Taylor R, Iuliano A, Bresee J et al. Global mortality associated with seasonal influenza epidemics: New burden estimates and predictors from the GLaMOR Project. Journal of Global Health. 2019;9(2).

28. WHO Coronavirus (COVID-19) Dashboard [Internet]. Covid19.who.int. 2022 [cited 14 June 2022]. Available from: https://covid19.who.int/

29. McKee M, Stuckler D. If the world fails to protect the economy, COVID-19 will damage health not just now but also in the future. Nature Medicine. 2020;26(5):640-642.

30. Abdelghani A, Bouazra H, Hayouni A, Slama S, Garrouche A, Mezghani S et al. Mounier–Kuhn syndrome: A rare cause of bronchial dilatation: A case report. Respiratory Medicine CME. 2009;2(4):164-166.

31. Sharma A, Gnanapandithan K, Sharma K, Sharma S. Relapsing polychondritis: a review. Clinical Rheumatology. 2013;32(11):1575-1583.

32. Kang E. Large Airway Diseases. Journal of Thoracic Imaging. 2011;26(4):249-262.

33. Scannell J, Blanckley A, Boldon H, Warrington B. Diagnosing the decline in pharmaceutical R&D efficiency. Nature Reviews Drug Discovery. 2012;11(3):191-200.

34. Ringel M, Scannell J, Baedeker M, Schulze U. Breaking Eroom's Law. Nature Reviews Drug Discovery. 2020;19(12):833-834.

35. van Haarst A, McGarvey L, Paglialunga S. Review of Drug Development Guidance to Treat Chronic Obstructive Pulmonary Disease: US and EU Perspectives. Clinical Pharmacology & Therapeutics. 2019;106(6):1222-1235.

36. Barnes P, Bonini S, Seeger W, Belvisi M, Ward B, Holmes A. Barriers to new drug development in respiratory disease. European Respiratory Journal. 2015;45(5):1197-1207.

37. Sou T, Bergström C. Contemporary Formulation Development for Inhaled Pharmaceuticals. Journal of Pharmaceutical Sciences. 2021;110(1):66-86.

38. Cazzola M. Moving to a Personalized Approach in Respiratory Medicine. From Academic Research to Regulatory Intervention. Frontiers in Drug Safety and Regulation. 2021;1.

39. Conn P. Sourcebook of Models for Biomedical Research. Humana Press; 2008.

40. Pantelouris E. Absence of Thymus in a Mouse Mutant. Nature. 1968;217(5126):370-371.

41. Suwara M, Green N, Borthwick L, Mann J, Mayer-Barber K, Barron L et al. IL-1α released from damaged epithelial cells is sufficient and essential to trigger inflammatory responses in human lung fibroblasts. Mucosal Immunology. 2013;7(3):684-693.

42. Wilke M, Buijs-Offerman R, Aarbiou J, Colledge W, Sheppard D, Touqui L et al. Mouse models of cystic fibrosis: Phenotypic analysis and research applications. Journal of Cystic Fibrosis. 2011;10:S152-S171.

43. Ghorani V, Boskabady M, Khazdair M, Kianmeher M. Experimental animal models for COPD: a methodological review. Tobacco Induced Diseases. 2017;15(1).

44. Aun M, Bonamichi-Santos R, Arantes-Costa F, Kalil J, Giavina-Bianchi P. Animal models of asthma: utility and limitations. Journal of Asthma and Allergy. 2017;10:293-301.

45. Lyons C, Lovchik J, Hutt J, Lipscomb M, Wang E, Heninger S et al. Murine Model of Pulmonary Anthrax: Kinetics of Dissemination, Histopathology, and Mouse Strain Susceptibility. Infection and Immunity. 2004;72(8):4801-4809.

46. Swearengen J. Choosing the right animal model for infectious disease research. Animal Models and Experimental Medicine. 2018;1(2):100-108.

47. Hardy, Jr. W, Essex M. FeLV-Induced Feline Acquired Immune Deficiency Syndrome. A Model For Human AIDS. Acquired Immunodeficiency Syndrome. 1986;37:353-376.

48. Tsolis R, Kingsley R, Townsend S, Ficht T, Adams L, Bäumler A. Of mice, calves, and men. Comparison of the mouse typhoid model with other Salmonella infections. Advances in experimental medicine and biology. 1999;473:261-274.

49. van Meer P, Graham M, Schuurman H. The safety, efficacy and regulatory triangle in drug development: Impact for animal models and the use of animals. European Journal of Pharmacology. 2015;759:3-13.

50. Tanner L, Single A. Animal Models Reflecting Chronic Obstructive Pulmonary Disease and Related Respiratory Disorders: Translating Pre-Clinical Data into Clinical Relevance. Journal of Innate Immunity. 2019;12(3):203-225.

51. Innes B, Dorin J. Submucosal gland distribution in the mouse has a genetic determination localized on Chromosome 9. Mammalian Genome. 2001;12(2):124-128.

52. Dean C, Snelgrove R. New Rules for Club Development: New Insights into Human Small Airway Epithelial Club Cell Ontogeny and Function. American Journal of Respiratory and Critical Care Medicine. 2018;198(11):1355-1356.

53. Russell W, Burch R. The principles of humane experimental technique. South Mimms, Potters Bar, Herts, England: Universities Federation for Animal Welfare; 1992.

54. Upadhyay S, Palmberg L. Air-Liquid Interface: Relevant In Vitro Models for Investigating Air Pollutant-Induced Pulmonary Toxicity. Toxicological Sciences. 2018;164(1):21-30.

55. Verma A, Singh A. Animal biotechnology. London, United Kingdom ;San Diego, CA, United States: Academic Press, an imprint of Elsevier; 2020.

56. Niu N, Wang L. In vitro human cell line models to predict clinical response to anticancer drugs. Pharmacogenomics. 2015;16(3):273-285.

57. Ben-David U, Siranosian B, Ha G, Tang H, Oren Y, Hinohara K et al. Genetic and transcriptional evolution alters cancer cell line drug response. Nature. 2018;560(7718):325-330.

58. Heijink I, Brandenburg S, Noordhoek J, Postma D, Slebos D, van Oosterhout A. Characterisation of cell adhesion in airway epithelial cell types using electric cell-substrate impedance sensing. European Respiratory Journal. 2009;35(4):894-903.

59. Hiemstra P, Grootaers G, van der Does A, Krul C, Kooter I. Human lung epithelial cell cultures for analysis of inhaled toxicants: Lessons learned and future directions. Toxicology in Vitro. 2018;47:137-146.

60. Ross A, Dailey L, Brighton L, Devlin R. Transcriptional Profiling of Mucociliary Differentiation in Human Airway Epithelial Cells. American Journal of Respiratory Cell and Molecular Biology. 2007;37(2):169-185.

61. Bucchieri F, Puddicombe S, Lordan J, Richter A, Buchanan D, Wilson S et al. Asthmatic Bronchial Epithelium Is More Susceptible to Oxidant-Induced Apoptosis. American Journal of Respiratory Cell and Molecular Biology. 2002;27(2):179-185.

62. Wark P, Johnston S, Bucchieri F, Powell R, Puddicombe S, Laza-Stanca V et al. Asthmatic bronchial epithelial cells have a deficient innate immune response to infection with rhinovirus. Journal of Experimental Medicine. 2005;201(6):937-947.

63. Devalia J, Bayram H, Abdelaziz M, Sapsford R, Davies R. Differences between Cytokine Release from Bronchial Epithelial Cells of Asthmatic Patients and Non–Asthmatic Subjects: Effect of Exposure to Diesel Exhaust Particles. International Archives of Allergy and Immunology. 1999;118(2-4):437-439.

64. Schulz C, Wolf K, Harth M, Krätzel K, Kunz-Schughart L, Pfeifer M. Expression and Release of Interleukin-8 by Human Bronchial Epithelial Cells from Patients with Chronic Obstructive Pulmonary Disease, Smokers, and Never-Smokers. Respiration. 2003;70(3):254-261.

65. Amatngalim G, Schrumpf J, Henic A, Dronkers E, Verhoosel R, Ordonez S et al. Antibacterial Defense of Human Airway Epithelial Cells from Chronic Obstructive Pulmonary Disease Patients Induced by Acute Exposure to Nontypeable Haemophilus influenzae: Modulation by Cigarette Smoke. Journal of Innate Immunity. 2017;9(4):359-374.

66. Gray T, Guzman K, Davis C, Abdullah L, Nettesheim P. Mucociliary differentiation of serially passaged normal human tracheobronchial epithelial cells. American Journal of Respiratory Cell and Molecular Biology. 1996;14(1):104-112.

67. Butler C, Hynds R, Gowers K, Lee D, Brown J, Crowley C et al. Rapid Expansion of Human Epithelial Stem Cells Suitable for Airway Tissue Engineering. American Journal of Respiratory and Critical Care Medicine. 2016;194(2):156-168.

68. Suprynowicz F, Upadhyay G, Krawczyk E, Kramer S, Hebert J, Liu X et al. Conditionally reprogrammed cells represent a stem-like state of adult epithelial cells. Proceedings of the National Academy of Sciences. 2012;109(49):20035-20040.

69. Mou H, Vinarsky V, Tata P, Brazauskas K, Choi S, Crooke A et al. Dual SMAD Signaling Inhibition Enables Long-Term Expansion of Diverse Epithelial Basal Cells. Cell Stem Cell. 2016;19(2):217-231.

70. Walters M, Gomi K, Ashbridge B, Moore M, Arbelaez V, Heldrich J et al. Generation of a human airway epithelium derived basal cell line with multipotent differentiation capacity. Respiratory Research. 2013;14(1).

71. Huang S, Islam M, O'Neill J, Hu Z, Yang Y, Chen Y et al. Efficient generation of lung and airway epithelial cells from human pluripotent stem cells. Nature Biotechnology. 2013;32(1):84-91.

72. Mertens T, Karmouty-Quintana H, Taube C, Hiemstra P. Use of airway epithelial cell culture to unravel the pathogenesis and study treatment in obstructive airway diseases. Pulmonary Pharmacology & Therapeutics. 2017;45:101-113.

73. Cao X, Coyle J, Xiong R, Wang Y, Heflich R, Ren B et al. Invited review: human air-liquid-interface organotypic airway tissue models derived from primary tracheobronchial epithelial cells—overview and perspectives. In Vitro Cellular & Developmental Biology - Animal. 2020;57(2):104-132.

74. Whitcutt M, Adler K, Wu R. A biphasic chamber system for maintaining polarity of differentiation of culture respiratory tract epithelial cells. In Vitro Cellular & Developmental Biology. 1988;24(5):420-428.

75. de Jong P, van Sterkenburg M, Hesseling S, Kempenaar J, Mulder A, Mommaas A et al. Ciliogenesis in human bronchial epithelial cells cultured at the air-liquid interface. American Journal of Respiratory Cell and Molecular Biology. 1994;10(3):271-277.

76. Loret T, Peyret E, Dubreuil M, Aguerre-Chariol O, Bressot C, le Bihan O et al. Air-liquid interface exposure to aerosols of poorly soluble nanomaterials induces different biological activation levels compared to exposure to suspensions. Particle and Fibre Toxicology. 2016;13(1).

77. Wawrzyniak P, Wawrzyniak M, Wanke K, Sokolowska M, Bendelja K, Rückert B et al. Regulation of bronchial epithelial barrier integrity by type 2 cytokines and histone deacetylases in asthmatic patients. Journal of Allergy and Clinical Immunology. 2017;139(1):93-103.

78. Hardyman M, Wilkinson E, Martin E, Jayasekera N, Blume C, Swindle E et al. TNF-α–mediated bronchial barrier disruption and regulation by src-family kinase activation. Journal of Allergy and Clinical Immunology. 2013;132(3):665-675.e8.

79. Paw M, Wnuk D, Jakieła B, Bochenek G, Sładek K, Madeja Z et al. Responsiveness of human bronchial fibroblasts and epithelial cells from asthmatic and non-asthmatic donors to the transforming growth factor-β1 in epithelial-mesenchymal trophic unit model. BMC Molecular and Cell Biology. 2021;22(1).

80. Yonker L, Mou H, Chu K, Pazos M, Leung H, Cui D et al. Development of a Primary Human Co-Culture Model of Inflamed Airway Mucosa. Scientific Reports. 2017;7(1).

81. He R, Braakhuis H, Vandebriel R, Staal Y, Gremmer E, Fokkens P et al. Optimization of an air-liquid interface in vitro cell co-culture model to estimate the hazard of aerosol exposures. Journal of Aerosol Science. 2021;153:105703.

82. Frantz C, Stewart K, Weaver V. The extracellular matrix at a glance. Journal of Cell Science. 2010;123(24):4195-4200.

83. Coppolino M, Dedhar S. Bi-directional signal transduction by integrin receptors. The International Journal of Biochemistry & Cell Biology. 2000;32(2):171-188.

84. Aruffo A, Stamenkovic I, Melnick M, Underhill C, Seed B. CD44 is the principal cell surface receptor for hyaluronate. Cell. 1990;61(7):1303-1313.

85. Hardwick C, Hoare K, Owens R, Hohn H, Hook M, Moore D et al. Molecular cloning of a novel hyaluronan receptor that mediates tumor cell motility. Journal of Cell Biology. 1992;117(6):1343-1350.

86. Xian X, Gopal S, Couchman J. Syndecans as receptors and organizers of the extracellular matrix. Cell and Tissue Research. 2009;339(1):31-46.

87. Ferri N, Carragher N, Raines E. Role of Discoidin Domain Receptors 1 and 2 in Human Smooth Muscle Cell-Mediated Collagen Remodeling. The American Journal of Pathology. 2004;164(5):1575-1585.

88. Meyaard L. The inhibitory collagen receptor LAIR-1 (CD305). Journal of Leukocyte Biology. 2008;83(4):799-803.

89. Elango J, Hou C, Bao B, Wang S, Maté Sánchez de Val J, Wenhui W. The Molecular Interaction of Collagen with Cell Receptors for Biological Function. Polymers. 2022;14(5):876.

90. Alberts B, Johnson A, Lewis J, Raff M, Roberts K, Walter P. Molecular biology of the cell. 4th ed. New York: Garland Science; 2002.

91. Teoh C, Tan S, Tran T. Integrins as Therapeutic Targets for Respiratory Diseases. Current Molecular Medicine. 2015;15(8):714-734.

92. Mezu-Ndubuisi O, Maheshwari A. The role of integrins in inflammation and angiogenesis. Pediatric Research. 2020;89(7):1619-1626.

93. Schwartz M, Assoian R. Integrins and cell proliferation: regulation of cyclin-dependent kinases via cytoplasmic signaling pathways. Journal of Cell Science. 2001;114(14):2553-2560.

94. Hood J, Cheresh D. Role of integrins in cell invasion and migration. Nature Reviews Cancer. 2002;2(2):91-100.

95. Gilmore A, Metcalfe A, Romer L, Streuli C. Integrin-Mediated Survival Signals Regulate the Apoptotic Function of Bax through Its Conformation and Subcellular Localization. Journal of Cell Biology. 2000;149(2):431-446.

96. Vitillo L, Kimber S. Integrin and FAK Regulation of Human Pluripotent Stem Cells. Current Stem Cell Reports. 2017;3(4):358-365.

97. SHEPPARD D. Functions of Pulmonary Epithelial Integrins: From Development to Disease. Physiological Reviews. 2003;83(3):673-686.

98. Weinacker A, Ferrando R, Elliott M, Hogg J, Balmes J, Sheppard D. Distribution of integrins alpha v beta 6 and alpha 9 beta 1 and their known ligands, fibronectin and tenascin, in human airways. American Journal of Respiratory Cell and Molecular Biology. 1995;12(5):547-556.

99. Martino F, Perestrelo A, Vinarský V, Pagliari S, Forte G. Cellular Mechanotransduction: From Tension to Function. Frontiers in Physiology. 2018;9.

100. Luo J, Walker M, Xiao Y, Donnelly H, Dalby M, Salmeron-Sanchez M. The influence of nanotopography on cell behaviour through interactions with the extracellular matrix – A review. Bioactive Materials. 2022;15:145-159.

101. Baumgart F. Stiffness — an unknown world of mechanical science?. Injury. 2000;31:14-84.

102. Gere J. Mechanics of materials. 6th ed. Thomson Brooks/Cole; 2004.

103. Lekka M, Gnanachandran K, Kubiak A, Zieliński T, Zemła J. Traction force microscopy – Measuring the forces exerted by cells. Micron. 2021;150:103138.

104. García J, García A. Sensing rigidity. Nature Materials. 2014;13(6):539-540.

105. Martino F, Perestrelo A, Vinarský V, Pagliari S, Forte G. Cellular Mechanotransduction: From Tension to Function. Frontiers in Physiology. 2018;9.

106. Yeh Y, Hur S, Chang J, Wang K, Chiu J, Li Y et al. Matrix Stiffness Regulates Endothelial Cell Proliferation through Septin 9. PLoS ONE. 2012;7(10):e46889.

107. Razinia Z, Castagnino P, Xu T, Vázquez-Salgado A, Puré E, Assoian R. Stiffness-dependent motility and proliferation uncoupled by deletion of CD44. Scientific Reports. 2017;7(1).

108. Saha K, Keung A, Irwin E, Li Y, Little L, Schaffer D et al. Substrate Modulus Directs Neural Stem Cell Behavior. Biophysical Journal. 2008;95(9):4426-4438.

109. Qiu Y, Bayomy A, Gomez M, Bauer M, Du P, Yang Y et al. A role for matrix stiffness in the regulation of cardiac side population cell function. American Journal of Physiology-Heart and Circulatory Physiology. 2015;308(9):H990-H997.

110. Shkumatov A, Thompson M, Choi K, Sicard D, Baek K, Kim D et al. Matrix stiffness-modulated proliferation and secretory function of the airway smooth muscle cells. American Journal of Physiology-Lung Cellular and Molecular Physiology. 2015;308(11):L1125-L1135.

111. Shi Y, Dong Y, Duan Y, Jiang X, Chen C, Deng L. Substrate stiffness influences TGF-β1-induced differentiation of bronchial fibroblasts into myofibroblasts in airway remodeling. Molecular Medicine Reports. 2012;7(2):419-424.

112. Moore M, Herzog E. Regulation and Relevance of Myofibroblast Responses in Idiopathic Pulmonary Fibrosis. Current Pathobiology Reports. 2013;1(3):199-208.

113. Asano S, Ito S, Takahashi K, Furuya K, Kondo M, Sokabe M et al. Matrix stiffness regulates migration of human lung fibroblasts. Physiological Reports. 2017;5(9):e13281.

114. Balestrini J, Chaudhry S, Sarrazy V, Koehler A, Hinz B. The mechanical memory of lung myofibroblasts. Integrative Biology. 2012;4(4):410.

115. Chandrasekaran A, Kouthouridis S, Lee W, Lin N, Ma Z, Turner M et al. Magnetic microboats for floating, stiffness tunable, air–liquid interface epithelial cultures. Lab on a Chip. 2019;19(17):2786-2798.

116. Brunetti V, Maiorano G, Rizzello L, Sorce B, Sabella S, Cingolani R et al. Neurons sense nanoscale roughness with nanometer sensitivity. Proceedings of the National Academy of Sciences. 2010;107(14):6264-6269.

117. Yang Y, Wang K, Gu X, Leong K. Biophysical Regulation of Cell Behavior—Cross Talk between Substrate Stiffness and Nanotopography. Engineering. 2017;3(1):36-54.

118. Abagnale G, Steger M, Nguyen V, Hersch N, Sechi A, Joussen S et al. Surface topography enhances differentiation of mesenchymal stem cells towards osteogenic and adipogenic lineages. Biomaterials. 2015;61:316-326.

119. Wang K, Bruce A, Mezan R, Kadiyala A, Wang L, Dawson J et al. Nanotopographical Modulation of Cell Function through Nuclear Deformation. ACS Applied Materials & Interfaces. 2016;8(8):5082-5092.

120. Jin Y, Liu L, Yu P, Lin F, Shi X, Guo J et al. Emergent Differential Organization of Airway Smooth Muscle Cells on Concave and Convex Tubular Surface. Frontiers in Molecular Biosciences. 2021;8.

121. Soleas J, Waddell T, McGuigan A. Topographically grooved gel inserts for aligning epithelial cells during air–liquid-interface culture. Biomaterials Science. 2015;3(1):121-133.

122. Wang J, Li B. Mechanics rules cell biology. BMC Sports Science, Medicine and Rehabilitation. 2010;2(1).

123. Vining K, Mooney D. Mechanical forces direct stem cell behaviour in development and regeneration. Nature Reviews Molecular Cell Biology. 2017;18(12):728-742.

124. Sul B, Wallqvist A, Morris M, Reifman J, Rakesh V. A computational study of the respiratory airflow characteristics in normal and obstructed human airways. Computers in Biology and Medicine. 2014;52:130-143.

125. Sethi K, Cram E, Zaidel-Bar R. Stretch-induced actomyosin contraction in epithelial tubes: Mechanotransduction pathways for tubular homeostasis. Seminars in Cell & Developmental Biology. 2017;71:146-152.

126. Lin J, Chen Y, Wu C, Hsieh C, Pei D, Liang Y et al. Identification of Normal Blood Pressure in Different Age Group. Medicine (Baltimore). 2016;95(14):e3188.

127. Lee S, Lueck C. Cerebrospinal Fluid Pressure in Adults. Journal of Neuro-Ophthalmology. 2014;34(3):278-283.

128. Button B, Boucher R. Role of mechanical stress in regulating airway surface hydration and mucus clearance rates. Respiratory Physiology & Neurobiology. 2008;163(1-3):189-201.

129. Liu C, Li Q, Zhou X, Kolosov V, Perelman J. Cortactin mediates elevated shear stress-induced mucin hypersecretion via actin polymerization in human airway epithelial cells. The International Journal of Biochemistry & Cell Biology. 2013;45(12):2756-2763.

130. Even-Tzur Davidovich N, Kloog Y, Wolf M, Elad D. Mechanophysical Stimulations of Mucin Secretion in Cultures of Nasal Epithelial Cells. Biophysical Journal. 2011;100(12):2855-2864.

131. Tarran R, Button B, Picher M, Paradiso A, Ribeiro C, Lazarowski E et al. Normal and Cystic Fibrosis Airway Surface Liquid Homeostasis. The effect of phasic shear stress and viral infections. Journal of Biological Chemistry. 2005;280(42):35751-35759.

132. Winters S, Davis C, Boucher R. Mechanosensitivity of mouse tracheal ciliary beat frequency: roles for $Ca^{2+}$, purinergic signaling, tonicity, and viscosity. American Journal of Physiology-Lung Cellular and Molecular Physiology. 2007;292(3):L614-L624.

133. Sidhaye V, Schweitzer K, Caterina M, Shimoda L, King L. Shear stress regulates aquaporin-5 and airway epithelial barrier function. Proceedings of the National Academy of Sciences. 2008;105(9):3345-3350.

134. Neishabouri A, Soltani Khaboushan A, Daghigh F, Kajbafzadeh A, Majidi Zolbin M. Decellularization in Tissue Engineering and Regenerative Medicine: Evaluation, Modification, and Application Methods. Frontiers in Bioengineering and Biotechnology. 2022;10.

135. Parmaksiz M, Dogan A, Odabas S, Elçin A, Elçin Y. Clinical applications of decellularized extracellular matrices for tissue engineering and regenerative medicine. Biomedical Materials. 2016;11(2):022003.

136. McCrary M, Bousalis D, Mobini S, Song Y, Schmidt C. Decellularized tissues as platforms for in vitro modeling of healthy and diseased tissues. Acta Biomaterialia. 2020;111:1-19.

137. Porzionato A, Stocco E, Barbon S, Grandi F, Macchi V, De Caro R. Tissue-Engineered Grafts from Human Decellularized Extracellular Matrices: A Systematic Review and Future Perspectives. International Journal of Molecular Sciences. 2018;19(12):4117.

138. Wainwright D, Bury S. Acellular Dermal Matrix in the Management of the Burn Patient. Aesthetic Surgery Journal. 2011;31(7 Supplement):13S-23S.

139. Lin C, Hsia K, Ma H, Lee H, Lu J. In Vivo Performance of Decellularized Vascular Grafts: A Review Article. International Journal of Molecular Sciences. 2018;19(7):2101.

140. Petersen T, Calle E, Zhao L, Lee E, Gui L, Raredon M et al. Tissue-Engineered Lungs for in Vivo Implantation. Science. 2010;329(5991):538-541.

141. Remlinger N, Wearden P, Gilbert T. Procedure for Decellularization of Porcine Heart by Retrograde Coronary Perfusion. Journal of Visualized Experiments. 2012;(70).

142. Granato A, da Cruz E, Rodrigues-Junior D, Mosini A, Ulrich H, Rodrigues B et al. A novel decellularization method to produce brain scaffolds. Tissue and Cell. 2020;67:101412.

143. Piccoli M, Trevisan C, Maghin E, Franzin C, Pozzobon M. Mouse Skeletal Muscle Decellularization. Methods in Molecular Biology. 2017;:87-93.

144. Belviso I, Romano V, Sacco A, Ricci G, Massai D, Cammarota M et al. Decellularized Human Dermal Matrix as a Biological Scaffold for Cardiac Repair and Regeneration. Frontiers in Bioengineering and Biotechnology. 2020;8.

145. Mazza G, Rombouts K, Rennie Hall A, Urbani L, Vinh Luong T, Al-Akkad W et al. Decellularized human liver as a natural 3D-scaffold for liver bioengineering and transplantation. Scientific Reports. 2015;5(1).

146. Skolasinski S, Panoskaltsis-Mortari A. Decellularization of Intact Lung Tissue Through Vasculature and Airways Using Negative and Positive Pressure. Methods in Molecular Biology. 2017;:307-315.

147. Alshaikh A, Padma A, Dehlin M, Akouri R, Song M, Brännström M et al. Decellularization of the mouse ovary: comparison of different scaffold generation

protocols for future ovarian bioengineering. Journal of Ovarian Research. 2019;12(1).

148. Pan M, Hu P, Cheng Y, Cai L, Rao X, Wang Y et al. An efficient method for decellularization of the rat liver. Journal of the Formosan Medical Association. 2014;113(10):680-687.

149. Hong P, Bezuhly M, Graham M, Gratzer P. Efficient decellularization of rabbit trachea to generate a tissue engineering scaffold biomatrix. International Journal of Pediatric Otorhinolaryngology. 2018;112:67-74.

150. Magden G, Vural C, Bayrak B, Ozdogan C, Kenar H. Composite sponges from sheep decellularized small intestinal submucosa for treatment of diabetic wounds. Journal of Biomaterials Applications. 2020;36(1):113-127.

151. Sullivan D, Mirmalek-Sani S, Deegan D, Baptista P, Aboushwareb T, Atala A et al. Decellularization methods of porcine kidneys for whole organ engineering using a high-throughput system. Biomaterials. 2012;33(31):7756-7764.

152. Gerli M, Guyette J, Evangelista-Leite D, Ghoshhajra B, Ott H. Perfusion decellularization of a human limb: A novel platform for composite tissue engineering and reconstructive surgery. PLOS ONE. 2018;13(1):e0191497.

153. Rabbani M, Zakian N, Alimoradi N. Contribution of physical methods in decellularization of animal tissues. Journal of Medical Signals & Sensors. 2021;11(1):1.

154. Gilpin A, Yang Y. Decellularization Strategies for Regenerative Medicine: From Processing Techniques to Applications. BioMed Research International. 2017;2017:1-13.

155. Nazari M, Kurdi M, Heerklotz H. Classifying Surfactants with Respect to Their Effect on Lipid Membrane Order. Biophysical Journal. 2012;102(3):498-506.

156. Maghsoudlou P, Totonelli G, Loukogeorgakis S, Eaton S, De Coppi P. A Decellularization Methodology for the Production of a Natural Acellular Intestinal Matrix. Journal of Visualized Experiments. 2013;(80).

157. Alizadeh M, Rezakhani L, Soleimannejad M, Sharifi E, Anjomshoa M, Alizadeh A. Evaluation of vacuum washing in the removal of SDS from decellularized bovine pericardium: method and device description. Heliyon. 2019;5(8):e02253.

158. Schmitt A, Csiki R, Tron A, Saldamli B, Tübel J, Florian K et al. Optimized protocol for whole organ decellularization. European Journal of Medical Research. 2017;22(1).

159. McCrary M, Vaughn N, Hlavac N, Song Y, Wachs R, Schmidt C. Novel Sodium Deoxycholate-Based Chemical Decellularization Method for Peripheral Nerve. Tissue Engineering Part C: Methods. 2020;26(1):23-36.

160. Balestrini J, Gard A, Liu A, Leiby K, Schwan J, Kunkemoeller B et al. Production of decellularized porcine lung scaffolds for use in tissue engineering. Integrative Biology. 2015;7(12):1598-1610.

161. Petersen T, Calle E, Colehour M, Niklason L. Matrix Composition and Mechanics of Decellularized Lung Scaffolds. Cells Tissues Organs. 2012;195(3):222-231.

162. Kim J, Koh Y, Kim J, Seo D. Development of a decellularization method to produce nerve allografts using less invasive detergents and hyper/hypotonic solutions. Journal of Plastic, Reconstructive & Aesthetic Surgery. 2016;69(12):1690-1696.

163. Yamanaka H, Morimoto N, Yamaoka T. Decellularization of submillimeter-diameter vascular scaffolds using peracetic acid. Journal of Artificial Organs. 2020;23(2):156-162.

164. Sengyoku H, Tsuchiya T, Obata T, Doi R, Hashimoto Y, Ishii M et al. Sodium hydroxide based non-detergent decellularizing solution for rat lung. Organogenesis. 2018;14(2):94-106.

165. Montoya C, McFetridge P. Preparation of *Ex Vivo*–Based Biomaterials Using Convective Flow Decellularization. Tissue Engineering Part C: Methods. 2009;15(2):191-200.

166. Lumpkins S, Pierre N, McFetridge P. A mechanical evaluation of three decellularization methods in the design of a xenogeneic scaffold for tissue engineering the temporomandibular joint disc. Acta Biomaterialia. 2008;4(4):808-816.

167. Deeken C, White A, Bachman S, Ramshaw B, Cleveland D, Loy T et al. Method of preparing a decellularized porcine tendon using tributyl phosphate. Journal of Biomedical Materials Research Part B: Applied Biomaterials. 2010;96B(2):199-206.

168. Cornelison R, Wellman S, Park J, Porvasnik S, Song Y, Wachs R et al. Development of an apoptosis-assisted decellularization method for maximal preservation of nerve tissue structure: apoptosis-assisted decellularization for maximal nerve tissue preservation. Acta Biomaterialia. 2018;77:116-126.

169. Rahman S, Griffin M, Naik A, Szarko M, Butler P. Optimising the decellularization of human elastic cartilage with trypsin for future use in ear reconstruction. Scientific Reports. 2018;8(1).

170. Prasertsung I, Kanokpanont S, Bunaprasert T, Thanakit V, Damrongsakkul S. Development of acellular dermis from porcine skin using periodic pressurized technique. Journal of Biomedical Materials Research Part B: Applied Biomaterials. 2008;85B(1):210-219.

171. Wang Z, Sun F, Lu Y, Zhang B, Zhang G, Shi H. Rapid Preparation Method for Preparing Tracheal Decellularized Scaffolds: Vacuum Assistance and Optimization of DNase I. ACS Omega. 2021;6(16):10637-10644.

172. Crapo P, Gilbert T, Badylak S. An overview of tissue and whole organ decellularization processes. Biomaterials. 2011;32(12):3233-3243.

173. Phillips M, Maor E, Rubinsky B. Nonthermal Irreversible Electroporation for Tissue Decellularization. Journal of Biomechanical Engineering. 2010;132(9).

174. Funamoto S, Nam K, Kimura T, Murakoshi A, Hashimoto Y, Niwaya K et al. The use of high-hydrostatic pressure treatment to decellularize blood vessels. Biomaterials. 2010;31(13):3590-3595.

175. Taylor D, Sampaio L, Ferdous Z, Gobin A, Taite L. Decellularized matrices in regenerative medicine. Acta Biomaterialia. 2018;74:74-89.

176. McCrary M, Bousalis D, Mobini S, Song Y, Schmidt C. Decellularized tissues as platforms for in vitro modeling of healthy and diseased tissues. Acta Biomaterialia. 2020;111:1-19.

177. Lu T, Lin B, Kim J, Sullivan M, Tobita K, Salama G et al. Repopulation of decellularized mouse heart with human induced pluripotent stem cell-derived cardiovascular progenitor cells. Nature Communications. 2013;4(1).

178. Fedecostante M, Westphal K, Buono M, Sanchez Romero N, Wilmer M, Kerkering J et al. Recellularized Native Kidney Scaffolds as a Novel Tool in Nephrotoxicity Screening. Drug Metabolism and Disposition. 2018;46(9):1338-1350.

179. Wen X, Huan H, Wang X, Chen X, Wu L, Zhang Y et al. Sympathetic neurotransmitters promote the process of recellularization in decellularized liver matrix via activating the IL-6/Stat3 pathway. Biomedical Materials. 2016;11(6):065007.

180. Wassenaar J, Boss G, Christman K. Decellularized skeletal muscle as an in vitro model for studying drug-extracellular matrix interactions. Biomaterials. 2015;64:108-114.

181. Ojeh N, Navsaria H. An in vitro skin model to study the effect of mesenchymal stem cells in wound healing and epidermal regeneration. Journal of Biomedical Materials Research Part A. 2013;102(8):2785-2792.

182. Sood D, Chwalek K, Stuntz E, Pouli D, Du C, Tang-Schomer M et al. Fetal Brain Extracellular Matrix Boosts Neuronal Network Formation in 3D Bioengineered Model of Cortical Brain Tissue. ACS Biomaterials Science & Engineering. 2015;2(1):131-140.

183. Chen H, Wei Z, Sun J, Bhattacharya A, Savage D, Serda R et al. A recellularized human colon model identifies cancer driver genes. Nature Biotechnology. 2016;34(8):845-851.

184. Mishra D, Thrall M, Baird B, Ott H, Blackmon S, Kurie J et al. Human Lung Cancer Cells Grown on Acellular Rat Lung Matrix Create Perfusable Tumor Nodules. The Annals of Thoracic Surgery. 2012;93(4):1075-1081.

185. Mishra D, Sakamoto J, Thrall M, Baird B, Blackmon S, Ferrari M et al. Human Lung Cancer Cells Grown in an Ex Vivo 3D Lung Model Produce Matrix Metalloproteinases Not Produced in 2D Culture. PLoS ONE. 2012;7(9):e45308.

186. Booth A, Hadley R, Cornett A, Dreffs A, Matthes S, Tsui J et al. Acellular Normal and Fibrotic Human Lung Matrices as a Culture System for *In Vitro* Investigation. American Journal of Respiratory and Critical Care Medicine. 2012;186(9):866-876.

187. Thanapirom K, Caon E, Papatheodoridi M, Frenguelli L, Al-Akkad W, Zhenzhen Z et al. Optimization and Validation of a Novel Three-Dimensional Co-

Culture System in Decellularized Human Liver Scaffold for the Study of Liver Fibrosis and Cancer. Cancers. 2021;13(19):4936.

188. Fu H, Tian Y, Zhou L, Zhou D, Tan R, Stolz D et al. Tenascin-C Is a Major Component of the Fibrogenic Niche in Kidney Fibrosis. Journal of the American Society of Nephrology. 2016;28(3):785-801.

189. Sensi F, D'Angelo E, Piccoli M, Pavan P, Mastrotto F, Caliceti P et al. Recellularized Colorectal Cancer Patient-Derived Scaffolds as In Vitro Pre-Clinical 3D Model for Drug Screening. Cancers. 2020;12(3):681.

190. Melo E, Kasper J, Unger R, Farré R, Kirkpatrick C. Development of a Bronchial Wall Model: Triple Culture on a Decellularized Porcine Trachea. Tissue Engineering Part C: Methods. 2015;21(9):909-921.

191. Hedström U, Hallgren O, Öberg L, DeMicco A, Vaarala O, Westergren-Thorsson G et al. Bronchial extracellular matrix from COPD patients induces altered gene expression in repopulated primary human bronchial epithelial cells. Scientific Reports. 2018;8(1).

192. Hedström U, Öberg L, Vaarala O, Dellgren G, Silverborn M, Bjermer L et al. Impaired Differentiation of Chronic Obstructive Pulmonary Disease Bronchial Epithelial Cells Grown on Bronchial Scaffolds. American Journal of Respiratory Cell and Molecular Biology. 2021;65(2):201-213.

193. Chirila T, Harkin D. Biomaterials and Regenerative Medicine in Ophthalmology. 2nd ed. Woodhead publishing series in Biomaterials; 2016.

194. Catoira M, Fusaro L, Di Francesco D, Ramella M, Boccafoschi F. Overview of natural hydrogels for regenerative medicine applications. Journal of Materials Science: Materials in Medicine. 2019;30(10).

195. Appel E, Loh X, Jones S, Biedermann F, Dreiss C, Scherman O. Ultrahigh-Water-Content Supramolecular Hydrogels Exhibiting Multistimuli Responsiveness. Journal of the American Chemical Society. 2012;134(28):11767-11773.

196. Unal A, West J. Synthetic ECM: Bioactive Synthetic Hydrogels for 3D Tissue Engineering. Bioconjugate Chemistry. 2020;31(10):2253-2271.

197. Lau H, Kiick K. Opportunities for Multicomponent Hybrid Hydrogels in Biomedical Applications. Biomacromolecules. 2014;16(1):28-42.

198. Li X, Sun Q, Li Q, Kawazoe N, Chen G. Functional Hydrogels With Tunable Structures and Properties for Tissue Engineering Applications. Frontiers in Chemistry. 2018;6.

199. Zhao Z, Vizetto-Duarte C, Moay Z, Setyawati M, Rakshit M, Kathawala M et al. Composite Hydrogels in Three-Dimensional in vitro Models. Frontiers in Bioengineering and Biotechnology. 2020;8.

200. Jensen C, Teng Y. Is It Time to Start Transitioning From 2D to 3D Cell Culture?. Frontiers in Molecular Biosciences. 2020;7.

201. Smithmyer M, Sawicki L, Kloxin A. Hydrogel scaffolds as *in vitro* models to study fibroblast activation in wound healing and disease. Biomater Sci. 2014;2(5):634-650.

202. Narkhede A, Crenshaw J, Crossman D, Shevde L, Rao S. An in vitro hyaluronic acid hydrogel based platform to model dormancy in brain metastatic breast cancer cells. Acta Biomaterialia. 2020;107:65-77.

203. Zhang W, Du A, Liu S, Lv M, Chen S. Research progress in decellularized extracellular matrix-derived hydrogels. Regenerative Therapy. 2021;18:88-96.

204. Saldin L, Cramer M, Velankar S, White L, Badylak S. Extracellular matrix hydrogels from decellularized tissues: Structure and function. Acta Biomaterialia. 2017;49:1-15.

205. Fernández-Pérez J, Ahearne M. The impact of decellularization methods on extracellular matrix derived hydrogels. Scientific Reports. 2019;9(1).

206. Saheli M, Sepantafar M, Pournasr B, Farzaneh Z, Vosough M, Piryaei A et al. Three-dimensional liver-derived extracellular matrix hydrogel promotes liver organoids function. Journal of Cellular Biochemistry. 2018;119(6):4320-4333.

207. Chaimov D, Baruch L, Krishtul S, Meivar-levy I, Ferber S, Machluf M. Innovative encapsulation platform based on pancreatic extracellular matrix achieve substantial insulin delivery. Journal of Controlled Release. 2017;257:91-101.

208. Nagao R, Xu J, Luo P, Xue J, Wang Y, Kotha S et al. Decellularized Human Kidney Cortex Hydrogels Enhance Kidney Microvascular Endothelial Cell Maturation and Quiescence. Tissue Engineering Part A. 2016;22(19-20):1140-1150.

209. Paduano F, Marrelli M, White L, Shakesheff K, Tatullo M. Odontogenic Differentiation of Human Dental Pulp Stem Cells on Hydrogel Scaffolds Derived from Decellularized Bone Extracellular Matrix and Collagen Type I. PLOS ONE. 2016;11(2):e0148225.

210. Dabaghi M, Saraei N, Carpio M, Nanduri V, Ungureanu J, Babi M et al. A Robust Protocol for Decellularized Human Lung Bioink Generation Amenable to 2D and 3D Lung Cell Culture. Cells. 2021;10(6):1538.

211. Pouliot R, Young B, Link P, Park H, Kahn A, Shankar K et al. Porcine Lung-Derived Extracellular Matrix Hydrogel Properties Are Dependent on Pepsin Digestion Time. Tissue Engineering Part C: Methods. 2020;26(6):332-346.

212. Ravindra A, D'Angelo W, Zhang L, Reing J, Johnson S, Myerburg M et al. Human Bronchial Epithelial Cell Growth on Homologous Versus Heterologous Tissue Extracellular Matrix. Journal of Surgical Research. 2021;263:215-223.

213. Morishima Y, Nomura A, Uchida Y, Noguchi Y, Sakamoto T, Ishii Y et al. Triggering the Induction of Myofibroblast and Fibrogenesis by Airway Epithelial Shedding. American Journal of Respiratory Cell and Molecular Biology. 2001;24(1):1-11.

214. Rüdiger D, Kick K, Goychuk A, Vollmar A, Frey E, Zahler S. Cell-Based Strain Remodeling of a Nonfibrous Matrix as an Organizing Principle for Vasculogenesis. Cell Reports. 2020;32(6):108015.

215. Zuo Q, Mogol A, Liu Y, Santaliz Casiano A, Chien C, Drnevich J et al. Targeting Metabolic Adaptations in the Breast Cancer–Liver Metastatic Niche Using Dietary Approaches to Improve Endocrine Therapy Efficacy. Molecular Cancer Research. 2022;20(6):923-937.

216. Kleinman H, Kim K, Kang H. Matrigel uses in cell biology and for the identification of thymosin β4, a mediator of tissue regeneration. Applied Biological Chemistry. 2018;61(6):703-708.

217. Benton G, Arnaoutova I, George J, Kleinman H, Koblinski J. Matrigel: From discovery and ECM mimicry to assays and models for cancer research. Advanced Drug Delivery Reviews. 2014;79-80:3-18.

218. Passaniti A, Kleinman H, Martin G. Matrigel: history/background, uses, and future applications. Journal of Cell Communication and Signaling. 2021;.

219. Brown B, Valentin J, Stewart-Akers A, McCabe G, Badylak S. Macrophage phenotype and remodeling outcomes in response to biologic scaffolds with and without a cellular component. Biomaterials. 2009;30(8):1482-1491.

220. Haykal S, Salna M, Zhou Y, Marcus P, Fatehi M, Frost G et al. Double-Chamber Rotating Bioreactor for Dynamic Perfusion Cell Seeding of Large-Segment Tracheal Allografts: Comparison to Conventional Static Methods. Tissue Engineering Part C: Methods. 2014;20(8):681-692.

221. Conconi M, Coppi P, Liddo R, Vigolo S, Zanon G, Parnigotto P et al. Tracheal matrices, obtained by a detergent-enzymatic method, support in vitro the adhesion of chondrocytes and tracheal epithelial cells. Transplant International. 2005;18(6):727-734.

222. Butler C, Hynds R, Crowley C, Gowers K, Partington L, Hamilton N et al. Vacuum-assisted decellularization: an accelerated protocol to generate tissue-engineered human tracheal scaffolds. Biomaterials. 2017;124:95-105.

223. Lee H, Marin-Araujo A, Aoki F, Haykal S, Waddell T, Amon C et al. Computational fluid dynamics for enhanced tracheal bioreactor design and long-segment graft recellularization. Scientific Reports. 2021;11(1).

224. de Hilster R, Sharma P, Jonker M, White E, Gercama E, Roobeek M et al. Human lung extracellular matrix hydrogels resemble the stiffness and viscoelasticity of native lung tissue. American Journal of Physiology-Lung Cellular and Molecular Physiology. 2020;318(4):L698-L704.

225. Pouliot R, Link P, Mikhaiel N, Schneck M, Valentine M, Kamga Gninzeko F et al. Development and characterization of a naturally derived lung extracellular matrix hydrogel. Journal of Biomedical Materials Research Part A. 2016;104(8):1922-1935.

226. Giobbe G, Crowley C, Luni C, Campinoti S, Khedr M, Kretzschmar K et al. Extracellular matrix hydrogel derived from decellularized tissues enables endodermal organoid culture. Nature Communications. 2019;10(1).

227. Martinez-Garcia F, de Hilster R, Sharma P, Borghuis T, Hylkema M, Burgess J et al. Architecture and Composition Dictate Viscoelastic Properties of Organ-Derived Extracellular Matrix Hydrogels. Polymers. 2021;13(18):3113.

228. Valencia L, Canalejas-Tejero V, Clemente M, Fernaud I, Holgado M, Jorcano J et al. A new microfluidic method enabling the generation of multi-layered tissues-on-chips using skin cells as a proof of concept. Scientific Reports. 2021;11(1).

229. Wevers N, Kasi D, Gray T, Wilschut K, Smith B, van Vught R et al. A perfused human blood–brain barrier on-a-chip for high-throughput assessment of barrier function and antibody transport. Fluids and Barriers of the CNS. 2018;15(1).

230. Saldin L, Cramer M, Velankar S, White L, Badylak S. Extracellular matrix hydrogels from decellularized tissues: Structure and function. Acta Biomaterialia. 2017;49:1-15.

231. Kim D, Wu X, Young A, Haynes C. Microfluidics-Based in Vivo Mimetic Systems for the Study of Cellular Biology. Accounts of Chemical Research. 2014;47(4):1165-1173.

232. Rapp. B. Microfluidics: Modelling, Mechanics and Mathematics. Elsevier; 2017.

233. Pham P, Goel P, Kumar S, Yadav K. 21st Century Surface Science. IntechOpen; 2020.

234. Bhatia S, Ingber D. Microfluidic organs-on-chips. Nature Biotechnology. 2014;32(8):760-772.

235. Hassan S, Sebastian S, Maharjan S, Lesha A, Carpenter A, Liu X et al. Liver-on-a-Chip Models of Fatty Liver Disease. Hepatology. 2020;71(2):733-740.

236. Xiang Y, Wen H, Yu Y, Li M, Fu X, Huang S. Gut-on-chip: Recreating human intestine in vitro. Journal of Tissue Engineering. 2020;11:204173142096531.

237. Ashammakhi N, Wesseling-Perry K, Hasan A, Elkhammas E, Zhang Y. Kidney-on-a-chip: untapped opportunities. Kidney International. 2018;94(6):1073-1086.

238. Zhang Q, Sito L, Mao M, He J, Zhang Y, Zhao X. Current advances in skin-on-a-chip models for drug testing. Microphysiological Systems. 2018;1:1-1.

239. Shrestha J, Razavi Bazaz S, Aboulkheyr Es H, Yaghobian Azari D, Thierry B, Ebrahimi Warkiani M et al. Lung-on-a-chip: the future of respiratory disease models and pharmacological studies. Critical Reviews in Biotechnology. 2020;40(2):213-230.

240. Huh D, Matthews B, Mammoto A, Montoya-Zavala M, Hsin H, Ingber D. Reconstituting Organ-Level Lung Functions on a Chip. Science. 2010;328(5986):1662-1668.

241. Humayun M, Chow C, Young E. Microfluidic lung airway-on-a-chip with arrayable suspended gels for studying epithelial and smooth muscle cell interactions. Lab on a Chip. 2018;18(9):1298-1309.

242. Si L, Bai H, Rodas M, Cao W, Oh C, Jiang A et al. A human-airway-on-a-chip for the rapid identification of candidate antiviral therapeutics and prophylactics. Nature Biomedical Engineering. 2021;5(8):815-829.

243. Liu Z, Mackay S, Gordon D, Anderson J, Haithcock D, Garson C et al. Co-cultured microfluidic model of the airway optimized for microscopy and micro-optical coherence tomography imaging. Biomedical Optics Express. 2019;10(10):5414.

244. Humayun M, Chow C, Young E. Microfluidic lung airway-on-a-chip with arrayable suspended gels for studying epithelial and smooth muscle cell interactions. Lab on a Chip. 2018;18(9):1298-1309.

245. Park J, Ryu H, Lee B, Ha D, Ahn M, Kim S et al. Development of a functional airway-on-a-chip by 3D cell printing. Biofabrication. 2018;11(1):015002.

246. Sellgren K, Butala E, Gilmour B, Randell S, Grego S. A biomimetic multicellular model of the airways using primary human cells. Lab Chip. 2014;14(17):3349-3358.

247. Barkal L, Procknow C, Álvarez-García Y, Niu M, Jiménez-Torres J, Brockman-Schneider R et al. Microbial volatile communication in human organotypic lung models. Nature Communications. 2017;8(1).

248. Gijzen L, Yousef Yengej F, Schutgens F, Vormann M, Ammerlaan C, Nicolas A et al. Culture and analysis of kidney tubuloids and perfused tubuloid cells-on-a-chip. Nature Protocols. 2021;16(4):2023-2050.

249. Wevers N, Kasi D, Gray T, Wilschut K, Smith B, van Vught R et al. A perfused human blood–brain barrier on-a-chip for high-throughput assessment of barrier function and antibody transport. Fluids and Barriers of the CNS. 2018;15(1).

250. Beaurivage C, Kanapeckaite A, Loomans C, Erdmann K, Stallen J, Janssen R. Development of a human primary gut-on-a-chip to model inflammatory processes. Scientific Reports. 2020;10(1).

251. Evans M, Van Winkle L, Fanucchi M, Plopper C. The Attenuated Fibroblast Sheath of the Respiratory Tract Epithelial–Mesenchymal Trophic Unit. American Journal of Respiratory Cell and Molecular Biology. 1999;21(6):655-657.

252. Plopper C, Smiley-Jewell S, Miller L, Fanucchi M, Evans M, Buckpitt A et al. Asthma/Allergic Airways Disease: Does Postnatal Exposure to Environmental Toxicants Promote Airway Pathobiology?. Toxicologic Pathology. 2007;35(1):97-110.

253. Holgate S, Arshad H, Roberts G, Howarth P, Thurner P, Davies D. A new look at the pathogenesis of asthma. Clinical Science. 2009;118(7):439-450.

254. Behzad A, McDonough J, Seyednejad N, Hogg J, Walker D. The Disruption of the Epithelial Mesenchymal Trophic Unit in COPD. COPD: Journal of Chronic Obstructive Pulmonary Disease. 2009;6(6):421-431.

255. Osei E, Booth S, Hackett T. What Have In Vitro Co-Culture Models Taught Us about the Contribution of Epithelial-Mesenchymal Interactions to Airway Inflammation and Remodeling in Asthma?. Cells. 2020;9(7):1694.

256. Nishioka M, Venkatesan N, Dessalle K, Mogas A, Kyoh S, Lin T et al. Fibroblast-epithelial cell interactions drive epithelial-mesenchymal transition differently in cells from normal and COPD patients. Respiratory Research. 2015;16(1).

257. Sidhu S, Yuan S, Innes A, Kerr S, Woodruff P, Hou L et al. Roles of epithelial cell-derived periostin in TGF-β activation, collagen production, and collagen gel elasticity in asthma. Proceedings of the National Academy of Sciences. 2010;107(32):14170-14175.

258. Pohl C, Hermanns M, Uboldi C, Bock M, Fuchs S, Dei-Anang J et al. Barrier functions and paracellular integrity in human cell culture models of the proximal respiratory unit. European Journal of Pharmaceutics and Biopharmaceutics. 2009;72(2):339-349.

259. Abs V, Bonicelli J, Kacza J, Zizzadoro C, Abraham G. Equine bronchial fibroblasts enhance proliferation and differentiation of primary equine bronchial epithelial cells co-cultured under air-liquid interface. PLOS ONE. 2019;14(11):e0225025.

260. Ishikawa S, Ishimori K, Ito S. A 3D epithelial–mesenchymal co-culture model of human bronchial tissue recapitulates multiple features of airway tissue remodeling by TGF-β1 treatment. Respiratory Research. 2017;18(1).

261. Bucchieri F, Pitruzzella A, Fucarino A, Gammazza A, Bavisotto C, Marcianò V et al. Functional characterization of a novel 3D model of the epithelial-mesenchymal trophic unit. Experimental Lung Research. 2017;43(2):82-92.

262. Tan Q, Choi K, Sicard D, Tschumperlin D. Human airway organoid engineering as a step toward lung regeneration and disease modeling. Biomaterials. 2017;113:118-132.

263. Lee D, Cardinale D, Nigro E, Butler C, Rutman A, Fassad M et al. Higher throughput drug screening for rare respiratory diseases: readthrough therapy in primaryet ciliary dyskinesia. European Respiratory Journal. 2021;58(4):2000455.

264. Bluhmki T, Bitzer S, Gindele J, Schruf E, Kiechle T, Webster M et al. Development of a miniaturized 96-Transwell air–liquid interface human small airway epithelial model. Scientific Reports. 2020;10(1).

265. Peters-Hall J, Coquelin M, Torres M, LaRanger R, Alabi B, Sho S et al. Long-term culture and cloning of primary human bronchial basal cells that maintain multipotent differentiation capacity and CFTR channel function. American Journal of Physiology-Lung Cellular and Molecular Physiology. 2018;315(2):L313-L327.

266. Leung C, Wadsworth S, Yang S, Dorscheid D. Structural and functional variations in human bronchial epithelial cells cultured in air-liquid interface using different growth media. American Journal of Physiology-Lung Cellular and Molecular Physiology. 2020;318(5):L1063-L1073.

267. Rayner R, Makena P, Prasad G, Cormet-Boyaka E. Optimization of Normal Human Bronchial Epithelial (NHBE) Cell 3D Cultures for in vitro Lung Model Studies. Scientific Reports. 2019;9(1).

268. Jackson N, Everman J, Chioccioli M, Feriani L, Goldfarbmuren K, Sajuthi S et al. Single-Cell and Population Transcriptomics Reveal Pan-epithelial Remodeling in Type 2-High Asthma. Cell Reports. 2020;32(1):107872.

269. Gao Y, Xu X, Ding K, Liang Y, Jiang D, Dai H. Rapamycin Inhibits Transforming Growth Factor β1-Induced Fibrogenesis in Primary Human Lung Fibroblasts. Yonsei Medical Journal. 2013;54(2):437.

270. Phan S. Biology of Fibroblasts and Myofibroblasts. Proceedings of the American Thoracic Society. 2008;5(3):334-337.

271. Wang W, Pearson A, Kutys M, Choi C, Wozniak M, Baker B et al. Extracellular matrix alignment dictates the organization of focal adhesions and directs uniaxial cell migration. APL Bioengineering. 2018;2(4):046107.

272. Ancel J, Belgacemi R, Diabasana Z, Perotin J, Bonnomet A, Dewolf M et al. Impaired Ciliary Beat Frequency and Ciliogenesis Alteration during Airway Epithelial Cell Differentiation in COPD. Diagnostics. 2021;11(9):1579.

273. Tchao R. Epithelial cell interaction in air-liquid interface culture. In Vitro Cellular & Developmental Biology. 1989;25(5):460-465.

274. Hamilton N, Lee D, Gowers K, Butler C, Maughan E, Jevans B et al. Bioengineered airway epithelial grafts with mucociliary function based on collagen IV- and laminin-containing extracellular matrix scaffolds. European Respiratory Journal. 2020;55(6):1901200.

275. Balestrini J, Gard A, Gerhold K, Wilcox E, Liu A, Schwan J et al. Comparative biology of decellularized lung matrix: Implications of species mismatch in regenerative medicine. Biomaterials. 2016;102:220-230.

276. Vormann M, Vriend J, Lanz H, Gijzen L, van den Heuvel A, Hutter S et al. Implementation of a Human Renal Proximal Tubule on a Chip for Nephrotoxicity and Drug Interaction Studies. Journal of Pharmaceutical Sciences. 2021;110(4):1601-1614.

277. Nicolas A, Schavemaker F, Kosim K, Kurek D, Haarmans M, Bulst M et al. High throughput transepithelial electrical resistance (TEER) measurements on perfused membrane-free epithelia. Lab on a Chip. 2021;21(9):1676-1685.

278. Petrosyan A, Cravedi P, Villani V, Angeletti A, Manrique J, Renieri A et al. A glomerulus-on-a-chip to recapitulate the human glomerular filtration barrier. Nature Communications. 2019;10(1).

279. Kosim K, Schilt I, Lanz H, Vulto P, Kurek D. Intestinal Epithelium Tubules on a Chip. Methods in Molecular Biology. 2021;:87-105.

280. Trietsch B, Naumovska E, Kurek D, Saleh A, Lanz H, Joore J et al. Membrane-free culture and real-time barrier integrity assessment of perfused intestinal epithelium tubes. Drug Metabolism and Pharmacokinetics. 2018;33(1):S45-S46.

281. Gijzen L, Marescotti D, Raineri E, Nicolas A, Lanz H, Guerrera D et al. An Intestine-on-a-Chip Model of Plug-and-Play Modularity to Study Inflammatory Processes. SLAS Technology. 2020;25(6):585-597.

282. Naumovska E, Aalderink G, Wong Valencia C, Kosim K, Nicolas A, Brown S et al. Direct On-Chip Differentiation of Intestinal Tubules from Induced Pluripotent Stem Cells. International Journal of Molecular Sciences. 2020;21(14):4964.

283. Balcells M, Suárez M, Vázquez M, Edelman E. Cells in fluidic environments are sensitive to flow frequency. Journal of Cellular Physiology. 2005;204(1):329-335.

284. Zhu Y, Abdullah L, Doyle S, Nguyen K, Ribeiro C, Vasquez P et al. Baseline Goblet Cell Mucin Secretion in the Airways Exceeds Stimulated Secretion over Extended Time Periods, and Is Sensitive to Shear Stress and Intracellular Mucin Stores. PLOS ONE. 2015;10(5):e0127267.

285. Sidhaye V, Schweitzer K, Caterina M, Shimoda L, King L. Shear stress regulates aquaporin-5 and airway epithelial barrier function. Proceedings of the National Academy of Sciences. 2008;105(9):3345-3350.

286. Baker E, Baines D. Airway Glucose Homeostasis: A New Target in the Prevention and Treatment of Pulmonary Infection. Chest. 2018;153(2):507-514.

287. Baker E, Clark N, Brennan A, Fisher D, Gyi K, Hodson M et al. Hyperglycemia and cystic fibrosis alter respiratory fluid glucose concentrations estimated by breath condensate analysis. Journal of Applied Physiology. 2007;102(5):1969-1975.

288. Indicator Metadata Registry Details [Internet]. Who.int. 2022 [cited 15 June 2022].

Available from: https://www.who.int/data/gho/indicator-metadata-registry/imr-details/2380#:~:text=The%20expected%20values%20for%20normal,and%20monitoring%20glycemia%20are%20recommended.

289. Mallia P, Webber J, Gill S, Trujillo-Torralbo M, Calderazzo M, Finney L et al. Role of airway glucose in bacterial infections in patients with chronic obstructive pulmonary disease. Journal of Allergy and Clinical Immunology. 2018;142(3):815-823.e6.

290. Bearham J, Garnett J, Schroeder V, Biggart M, Baines D. Effective glucose metabolism maintains low intracellular glucose in airway epithelial cells after exposure to hyperglycemia. American Journal of Physiology-Cell Physiology. 2019;317(5):C983-C992.

291. Mavin E, Verdon B, Carrie S, Saint-Criq V, Powell J, Kuttruff C et al. Real-time measurement of cellular bioenergetics in fully differentiated human nasal epithelial cells grown at air-liquid-interface. American Journal of Physiology-Lung Cellular and Molecular Physiology. 2020;318(6):L1158-L1164.

292. Bovard D, Sandoz A, Luettich K, Frentzel S, Iskandar A, Marescotti D et al. A lung/liver-on-a-chip platform for acute and chronic toxicity studies. Lab on a Chip. 2018;18(24):3814-3829.

293. Morgan R, Manfredi C, Easley K, Watkins L, Hunt W, Goudy S et al. A medium composition containing normal resting glucose that supports differentiation of primary human airway cells. Scientific Reports. 2022;12(1).

294. Gerovac B, Valencia M, Baumlin N, Salathe M, Conner G, Fregien N. Submersion and Hypoxia Inhibit Ciliated Cell Differentiation in a Notch-Dependent Manner. American Journal of Respiratory Cell and Molecular Biology. 2014;51(4):516-525.

295. Kadota T, Fujita Y, Araya J, Ochiya T, Kuwano K. Extracellular vesicle-mediated cellular crosstalk in lung repair, remodelling and regeneration. European Respiratory Review. 2022;31(163):210106.

296. Chuo S, Chien J, Lai C. Imaging extracellular vesicles: current and emerging methods. Journal of Biomedical Science. 2018;25(1).

297. Pastor L, Vera E, Marin J, Sanz-Rubio D. Extracellular Vesicles from Airway Secretions: New Insights in Lung Diseases. International Journal of Molecular Sciences. 2021;22(2):583.

298. Kadota T, Fujita Y, Araya J, Watanabe N, Fujimoto S, Kawamoto H et al. Human bronchial epithelial cell-derived extracellular vesicle therapy for pulmonary fibrosis via inhibition of TGF-β-WNT crosstalk. Journal of Extracellular Vesicles. 2021;10(10).

299. Gabbiani G. The myofibroblast in wound healing and fibrocontractive diseases. The Journal of Pathology. 2003;200(4):500-503.

300. Moore M, Herzog E. Regulation and Relevance of Myofibroblast Responses in Idiopathic Pulmonary Fibrosis. Current Pathobiology Reports. 2013;1(3):199-208.

301. Fujita Y, Araya J, Ito S, Kobayashi K, Kosaka N, Yoshioka Y et al. Suppression of autophagy by extracellular vesicles promotes myofibroblast differentiation in COPD pathogenesis. Journal of Extracellular Vesicles. 2015;4(1):28388.

302. Kadota T, Yoshioka Y, Fujita Y, Araya J, Minagawa S, Hara H et al. Extracellular Vesicles from Fibroblasts Induce Epithelial-Cell Senescence in Pulmonary Fibrosis. American Journal of Respiratory Cell and Molecular Biology. 2020;63(5):623-636.

303. de Haan L, Suijker J, van Roey R, Berges N, Petrova E, Queiroz K et al. A Microfluidic 3D Endothelium-on-a-Chip Model to Study Transendothelial Migration of T Cells in Health and Disease. International Journal of Molecular Sciences. 2021;22(15):8234.

304. Frenkel N, Poghosyan S, Alarcón C, García S, Queiroz K, van den Bent L et al. Long-Lived Human Lymphatic Endothelial Cells to Study Lymphatic Biology and Lymphatic Vessel/Tumor Coculture in a 3D Microfluidic Model. ACS Biomaterials Science & Engineering. 2021;7(7):3030-3042.

305. Schutgens F, Rookmaaker M, Margaritis T, Rios A, Ammerlaan C, Jansen J et al. Tubuloids derived from human adult kidney and urine for personalized disease modeling. Nature Biotechnology. 2019;37(3):303-313.

306. Junaid A, Duinen V, Stam W, Dólleman S, Yang W, Rijke Y et al. A Microfluidics-Based Screening Tool to Assess the Impact of Blood Plasma Factors on Microvascular Integrity. Advanced Biology. 2021;5(11):2100954.

307. Hagiwara Y, Kumagai H, Ouwerkerk N, Gijzen L, Annida R, Bokkers M et al. A Novel In Vitro Membrane Permeability Methodology Using Three-dimensional Caco-2 Tubules in a Microphysiological System Which Better Mimics In Vivo Physiological Conditions. Journal of Pharmaceutical Sciences. 2022;111(1):214-224.

308. Wevers N, Nair A, Fowke T, Pontier M, Kasi D, Spijkers X et al. Modeling ischemic stroke in a triculture neurovascular unit on-a-chip. Fluids and Barriers of the CNS. 2021;18(1).

309. Vormann M, Tool L, Ohbuchi M, Gijzen L, van Vught R, Hankemeier T et al. Modelling and Prevention of Acute Kidney Injury through Ischemia and Reperfusion in a Combined Human Renal Proximal Tubule/Blood Vessel-on-a-Chip. Kidney360. 2021;3(2):217-231.

310. Jung O, Tung Y, Sim E, Chen Y, Lee E, Ferrer M et al. Development of human-derived, three-dimensional respiratory epithelial tissue constructs with perfusable microvasculature on a high-throughput microfluidics screening platform. Biofabrication. 2022;14(2):025012.

311. Schneider K, Rohringer S, Kapeller B, Grasl C, Kiss H, Heber S et al. Riboflavin-mediated photooxidation to improve the characteristics of decellularized human arterial small diameter vascular grafts. Acta Biomaterialia. 2020;116:246-258.

312. Heng J, Yazid M, Abdul Rahman M, Sulaiman N. Coatings in Decellularized Vascular Scaffolds for the Establishment of a Functional Endothelium: A Scoping Review of Vascular Graft Refinement. Frontiers in Cardiovascular Medicine. 2021;8.

313. Vulto P, Joore J. Adoption of organ-on-chip platforms by the pharmaceutical industry. Nature Reviews Drug Discovery. 2021;20(12):961-962.

314. Taeusch H, Gleason C, Ballard R. Avery's diseases of the newborn. 5th ed. W.B. Saunders; 2005.

315. Moscoso G, Nandra K, Driver M. Ciliogenesis and Ciliation of the Respiratory Epithelium in the Human Fetal Cartilaginous Trachea. Pathology - Research and Practice. 1989;184(2):161-167.

316. Park H, O'Sullivan M, Vallarino J, Shumyatcher M, Himes B, Park J et al. Transcriptomic response of primary human airway epithelial cells to flavoring chemicals in electronic cigarettes. Scientific Reports. 2019;9(1).

317. Joshi M, Goraya H, Joshi A, Bartter T. Climate change and respiratory diseases. Current Opinion in Pulmonary Medicine. 2020;26(2):119-127.

318. Preibisch S, Saalfeld S, Tomancak P. Globally optimal stitching of tiled 3D microscopic image acquisitions. Bioinformatics. 2009;25(11):1463-1465.

319. Sampaio P, da Silva M, Vale I, Roxo-Rosa M, Pinto A, Constant C et al. CiliarMove: new software for evaluating ciliary beat frequency helps find novel mutations by a Portuguese multidisciplinary team on primary ciliary dyskinesia. ERJ Open Research. 2021;7(1):00792-2020.

320. Leung C, Wadsworth S, Yang S, Dorscheid D. Structural and functional variations in human bronchial epithelial cells cultured in air-liquid interface using different growth media. American Journal of Physiology-Lung Cellular and Molecular Physiology. 2020;318(5):L1063-L1073.

321. Kouthouridis S, Goepp J, Martini C, Matthes E, Hanrahan J, Moraes C. Oxygenation as a driving factor in epithelial differentiation at the air–liquid interface. Integrative Biology. 2021;13(3):61-72.

322. Noguchi M, Furukawa K, Morimoto M. Pulmonary neuroendocrine cells: physiology, tissue homeostasis and disease. Disease Models & Mechanisms. 2020;13(12).

323. Li X, Balagam R, He T, Lee P, Igoshin O, Levine H. On the mechanism of long-range orientational order of fibroblasts. Proceedings of the National Academy of Sciences. 2017;114(34):8974-8979.

324. Robinson NB, Krieger K, Khan FM, Huffman W, Chang M, Naik A et al. The current state of Animal Models in research: A Review. International Journal of Surgery. 2019;72:9–13.

325. Walters MS, Gomi K, Ashbridge B, Moore MA, Arbelaez V, Heldrich J et al. Generation of a human airway epithelium derived basal cell line with multipotent differentiation capacity. Respiratory Research. 2013;14(1).

326. Kuek LE, Griffin P, Martinello P, Graham AN, Kalitsis P, Robinson PJ et al. Identification of an immortalized human airway epithelial cell line with dyskinetic cilia. American Journal of Respiratory Cell and Molecular Biology. 2018;59(3):375–82.

327. Grant J, Özkan A, Oh C, Mahajan G, Prantil-Baun R, Ingber DE. Simulating drug concentrations in PDMS microfluidic organ chips. Lab on a Chip. 2021;21(18):3509–19.

328. Plebani R, Potla R, Soong M, Bai H, Izadifar Z, Jiang A et al. Modeling pulmonary cystic fibrosis in a human lung airway-on-a-chip. Journal of Cystic Fibrosis. 2022;21(4):606–15.

329. Henry OY, Villenave R, Cronce MJ, Leineweber WD, Benz MA, Ingber DE. Organs-on-chips with integrated electrodes for trans-epithelial electrical resistance (teer) measurements of human epithelial barrier function. Lab on a Chip. 2017;17(13):2264–71.

330. Si L, Bai H, Oh CY, Jin L, Prantil-Baun R, Ingber DE. Clinically relevant influenza virus evolution reconstituted in a human lung airway-on-a-chip. Microbiology Spectrum. 2021;9(2).

331. Skardal A, Murphy SV, Devarasetty M, Mead I, Kang H-W, Seol Y-J et al. Multi-tissue interactions in an integrated three-tissue organ-on-a-chip platform. Scientific Reports. 2017;7(1).

332. Hashimoto R, Takahashi J, Shirakura K, Funatsu R, Kosugi K, Deguchi S et al. SARS-COV-2 disrupts respiratory vascular barriers by suppressing Claudin-5 expression. Science Advances. 2022;8(38).

333. Fernandes J, Karra N, Bowring J, Reale R, James J, Blume C et al. Real-time monitoring of epithelial barrier function by impedance spectroscopy in a microfluidic platform. Lab on a Chip. 2022;22(10):2041–54.

334. Nawroth J, Lucchesi C, Cheng D, Shukla A, Ngyuen J, Shroff T et al. A micro-engineered airway lung-chip models key features of viral-induced exacerbation of asthma. 2020;

335. Coppeta JR, Mescher MJ, Isenberg BC, Spencer AJ, Kim ES, Lever AR et al. A portable and reconfigurable multi-organ platform for drug development with onboard microfluidic flow control. Lab on a Chip. 2017;17(1):134–44.

336. Edington CD, Chen WL, Geishecker E, Kassis T, Soenksen LR, Bhushan BM et al. Interconnected microphysiological systems for Quantitative Biology and Pharmacology Studies. Scientific Reports. 2018;8(1).

337. Schimek K, Frentzel S, Luettich K, Bovard D, Rütschle I, Boden L et al. Human multi-organ chip co-culture of bronchial lung culture and liver spheroids for substance exposure studies. Scientific Reports. 2020;10(1).

338. Stucki AO, Stucki JD, Hall SR, Felder M, Mermoud Y, Schmid RA et al. A lung-on-a-chip array with an integrated bio-inspired respiration mechanism. Lab on a Chip. 2015;15(5):1302–10.

339. Mermoud Y, Felder M, Stucki JD, Stucki AO, Guenat OT. Microimpedance tomography system to monitor cell activity and membrane movements in a breathing lung-on-chip. Sensors and Actuators B: Chemical. 2018;255:3647–53.

340. Sun T, Swindle EJ, Collins JE, Holloway JA, Davies DE, Morgan H. On-chip epithelial barrier function assays using electrical impedance spectroscopy. Lab on a Chip. 2010;10(12):1611.

341. Blume C, Reale R, Held M, Millar TM, Collins JE, Davies DE et al. Temporal monitoring of differentiated human airway epithelial cells using microfluidics. PLOS ONE. 2015;10(10).

342. Blume C, Reale R, Held M, Loxham M, Millar TM, Collins JE et al. Cellular crosstalk between airway epithelial and endothelial cells regulates barrier functions during exposure to double-stranded RNA. Immunity, Inflammation and Disease. 2017;5(1):45–56.

343. Gupta G, Vallabani S, Bordes R, Bhattacharya K, Fadeel B. Development of microfluidic, serum-free bronchial epithelial cells-on-a-chip to facilitate a more realistic in vitro testing of nanoplastics. Frontiers in Toxicology. 2021;3.

344. Schneider CA, Rasband WS, Eliceiri KW. NIH Image to ImageJ: 25 years of image analysis. Nature Methods. 2012;9(7):671–675.

345. Schindelin J, Arganda-Carreras I, Frise E, Kaynig V, Longair M, Pietzsch T et al. Fiji: an open-source platform for biological-image analysis. Nature Methods. 2012;9(7):676–682.

346. Nof E, Zidan H, Artzy-Schnirman A, Mouhadeb O, Beckerman M, Bhardwaj S et al. Human Multi-Compartment Airways-on-chip platform for emulating respiratory airborne transmission: From nose to pulmonary acini. Frontiers in Physiology. 2022;13.

347. Jones B, Donovan C, Liu G, Gomez HM, Chimankar V, Harrison CL et al. Animal models of COPD: What do they tell us? Respirology. 2016;22(1):21–32.

348. Webb DC, McKenzie AN, Koskinen AM, Yang M, Mattes Joërg, Foster PS. Integrated signals between IL-13, IL-4, and il-5 Regulate Airways hyperreactivity. The Journal of Immunology. 2000;165(1):108–13.

349. Foster PS, Hogan SP, Ramsay AJ, Matthaei KI, Young IG. Interleukin 5 deficiency abolishes eosinophilia, airways hyperreactivity, and lung damage in a mouse asthma model. Journal of Experimental Medicine. 1996;183(1):195–201.

350. Picollet-D'hahan N, Zuchowska A, Lemeunier I, Le Gac S. Multiorgan-on-a-chip: A systemic approach to model and Decipher Inter-organ communication. Trends in Biotechnology. 2021;39(8):788–810.

351. Armutcu F. Organ crosstalk: The potent roles of inflammation and fibrotic changes in the course of Organ Interactions. Inflammation Research. 2019;68(10):825–39.

352. Chancharoenthana W, Leelahavanichkul A. Acute kidney injury spectrum in patients with chronic liver disease: Where do we stand? World Journal of Gastroenterology. 2019;25(28):3684–703.

353. Basrai Z. Increased risk of myocardial infarction and stroke following exacerbation of COPD. The Journal of Emergency Medicine. 2010;39(5):709–10.

354. Brusselle GG, Kips JC, Tavernier JH, Heyden JG, Cuvelier CA, Pawels RA et al. Attenuation of allergic airway inflammation in IL-4 deficient mice. Clinical Experimental Allergy. 1994;24(1):73–80.

355. Cohn L, Herrick C, Niu N, Homer RJ, Bottomly K. IL-4 promotes airway eosinophilia by suppressing IFN-γ production: Defining a novel role for IFN-γ in the regulation of allergic airway inflammation. The Journal of Immunology. 2001;166(4):2760–7.

356. Foster PS, Yang M, Herbert C, Kumar RK. CD4+ T-lymphocytes regulate airway remodeling and hyper-reactivity in a mouse model of chronic asthma. Laboratory Investigation. 2002;82(4):455–62.

357. Wiegman CH, Michaeloudes C, Haji G, Narang P, Clarke CJ, Russell KE et al. Oxidative stress–induced mitochondrial dysfunction drives inflammation and airway smooth muscle remodeling in patients with chronic obstructive pulmonary disease. Journal of Allergy and Clinical Immunology. 2015;136(3):769–80.

358. He S, Li L, Sun S, Zeng Z, Lu J, Xie L. A novel murine chronic obstructive pulmonary disease model and the pathogenic role of MicroRNA-21. Frontiers in Physiology. 2018;9.

359. Churg A, Wang RD, Tai H, Wang X, Xie C, Wright JL. Tumor necrosis factor-α drives 70% of cigarette smoke–induced emphysema in the mouse. American Journal of Respiratory and Critical Care Medicine. 2004;170(5):492–8.